Endwall Blockage in Axial Compressors

by

Amrit Singh Khalsa

Submitted to the Department of Aeronautics and Astronautics in partial fulfillment of the requirements for the degree of

Doctor of Philosophy
at the

Massachusetts Institute of Technology

June 1996

Author.....
Department of Aeronautics and Astronautics
April 4, 1996

Certified by.....
Professor Ian A. Waitz
Thesis Supervisor

Certified by.....
Professor Edward M. Greitzer

Certified by.....
Dr. Choon S. Tan
Principal Research Engineer

Certified by.....
Professor Manuel Martinez-Sanchez

Accepted by.....
Professor Harold Y. Wachman
Chairman, Department Graduate Committee

Endwall Blockage in Axial Compressors

by

Amrit Singh Khalsa

Submitted to the Department of Aeronautics and
Astronautics in partial fulfillment of the requirements for
the degree of Doctor of Philosophy

Abstract

An analysis has been developed to estimate tip clearance flow related blockage in axial compressors. Numerical simulations, experiments in a low speed rotating rig, and in a specifically designed wind tunnel test section were used to define the flow features that impact blockage, and to quantify the links between the parametric trends of endwall blockage and design parameter variations. The analysis allows prediction of the trends of endwall blockage in axial compressors due to changes in clearance height, stagger angle, inlet boundary layer thickness, loading level and loading profile, solidity, and clearance jet total pressure.

The blockage model proposed assumes that the clearance leakage jet and the free stream fluid interact such that the kinetic energy of the velocity components normal to their resultant direction is lost. The velocity defect associated with this loss grows in the adverse pressure gradient within the blade row. Absolute values of clearance related blockage were calculated with an average error of 33% for the cases tested. More importantly perhaps, trends in blockage with changes in design parameters are captured within 8%.

The double leakage of fluid from one clearance gap into the adjacent blade's tip gap, a previously unreported flow field feature, is described; and a method for predicting when this phenomenon will exist is developed.

Three techniques for reducing endwall blockage are evaluated: increasing the clearance jet total pressure, three-dimensional blade design to reduce the tip region blade loading, and increasing the mixing between the jet and the free stream.

Thesis Supervisor: Professor Ian A. Waitz

Acknowledgments

This work was carried out with the financial support of the NASA Lewis Research Center, with Mr. G. Skoch and Dr. A. Strazisar program monitors of grant #NAG3-1237; and the Air Force Office of Scientific Research, Air Force Research in Aeropropulsion Technology (AFRAPT) grant # F49620-94-1-0307, with Dr. J. McMichael program monitor. I am grateful for this support. I would also like to thank Professor Ed Greitzer, the contract Principal Investigator, and Holly Rathbun, Gas Turbine Laboratory Financial Officer, for allowing me the freedom to do research without worrying about the financial support.

I am also thankful for my thesis committee, consisting of Prof. Ian Waitz, Prof. Ed Greitzer, Dr. Choon Tan, and Prof. Manuel Martinez-Sanchez. For their useful consultations I would like to thank Professors Nick Cumpsty and Frank Marble. And for the opportunity to take data on the Deverson Rig I am thankful to both Rolls Royce and the Whittle Laboratory at Cambridge University, especially Mike Howard and Prof. Nick Cumpsty.

Many of my fellow students helped me with this research, but I would especially like to thank Syed Arif Khalid, John Bolger, and John Brookfield for giving me the benefits of their knowledge and their time.

Of course my family played the largest role in getting me to where I am, and I am thankful for their support, encouragement, acceptance, and their values.

And lastly I'd like to express my gratitude to Mukhia Singh Sahib Gurucharan Singh Khalsa and Siri Singh Sahib Bhai Sahib Harbajan Singh Khalsa Yogiji for being true teachers to me.

Contents

List of Figures

Nomenclature

A_b	Blockage
b	Wake height parameter in integral wake mixing model
c	Chord
C_D	Discharge coefficient
C_x	Axial velocity
CP_S	Static pressure coefficient, $\frac{\overline{P_{S,exit}}^{a} - \overline{P_{S,inlet}}}{Q_{inlet}}$
CP_T	Total pressure coefficient, $\frac{\overline{P_{T,exit}}^{a} - \overline{P_{T,inlet}}}{Q_{inlet}}$
Δl	Length of one chordwise segment of the leakage jet
h	Blade height
$\dot{m}$	Mass flux
P_S	Static pressure
P_T	Total pressure
Q_{inlet}	Inlet free streram average dynamic head, $\overline{P_{T,inlet}} - \overline{P_{S,inlet}}$
r	radius
Re	Reynolds number based on chord and relative inlet velocity
s	Staggered spacing
U	Velocity
V	Velocity
α	Angle between leakage jet and blade surface
α_0	Ratio of velocity in defect to free stream
β	Wake depth parameter in integral wake mixing model
β_e	Relative flow exit angle

β_{vm}	Relative vector mean flow angle
γ	stagger angle
δ^*	Displacement thickness
ΔP_P	Passage pressure rise
ΔP_B	Pressure difference across the blade
ζ	mean leakage angle
ρ	Density
Ψ	Pressure rise coefficient
σ	solidity
Θ	Momentum thickness
Θ	Angle between blade stagger and jet-free stream interaction line
τ	Clearance height

Subscripts

clrnc	quantity at clearance exit
edge	quantity at the edge of the defect region
exit	quantity at the passage exit
FS	Free stream
in	quantity at inlet
L	leakage jet
local	quantity locally defined
PS	One the pressure surface
SS	On the suction surface
sw	Streamwise direction
2τ	at inlet two clearance heights from endwall

Operators

$\overline{(\ )}^a$	Area average
$\overline{(\ )}^m$	Mass average

Chapter 1: Introduction

1.1 Background

The flow in the endwall region of axial compressors is critical to the performance and stability of the compressor. The flow through the clearance between the rotor blades and adjacent non-rotating casing reduces compressor efficiency, and can play a role in stall inception. Wisler (1981) suggests that half or more of the loss in an axial compressor is due to the flow in this endwall region. Figure 1-1, from Wisler (1985a), illustrates the effect of tip clearance on compressor efficiency, stall margin, and stalling pressure rise. Figure 1-2 shows the effect of tip clearance on pressure rise versus mass flow characteristics from Smith and Cumpsty (1984). As the tip clearance is increased, the pressure rise and the stable flow range of the compressor is reduced.

Khalid (1995a) argued that the flattening of the characteristics in Figure 1-2 at lower mass flows is primarily due to increased blockage, in other words a reduction in effective flow area due to a velocity defect associated with the tip clearance flow. As the tip clearance gap is increased, velocity defects in the endwall region become deeper and larger in scale, reducing the effective area, the amount of diffusion, and hence the pressure rise.

The effects of endwall blockage on performance (pressure rise) and stability (stall) motivate the need for a better understanding of the endwall flow field. Cumpsty (1989) has stated that the endwall region of axial compressors is the most important and the least well understood area of the compressor; blockage and loss are currently predicted by correlations.

The reduction in stable operating range due to tip clearance, as illustrated in Figure 1-2,

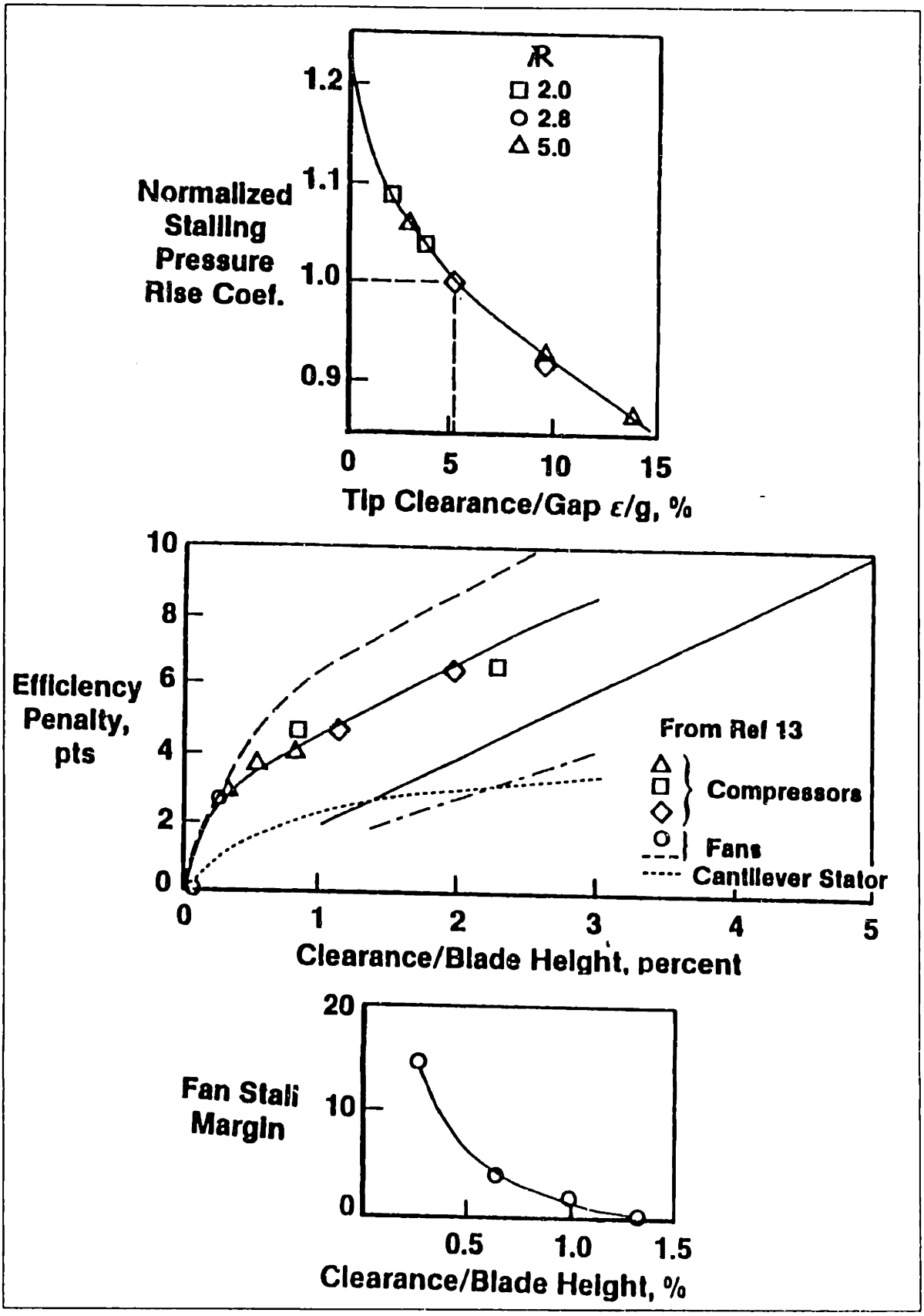

Figure 1-1: Effects of Tip Clearance, from Wisler (1985a)

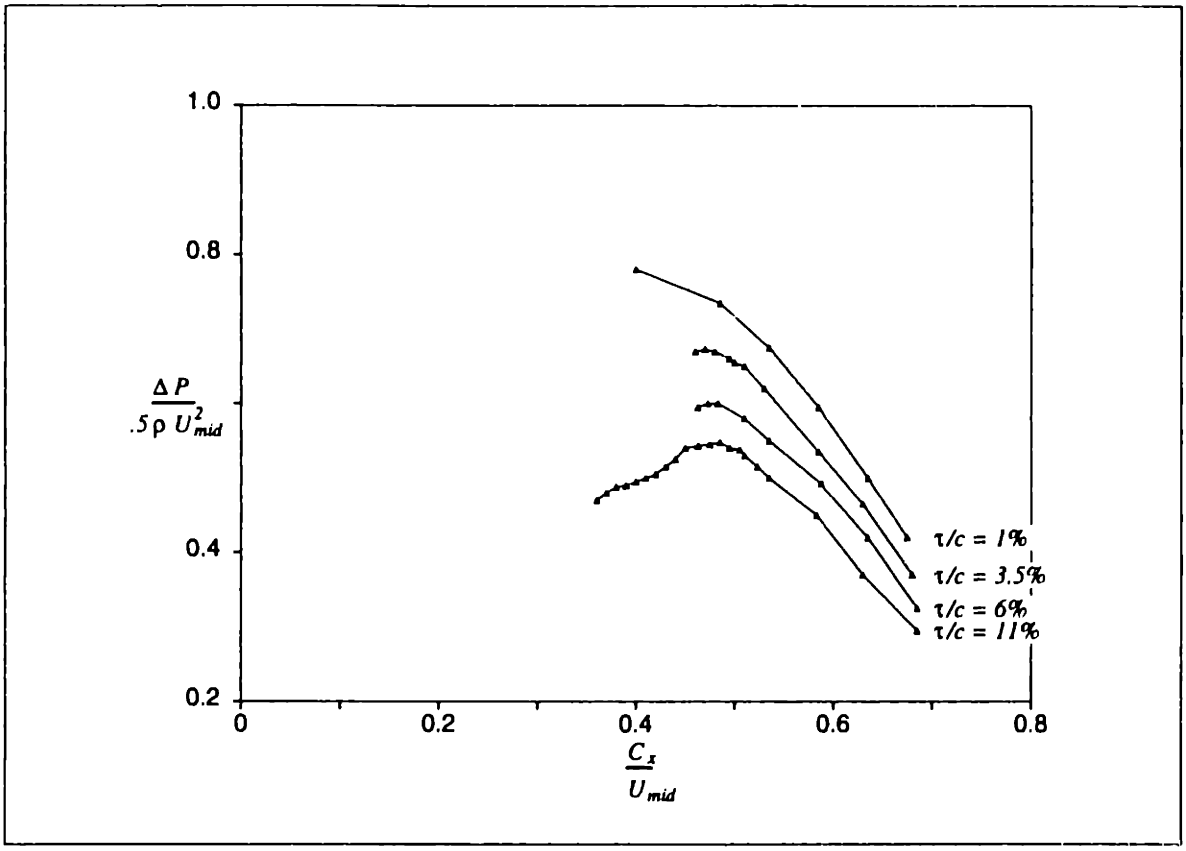

Figure 1-2: Compressor Characteristics for Various Tip Clearance Sizes from Smith and Cumpsty (1984)

has prompted research into alleviation schemes. Favorable modifications to the endwall flow field have been achieved by employing casing treatments, axial slots or circumferential grooves cut into the casing above the blade tips. The design of these treatments is still largely empirical. These endwall modifications have shown (see for example Fujita and Takata, 1984) stall margin improvements of up to 20%, but with a performance penalty (a decrease in the maximum efficiency) of 3 percentage points. Increased understanding of the physical processes associated with endwall blockage should pout the design of casing treatments on a more rational basis.

1.2 Previous Studies

This thesis develops a physically-based methodology for the study of endwall blockage, analyzes the parametric trends of endwall blockage, and develops a blockage prediction method. In this section relevant studies that set the context for this research are discussed.

Investigations of the flow field with smooth endwalls are first reviewed, followed by a discussion of casing treatment flow fields.

1.2.1 Clearance Flows with Smooth Endwalls

Khalid's (1995a) research was the background for much of this thesis. Khalid used three-dimensional Navier-Stokes solutions to calculate the blockage due to endwall flows. One of Khalid's major contributions was a methodology for quantifying blockage. This method is used in the present investigation, and will be described in detail in Chapter 2.

To present his results Khalid uses the following two parameters:

$$\frac{A_b \cdot \cos(\beta_e)}{\tau s / \sin(\beta_{vm})} \quad \text{and} \quad \frac{\overline{\Delta P_S}^a - \overline{\Delta P_T}^a}{Q_{2\tau}}.$$

The first parameter is the endwall blockage, A_b, multiplied by both the cosine of the exit flow angle, β_e, and the sine of the vector mean flow angle, β_{vm}, and divided by the clearance height, τ, times the blade stagger spacing, s. The second parameter is a loading parameter defined as the static pressure coefficient minus the relative total pressure coefficient. Both of these pressure coefficients are the pressure difference, static and total pressures respectively, between the exit and inlet planes divided by the inlet dynamic head. If these two parameters are plotted versus one another, as shown in Figure 1-3, data from the variety of configurations at various axial locations collapse onto a single trend line. This trend could be used to predict endwall blockage if the loading parameter could be estimated in the design process.

Khalid also suggested a two-dimensional wake model as a conceptual framework to view clearance related blockage. In this model the fluid leaking over the blade tips is divided into chordwise pieces with each piece treated as a wake growing in a pressure gradient. Khalid used the two-dimensional integral wake theory of Hill, et al. (1963) to describe the evolution of these wake segments as they pass from the blade tip to the exit plane of the passage. The inputs to the model are the wake initial conditions, described by a depth and

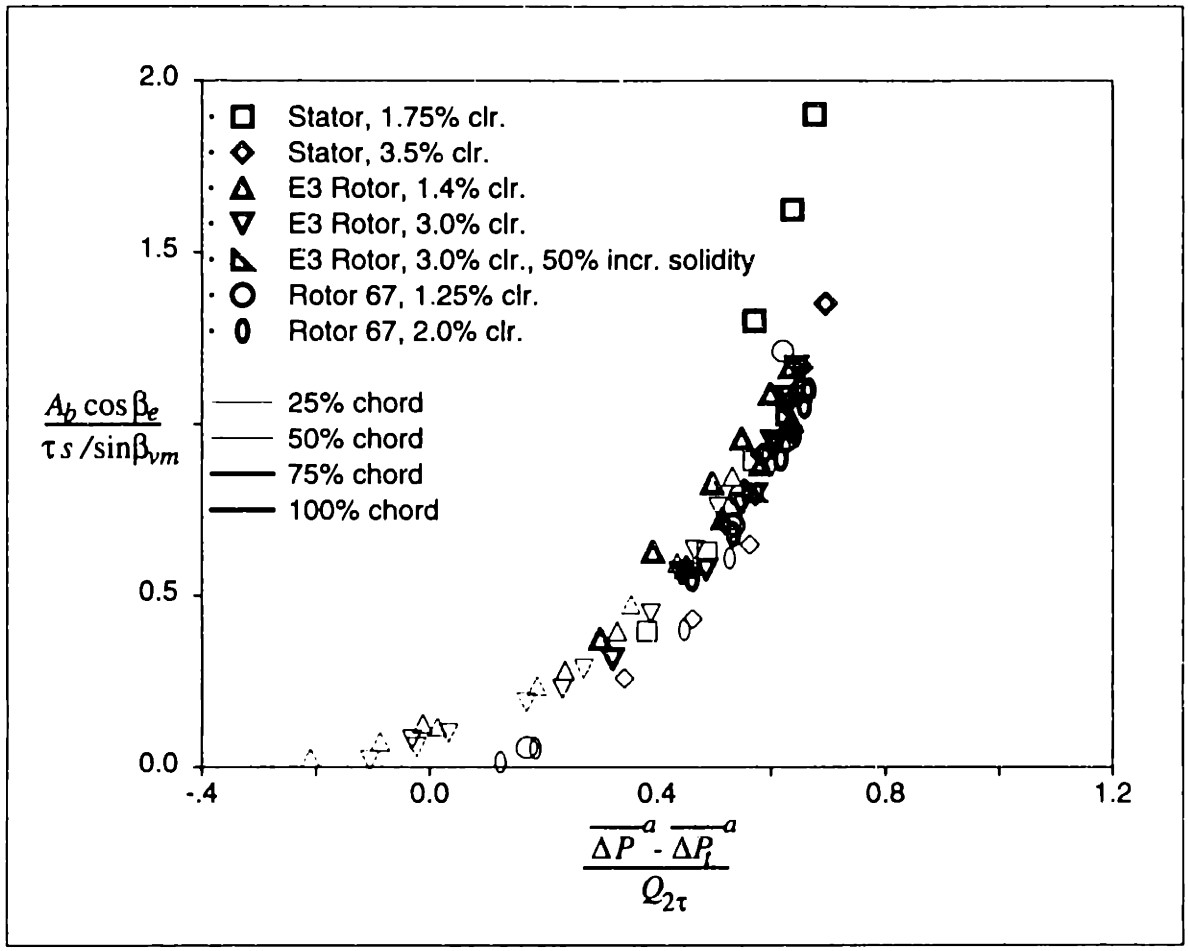

Figure 1-3: Normalized Blockage versus Loading Parameter from Khalid (1995)

a width with an assumed cosine shaped profile, the pressure field that the wake traverses, and a model for the eddy viscosity of the wake. Khalid used the Navier-Stokes results for the streamwise velocity just inboard of the blade suction surface to define the initial wake depth and width. The results of his model are replotted here as Figure 1-4, where the computational solutions plotted in Figure 1-3 were processed through the integral wake model. The loading values in the figure are identical to those in Figure 1-3. The model captured the overall qualitative trend of blockage with loading, but under-predicted the blockage by up to a factor of 2. In Chapter 4 a different model for endwall blockage is presented and evaluated.

Another research effort that helped provide direction to the present investigation was conducted by Storer (1991) who carried out experiments and computations for a rectilinear compressor cascade with tip clearance. Storer showed that three-dimensional Navier-

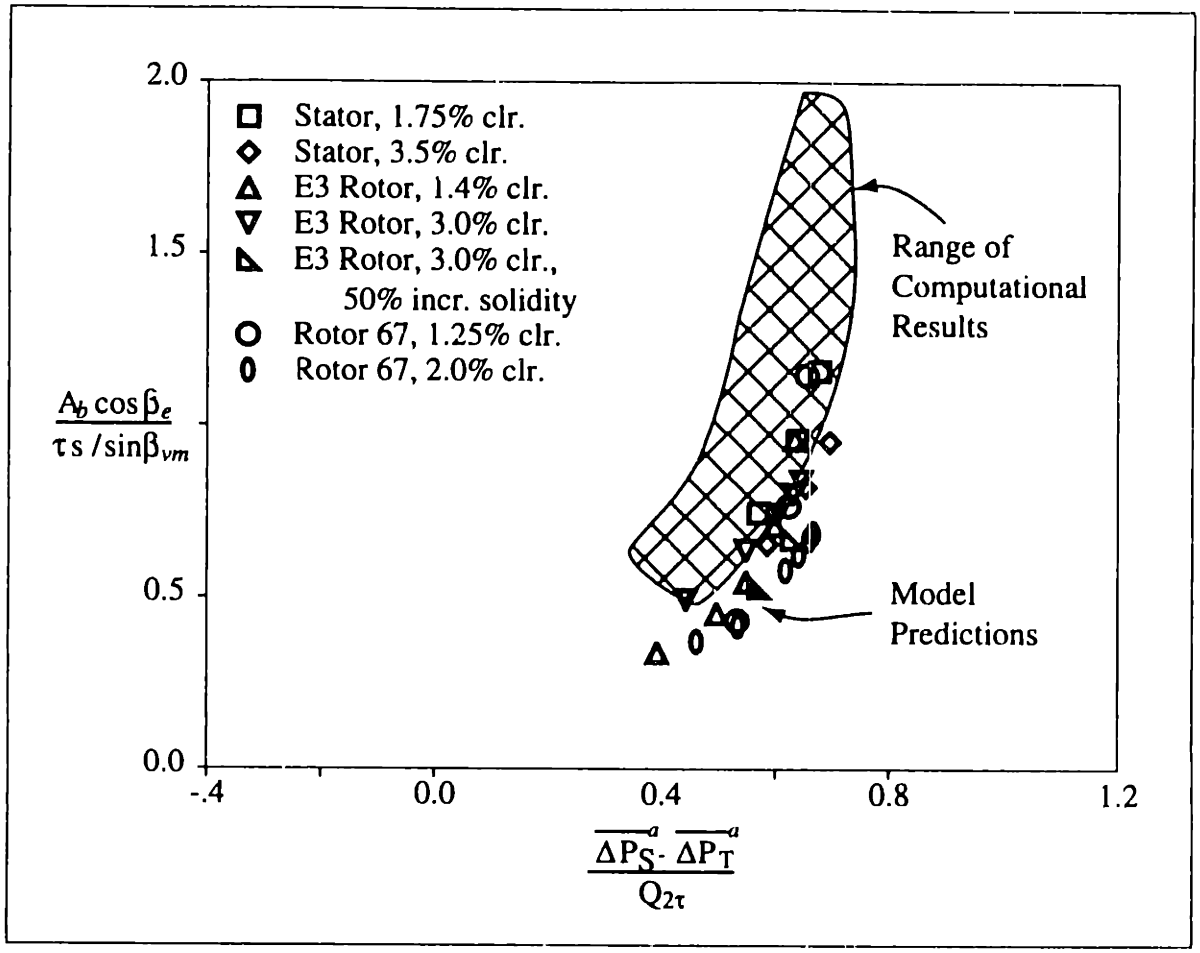

Figure 1-4: Model Blockage Predictions versus Loading Parameter, from Khalid (1995b)

Stokes calculations captured the observed trends of radial profiles of endwall loss and deviation with clearance changes. Storer also extended the work of Rains (1954), showing that the leakage flow can be modelled as an inviscid jet minimally influenced by the casing wall. His simplified model of the leakage jet is drawn schematically in Figure 1-5. Storer derived, and supported with data, a simple equation relating the leakage jet angle to the local pressure difference across the blade:

$$\alpha = \tan^{-1}\left[\sqrt{\frac{CP_{PS} - CP_{SS}}{CP_{T_{in}} - CP_{SS}}}\right], \qquad (1.1)$$

where α is the local leakage angle between the jet and the mean chord line, CP_{SS} and CP_{PS} are the pressure coefficients on the blade suction surface and pressure surface respectively, and CP_{Tin} is the inlet total pressure. This equation follows from the assump-

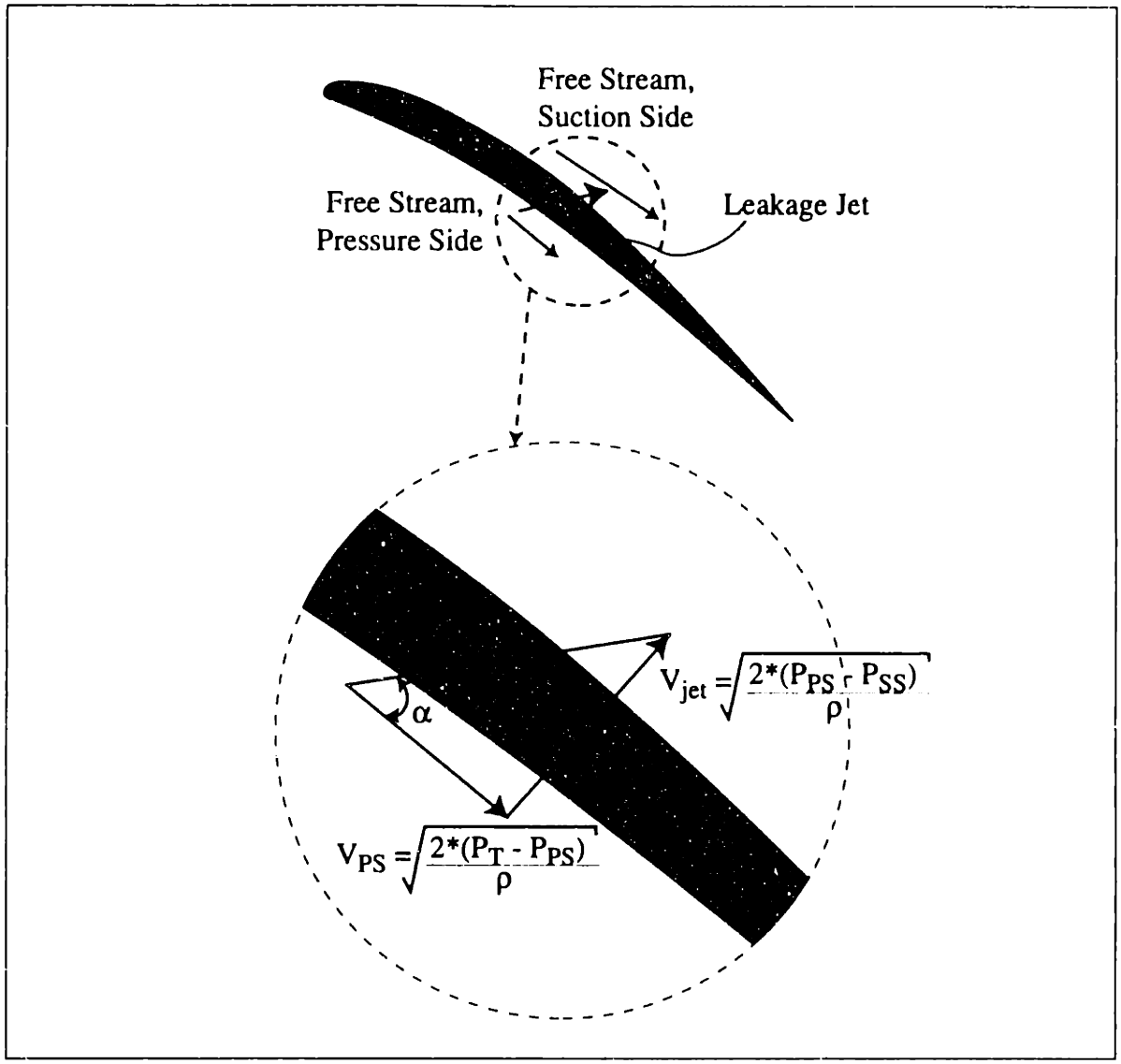

Figure 1-5: Schematic of a Pressure Driven Leakage Jet

tions that the free stream has undergone no loss, that no loss is generated within the tip clearance gap, and that the streamwise velocity of the leakage jet is the same as the pressure side free stream velocity (*i.e.*, the pressure gradients across the blade are much greater than those along the chord). The idea of a pressure driven leakage jet was first proposed by Rains (1954). The view of the leakage jet as pressure driven is used in this thesis to explain some of the parametric trends observed in the blockage data (Chapter 3), and in describing the endwall blockage (Chapter 4). How well the inviscid jet theory (Equation 1.1) predicts the observed leakage angles is evaluated in Section 3.2.

Loss due to tip clearance flow was examined by Storer and Cumpsty (1994), who found

that most of the loss occurs as the clearance jet mixes with the free stream flow, with little loss occurring within the clearance passage itself. This supports the use of Equation 1.1 for calculating the leakage angle of the clearance jet. Using a control volume analysis they showed that the mixed out loss due to the clearance jet can be computed from the clearance area and the mean leakage angle of the jet with respect to the free stream. Storer and Cumpsty showed further that the fully mixed out loss associated with the tip clearance flow can be predicted to within 5% (for $\tau/c>1\%$) using a control volume analysis. This analysis used the chordwise-averaged leakage angle and the clearance to passage area ratio as input parameters.

1.2.2 Casing Treatment

Smith and Cumpsty (1984) performed experiments with different clearance levels with and without casing treatment. The treatments they examined were 60° skewed axial slots extending over the middle 73% of the axial chord and having a 70% open area. They concluded that the removal of high loss fluid from the rear of the passage and its reinjection towards the front of the passage as a high relative total pressure jet were the primary processes acting to improve stall margin. They also observed that the effect of flow unsteadiness near the slots was small, suggesting that steady-state computational methods, such as that used in this thesis, may adequately simulate casing treatments.

Lee and Greitzer (1990) examined the effect of mass injection and removal separately by testing a cantilevered stator with a slotted hub. They examined 60° skewed axial slots with a 50% open area and varied the axial location and extent of the slots. Both mass injection and removal improved stall margin; but neither was as effective as the treatment where both were present, which increased stalling pressure rise by almost 80%. They also observed a correlation between the stalling pressure rise increase and the streamwise momentum flux of the injected flow, suggesting that energizing the high loss fluid is one mechanism for casing treatment's effectiveness.

Crook et al. (1993) used three-dimensional computations to examine the flow field of a cantilevered stator with and without endwall treatment on the hub. The treatment geome-

try studied was 60° skewed axial grooves extending from 5% to 95% chord. The effect of the treatment was simulated by imposing mass injection and removal, of 3.5% of the inlet mass flux, through the hub boundary. The amount was based on measurements by Johnson (1985) and Smith and Cumpsty (1982). The computations confirmed that the effectiveness of the treatment is due both to the removal of low total pressure fluid from the rear of the passage and the injection of high total pressure fluid towards the front. Streamline traces indicated that the injected fluid energizes the vortex core, increasing the core total pressure, but also that a significant fraction of the injected fluid simply passes through the passage without interacting significantly with the clearance flow. This suggests that more mass than is necessary is being injected.

Cho (1995) analyzed casing treatment over a transonic rotor blade row using an approach similar to Crook et al. (1993). His work is significant in that it uses the blockage framework of Khalid (1995) to examine casing treatment effectiveness, rather than stall margin improvement. Cho found that blowing alone did energize the endwall fluid, reducing blockage by 18% near stall; but that the removal of endwall fluid due to suction resulted in a larger reduction, almost 90%, in blockage. Cho's work was used for this thesis as a benchmark for the wind tunnel tests that are discussed in Chapter 5.

1.3 Problem Statement

The primary goals of this research were to:

- Identify and quantify the flow features that influence endwall blockage.
- Link these flow features to design parameters.
- Suggest quantitative criteria for blockage management.

In the course of the work the following questions are also addressed:

- What alterations of the leakage flow have the greatest leverage on blockage and pressure rise?
- Can a simple predictive scheme for endwall blockage be developed?

1.4 Approach

Data from many sources were brought together in this investigation. Endwall blockage at the trailing edge plane, using Khalid's (1995) definition, was the primary parameter of interest. Steady three-dimensional, Reynolds-averaged, Navier-Stokes computations were used, allowing detailed flow field investigation. Tests in a wind tunnel simulation of endwall flow were used to isolate key design parameters. Data from a low speed rotating compressor rig were used not only to support and confirm the computations, but also to test the ideas on another blade geometry.

1.5 Contributions of the Thesis

This thesis defines a set of parameters, different than those proposed previously, with which to present blockage data (Section 2.2). Blockage data from computations, rotating rig experiments, and a wind tunnel model follow a common trend when plotted using these parameters. Detailed measurements were made at the trailing edge of a rotating compressor rig, and the blockage was compared to Navier-Stokes solutions (Section 2.3). This work also quantifies and explains trends of endwall blockage with design parameters such as the clearance height, stagger, solidity, blade loading profile, and inlet boundary layer thickness (Section 3.3). A previously unreported flow phenomenon, the double leakage of clearance fluid, is described (subsection 3.2.3). A model is presented to predict when double leakage will occur, and its impact on endwall blockage is estimated. A simplified model is developed to describe and predict endwall blockage (Chapter 4). The model predicts changes in blockage for changes in design parameters such as stagger, solidity, clearance, and inlet boundary layer thickness (Section 4.4). The endwall blockage model was also used to suggest blockage reduction schemes, and to quantify flow field alterations needed to achieve blockage reduction (Chapter 5). The results indicate that the blockage reduction due to the mass injection regions of skewed axial slot casing treatments is due to the increase in clearance jet total pressure caused by the treatment.

1.6 Organization of the Thesis

In Chapter 2 the methodology, experimental details, and the rotating rig and computational data sets used in this investigation are described. A wind tunnel model of the tip clearance flow is described and the results from experiments in the wind tunnel are compared to the rotating rig data. In Chapter 3 the endwall flow features that impact the clearance jet are discussed, the experimentally observed parametric trends of blockage are examined, and the physical processes that link variations in design parameters to endwall blockage variations are explored. In Chapter 4 an analytical model for the development of clearance related blockage is presented and its implications explored. Suggestions for reducing blockage are presented and evaluated in Chapter 5. In Chapter 6 the results and conclusions of this thesis are summarized, and suggestions for future work are made.

Chapter 2: Methodology

2.1 Introduction

In this chapter the parameters used to quantify and present the blockage results are described, with the focus on how and why they capture the important physical processes of endwall blockage growth. A one-dimensional model of a velocity defect growing in an adverse pressure gradient is utilized to help motivate the appropriate parameters. The details of the experiments, both physical and computational, which were carried out to achieve the research goals are then presented. The experimental results are given, and the computational and the rotating rig data are compared. Finally, a wind tunnel model for the clearance jet is discussed, the experiments performed to verify this model are described, and their results are presented.

2.2 Physically-Based Parameters for Blockage Analysis

2.2.1 Introduction

A starting point for the discussion is the concept of blockage, defined as the reduction in effective flow area due to regions of low velocity. A common example is the displacement thickness concept for boundary layers, which represents the amount of effective flow area reduction the boundary layer causes. The displacement thickness is shown schematically in Figure 2-1. For incompressible, constant density flows, the effective flow area is related to the free stream velocity and the mass flux, as shown in Equation 2.1.

$$\int u dy = \frac{\dot{m}}{\rho} = U_{F.} \quad A_{eff}, \tag{2.1}$$

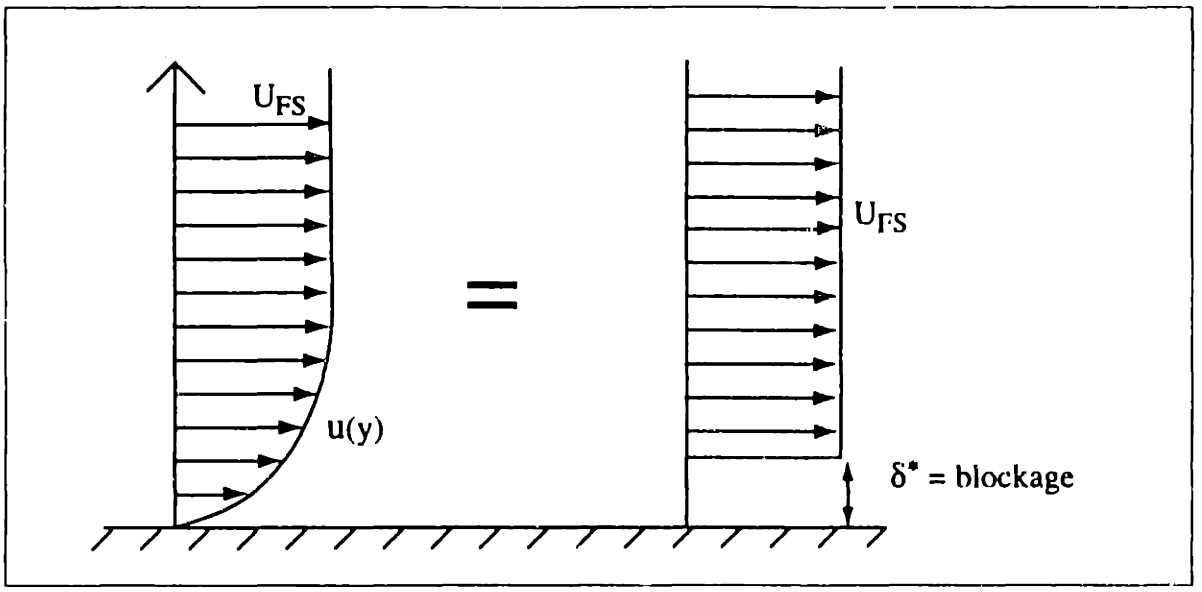

Figure 2-1: Blockage Schematic

where A_{eff} is the effective area and U_{FS} is the free stream velocity.

For inviscid, incompressible flows, Bernoulli's equation can be used to relate the free stream velocity to the static pressure. An increase in blockage reduces the effective flow area, lowering the amount of diffusion and hence the static pressure rise in a diffusing flow such as a compressor blade passage.

Recently, Khalid (1995a) put forward a definition for endwall blockage that extended the displacement thickness concept to the three-dimensional flow field found in the endwall region of compressors. Khalid's definition for endwall blockage, A_b, which is used through this thesis to quantify endwall blockage, can be written:

$$A_b = \iint \left(1 - \frac{v_{sw}}{V_{edge}} \right) dA \ .$$

The quantity v_{sw} is the streamwise velocity, V_{edge} is the velocity at the edge of the blockage region, and the integral is taken over the blockage region. More details on the procedure used to calculate A_b from experimental data is given in Appendix A.

The endwall blockage region is identified using the magnitude of the velocity gradient. Figure 2-2 shows an example of the blockage region from one of the computational solu-

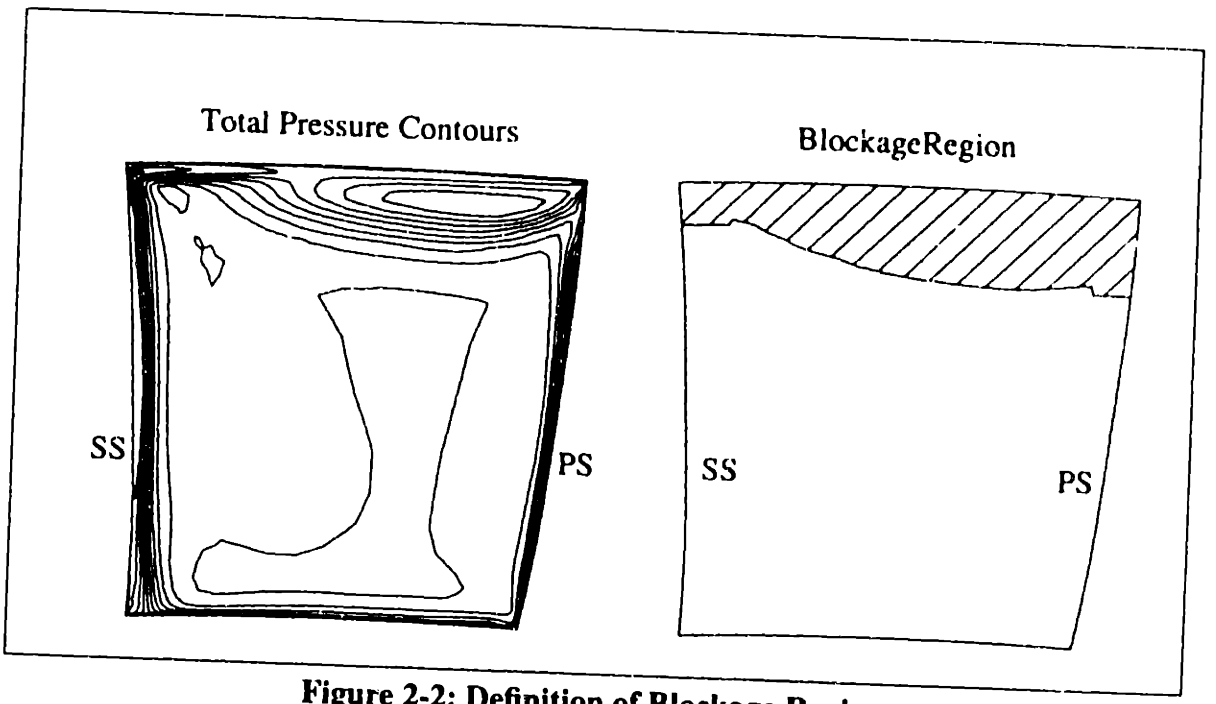

Figure 2-2: Definition of Blockage Region

tions for a low speed rotor compared to the region of high loss. The view in this figure is of the trailing edge plane, with the blade pressure and suction sides as indicated by PS and SS respectively. The total pressure coefficient contour intervals are 0.05 Q_{in}. This method of quantifying blockage is an application in three-dimensions of the displacement thickness for boundary layers, being responsible for changes in core region velocity changes, and hence passage pressure rise.

2.2.2 One-Dimensional Model

To help in understanding the behavior of velocity defects passing through pressure gradients and to offer a starting point for the development of predictive methods we first present a simple description of the process. This suggests the use of a set of parameters that collapse the blockage data onto a single trend line.

We consider a quasi-one dimensional flow and examine, with no mixing, a velocity defect passing through an adverse pressure gradient. This represents the leakage jet as a top hat profile velocity defect in a constant density, inviscid, incompressible flow. Figure 2-3 shows a schematic of the flow.

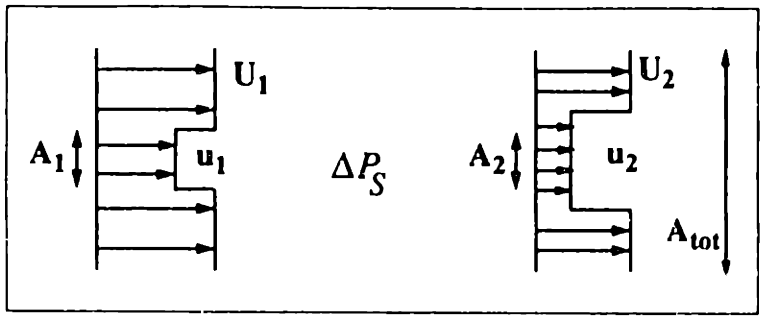

Figure 2-3: Schematic of Simple Model

The initial normalized velocity defect has a magnitude $\alpha_0 \equiv u_1/U_1$ and an extent of A_1. Of interest is the effective blocked area, A_{b_2}, at station 2, after the pressure rise. A_{b_2} is defined as

$$A_{b_2} \equiv \left(1 - \frac{u_2}{U_2}\right) \bullet A_2 \,. \tag{2.2}$$

Using the continuity and Bernoulli's equations to express u_2/U_2 gives

$$\frac{A_{b_2}}{A_1} = \alpha_0 \left[(\alpha_0^2 - CP_S)^{-1/2} - (1 - CP_S)^{-1/2} \right] \tag{2.3}$$

$$\text{where } CP_S \equiv \frac{\Delta P_S}{\frac{1}{2}\rho U_1^2}. \tag{2.4}$$

There are two points to note. First, Equation 2.3 shows that blockage is a function of both α_0 and CP_S. This is illustrated Figure 2-4(a), which shows A_b/A_1 versus CP_S for four different values of α_0 spanning the values observed in the flow fields examined in this thesis.

The second point, also seen in Figure 2-4(a), is the asymptotic behavior of each curve. There is a 'critical' value of CP_S, where the blockage increases rapidly, dependent on the initial defect. From Equation 2.3, the blockage will asymptote at a pressure rise coefficient equal to α_0^2.

The initial defect α_0 is not convenient for use with compressor leakage jets, so we rewrite

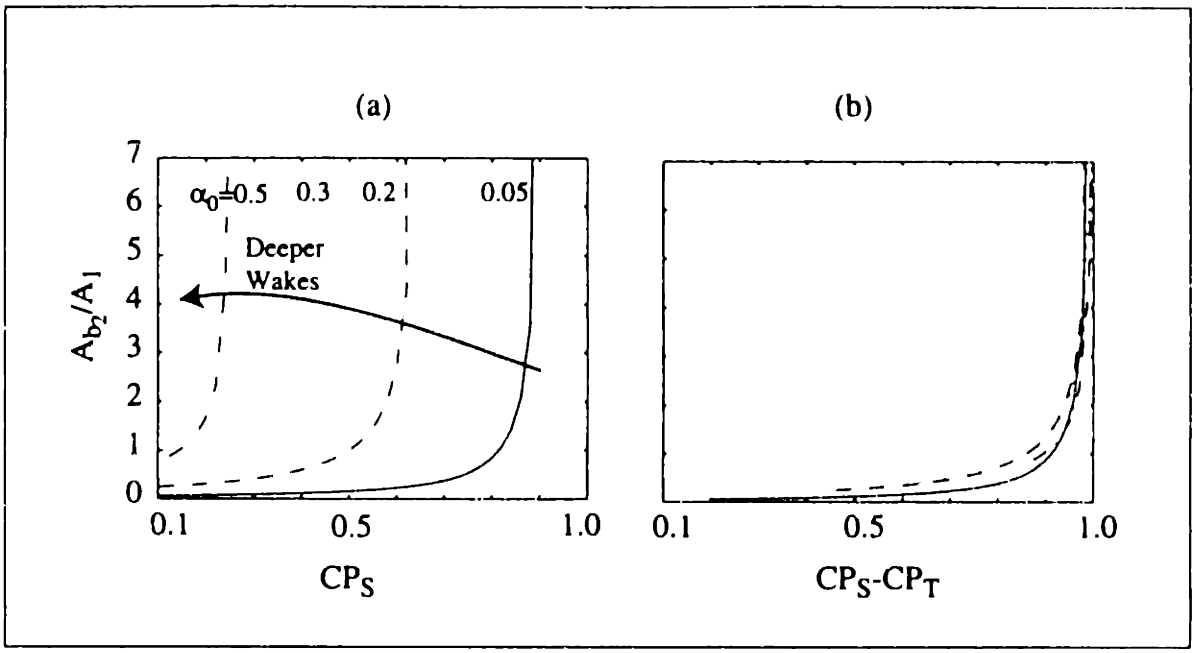

Figure 2-4: One-Dimensional Model Results: (a) Blockage as a Function of CP_S, (b) Blockage as a Function of CP_S-CP_T

Equation 2.3 using an exit plane total pressure coefficient, defined as follows:

$$CP_T \equiv \frac{P_{T,\,defect} - P_{T,\,freestream}}{Q_{in,\,freestream}} = \alpha_0^2 - 1 < 0.$$

With this definition, Equation 2.3 can be rewritten as

$$\frac{A_{b_2}}{A_1} = \sqrt{1 + CP_T} \bullet \{ [1 - (CP_S - CP_T)]^{-1/2} - (1 - CP_S)^{-1/2} \}. \qquad (2.5)$$

The advantage of writing the equation this way is that the blockage asymptote occurs when CP_S-CP_T = 1. Figure 2-4(b) shows how the different initial conditions are nearly collapsed to a single trend when blockage is plotted against this loading parameter CP_S-CP_T. Thus, although blockage depends on other parameters than CP_S-CP_T, Figure 2-4 demonstrates that, within the range of initial defects and static pressure rises observed in the compressor flow fields examined in this thesis, the primary trend is captured by the dependence on CP_S-CP_T.

Another way to understand why the curves in Figure 2-4(b) asymptote at CP_S-CP_T = 1 is

note that the loading parameter is related to the defect dynamic head as follows:

$$CP_S - CP_T = 1 - \frac{Q_{defect}}{Q_{in}} = 1 - \frac{u_2^2}{U_{in}^2} \quad . \tag{2.6}$$

Blockage will asymptote when the defect velocity decelerates to zero, which will occur when the loading parameter equals one.

The CP_S and CP_T parameters in the 1-D simplified description can be extended to an actual compressor tip leakage flow by defining the exit conditions as averages over the blockage region. The CP_T as used through this thesis is an average, taken over the blockage region rather than the entire passage.

Defining Pressure Coefficients

Khalid (1995a) defines a loading parameter referenced to inlet values. Exit average static and total pressures are calculated by area-averaging over the blockage region (the hatched region in Figure 2-2). These pressures are then referenced to values far upstream at a distance of 2 clearance heights from the endwall. This is illustrated in Figure 2-5. The 2τ definition is somewhat arbitrary, but was based on a representative distance of the clearance related blockage from the endwall. The low speed loading parameter Khalid used can be written as:

$$\text{loading parameter} = \frac{\overline{P_{S,\text{exit}}}^{a} - P_{S,\text{inlet } 2\tau}}{Q_{inlet,\,2\tau}} - \frac{\overline{P_{T,\text{exit}}}^{a} - P_{T,\text{inlet } 2\tau}}{Q_{inlet,\,2\tau}}. \tag{2.7}$$

Equation 2.4 suggests that normalizing by the inlet free stream values, rather than the 2τ values as in Equation 2.7, may be more useful in understanding the blockage trends. At the inlet plane in Figure 2-5 the demarkation between the exit plane velocity defect and the free stream fluid is shown. For the cases examined here the free stream fluid (defined as fluid at the edge of the blockage region) originated from approximately between 4 and 15 clearance heights from the endwall[1]. For the loading parameter definition used in this thesis the inlet reference values are defined as averages over this region of the free

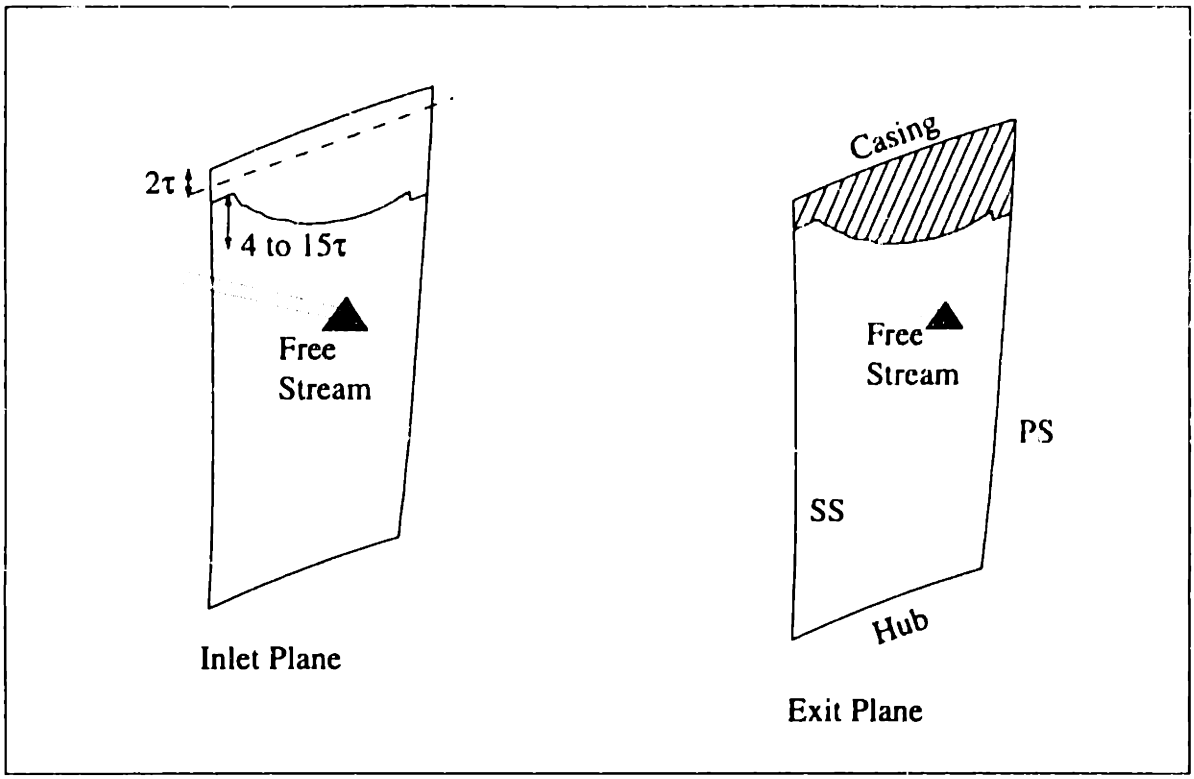

Figure 2-5: Inlet Normalization Schematic

stream[1].

The difference between this free stream normalization and the 2τ normalization is approximately 5%, but the free stream normalization is consistent with the simplified one-dimensional analysis given above. Figure 2-6 shows the CFD results from Khalid (1995a) presented using the 2τ normalization, and Figure 2-7 shows the same data presented with the suggested inlet freestream normalization. Data from five geometries are shown, three for a low speed rotor (LSR) and two for a low speed stator (LSS). There is a slight shift of the data to the right using the free stream normalization, but the trends and the comparisons of each geometry relative to the others are identical.

1. Changing these values that define the inlet free stream by several clearance heights did not significantly affect the results (< 3%). The choice of these values is somewhat arbitrary, but was based on observations of the cases studied here. Because of the insensitivity of the results to the precise choice of free stream regions, the definitions proposed here should apply to a broad range of compressor geometries.

1. The inlet relative total pressure is generally not radially uniform.

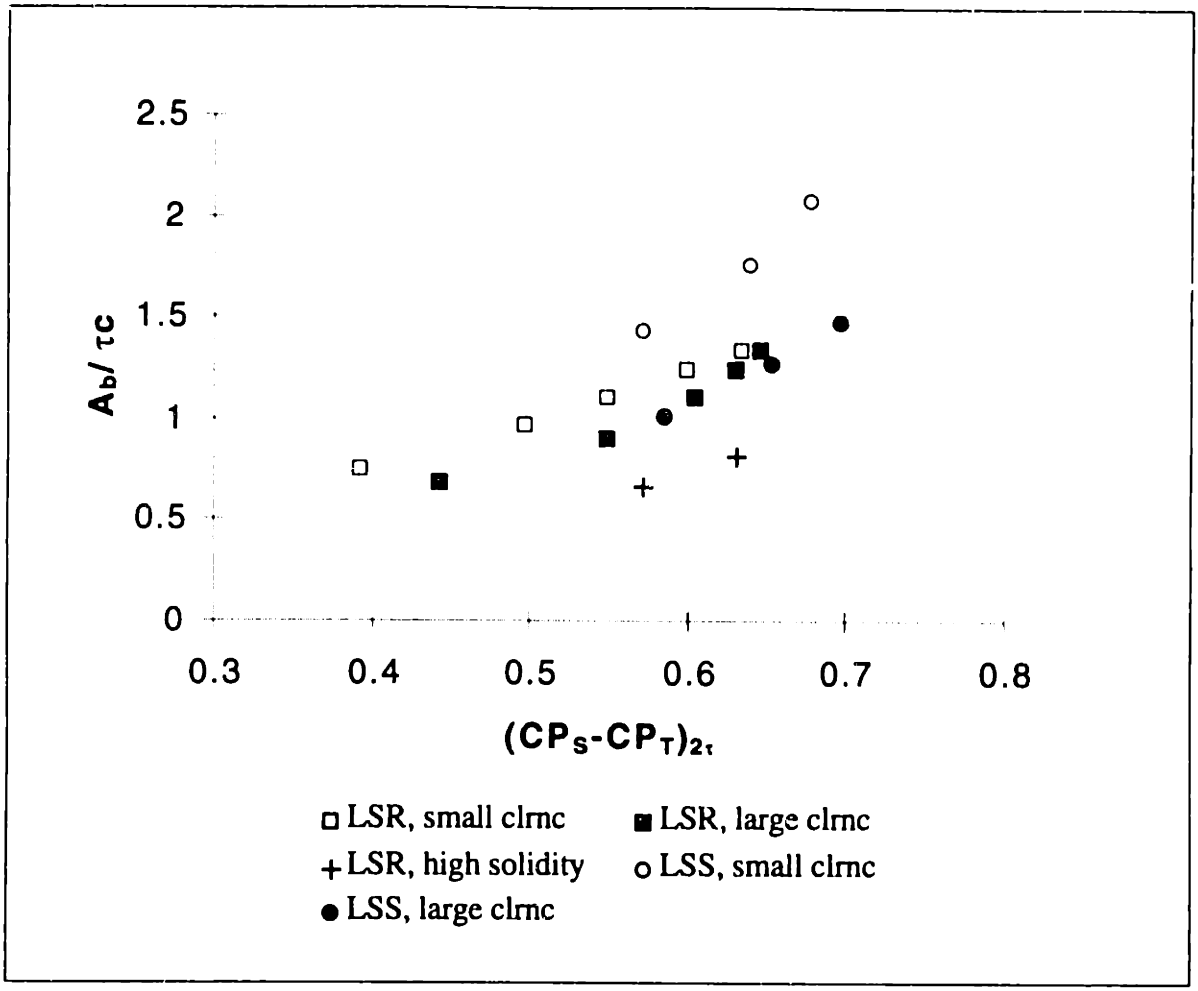

Figure 2-6: CFD Results Using Inlet 2τ Normalization, from Khalid (1995a), Normalized Blockage versus 2τ Loading Parameter

Blockage Normalization and Blockage Development Along the Chord

One conclusion presented by Khalid (1995a) is that the blockage does not depend on the chord length. It is argued here that this conclusion is incorrect, and an alternative explanation for the trend of the data is presented.

The data that lead to Khalid's conclusion are shown in Figure 2-8 where the blockage normalized by the clearance area, τc, is plotted at both 100% and 50% chord for five compressor geometries. If the data at 50% chord (which is normalized by half the blade chord times the clearance height) were reduced by a factor of two, i.e., if the data were normalized by the entire clearance area, they would fall along the same trend line as the 100%

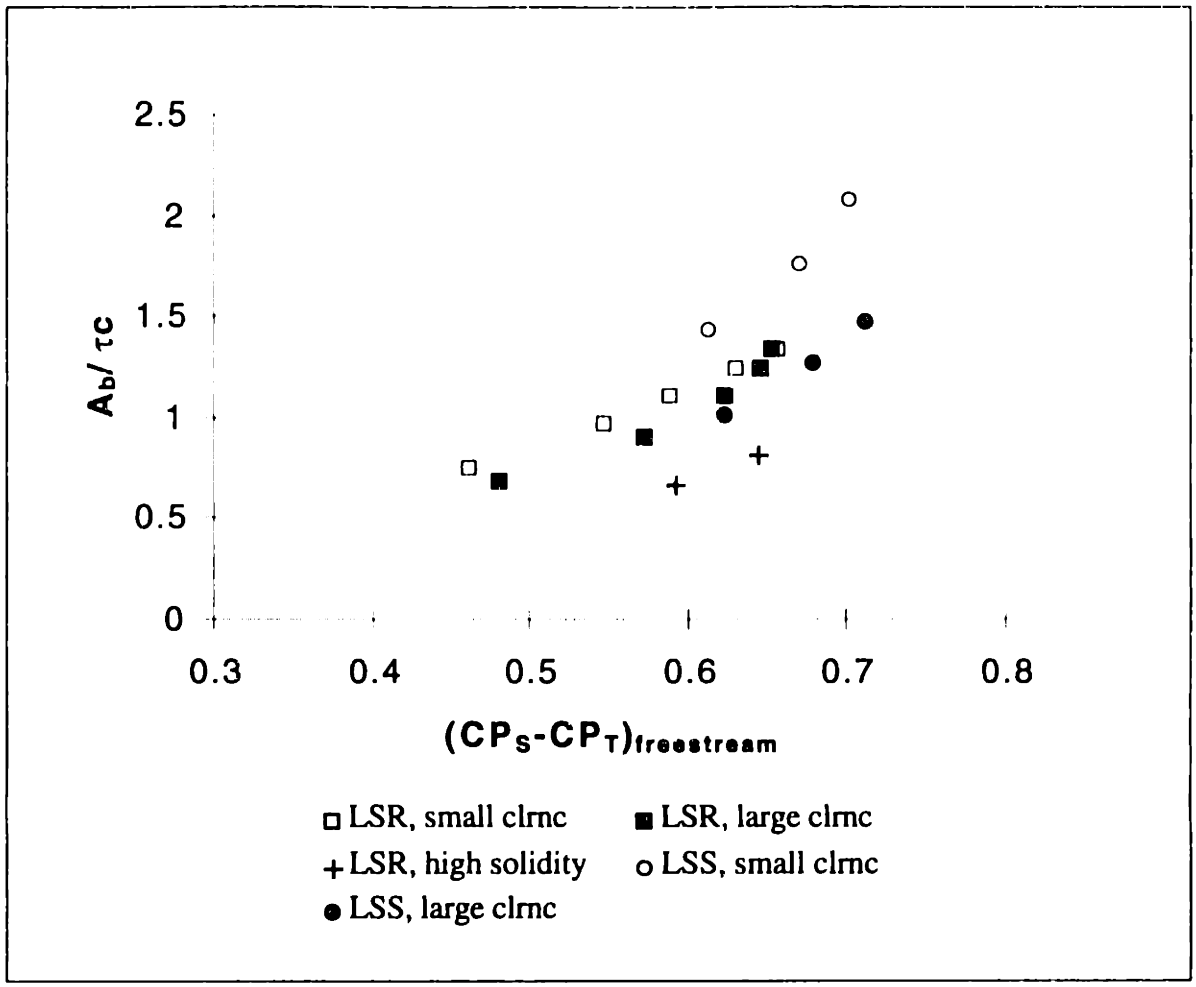

Figure 2-7: CFD Normalized Blockage Results Using Inlet Freestream Normalization

chord data. Hence Khalid sought a different normalization that did not depend on chord. Noting how blockage would parametrically behave, he multiplied the blockage normalized by chord by the ratio of the passage loading to the blade loading as follows:

$$\frac{A_b}{\tau c}\cdot\frac{\Delta P_{passage}}{\Delta P_{blade}} = \frac{A_b}{\tau c}\cdot\frac{c}{s\cdot\sin(\beta_{vm})} = \frac{A_b}{\tau s/\sin\beta_{vm}}.$$

A schematic of this situation is given in Figure 2-9. Using this normalization for blockage the CFD data are shown in Figure 2-10. The data collapse to a broad trend line.

An alternative explanation for this attribute of the 50% chord data is found if the clearance jet is considered as a series of discrete chordwise sections, each having some initial defect (set by the mixing of the jet and the free stream) that grows as it passes to the exit of the

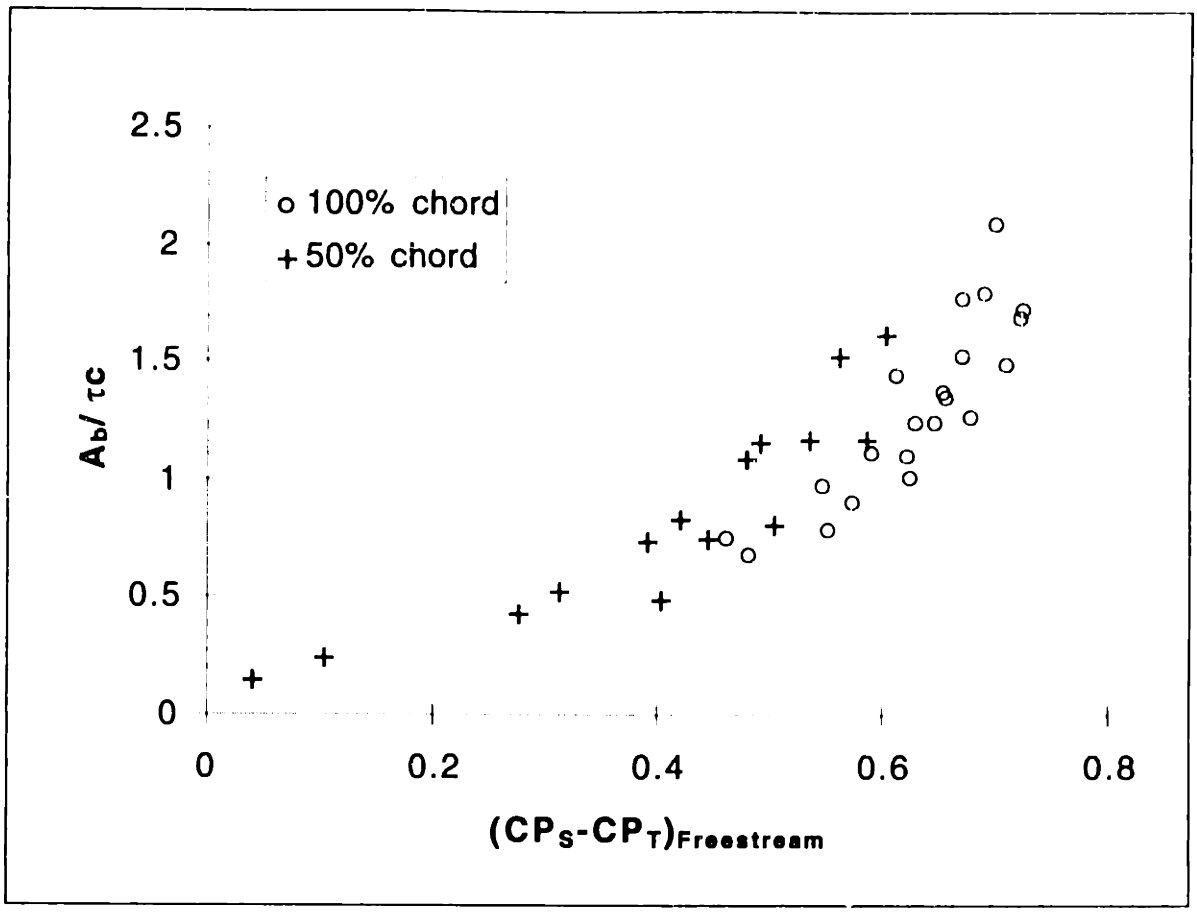

Figure 2-8: 50% and 100% Chord Blockage

passage. For each of these chordwise segments the pressure rise coefficient that determines the blockage growth is the exit static pressure minus the **local** static pressure, normalized by the **local** free stream dynamic head. At each chordwise location, the defect is considered to "begin" immediately as the clearance jet exits from the gap. An appropriate "local" pressure rise coefficient is thus the exit static pressure minus the blade suction surface pressure at that chordwise location, normalized by the dynamic head of the freestream fluid local to that location.[1]

Once the local static pressure rise has been determined for each chordwise segment of the leakage flow, an average must be taken to define a single pressure rise parameter. To weight the average more heavily where the leakage flow is highest, and presumedly the

1. This situation is analogous to the standard definition for diffusion factor. The diffusion factor includes not just the overall pressure rise of a blade row, but also approximates the effect of the suction surface pressure distribution, i.e., the diffusion from the suction surface minimum pressure point to the exit. The local pressure rise parameter proposed here takes account of fact that the freestream accelerates and decelerates along the chord.

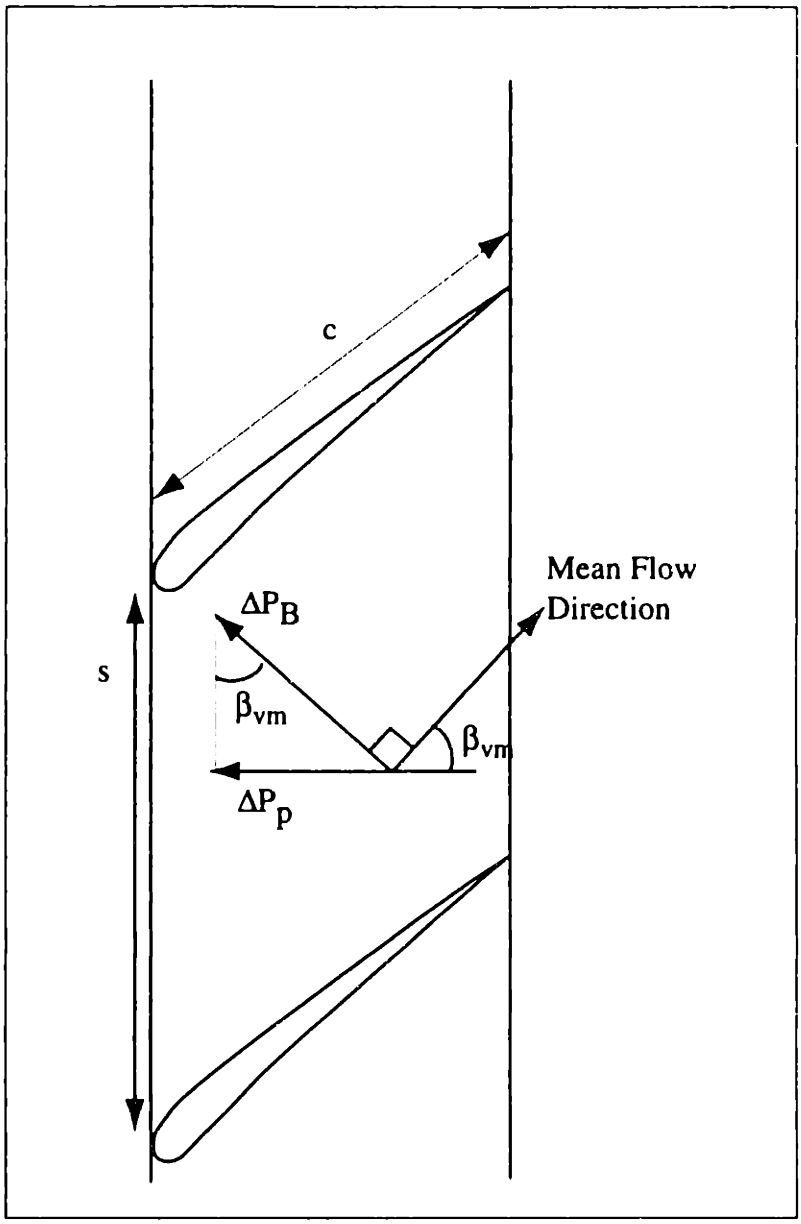

Figure 2-9: Schematic Used for Khalid's Blockage Normalization

contribution to blockage is greatest, the average computed here is a mass-average, with each section being weighted by the amount of mass flux through the clearance gap at that location[1]. The final form of the local loading parameter is as follows:

1. Little difference was observed if an area average was used.

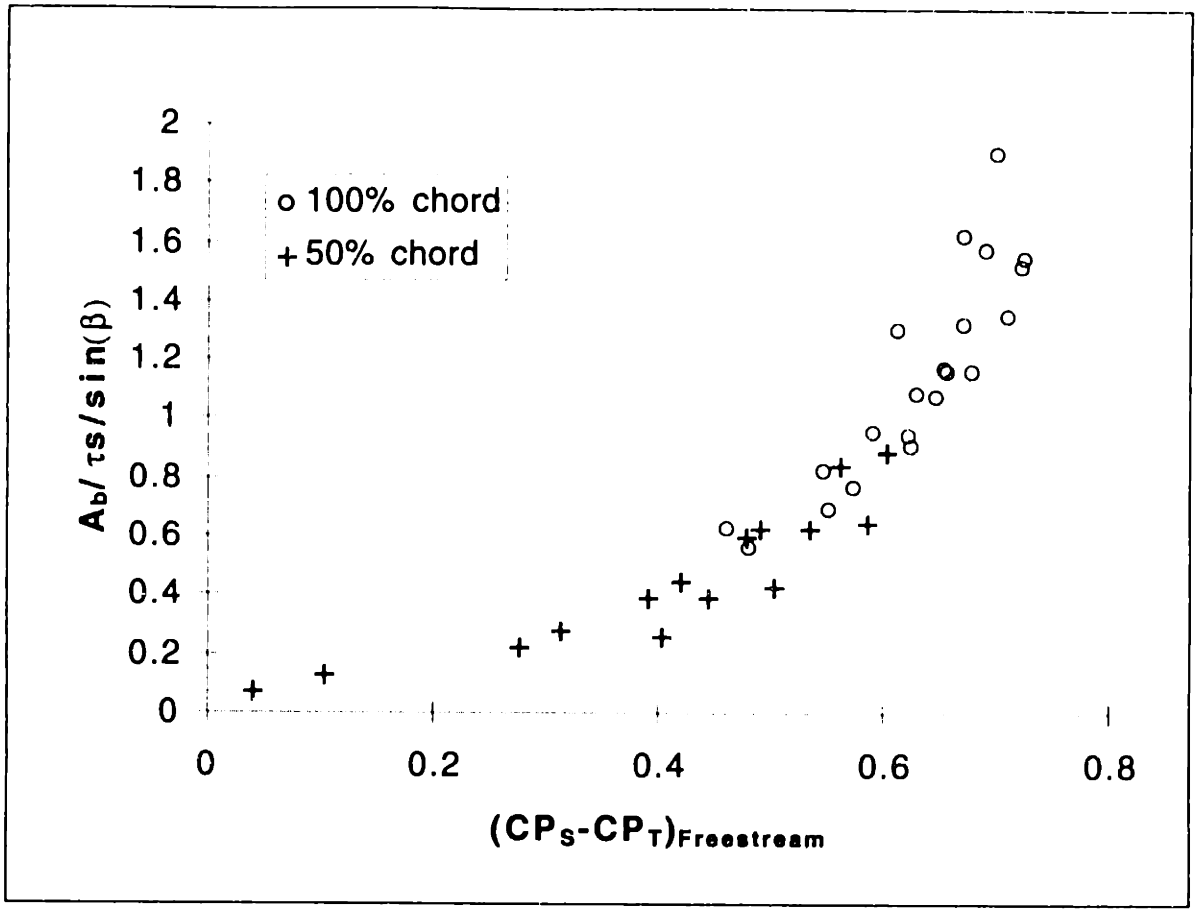

Figure 2-10: Blockage Normalized Using Khalid's Definition

$$\text{loading parameter} = \left[\frac{\overline{P_{S,\text{exit}}}^{a} - P_{S,\text{local}}}{Q_{\text{local}}}\right]^{m} - \left[\frac{\overline{P_{T,\text{exit}}}^{a} - P_{T,\text{inlet,freestream}}}{Q_{\text{local}}}\right]^{m}$$
$$= (CP_S - CP_T)_{\text{local}},$$

where $\overline{(\,)}^{a}$ and $\overline{(\,)}^{m}$ denote area averaging and mass averaging respectively, and the local freestream total pressure is assumed to be equal to the inlet total pressure. Details of the calculation procedure used in computing this local loading parameter are given in Appendix A.

Using this definition of the local loading parameter, the CFD blockage data is shown in Figure 2-11. As can be seen, the 50% and 100% chord data again fall onto a single broad trend line, with the blockage normalized by the clearance area. The degree of collapse of the data is not as tight as in Figure 2-10, but it is felt that the physical understanding asso-

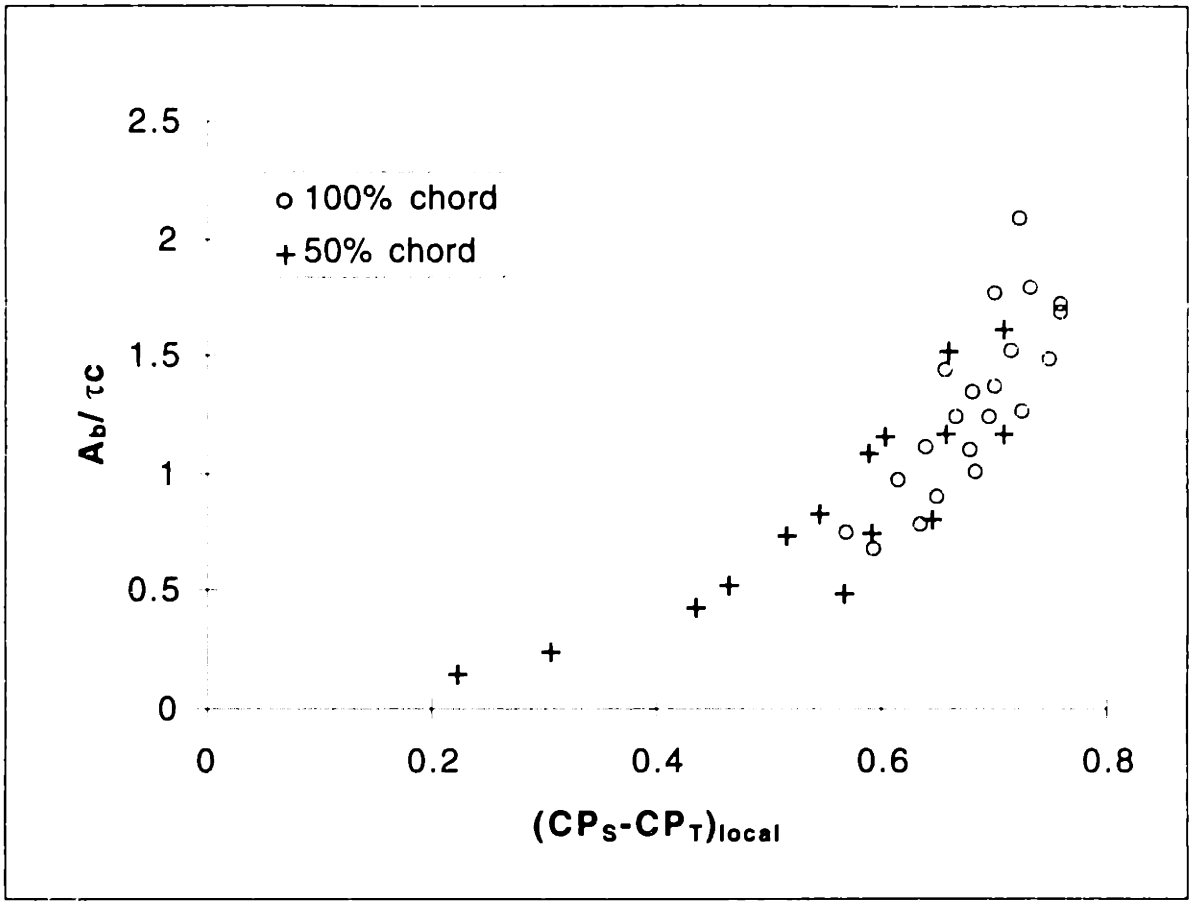

Figure 2-11: CFD Blockage Results versus Local Loading Parameter

ciated with this normalization is sufficient rationale to support its use in this study.

To summarize, a primary goal of the present investigation was to define, and quantitatively assess, the key elements that contribute to clearance blockage. To enable this parametric evaluation a parameter set was needed. The proposed parameters are the blockage normalized by the clearance area and multiplied by the cosine of the exit flow angle and a loading parameter, CP_S-CP_T, based on local quantities. These parameters will be used throughout this thesis as the common units of comparison between the examined data sets. Trends of normalized blockage versus local loading parameter were used to compare experimental data to computational solutions (subsection 2.4.3) and the wind tunnel model results to the rotating rig data (Section 2.5).

2.3 Low Speed Compressor Rotor

2.3.1 Experimental Description

Because of the uncertainty associated with the mixing models used in the Navier-Stokes solver, confirmation of the computed blockage trends was sought in a rotating rig experiment. Tests were performed in the Deverson low speed compressor rig at the Whittle Laboratory of Cambridge University. The facility consisted of a calibrated bellmouth inlet with honeycomb flow straighteners, casing boundary layer thickening tabs, inlet guide vanes, rotor (51 blades), stator (49 blades) with a hub-to-tip ratio of 0.8, and auxiliary exhaust fan. The facility is shown schematically in Figure 2-12. The inlet guide vanes are

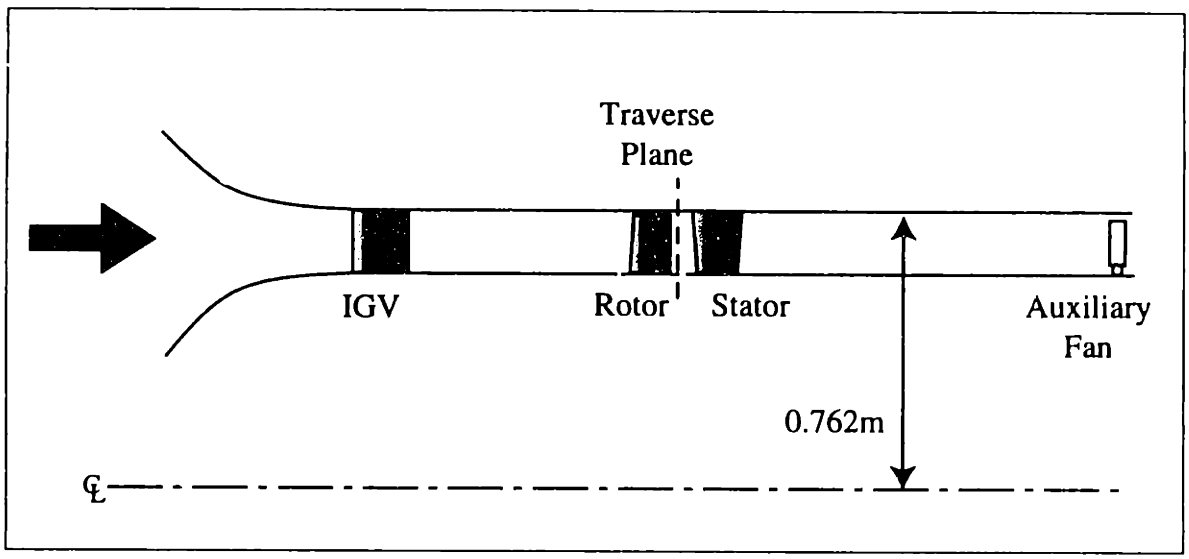

Figure 2-12: Schematic of Deverson Rig

3.2 rotor chords upstream of the rotor leading edge, imparting swirl to the flow, but allowing the circumferential non-uniformities due to IGV wakes to mix out. The rotor and stator blading is representative of a modern HP compressor stage, with controlled diffusion airfoils. The primary features of the blading are summarized in Table 2-1. All data were

tip chord	tip solidity	hub/tip ratio	tip camber	inlet δ^*/τ	design C_x/U_{tip}
118.7mm	1.26	0.80	25.4°	2.0	.63

Table 2-1: Deverson Rig Blading Parameters

collected at a rotor speed of 400 RPM, giving a Reynolds number based on tip speed and chord of approximately 245,000, with the mass flow controlled by the auxiliary fan.

Data were collected primarily with a slant hotwire. The hotwire was traversed radially 15% chord downstream of the rotor trailing edge. At each radial location phase-locked measurements were taken and ensemble-averaged for 8 different wire orientations. The data were processed using a hotwire calibration to calculate each of the three velocity components at rotor exit with 27 data points in the radial direction and 39 across the blade pitch. An error analysis was performed and is detailed in Appendix A. Based on this analysis the error of the rotor exit plane velocities is less than ±5.0 % with 95% confidence.

Trailing edge velocity data were taken at a number of points along a speedline. Speedlines were run for two stagger angles (40.5° and 44.7°) and two clearance levels (τ/c=1.24 and 3%). For the increased clearance tests, only three blades were cropped to increase their clearance. This circumferential non-uniformity in clearance was accounted for in the data reduction using the theory of Horlock and Greitzer (1983), which predicts the circumferential redistribution of flow coefficient for a given circumferential tip clearance variation. For the Deverson rig with three cropped blades, the flow coefficient local to those large clearance blades was estimated to be approximately 8% less than the mean flow coefficient. This difference was accounted for in the data reduction of the large clearance cases.

Data at the rotor trailing edge were analyzed using the technique for quantifying endwall blockage which was developed by Khalid (1995a). For each flow condition a blockage was calculated and normalized by the clearance area. Because of the essentially incompressible nature of the flow, the abscissa of the blockage plots, CP_S-CP_T, was computed directly from the velocity magnitude measured by the hotwire.

2.3.2 Experimental Results

Two representative contour plots of the relative velocity magnitude normalized by midspan blade speed are shown in Figure 2-13 for the datum stagger and clearance geometry. The triangles along the right hand edge indicate the radial measurement locations. For

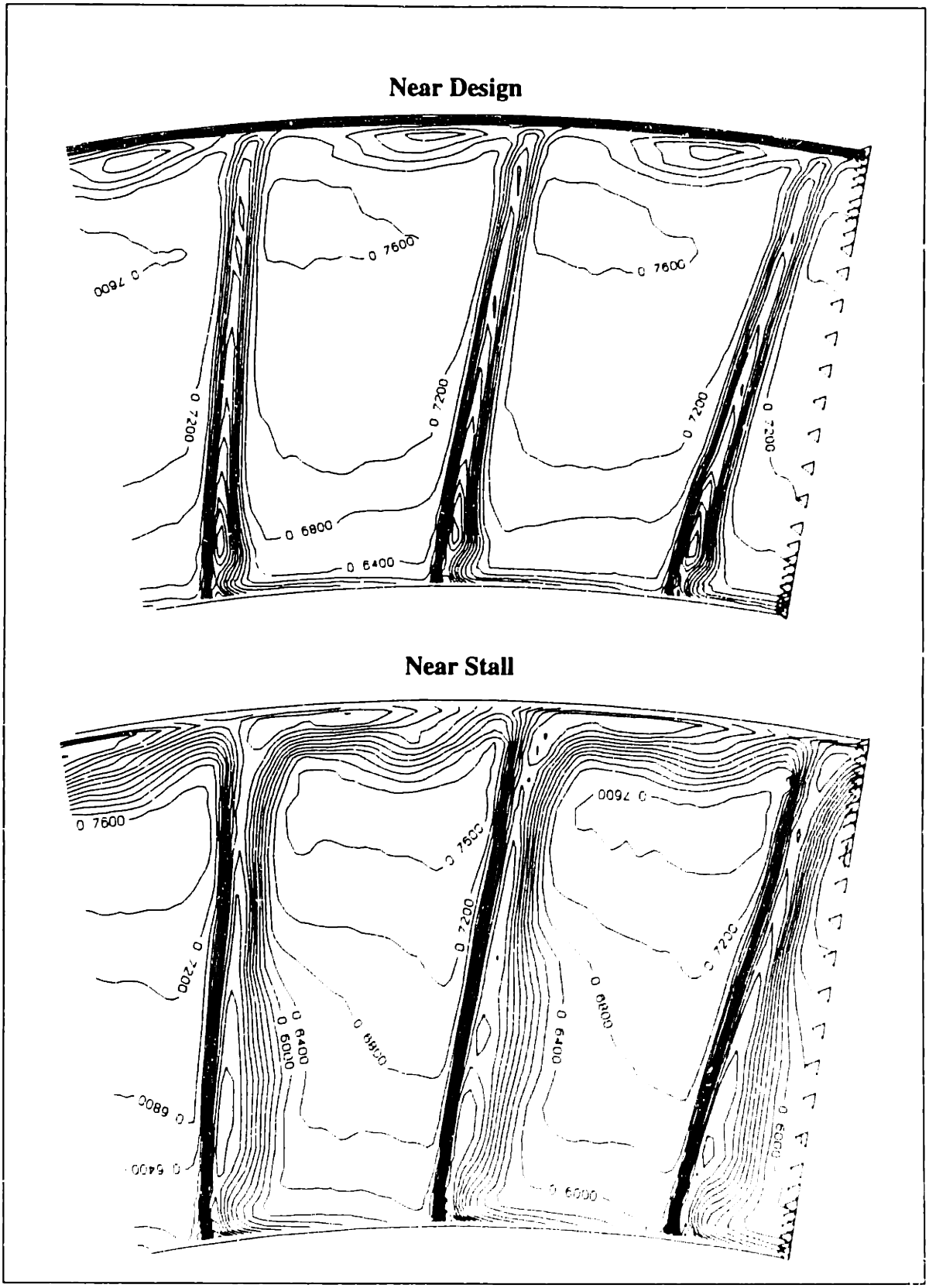

Figure 2-13: Relative Velocity, w/U_{tip}, Contours from Rotating Rig at Trailing Edge +15% Chord

both plots the contour intervals are 0.04 C_x/U_{tip}, and the direction of blade rotation is right to left.

A plot of blockage versus loading parameter, including all the data points taken on the Deverson rig, is shown in Figure 2-14. The highest loading points were at a flow coeffi-

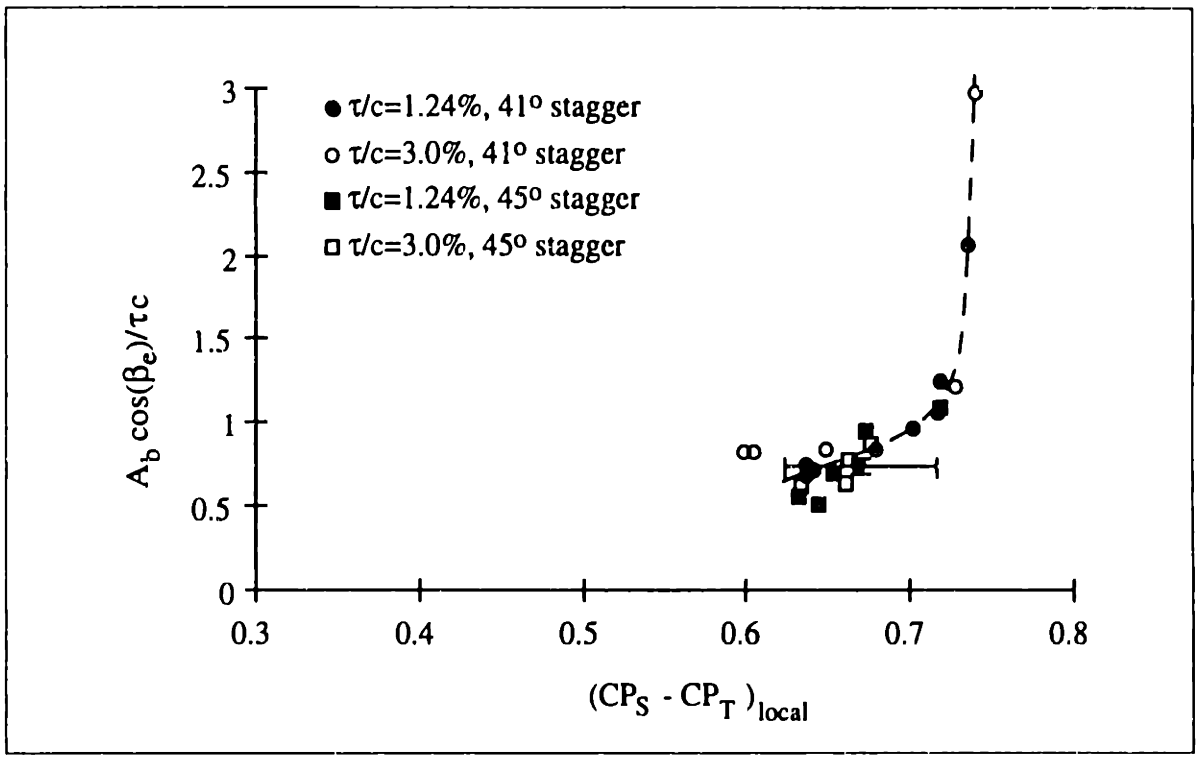

Figure 2-14: Blockage versus Loading Parameter from Rotating Rig Experiments, Two Clearance Heights, Two Stagger Angles

cient approximately 0.03 C_x/U_{tip} above the onset of rotating stall. Figure 2-14 shows an asymptotic trend similar to that seen in the simplified one-dimensional analysis described in subsection 2.2.2 (see Figure 2-4(b)). The primary difference between the data, Figure 2-14, and the one-dimensional results, Figure 2-4(b), is the location of the asymptote. The analysis shows the blockage asymptotes at a loading parameter of one, and the data shows a limiting loading parameter of approximately 0.72. This discrepancy is caused by the averaging used to calculate the local loading parameter used in plotting the data. Each chordwise section of the clearance jet undergoes a different static pressure rise[1] and a dif-

1. The exit pressure is the same for each streamtube, but the initial pressure, the pressure along the blade suction surface, has significant variations along the chord.

ferent amount of loss (as shown by the loss contours in Figure 2-2). The data asymptotes as the loading parameters of some of the clearance jet streamtubes approach one.

2.4 Compressor Computations

To elucidate the parametric trends of endwall blockage and to develop a blockage prediction method data from a variety of different geometries and conditions was used. Most of the parameter space was examined using computational solutions, many of which were obtained by Khalid. The computational methodology is briefly outlined below, and is fully described in Khalid (1995a). The geometries and flow conditions examined are also described below.

2.4.1 Computational Procedure

The three-dimensional Navier-Stokes flow solver used to obtain the solutions has been developed by Adamczyk, et al. (1989). The equations of motion are Reynolds-averaged, and discretized in cylindrical coordinates. The turbulent viscosity was modeled using the Baldwin and Lomax (1978) mixing length model, and both second and fourth order smoothing (artificial viscosity) were used in the inviscid regions of the flow field to maintain stability. As the flow solver is not well suited for very low Mach numbers, all solutions were obtained with an inlet Mach number of 0.3, approximately double the experimental Mach number. Khalid (1995a) showed that the solutions obtained were grid independent.

The clearance gap was not gridded in these solutions. The model suggested by Kirtley, et al. (1990) was used, in which the region from blade tip to casing is specified as periodic from pressure side to suction side of the passage. Flow enters the clearance gap on the pressure side of the blade, and an identical flow exits from the suction side. Khalid (1995a) explicitly addressed this modelling assumption and concluded that the clearance related blockage was adequately captured. By comparing the discharge coefficient from the numerical solutions to experiment he also concluded that the physical clearance is approximately equal to the specified computational clearance.

2.4.2 Description of Computational Cases

Smooth Wall

Two blade rows were examined, a cantilevered stator and a low speed rotor. The stator blade row examined was used in experiments at MIT as described by Johnson (1985). The blades were cantilevered from the casing so that a clearance existed between the blade tips and the rotating hub. Solutions were carried out for two tip clearances, 1.75% and 3.5% of chord. Loading was specified by an inlet flow angle distribution, with the baseline case using experimental near-stall data. This flow angle was increased uniformly over the span to obtain solutions at a number of mass flows, three for the tight clearance case, and five for the large clearance geometry.

The geometry of the low speed rotor was the General Electric E^3 Rotor B, described in detail in Wisler (1977). Solutions were computed for two clearance heights, 1.4% and 3.0% of chord. Loading was varied by specifying the hub static pressure at the exit of the computational domain. Two solutions were also obtained by Khalid (1995a) in which the blade spacing was reduced by 50%. Inlet data from experiments were used for the datum solutions. Solutions were also computed for a thickened inlet boundary layer (axial displacement thickness three times the datum) and no inlet boundary layer (axial velocity profile uniform to the endwall).

A summary of the compressor computations performed is given in Table 2-2 where the low speed stator is referred to as LSS and the low speed rotor as LSR.

Casing Treatment

To simulate casing treatment, the flow solver described above was modified (by Cho, 1995) in a manner similar to that of Crook, et al. (1993). The casing boundary condition was modified to allow flow through the casing. The casing treatment modelled was 60^0 axial-skewed slots extending from 5% to 95% chord. A schematic of the casing treatment geometry is shown in Figure 2-15. In the relative frame the flow into and out of the treatment is unsteady, but as experiments by Johnson (1985) have shown, a time-average

Blade	τ/c%	c/s	h/c	Stagger	Camber	inlet δ^*/τ
LSS	1.75	1.2	1.9	45°	30°	2.8
	3.5	1.2	1.9	45°	30°	1.4
LSR	1.4	1.1	1.2	56°	31°	2.6
	3.0	1.1	1.2	56°	31°	1.3
	3.0	1.6	1.2	56°	31°	1.3
	3.0	1.1	1.2	56°	31°	3.5
	3.0	1.1	1.2	56°	31°	0.0

Table 2-2: Geometric Parameters for Computed Solutions

velocity profile is a reasonable model of the unsteady flow field.

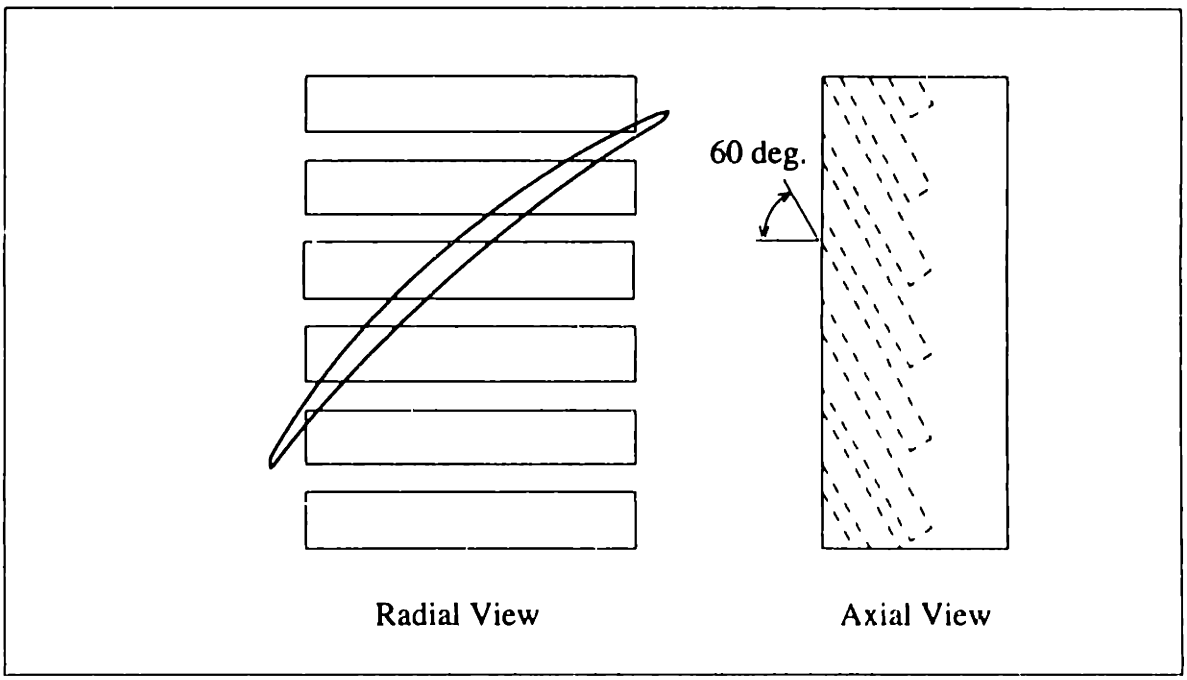

Figure 2-15: Schematic of Casing Treatment Geometry

Low-speed experiments with hub treatments by Johnson (1985) were used by Crook to define the radial velocity profile imposed at the casing, and this same profile is used in this study. The E^3 large clearance geometry was used, and the casing velocity profile is shown in Figure 2-16. In the front portion of the passage, flow is injected into the passage through the casing. In the rear of the passage, where the static pressure is high, flow is

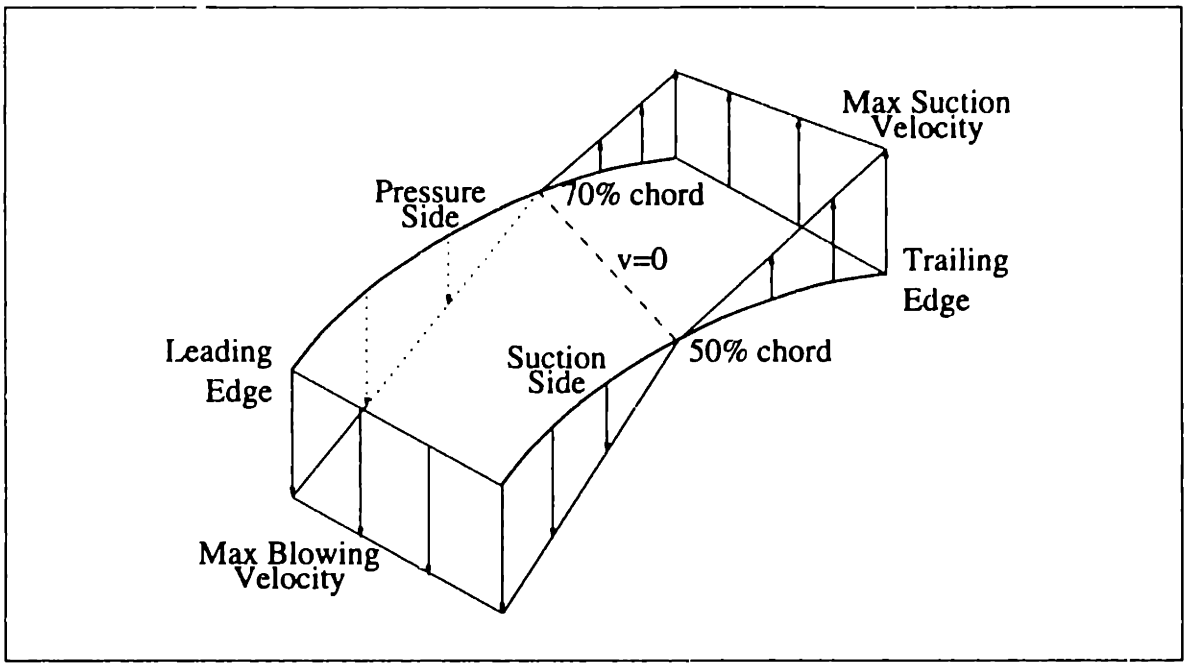

Figure 2-16: Imposed Casing Velocity Profile

removed from the passage out through the casing.

A series of solutions were computed for the specified geometry with casing treatment for various back pressures. The other parameter varied was the amount of mass blown into and removed from the passage (blowing and suction were balanced for all cases to ensure no net mass addition or removal). The datum cases were for 3.5% of the inlet mass flow removed and added, based on experimental measurements of Johnson (1985). A solution was also performed for a rate of mass blowing and suction equal to 1.75% of the inlet flow.

2.4.3 Computational Results

The blockage and loading parameter were calculated for each converged flow field solution. Figure 2-17 shows all the CFD results on a plot of blockage normalized by clearance area, versus local loading parameter CP_S-CP_T. As with the 1-D analysis, the data fall along one trend, with some scatter. There is a steeper increase in blockage at higher values of the loading parameter. The highest loading points in the CFD data set are from the highest specified back pressure at which a converged solution could be obtained.

The rotor computations are compared to the rotating rig tests in Figure 2-18. At low load-

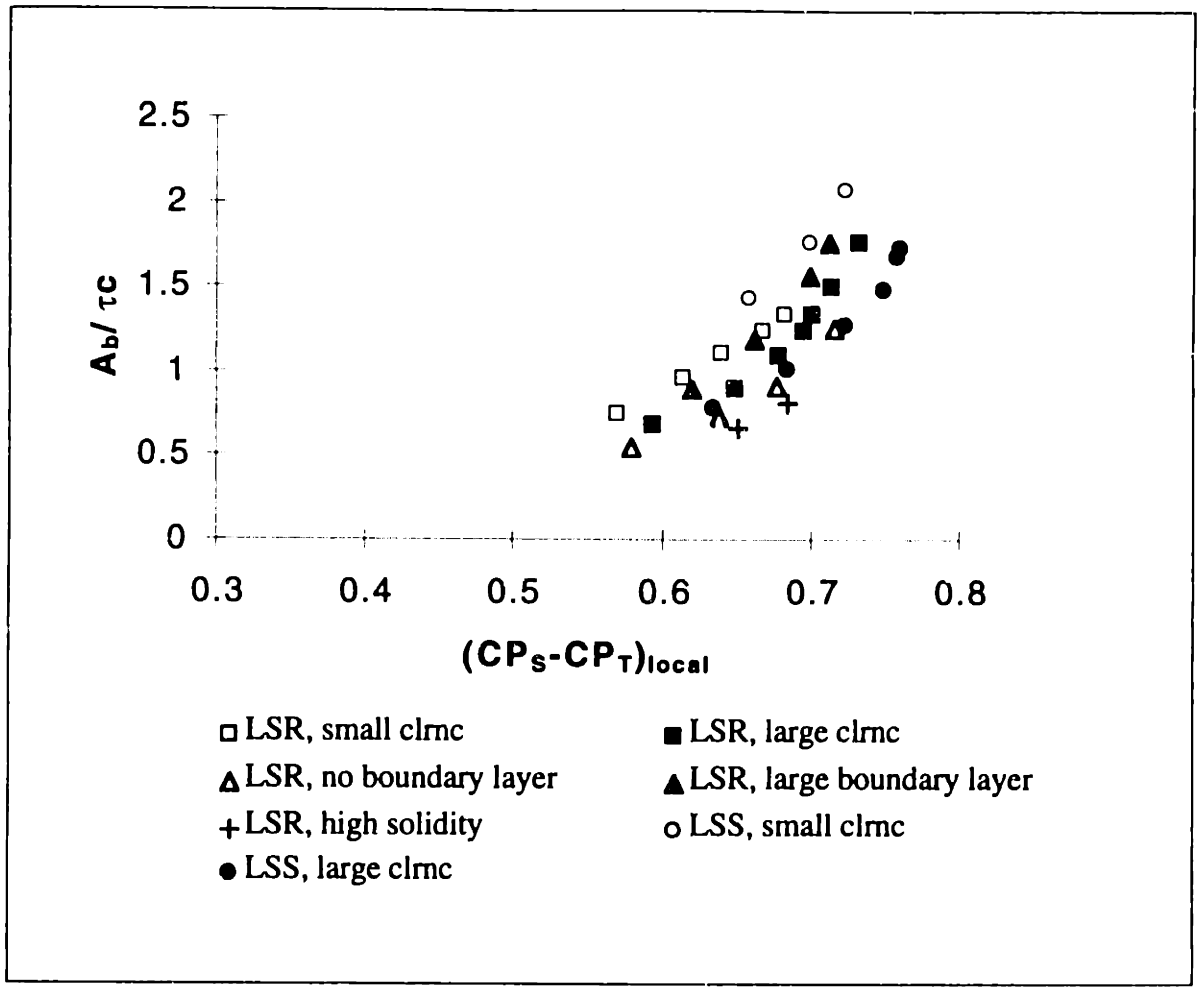

Figure 2-17: Blockage from Computational Solutions

ings, the blockage trends between the experimental and computed data are within experimental error. The limiting values of loading parameter between the two data sets differ by 3% of inlet dynamic head.

Even though the blade profiles were different in the computations and the rotating rig tests, the agreement of limiting loading parameter, which is a strong function of the mixing, with experimental data suggests that the CFD solutions can be a useful tool to explore the parameter space of the endwall blockage problem and to examine the phenomena associated with endwall blockage.

Because the computational solutions are used extensively to develop a blockage model (Chapter 4), which is dependent on the amount of turbulent mixing, further support for their validity was sought. The computed loss values were compared to the theory of Storer

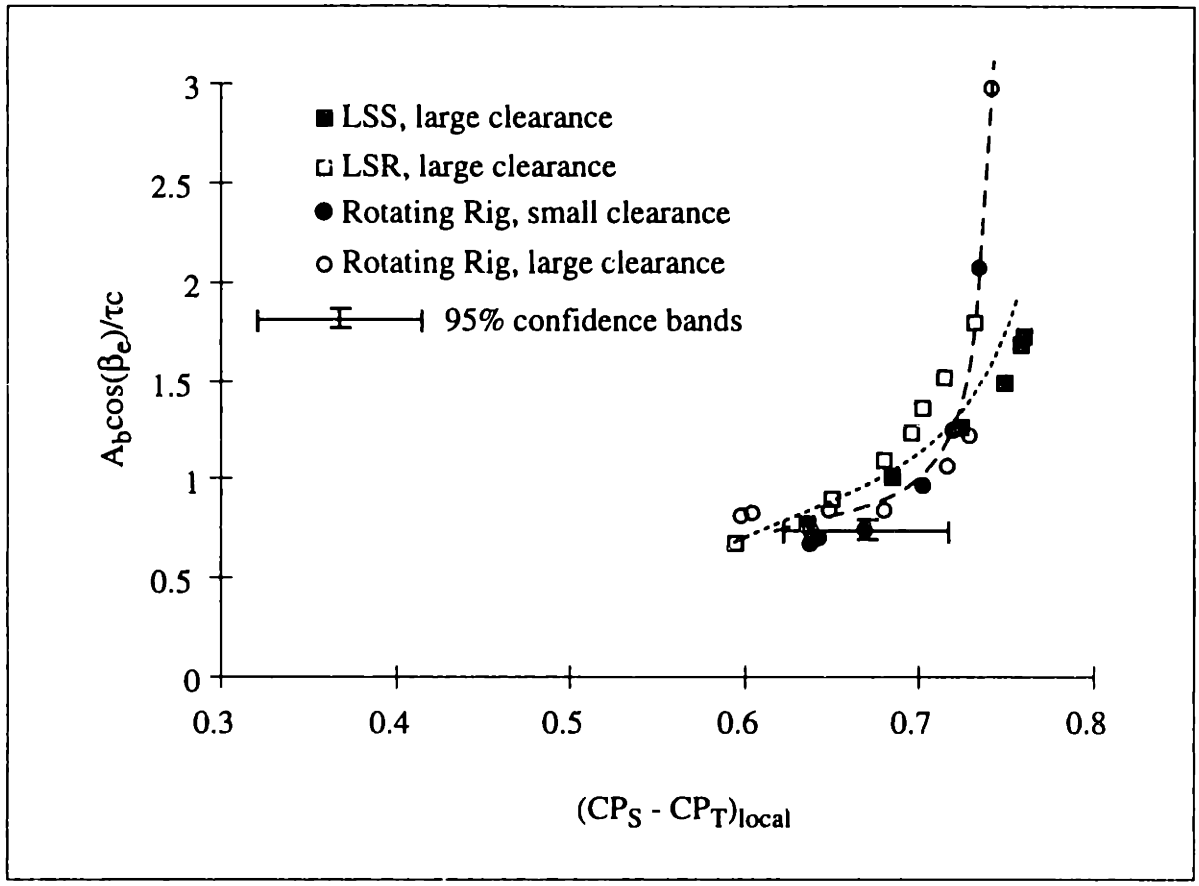

Figure 2-18: Comparison between CFD and Experiment

and Cumpsty (1994). They proposed the following expression for the average loss coefficient at the exit of a compressor passage due to tip clearance as a function of passage geometry, absolute flow angles, and the mass-averaged tip clearance leakage angle:

$$\frac{P_{T,exit} - P_{T,in}}{\frac{1}{2}\rho V_{in}^2} = \chi \sin\zeta \frac{2 + \chi \sin\zeta - 2\cos\zeta}{1 + \chi \sin\zeta^2} \bullet \frac{\cos^2\alpha_1}{\cos^2\alpha_2}. \qquad (2.8)$$

In Equation 2.8,

$$\chi \equiv C_D \frac{\sigma\frac{\tau}{c}}{\frac{h}{c}\cos\gamma},$$

$C_D = 0.8$ = discharge coefficient for the tip gap, σ = solidity, τ/c = tip clearance height to chord ratio, h/c = aspect ratio, γ = stagger angle, and ζ = average clearance jet leakage

angle.

Loss due to sources other than the leakage jet such as blade and hub boundary layers are not accounted for in this model, and hence the theory can only predict the change in loss, not the absolute level, unless a 'zero clearance' loss is known and added into the equation. Storer and Cumpsty found this loss prediction method to be accurate with 2% for τ/c above 1%.

Equation 2.8 predicts a difference in average exit plane loss coefficient of 0.006 between the low speed rotor, large clearance, low and high loading cases. The actual difference in loss coefficient is 0.0065. If Storer and Cumpsty's theory is assumed to accurately predict exit plane loss, this agreement is further support for the accuracy of the CFD solutions.

2.5 Wind Tunnel Simulation

2.5.1 Concept

Marble (1991) suggested that the key parameters of the tip clearance flow field were the angle between the jet and the free stream, the relative total pressures of the two streams, and the pressure gradient in which the jet interaction occurs. To enable the behavior of the tip leakage flow field to be studied with more control over various flow conditions than in a rotating rig experiment a simplified experiment was proposed based on these ideas. The compressor tip clearance flow was modelled as an axial slot jet entering a free stream within an adverse pressure gradient, as shown schematically in Figure 2-19.

The slot produces a symmetric vortex pair, similar to the wall bounded single vortex with its "image vortex" across the casing wall. The advantage of capturing the vortex/image-vortex interaction with a vortex pair is that this implementation includes the high total pressure at the casing boundary that exists in a compressor rotor (due to the relative motion of the wall) without the experimental complications of a moving wall. In the wind tunnel simulation, the symmetry plane between the two vortices represents the high total pressure casing boundary.

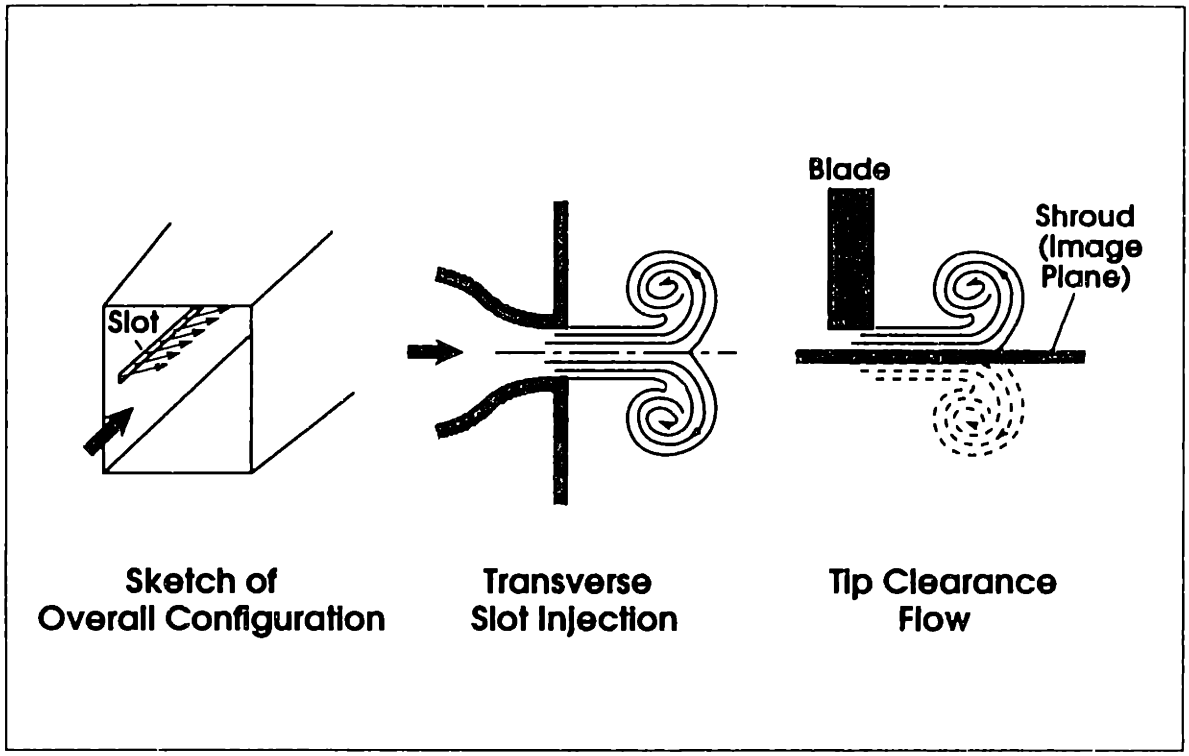

Figure 2-19: Wind Tunnel Concept

In the sections below the physical construction of the tunnel is described. The differences between the wind tunnel model and a compressor endwall flow field are described and their impact on blockage is evaluated in detail in Appendix B. The blockage trends from the tunnel are then presented and compared to data from the rotating rig experiments that were described in Section 2.3. The wind tunnel model was used to study the effect on blockage of increased jet total pressure, and this is discussed in the blockage reduction chapter, Chapter 5.

2.5.2 Physical Description

The wind tunnel test section was constructed to produce an adverse pressure gradient representative of that found in an axial compressor. In a manner similar to a compressor passage the free stream flow was simultaneously turned and diffused, creating a local minimum in pressure as the flow accelerated around a bend, and then an increase in pressure as the flow diffused. A schematic of the tunnel is shown in Figure 2-20. The curved wall in the test section is representative of the suction surface of a rotor blade, and it is through this wall that the leakage jet is injected.

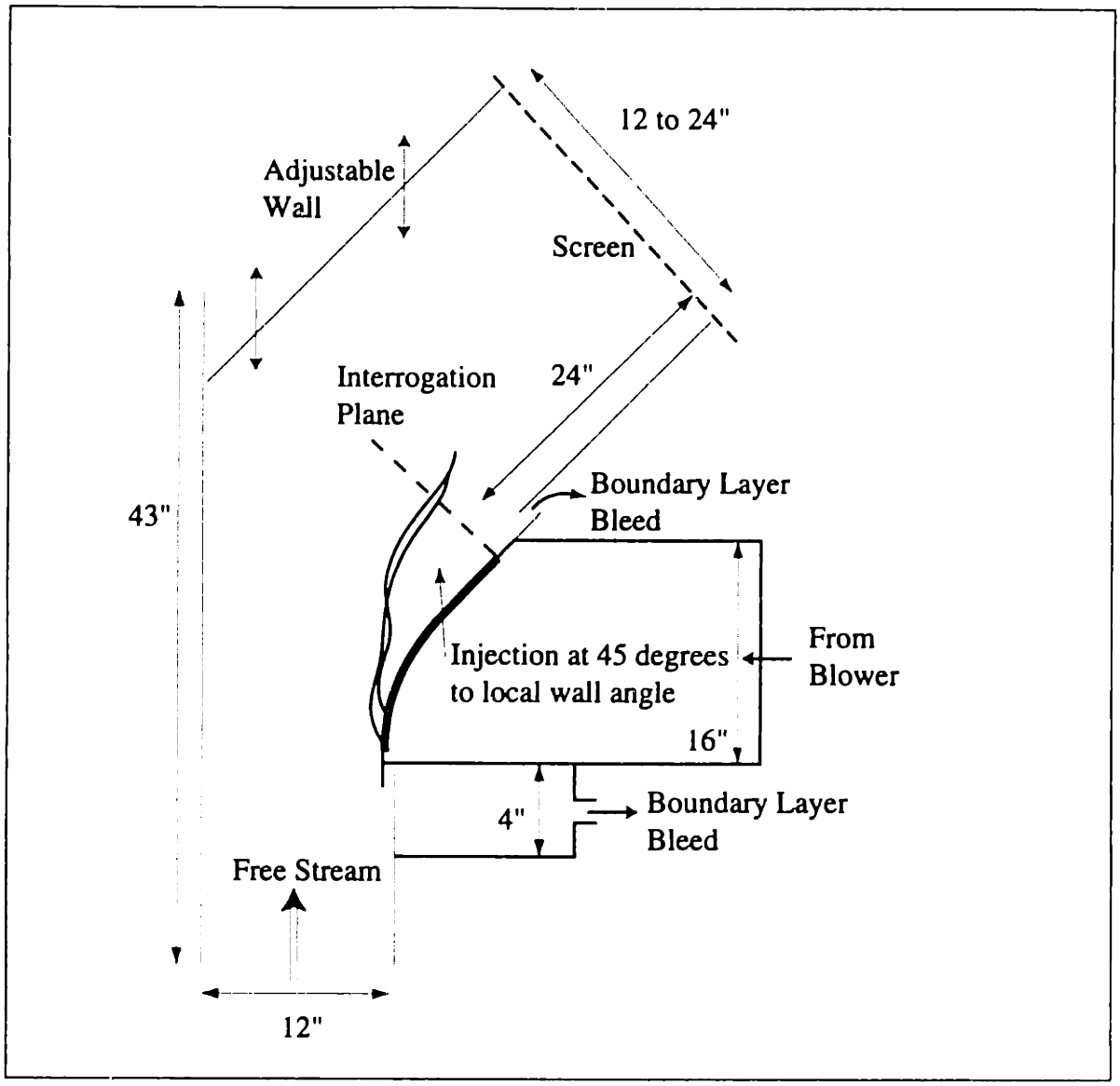

Figure 2-20: Wind Tunnel Test Section Schematic

Because of the strong adverse pressure gradients along the curved wall, a number of techniques were used to prevent boundary layer separation. A downstream screen was used to raise the pressure within the test section above atmospheric pressure so that regions of low momentum fluid could be bled off. Bleed slots with knife edges were used to remove the boundary layer just upstream and downstream of the curved wall. A downstream bleed was also necessary because the diffusion was not complete at the slot trailing edge. The continued diffusion downstream of the region of interest would cause the boundary layer to separate if it were not removed. The amount of fluid removed was adjusted until there was no streamline curvature either into or around the bleed slots, as indicated by a tuft wand.

The turning in the test section (45 degrees) produced secondary flows on the top and bottom walls, causing boundary layer fluid to move toward the curved wall. To remove the influence of this secondary flow, 1/8" gaps were left above and below the 12" high curved wall, allowing the boundary layers on the top and bottom wall to be bled out of the test section. Tuft wand tests showed that the streamline curvature introduced by these bleeds did not extend more than two inches from the top and bottom, well away from the region of interest which was more than four inches from either wall.

At some of the conditions tested, boundary layers on the walls without boundary layer bleeds would separate. To alleviate this problem, additional bleed slots in the tunnel walls were used. As previously described, the boundary layers on the curved wall were removed using bleeds with knife edges, but the other three walls of the tunnel were controlled by simple open slots as any streamline curvature would have only a local effect.

The simulation of the tip leakage flow was produced by blowing from a 1/4 inch slot located in the center of the tunnel as shown in the three-dimensional view of the tunnel in Figure 2-21. A box that could be pressurized independently of the main tunnel was used to create and control the jet. Immediately behind the slot inside the pressurized box was a set of turning vanes that turned the flow toward the free stream direction. Two sets of turning vanes were tested, with different (uniform) leakage angles along the chord. A schematic of the injection scheme is shown in Figure 2-22.

Storer and Cumpsty (1994) describe the mass averaged leakage angle in modern compressor clearance flows as typically being between 42 and 52 degrees. The injectors were thus designed to bound the parameter region of interest, creating jets that were 41^{o} and 54^{o} from the local free stream direction, uniform along the chord.

The box behind the slot was pressurized with a 0.75 horsepower blower. Valves between the blower and the box allowed the pressure in the box to be adjusted. Most tests were run with the total pressure of the jet matched to the total pressure of the free stream because, as measurements of Storer (1991) have shown, fluid leaking over the blade tips undergoes little loss within the gap, and the leakage and free stream fluid have approximately the

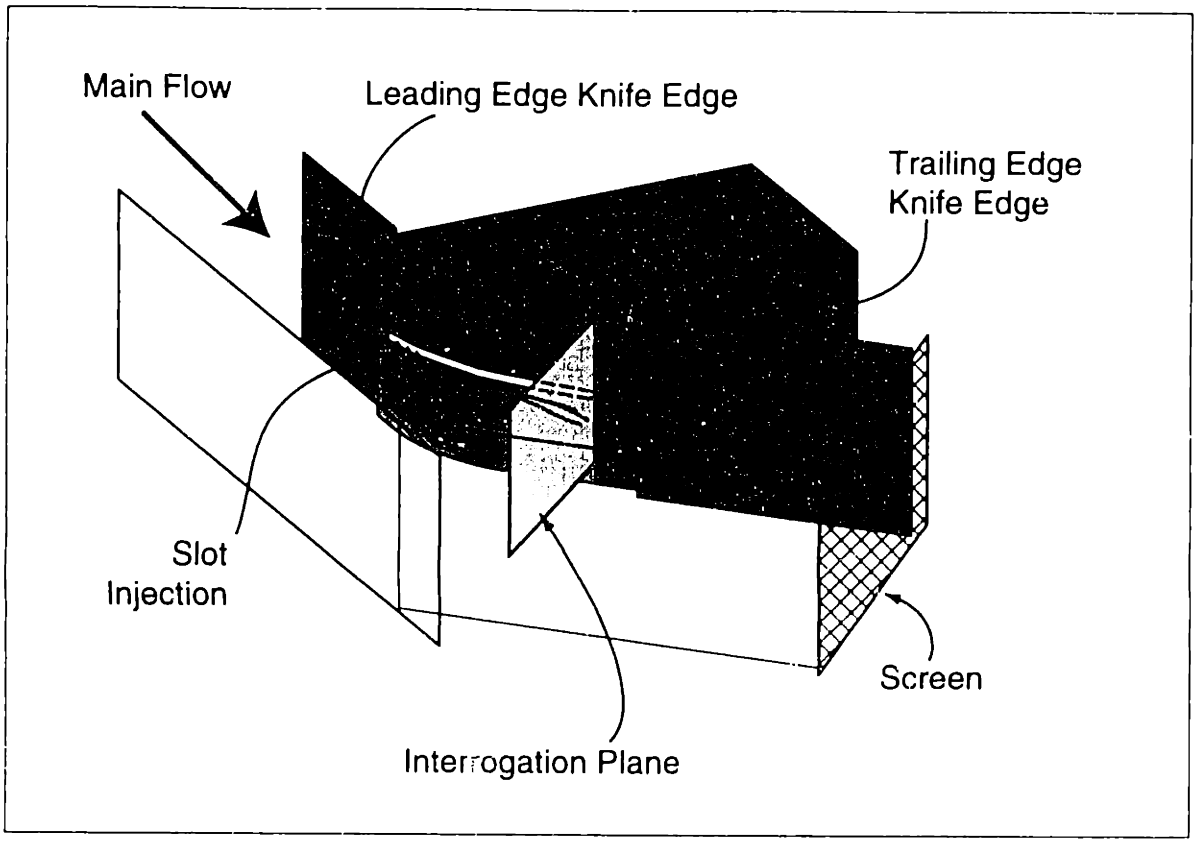

Figure 2-21: Three-Dimensional Schematic of Wind Tunnel Test Section

same total pressure.

The turning vanes were made of 0.008" thick copper, 0.25" high and 2.00" long. Twenty three vanes were individually bent to different turning angles so that the jet flow would be turned from unidirectional behind the slot to a constant angle to the local wall angle. The copper vanes were held between two pieces of wood. One side of the wood was cut to match the curve of the tunnel wall, and the other was rounded into a bellmouth inlet to the slot and the vanes.

The vortex pair produced by the jet injection was found to be sensitive to the inlet conditions to the injection slot. Small asymmetries in that inlet region caused large asymmetries in the vortex pair, and so a smooth bell-mouth inlet was made into the slot injector. Some asymmetry still remained, however, with one vortex being approximately 10% larger than the other. The impact of this imperfection on the flow field is addressed in Appendix B.

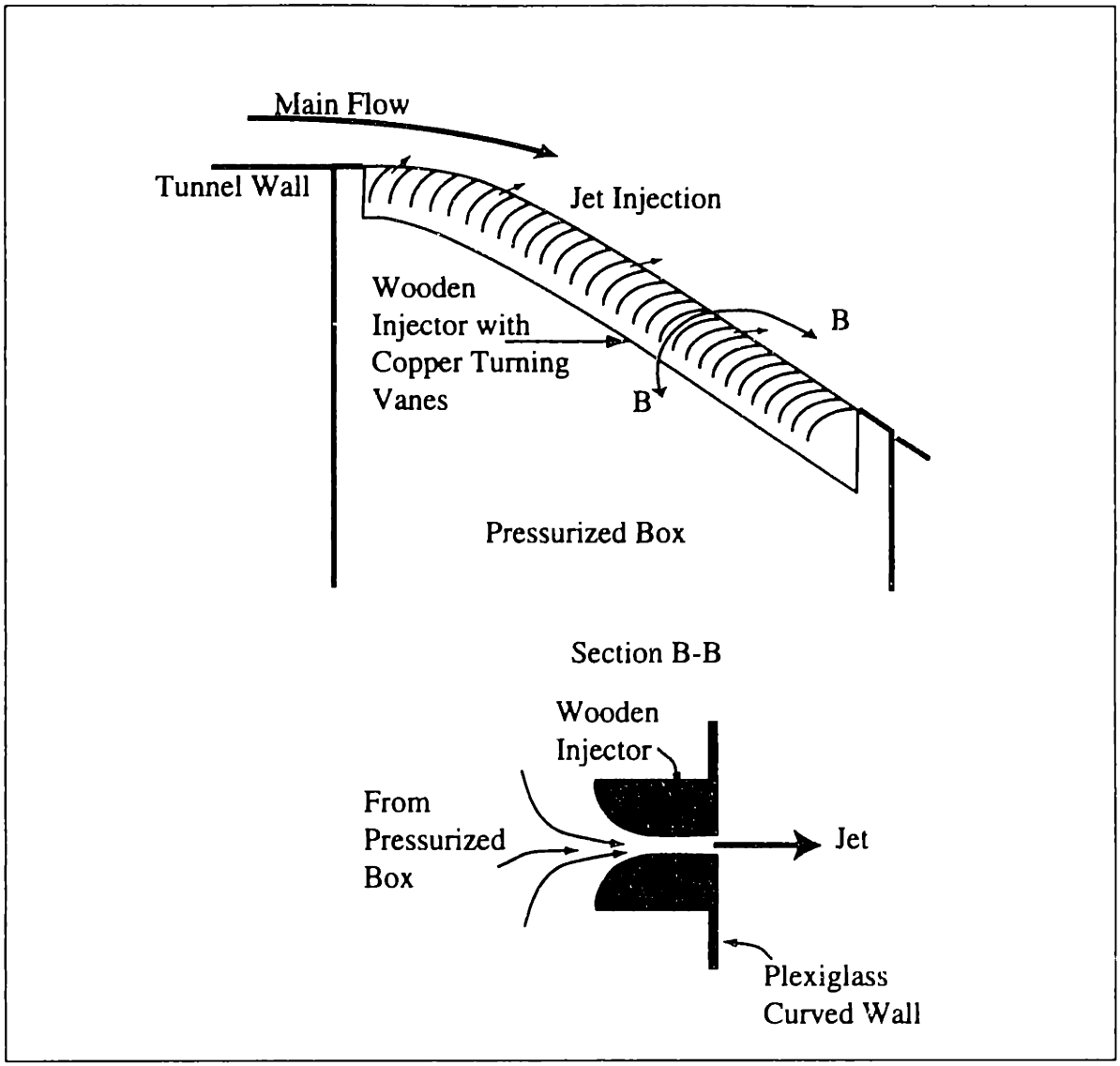

Figure 2-22: Schematic of Jet Injection Scheme

2.5.3 Instrumentation

The primary diagnostic tool for the wind tunnel tests was a seven hole pneumatic probe constructed and calibrated by the Aeroprobe Corporation. The probe tip was 0.10" in diameter. Having seven measurements allows for the five steady flow quantities of interest, three velocity components, static pressure, and total pressure, to be measured even when the flow is separated over part of the probe tip. The probe could operate with flow angles up to 80 degrees from the probe axis. A description of the probe is given in Rediniotis, et al. (1993). The probe measured dynamic head to within 1%, and both pitch and yaw angles to within 0.7^0.

The seven pressures from the probe, as well as the dynamic pressure from an upstream pitot-static probe, were measured using Auto-Tran Model 700 ±1 inch H_2O transducers, which had an accuracy of ±1 % of full scale. The 1-10 Volt output of the transducers was read by a computer through an Analog Devices RTI-815 analog-to-digital board. The transducers were calibrated using a slant manometer, and a probe calibration routine was used to compute the flow parameters.

The seven hole probe was inserted into the test section from the top, and traversed in two dimensions perpendicular to the curved wall at the slot trailing edge. At each measurement location the pressure transducers were allowed to reach equilibrium by waiting six seconds before taking data (the time constant for the transducers is approximately one second). The transducer voltages were sampled by the analog-to-digital board at 250 Hz for 2 seconds at each point and averaged.

To measure the static pressure along the curved wall of the tunnel 14 static pressure taps were used. These 1/16" diameter taps were connected to a multi-tube slant manometer. The upstream static and total pressures were also measured on the manometer board, allowing the wall static pressure coefficients to be measured directly.

A tuft wand and tufts attached to the tunnel walls were used to assess the boundary layer bleeds. The angles taken by tufts directly in front of the bleed knife edges were used as guides for setting the tunnel pressure (over atmospheric) and the bleed valve settings. Tufts along other walls of the tunnel indicated whether or not the boundary layers were attached.

Vaporized glycol smoke was introduced into the injection box to allow qualitative assessment of the symmetry and the unsteadiness of the vortex pair. The slot jet appeared white, showing up against the curved tunnel wall which was painted black.

The data reduction scheme and the estimation of experimental error for these measurements in the wind tunnel are described in Appendix A. An error propagation analysis was performed to determine that the normalized blockage calculation is accurate to ±0.141,

approximately ±14 %, and the loading parameter is accurate to ±0.035 , both with 95% confidence.

2.5.4 Comparison of Wind Tunnel Model to Compressor Flow Field

The wind tunnel test section just described was proposed as a means for simulating compressor tip clearance flows. The utility of the simulation was primarily judged by comparing the blockage trends measured in the wind tunnel to those observed in the rotating rig experiments described in Section 2.3. This comparison is presented below.

It is recognized that there are a number of differences between the wind tunnel and a compressor tip clearance flow fields. In the tunnel there was no moving casing applying a viscous force in the direction of the jet leakage, the leakage angle was constant along the chord, the vortex pair produced was slightly asymmetric, there was no adjacent blade, the pressure gradient was slightly different than in a compressor, and there was no inlet boundary layer. For each of these differences, their effects on blockage were estimated and found to be small (changing the blockage by less than 20%). The details of these analyses are given in Appendix B.

Wind Tunnel Data

Data were taken in the wind tunnel for two leakage angles (41^{o} and 54^{o}) over a range of loading parameters. The blockage data collected from these tests are presented in Figure 2-23. Representative error bars are shown based on the error analysis described in Appendix A. As in the simplified model, the results indicate an asymptotic trend of blockage as the loading parameter is increased.

The wind tunnel data and data from compressor tests are plotted together in Figure 2-24. The blockage levels and the limiting value of the loading parameter compare favorably between the two. A quantitative comparison shows that the limiting loading value for the two data sets are within 7%. The good agreement between the wind tunnel blockage data and the rotating rig data supports the validity of using the wind tunnel to simulate the compressor endwall blockage growth problem.

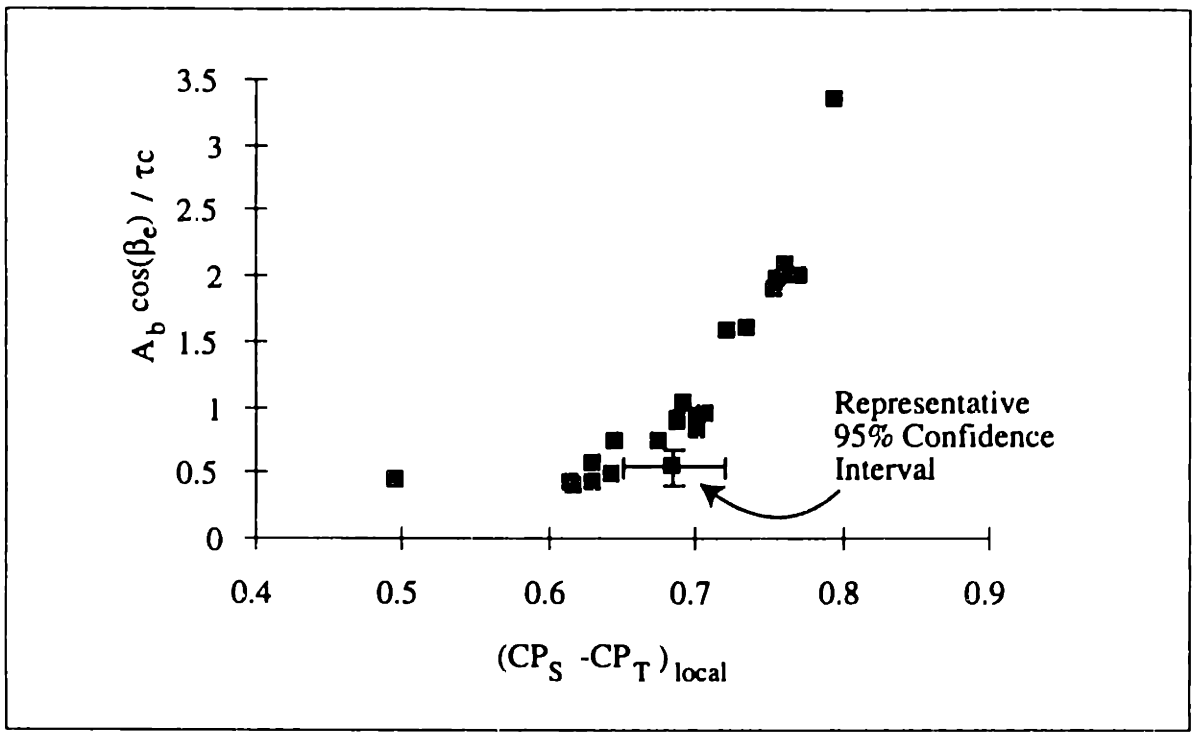

Figure 2-23: Wind Tunnel Blockage Results

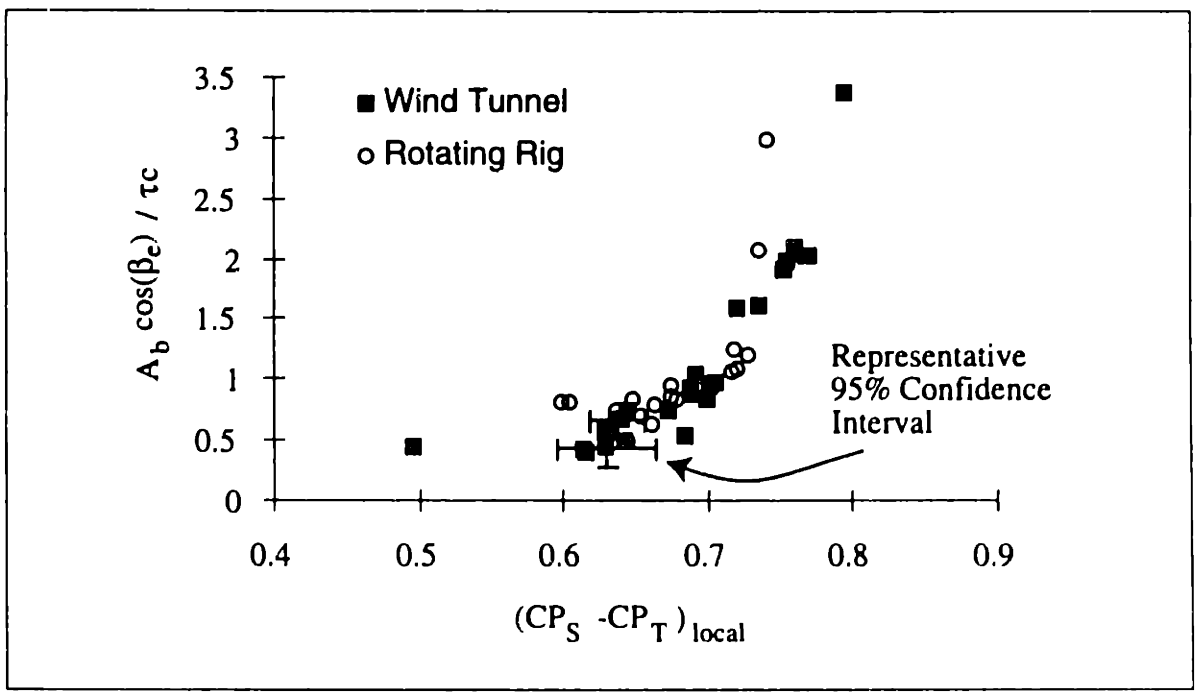

Figure 2-24: Blockage Comparison, Wind Tunnel and Rotating Rig

2.5.5 Summary of Wind Tunnel Simulation

To isolate the essential fluid mechanic processes that lead to endwall blockage, and to allow increased flexibility in exploring the parameter space a wind tunnel simulation of a

compressor tip clearance flow was tested. The effect on blockage of some of the flow features that are neglected in the wind tunnel were estimated using computational experiments, analysis, and reference to data in the literature. The details of these estimations are given in Appendix B. All estimates indicate that the wind tunnel should adequately capture the parametric trends of endwall blockage. The comparison of the wind tunnel blockage results to actual compressor data (Figure 2-24), indicates that the blockage trends of the wind tunnel simulation match the trends observed in a rotating rig to within 7%, supporting the use of the wind tunnel to explore the parameter space of the blockage problem. One specific area was investigated in this thesis, the effect of altering the total pressure distribution of the leakage jet as would occur with casing treatments. These experiments and their results are described and discussed in Section 5.3.

2.6 Chapter Summary

In Chapter 2 the figures of merit for discussing endwall blockage were explained. Computational and low speed compressor tests were described, with the results presented as plots of normalized blockage versus a loading parameter. A wind tunnel simulation of the clearance jet was also presented. The blockage trends, specifically the limiting loading parameter, observed in this model were within 7% of that observed in the rotating rig experiments.

A one-dimensional analysis of a velocity defect growing in an adverse pressure gradient was used to provide a physical underpinning for appropriate parameters to describe endwall blockage. The endwall blockage was normalized by the clearance area, τc. The parameter chosen to collapse this normalized blockage onto a single trend for various compressor configurations (rotor, stator, different inlet boundary layers, different solidities, different clearance sizes, different blade shapes, etc.) was a loading parameter based on the average static and total pressures within the blockage region referenced to local quantities along the chord. The trends of normalized blockage versus this local loading parameter are the primary metric used in this thesis.

The validity of using the computational solutions to probe the details of the flow field was supported by the agreement, to within 3%, of the limiting loading parameter for the computations and the rotating rig experiments.

Chapter 3: Flow Features and Parametric Trends of Endwall Related Blockage

3.1 Introduction

In Chapter 3 flow features relevant to the development of endwall blockage are discussed and the experimentally observed parametric trends of clearance related blockage are examined. The effects of swirl, stagger, blade loading (both the overall loading and the distribution along the chord), solidity, inlet boundary layer thickness, and clearance height on blockage are quantified, and the ranges of applicability are described.

Computational simulations of compressor blade rows are the primary form of evidence used to support the conclusions in this chapter. The modelling chapter, Chapter 4, addresses some of these parametric trends from a more theoretical and more general perspective. The blockage model that is proposed in Chapter 4 uses the clearance exit conditions as the initial conditions, and therefore some attention is given here as to how design changes influence the leakage jet total pressure, leakage angle, and mass flux.

3.2 Flow Features

This section describes endwall flow features that affect the clearance jet. The physical mechanisms that control the clearance jet leakage angle and total pressure are inferred from observations of the computational solutions. The ability to predict these conditions using the inviscid analysis of Storer (1990) is evaluated. These clearance jet conditions play an important role in the development of endwall blockage. This is quantified in

Chapter 4, where a model is developed for endwall blockage using these parameters as inputs.

3.2.1 Pressure Driven Leakage Jet

There is some disagreement in the literature as to the relative magnitudes of the forces driving the leakage jet. In the relative frame of the compressor rotor, the casing is moving in the same direction as the leakage jet, suggesting that viscous forces may act to "drag" fluid through the clearance gap. There are a number of pieces of evidence however, that strongly suggest that for most compressor blades the pressure force across the blade is more important than the viscous force.

Experimental evidence for the primarily inviscid nature of the leakage phenomenon was given by Storer (1991). His measurements of the radial distribution of the flow velocity exiting the clearance gap of a linear cascade show that the region of viscous influence is contained within the 20% of the clearance gap closest to the endwall.

Moyle (1991) presents data purported to be contradictory to this assumption. He measured wall shear on the casing beneath a compressor rotor and found a region just under the blade tips of zero wall shear. He inferred from this that the fluid must be moving at wall speed, and hence was being strongly influenced by viscous forces. However the pressure driven velocity, calculated from the blade pressures presented in Moyle (1991), is approximately 96% of wall speed. Rather than undermining the idea that compressor leakage jets are primarily pressure driven, Moyle's data actually support it.

Further support for the pressure driven nature of the clearance jet can be found in the results of the leakage vortex trajectory analysis of Chen, et al. (1991). They assume that the leakage flow is entirely inviscid, and their predictions of the leakage vortex trajectory are within 20% of the actual trajectories (measured as the distance from the blade suction surface to the vortex) for a broad range of compressor configurations. This agreement supports their original assumption that the jet is pressure driven.

The pressure driven/viscous driven question was also briefly examined by Khalid (1995a).

He computed a predicted clearance mass flux as a function of chordwise distance based on the assumption that the jet was entirely pressure driven, and compared this mass flux to that computed by the Navier-Stokes solver. This comparison is replotted in Figure 3-1, which shows agreement between actual and pressure-driven mass flux to within 6%.

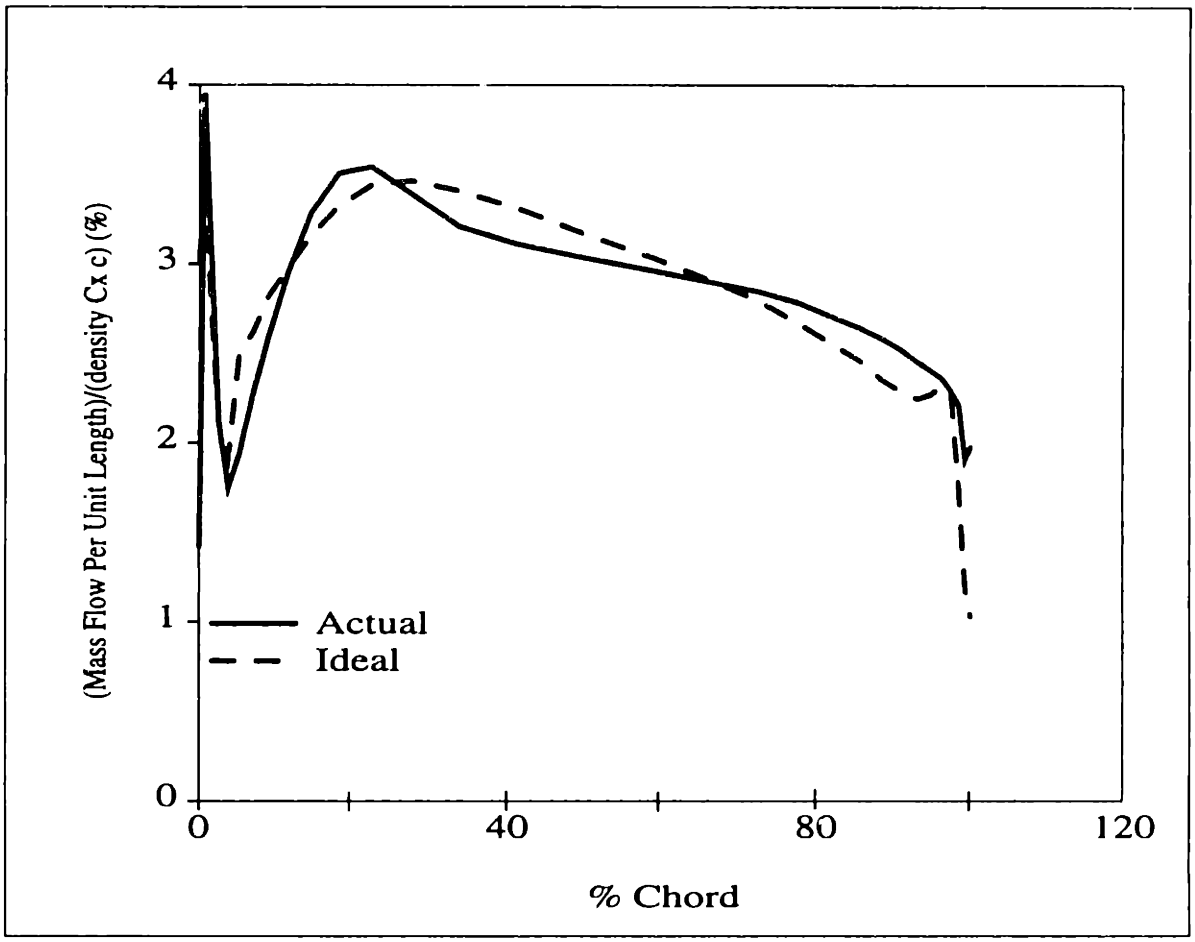

Figure 3-1: Pressure Driven versus Actual Clearance Mass Flux, from Khalid (1995)

One further piece of evidence for the validity of the assumption that the leakage jet is pressure driven comes from an analysis done by Chen (1991). By examining the ratio of the pressure driven velocity magnitude to the velocity that would be produced due to viscous forces alone, Chen derives a relation between the clearance to chord ratio and the Reynolds number based on chord and inlet relative velocity. Chen's analysis assumes that the flow in the leakage gap is laminar. The relation can be used to indicate when viscous forces will be important in the leakage flow and when they can be ignored. For

$$\frac{\tau}{c}\sqrt{Re} \geq 2.3 \tag{3.1}$$

the wall effects will be small (the velocity due to viscous effects will be less than one tenth the pressure driven velocity). For the low speed rotor calculations, $\frac{\tau}{c}\sqrt{Re} = 8.3$, and for the rotating rig experiments described in Section 2.3 $\frac{\tau}{c}\sqrt{Re} = 5.5$[1].

Evidence from a variety of sources, both experimental and theoretical, suggest that for the compressors examined in this thesis the leakage jet is primarily pressure driven. This conclusion helps to explain the usefulness of the wind tunnel simulation presented in Section 2.5, and also served as the foundation for the leakage angle predictions presented below.

3.2.2 Inviscid Leakage Angle Prediction Method

If the leakage jet is pressure driven, the leakage velocity, V_L, can be related to the blade pressure difference by applying Bernoulli's equation.

$$V_L = \sqrt{\frac{2 \cdot (P_{PS} - P_{SS})}{\rho}} = \sqrt{\frac{2 \cdot \Delta P_B}{\rho}}. \tag{3.2}$$

Storer (1991) assumes that the streamwise component of the fluid entering the clearance gap can be approximated by applying Bernoulli's Equation assuming that the total pressure is the same as the free stream, and that the appropriate static pressure is the blade pressure surface pressure just inboard from the tip. The streamwise component of the leakage velocity can be written

$$V_{SW} = \sqrt{\frac{2 \cdot (P_T - P_{PS})}{\rho}}. \tag{3.3}$$

If the streamwise velocity on the pressure side of the blade is convected unchanged across

1. In the experiments of Moyle (1991), this factor is greater than 4.0, also indicating that the leakage jet was primarily pressure driven in these experiments.

the tip gap the leakage angle can be written

$$\alpha = \tan^{-1}\left(\frac{V_L}{V_{SW}}\right) = \tan^{-1}\left(\sqrt{\frac{P_{PS}-P_{SS}}{P_T-P_{PS}}}\right), \tag{3.4}$$

where V_{SW} is the streamwise velocity component of the leakage jet, and P_T is the total pressure of the fluid entering the clearance gap.

To derive an expression for the mass averaged leakage angle, Storer (1991) makes the following three assumptions: 1) the chord-wise averaged blade pressure difference can be used to calculate the mean leakage velocity, 2) the total pressure of the clearance jet is equal to the total pressure of the free stream, and 3) the chord-wise averaged velocity along the pressure surface is equal to the average exit velocity. Thus the mean leakage angle, $\bar{\alpha}^m$, can be written

$$\bar{\alpha} = \tan^{-1}\left(\frac{\overline{V_L}}{V_{SW}}\right) \approx \tan^{-1}\left(\frac{\overline{V_L}}{V_{exit}}\right) = \tan^{-1}\left(\frac{\sqrt{\frac{\overline{\Delta P_B}}{Q_{in}}}}{\sqrt{1-\frac{\Delta P_P}{Q_{in}}}}\right). \tag{3.5}$$

As will be discussed in subsection 3.2.3, the assumption that the leakage jet total pressure is equal to the free stream total pressure is not always true. A method for estimating when this assumption will not be valid is presented.

3.2.3 Double Leakage

For the geometries examined in this thesis, Storer's assumption that the leakage jet total pressure is equal to the free stream total pressure was found to be invalid in some instances. For example, in the high loading, large clearance case shown in Figure 3-2 there are regions where the total pressure of the clearance jet is below the free stream total pressure by 45% of the inlet dynamic head. Neglecting this loss causes the inviscid leakage angle theory to underpredict the leakage angle at those locations by more than ten

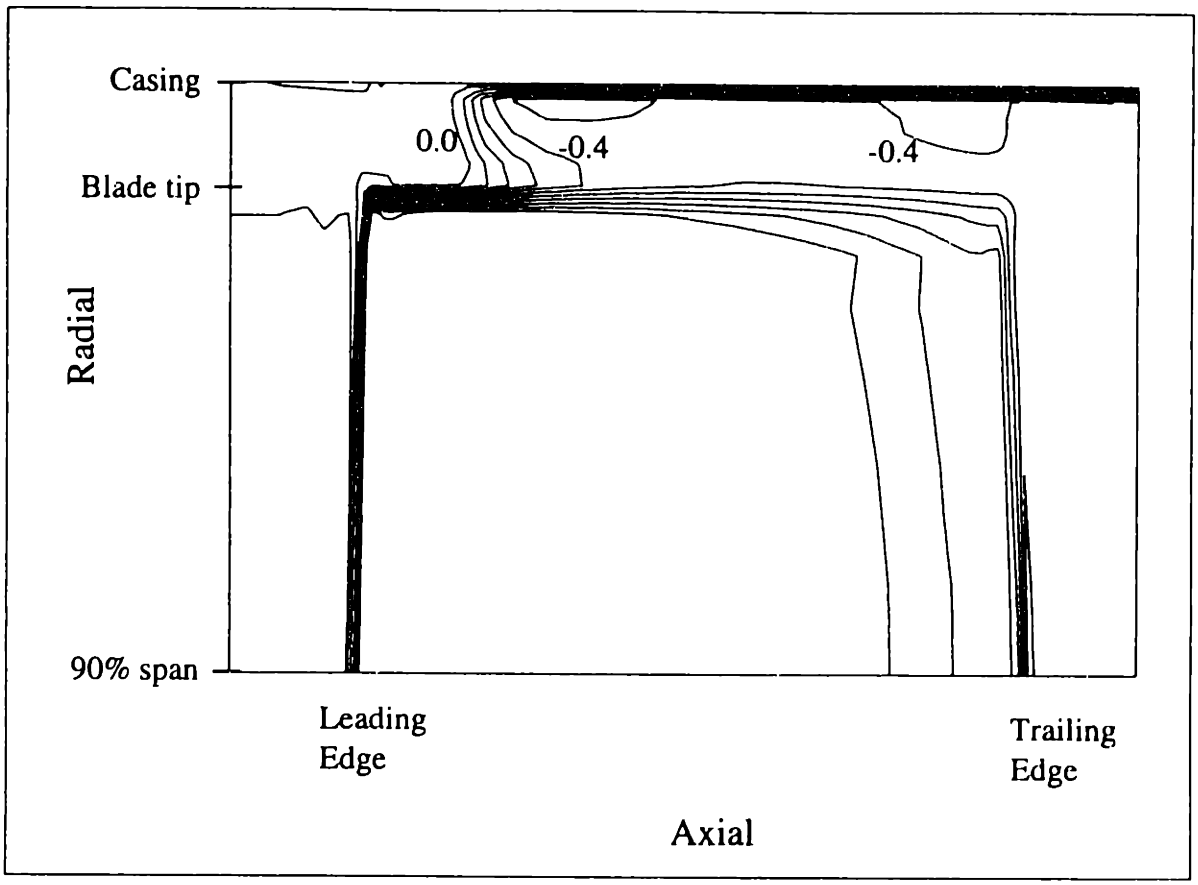

Figure 3-2: Total Pressure Coefficient at Clearance Gap Exit, Large Clearance, High Loading

degrees. Underprediction of the leakage angle by ten degrees is estimated (see Chapter 4) to reduce the blockage by approximately 30%. The factors that influence the accuracy of the angle prediction were thus examined in more detail.

The reduction in clearance jet total pressure is due to double leakage, *i.e.*, fluid leaking over one blade tip traversing the passage and entering the adjacent blade tip gap. The fluid which traverses the passage undergoes loss and enters the next gap with a reduced total pressure. The situation is shown schematically in Figure 3-3. Evidence for this phenomenon can be seen in Figure 3-4, showing streamlines traced from the exit the clearance of the blade at the top of the figure. Streamlines that exit the passage through the trailing edge plane are shown as dashed lines, and the streamlines that double leak are shown as solid lines.

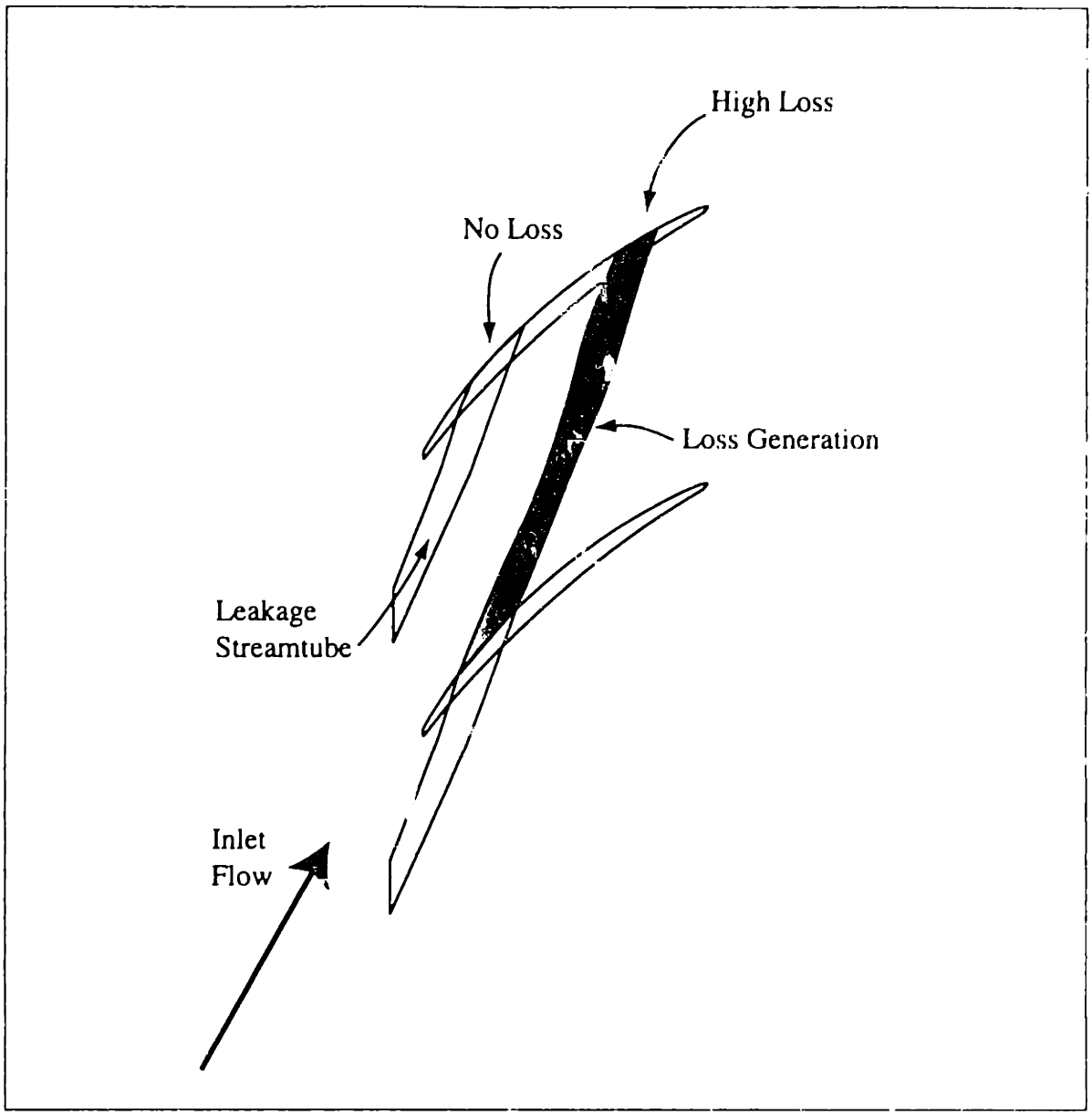

Figure 3-3: Double Leakage Schematic

Conditions at the Exit of the Clearance Gap

To accurately predict the clearance jet leakage angle, the total pressure of the fluid exiting the clearance gap must be known. This subsection examines the factors that influence the jet total pressure. The total pressure coefficient at the exit of the clearance gap for two representative cases is shown in Figures 3-5 and 3-6, showing a tangential view of the blades. Both figures are for the low speed rotor, small clearance geometry, with Figure 3-5 from a low loading condition, and Figure 3-6 from close to stall.

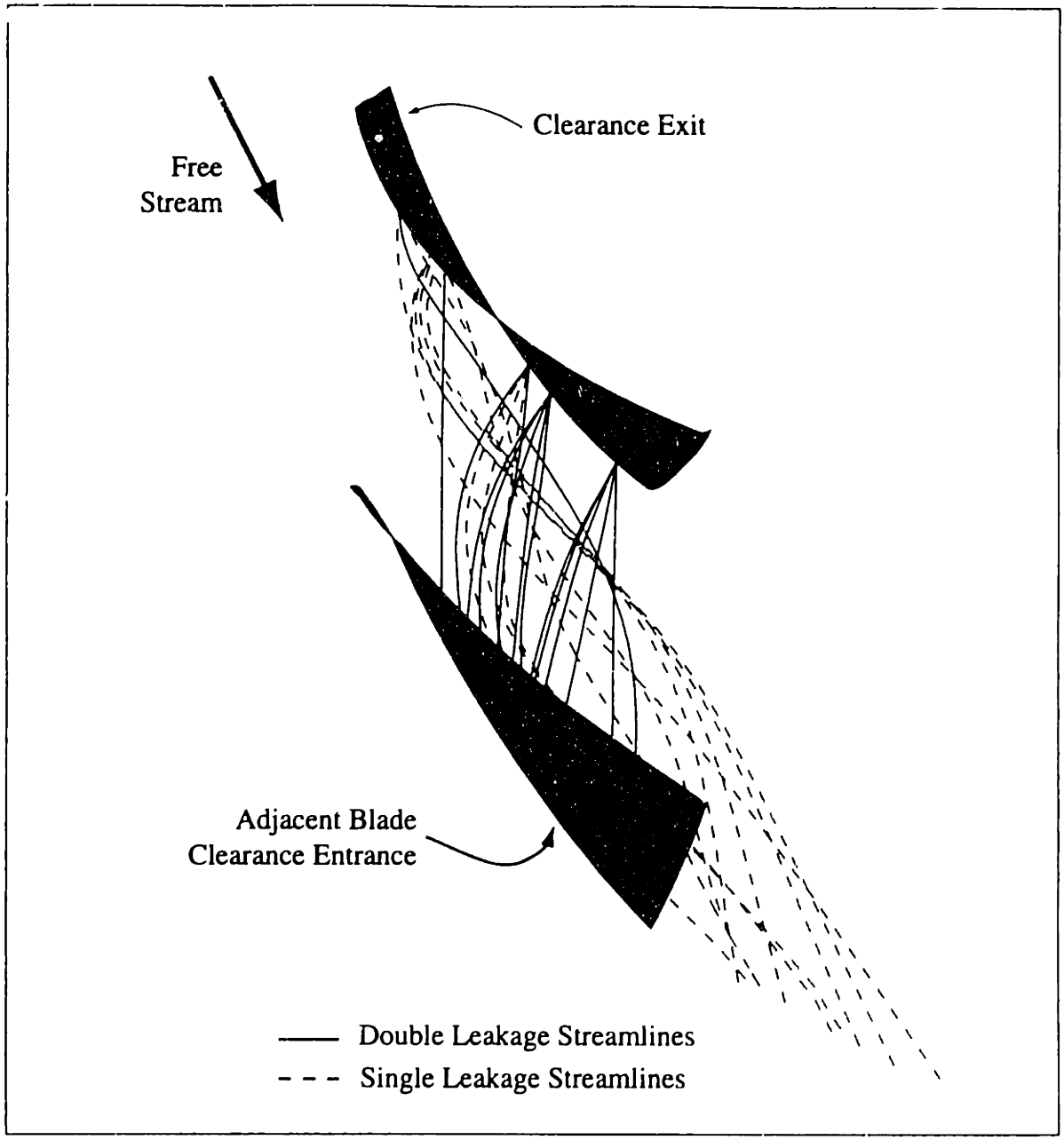

Figure 3-4: Streamlines Traced Downstream from the Clearance Exit

In Figure 3-5 there are only small regions within the tip gap with negative total pressure coefficient; the total pressure of the leakage jet is approximately equal to the free stream total pressure. In Figure 3-6 however, the total pressure coefficient over the rear 60% of chord is below -0.2.

The cause of this reduction in clearance jet total pressure can be seen in plots of total pressure coefficient contours in an axial-tangential plane at the blade tip radius. Two examples of such plots are given in Figures 3-7 and 3-8 which are for the same conditions as in Fig-

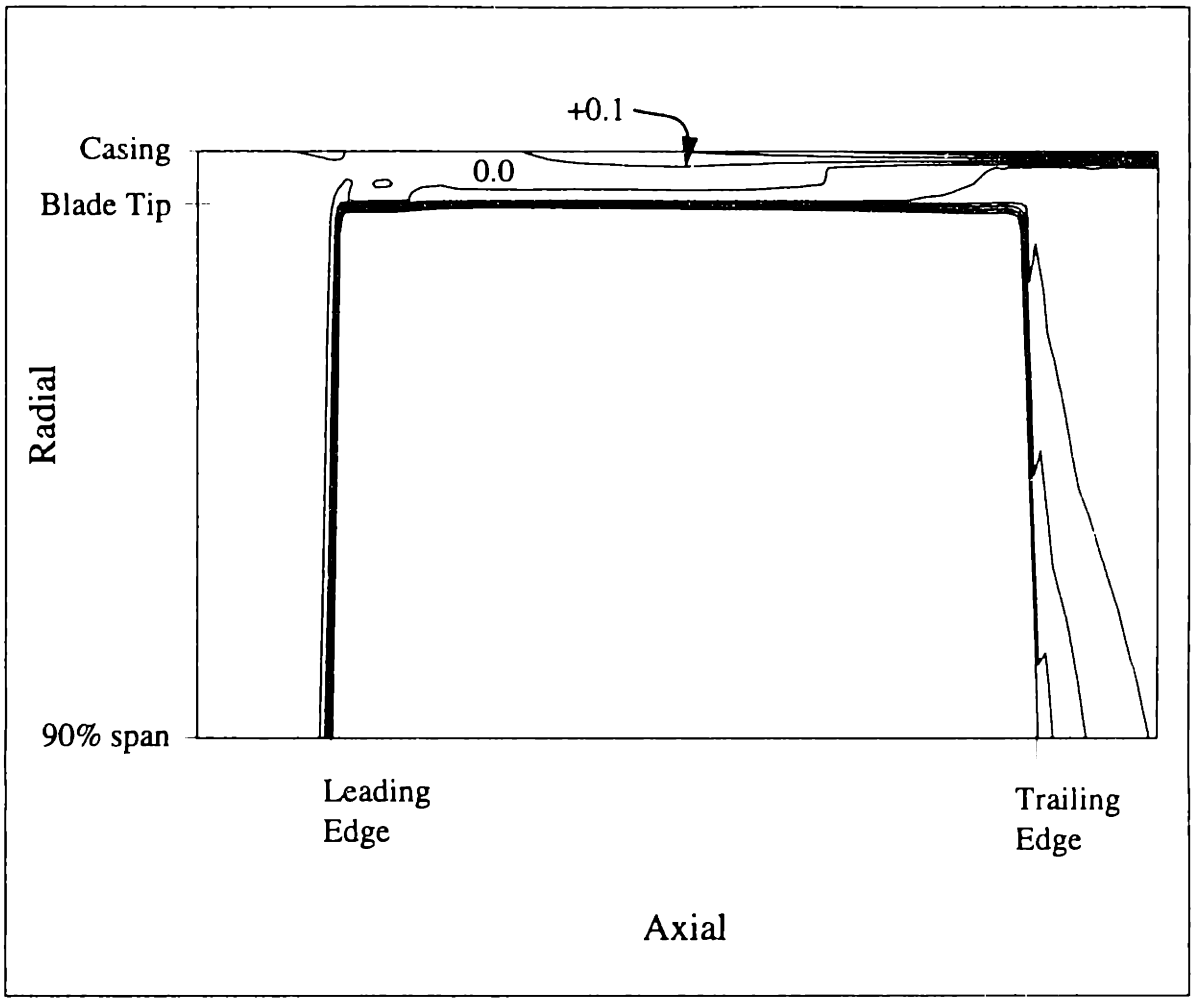

Figure 3-5: Total Pressure Coefficient at Clearance Gap Exit, Small Clearance, Low Loading

ures 3-5 and 3-6, respectively. A clear interface is visible in these figures between the free stream and the clearance jet. As loading is increased the trajectory of this interface moves forward in the passage, eventually impinging on the lower blade's pressure surface, as in Figure 3-8.

Behind the jet-free stream interface is a region of low total pressure fluid. Downstream of the point where this trajectory impinges on the lower blade's pressure surface, the total pressure of the fluid at the entrance to the clearance gap is lower than the free stream total pressure. Figure 3-8 shows that the jet-free stream interaction region intersects the lower blade's pressure surface at approximately 40% chord. Figure 3-6 shows that it is also at 40% chord that the total pressure of the clearance jet decreases.

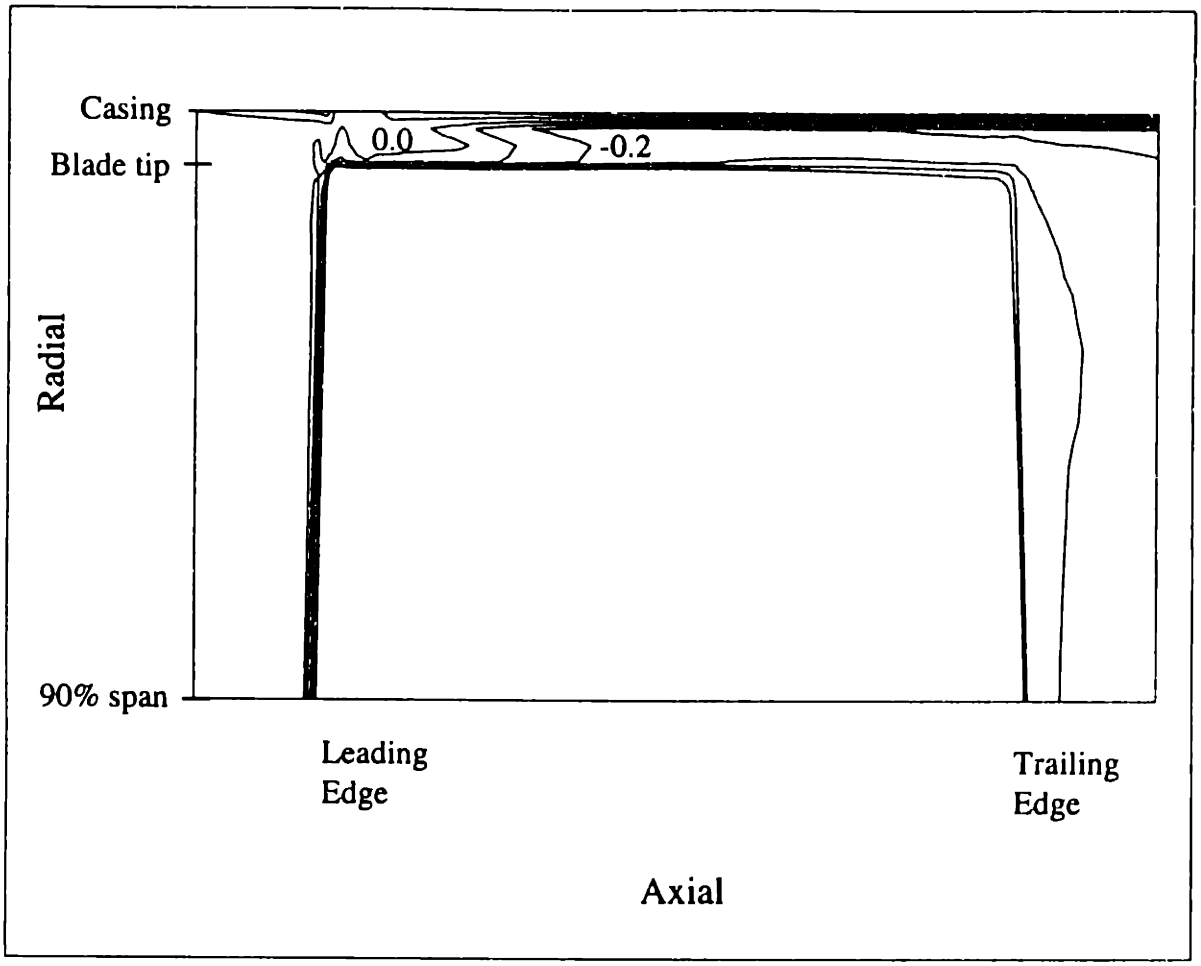

Figure 3-6: Total Pressure Coefficient at Clearance Gap Exit, Small Clearance, High Loading

When fluid from the leakage jet passes under a second blade, the total pressure of the clearance jet is reduced from the location at which the jet impinges upon the blade pressure surface to the trailing edge. If this reduction in total pressure is neglected, the leakage angle prediction will be too low, by as much as ten degrees.

Effect of Double Leakage on Leakage Angle Prediction

Leakage angles given by Storer's (1991) analysis are shown in Figure 3-9, which also shows mass averaged leakage angles computed from the Navier-Stokes solutions. For the $\tau/c=1.4\%$ geometry, Storer's analysis is accurate to roughly one degree. For the $\tau/c=3.0\%$ geometry, the agreement at low loading is also roughly a degree. At high loading however, the Storer's method underpredicts the mean leakage angle by ten degrees because the mean clearance jet total pressure is lower in the high loading large clearance cases (see for

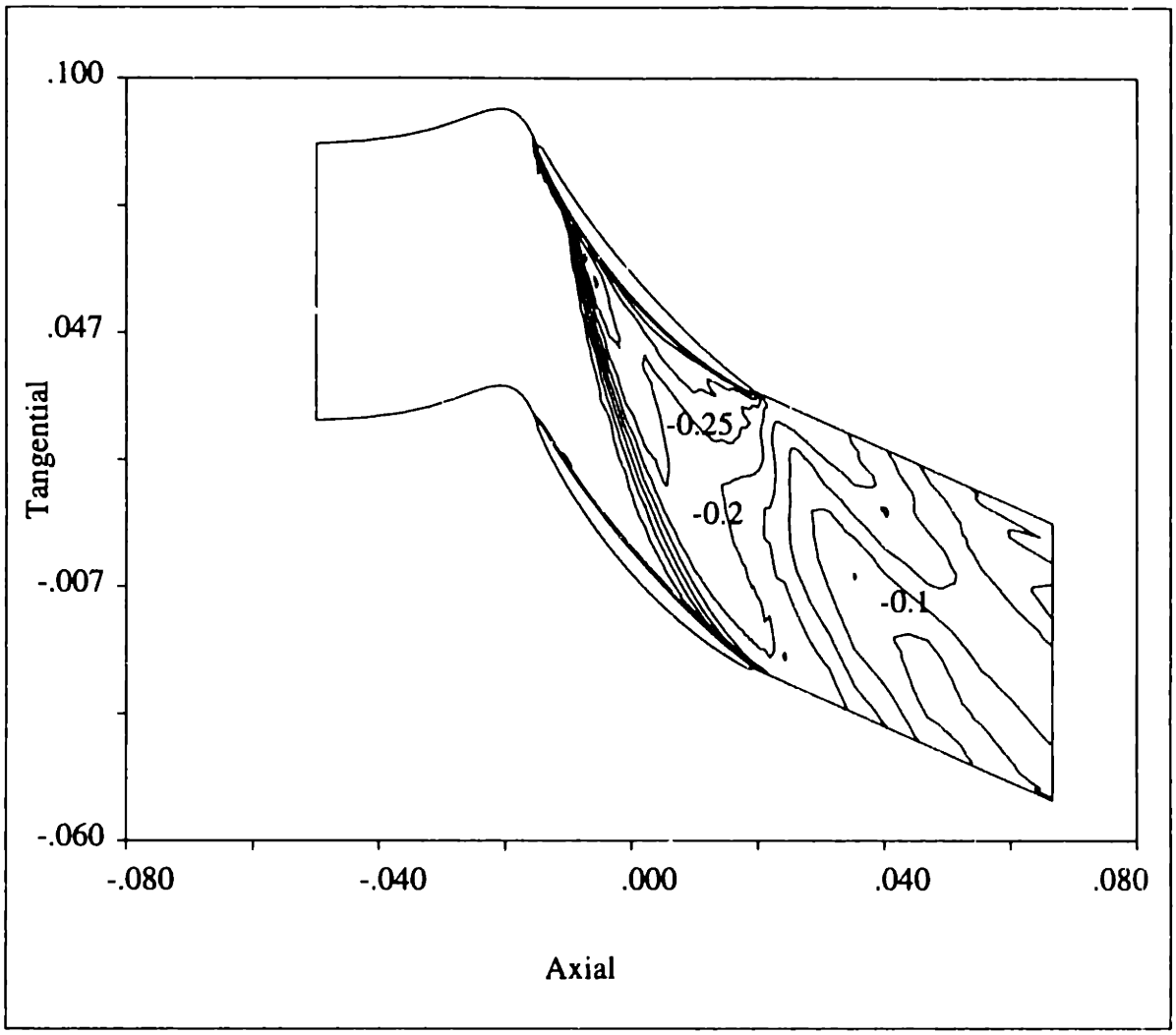

Figure 3-7: Total Pressure Coefficient Contours at the Blade Tip Radius, Low Loading

example Figure 3-2) due to double leakage than in the small clearance cases (as in Figure 3-6).

Prediction of Clearance Jet-Free Stream Interaction Trajectory

The line of interaction between the clearance jet and the free stream extends from close to the leading edge of the suction side of one blade across the passage, perhaps impinging on the pressure surface of the next blade. The location of this interaction region is used in the blockage model developed in Chapter 4, and it indicates where the clearance jet total pressure will be lower than the free stream total pressure.

With the assumption that the jet and free stream total pressures are equal, the theory of

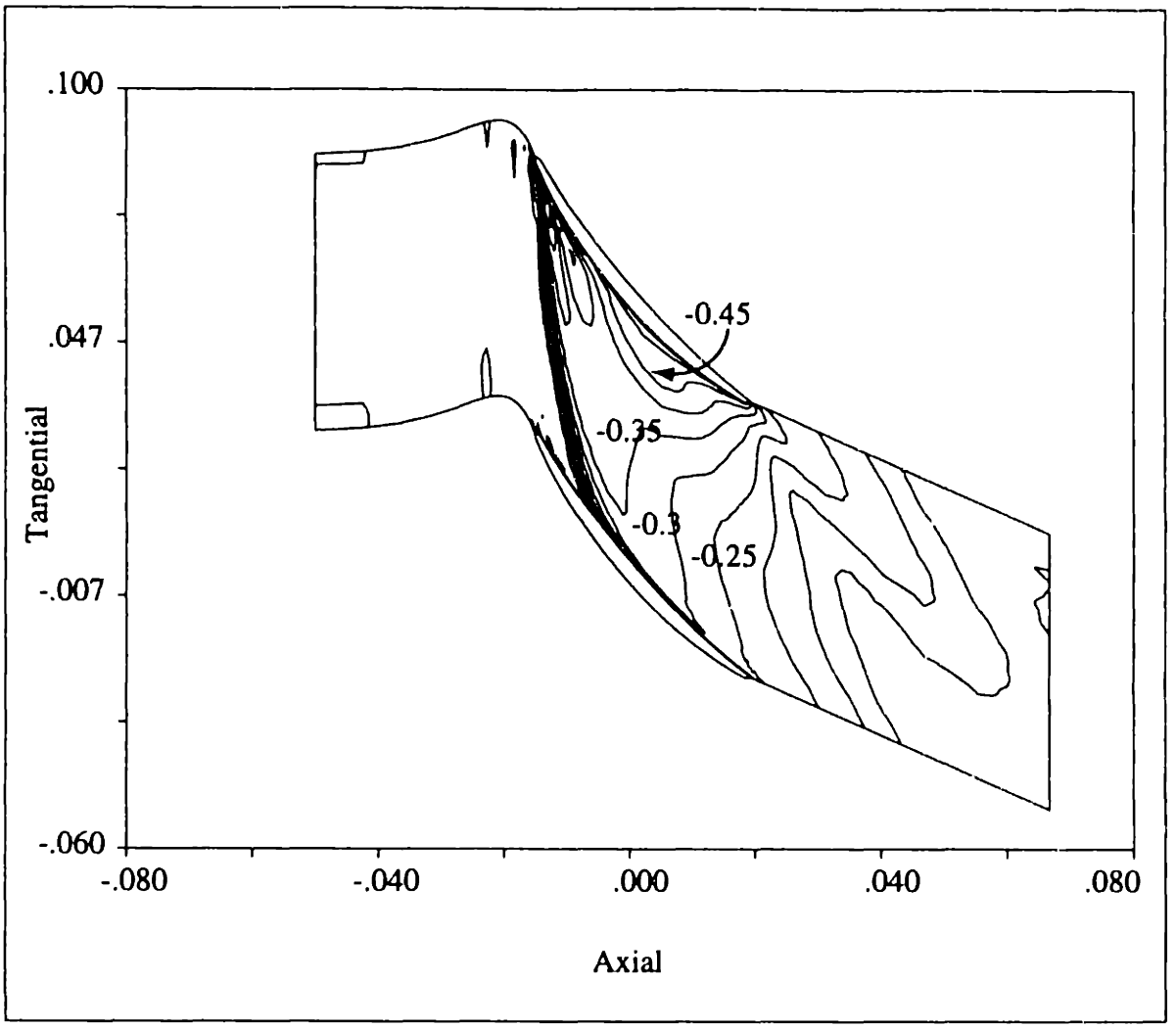

Figure 3-8: Total Pressure Coefficient Contours at the Blade Tip Radius, High Loading

Martinez-Sanchez and Gauthier (1990) can be used to predict the trajectory of the interaction region between the jet and the free stream. Their theory predicts that the line of the interaction zone makes an angle, Θ, to the blade stagger equal to half of the chordwise averaged clearance jet leakage angle, so

$$\bar{\Theta} = \frac{1}{2}\alpha^m. \tag{3.6}$$

This is shown schematically in Figure 3-10.

To extend this theory to situations where the total pressures of the two streams are unequal, a control volume analysis was performed. A schematic of the control volume

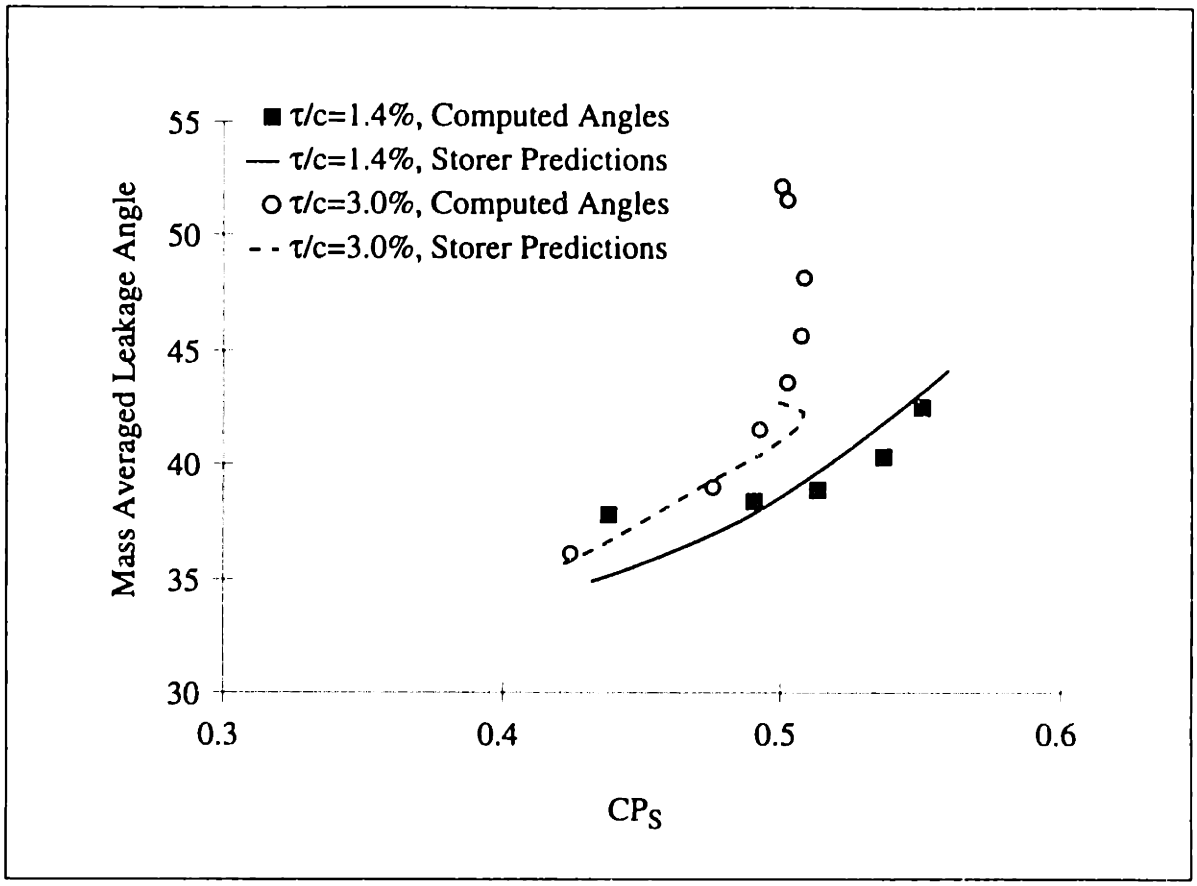

Figure 3-9: Actual and Predicted Leakage Angles, Assuming Clearance Jet Total Pressure Equal to Free Stream Total Pressure

used is shown in Figure 3-11, which shows a radial view of the flow field. Applying conservation of momentum in the direction normal to the vortex trajectory gives the following equation for the angle between the vortex trajectory and the blade stagger, Θ, in terms of the leakage angle, α, and the free stream to jet velocity ratio, V_{FS}/V_j:

$$\tan\Theta = \frac{\sin\alpha}{\left(\frac{V_{FS}}{V_j}\right) + \cos\alpha}, \tag{3.7}$$

which is equivalent to Equation 3.6 in the special case of the free stream and the jet velocity being equal.

Because V_{FS}/V_j varies along the chord the average Θ, $\bar{\Theta}$, is calculated by averaging Θ along the chord, not by using the average leakage angle, $\bar{\alpha}^m$, in Equation 3.6.

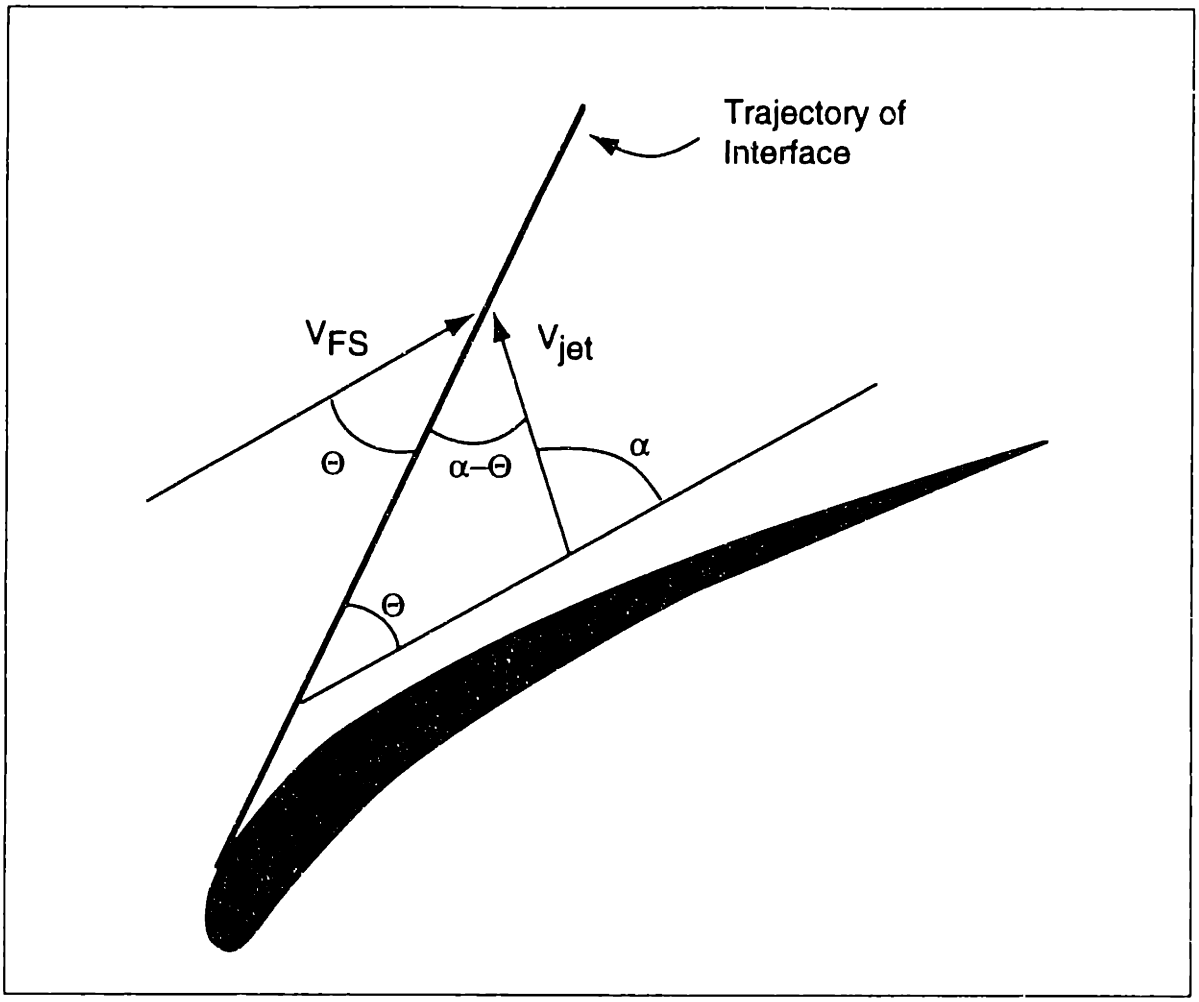

Figure 3-10: Martinez-Sanchez and Gauthier Model for Leakage Vortex Trajectory

For computational solutions examined here, this theory predicts the interaction region trajectory to within 5°. One example of the theoretical prediction is given in Figure 3-12 for the low speed rotor, small clearance, high loading solution.

The theory of Martinez-Sanchez and Gauthier predicts the location of the jet-free stream interface zone; but if this zone intersects the pressure side of the next blade, the theory can not predict the clearance jet total pressure behind the impingement location. Observations of the computed solutions indicate that this post-interface-impingement total pressure is lower (more loss) for larger clearances, larger inlet boundary layers, and higher solidities, but no model for the total pressure loss was developed.

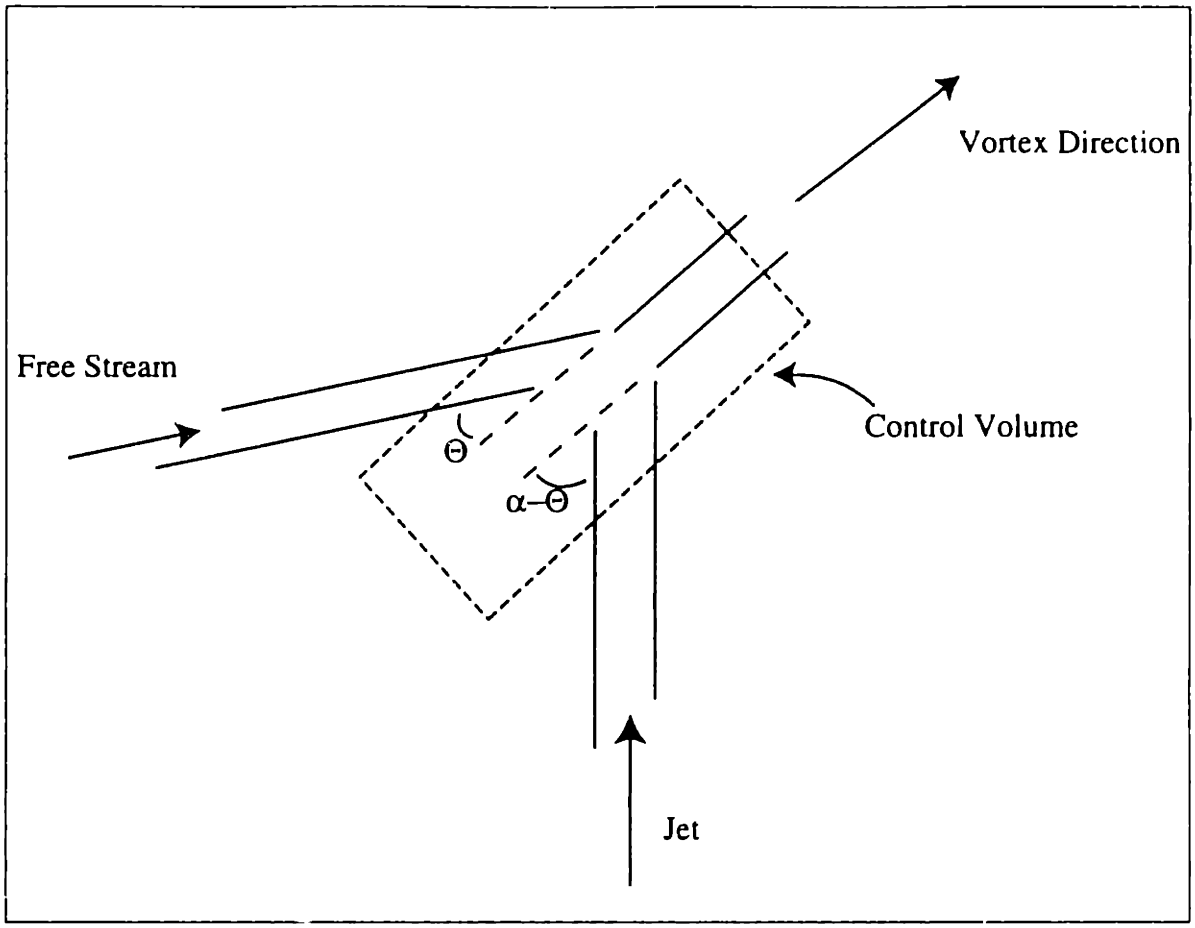

Figure 3-11: Jet-Free Stream Interaction Control Volume

Effect of Double Leakage on Exit Plane Loss

The loss at the clearance exit due to double leakage causes an increase in the exit plane loss. For example, the blockage region average total pressure coefficient for the $\tau/c=3.0\%$, high loading case (shown in Figure 3-2) is -0.23, whereas for the same static pressure rise, the $\tau/c=1.4\%$ geometry (with less loss at the clearance exit, as shown in Figure 3-6) has a total pressure coefficient of -0.13.

3.2.4 Flow Features Summary

It has been observed that for some conditions fluid from one tip gap crosses the passage and leaks through the adjacent blade's clearance gap. This double leakage fluid has a lower total pressure than the free stream fluid, causing one of the assumptions in the leakage angle prediction equation (Equation 3.5) to be invalid. This can result in the underprediction of the mean leakage angle by as much as 10 degrees, and as will be shown in

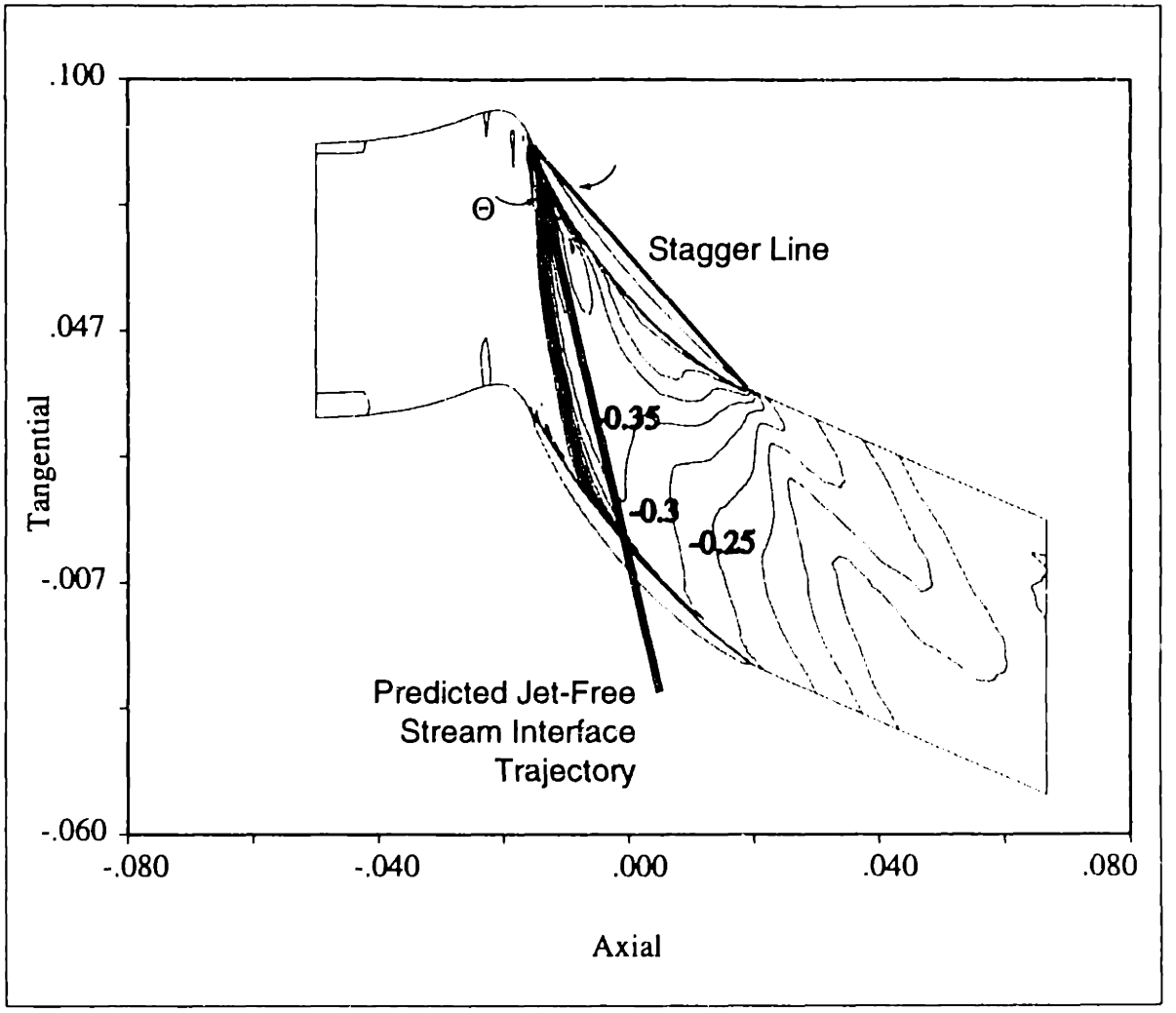

Figure 3-12: Trajectory Prediction from Martinez-Sanchez and Gauthier Theory

Chapter 4, this could cause the blockage prediction to be 30% too low.

The leakage angle and the clearance jet total pressure, both of which are affected by double leakage, are two of the inputs to the blockage model developed in Chapter 4. The observations of this section indicate the primary effects that influence these two quantities.

3.3 Parametric Trends

In this section data from the rotating rig tests and the computations are examined in more detail in more detail with respect to the parametric trends of exit blockage. The sections are organized by parameter, dealing with effects on endwall blockage of clearance height (subsection 3.3.1), stagger (subsection 3.3.2), overall passage loading (subsection 3.3.3),

inlet boundary layer thickness (subsection 3.3.4), solidity (subsection 3.3.5), blade loading profile (subsection 3.3.6), and swirl (subsection 3.3.7).

3.3.1 Clearance Height

For clearances below 1% of chord both Khalid (1995) and Storer (1991) have shown that endwall performance is not dominated by the leakage jet, but tends to display three-dimensional separation in the endwall-suction side corner where low momentum endwall fluid accumulates. The present study has examined clearance heights from 1.2 to 3.5% of chord, covering a range of interest for modern compressors, and hence the observations made here about the affect of clearance size on blockage are expected to be applicable to many compressor designs.

The effect of clearance size on endwall blockage can be seen in Figure 3-13, where the results from the rotating rig and the rotor computations are presented as two pairs of data points, with each pair consisting of a τ/c=1.4% and 3.0% case. Comparing the experimental data for large clearance to small clearance, and the computations for large to small clearance, shows less than 20% difference in normalized blockage across the entire speedline (all the points for the same geometry represent data taken at different points along an operating line). The data indicates that endwall blockage is directly proportional to clearance height. Doubling the clearance size will approximately double the exit plane blockage.

This trend can also be examined by considering the mass flux through the clearance gap for the different clearance sizes. For the same pressure rise across the blade row, the mass flux through the clearance scales with the clearance height, as shown by the computational results. A representative data pair shown in Table 3-3. For the same loading condition both the clearance mass flux and the blockage scale directly with clearance height. Hence the blockage normalized by the clearance area is relatively unchanged for the increase in tip gap.

Compared to the other parameters examined here, the clearance height is the parameter

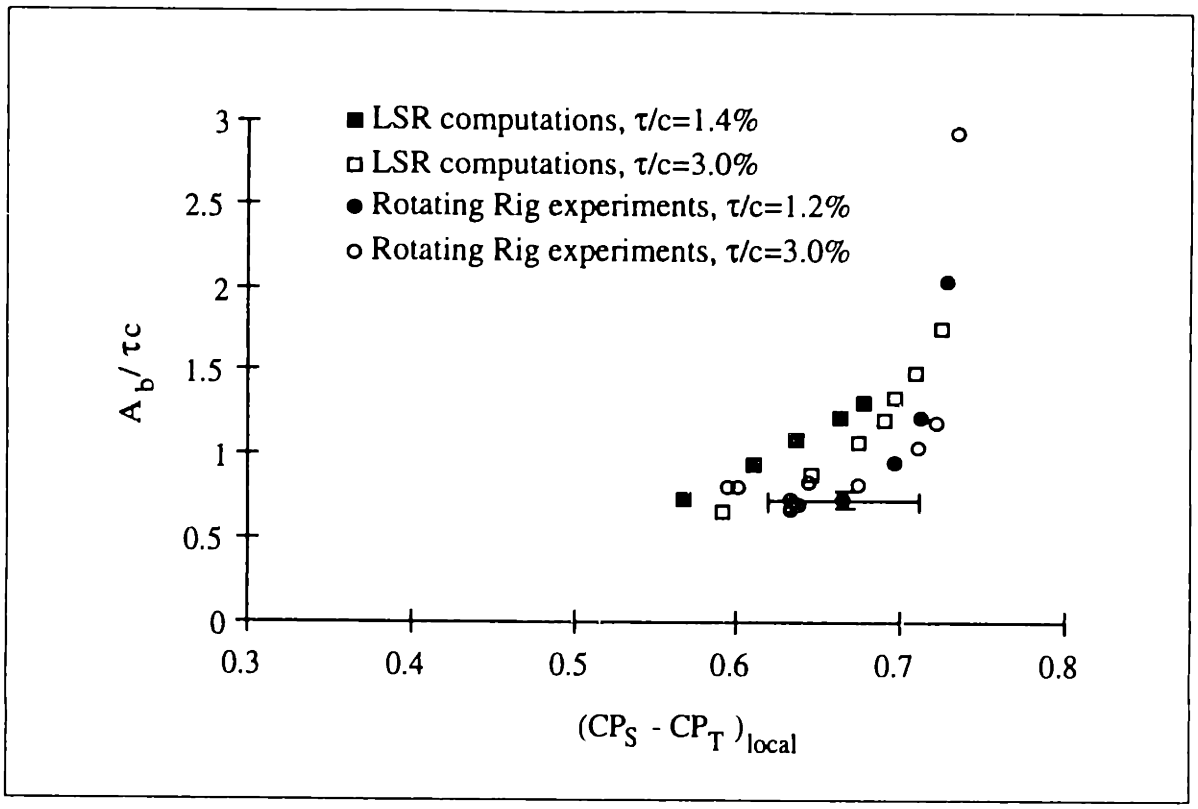

Figure 3-13: Effect of Clearance Height on Endwall Blockage, Blockage versus Loading Parameter

τ/c	CP_S	$\bar{\alpha}^m$	$A_b/\tau c$	$\Delta A_b/\tau c$	$\Delta \dot{m}_{clrnc}$
1.4%	.490	38^0	.972	-	-
3%	.492	42^0	1.102	+13%	+109%

Table 3-1: Effects of Clearance Height

which has the largest influence on blockage. Doubling the clearance will double the blockage. This is also the conclusion reached by Hunter and Cumpsty (1982), who measured the axial displacement thickness of the casing boundary layer for a number of compressor configurations. They argue that clearance height is the proper length scale with which to normalize the displacement thickness, and they plot their results and the data from Smith (1970) as exit displacement thickness normalized by clearance height versus the pressure rise normalized by the stalling pressure rise. The data from Hunter and Cumpsty (1982) and Smith (1970) are replotted in Figure 3-14, which include measurements for clearance heights from 1% to 4% of chord. Figure 3-14 shows that displacement thickness does scale approximately with clearance height.

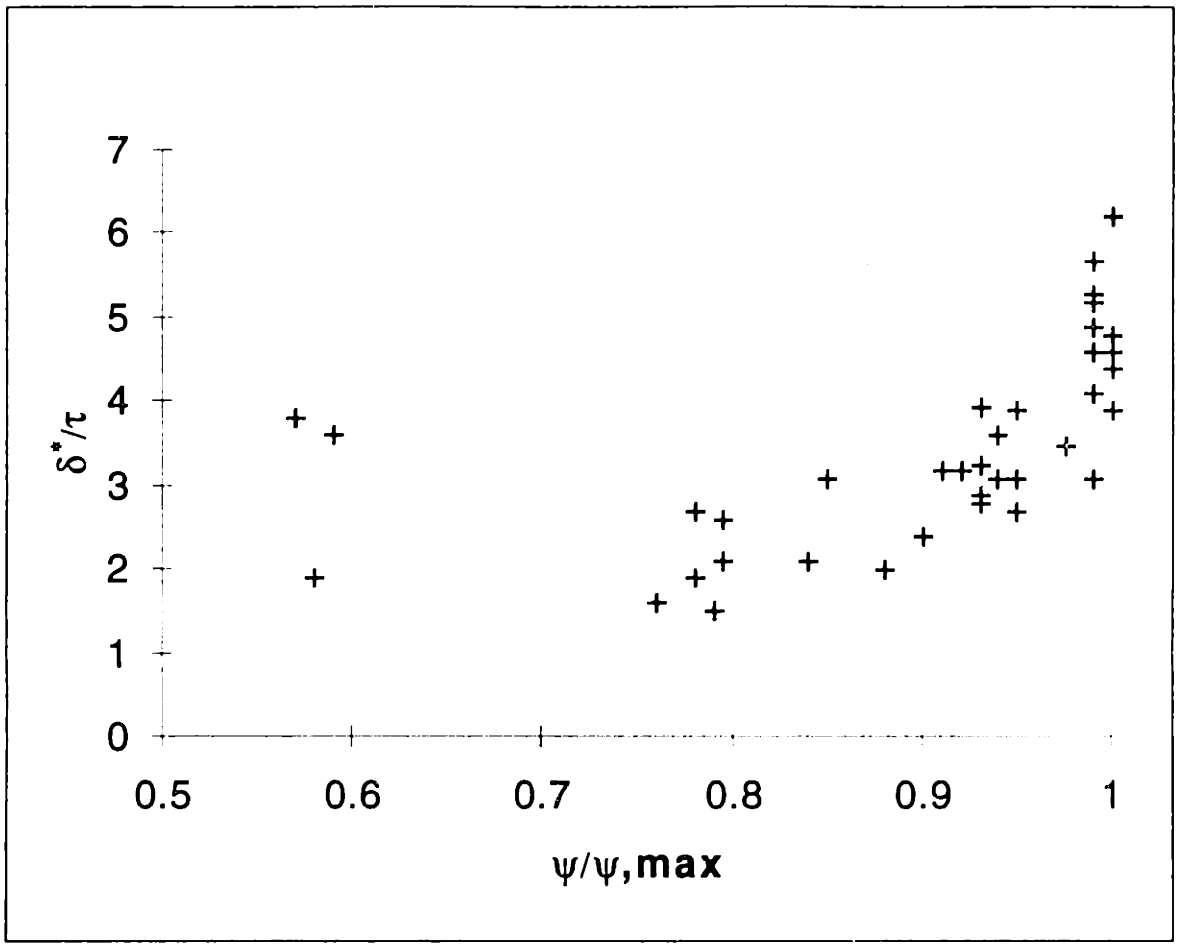

Figure 3-14: Data from Hunter and Cumpsty (1982) and Smith (1981), Displacement Thickness/Clearance versus Pressure Rise Coefficient/Maximum Pressure Rise Coefficient

3.3.2 Stagger

Data were taken on the Deverson rotor at tip stagger angles of 40.5^0 and 44.7^0. Referring to Figure 2-14, comparing the rotating rig data at the two staggers, the effect of these changes in stagger angle on blockage can be seen to be small, shifting the normalized blockage by 5-15% of the clearance area.

Because the experimentally studied stagger range does not cover the entire range of stagger angles of interest, a theoretical examination of the effect on blockage due to the stagger changes was performed. First the effect of stagger on the clearance leakage angle and mass flux was examined. Then the effect of these changes on blockage was calculated (subsection 4.4.1).

Figure 3-15 shows the effect of stagger on leakage angle and clearance mass flux. In the figure the solidity and the axial chord/clearance are fixed. Shown in Figure 3-15 are the

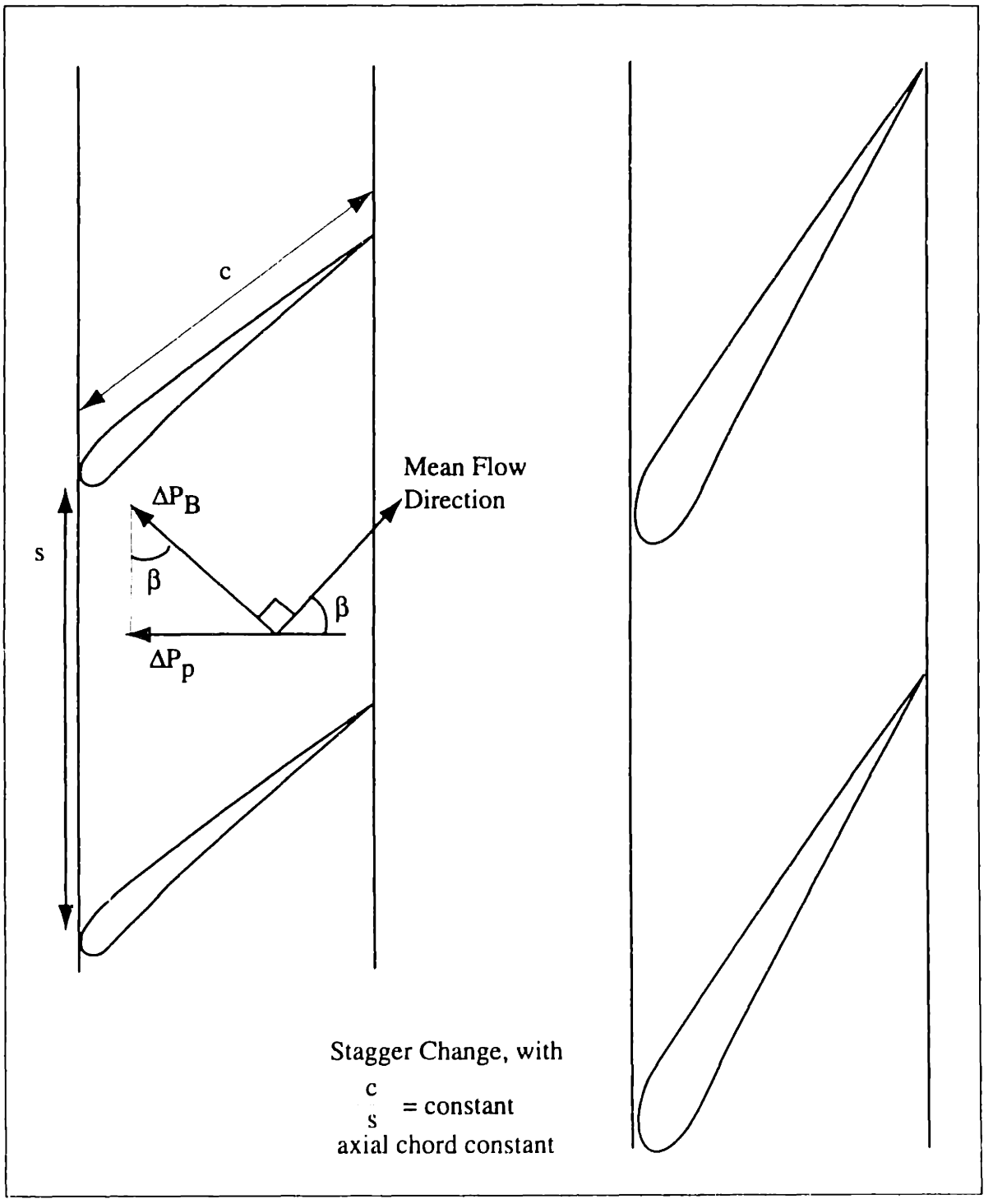

Figure 3-15: Schematic of Stagger Variation

axial pressure force due to the passage pressure rise, ΔP_P and the pressure difference across the blade, ΔP_B, which acts normal to the mean chord line of the blade. Assuming

the flow to be two-dimensional and neglecting viscous forces, balancing these two forces in the axial direction yields

$$\frac{\Delta P_P}{\Delta P_B} = \frac{c \cdot \sin\beta}{s}. \tag{3.8}$$

This equation was used with Equations 3.2 through 3.5 to assess the impact of stagger changes on the clearance mass flux and leakage angle. Figure 3-16 plots the percent change in clearance mass flux versus the amount of stagger increase for a variety of initial staggers. For staggers above 30°, the mass flux through the clearance, $\rho \cdot V_L \cdot \tau \cdot c$, increases as the stagger is increased, as shown in Figure 3-16. As the stagger angle approaches 90° the chord increases faster than the leakage velocity decreases, giving the rapidly rising curves in Figure 3-16, and the increased sensitivity of the higher initial staggers.

Plotting the change in clearance mass flux per unit chord (instead of the change in total clearance mass flux) is more useful in understanding trends in the normalized blockage. This parameter is plotted versus the change in stagger angle in Figure 3-17. Because of the reduction in leakage angle with increasing stagger angle, the clearance mass flux per unit chord is reduced as stagger angle is increased, by as much as 19% for the parameter range examined.

The effect of stagger angle on the mean leakage angle was examined, with the results given in Figure 3-18 for conditions corresponding to high loading: passage pressure rise coefficient of 0.5, with a solidity of 1.1. Figure 3-18 shows the average leakage angle versus stagger increase for the various initial stagger angles. As stagger is increased the mean leakage angle is reduced due to the reduction in blade pressure difference. The leakage angle is unaffected by the change in chord. The reduced leakage angle has two effects, both of which reduce the normalized blockage. The clearance mass flux per unit chord will be reduced, as shown in Figure 3-17, and the amount of shear between the jet and the passage flow will be reduced. As shown in Chapter 4, the leakage angle plays a role in setting the initial velocity defect, with a lower leakage angle giving a shallower initial veloc-

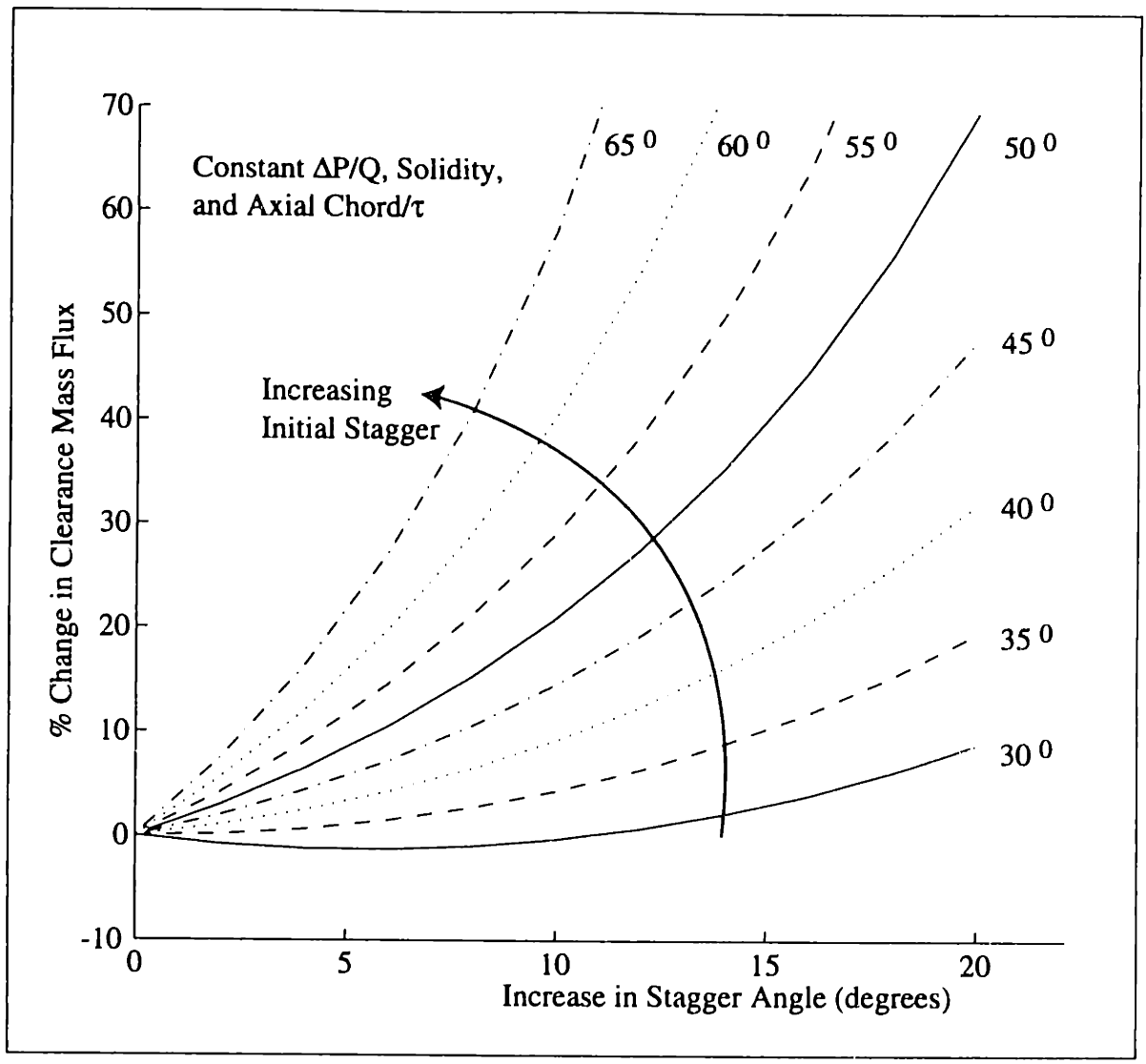

Figure 3-16: Effect of Changing Stagger Angle on Clearance Mass Flux, Percent Change in Clearance Mass Flux versus Change in Stagger for Staggers Between 30° and 65°

ity defect, and hence a lower exit plane blockage.

3.3.3 Overall Passage Loading

Increasing the passage loading increases the loading parameter CP_S-CP_T, and the blockage increases asymptotically, as shown in Figure 2-14, for example. It is instructive to look at what physical processes occur as passage loading is increased that cause this blockage trend.

Based on the one-dimensional analysis described in subsection 2.2.2, there are only two

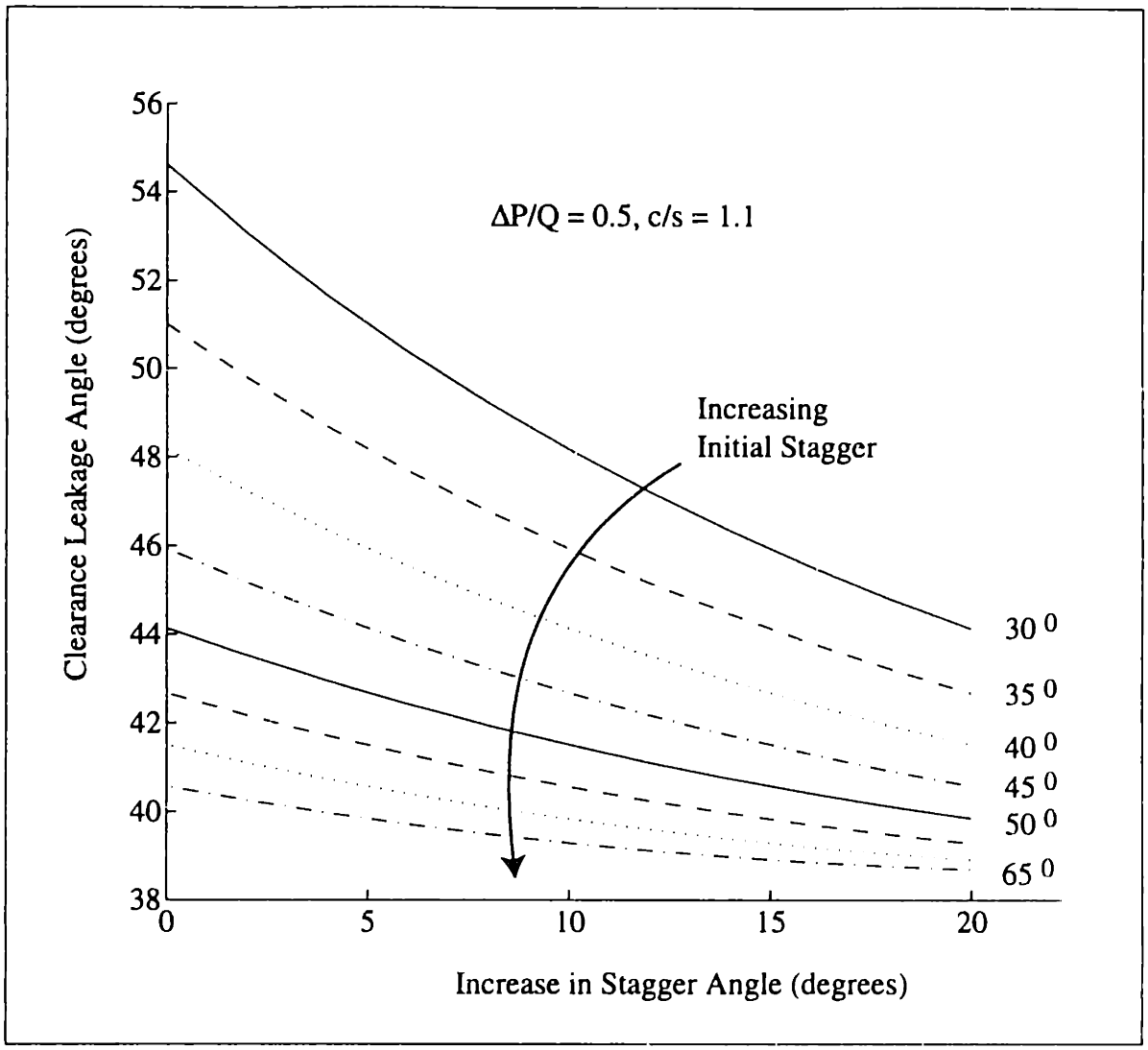

Figure 3-17: Effect of Changing Stagger Angle on Clearance Mass Flux per Unit Chord for Initial Staggers Between 30° and 65° for Constant Non-Dimensional Pressure Rise

quantities that set the blockage growth, the static pressure rise and the initial defect. Both of these change when the passage loading varies. The loading is equivalent to the static pressure rise across the blade row. The increased loading also causes the leakage angle to increase, resulting in increased velocity difference between the free stream and the clearance jet, and hence a deeper defect. As was illustrated in Figure 2-4(b), the asymptotic trend of blockage with static pressure rise tends to collapse for various initial conditions when the blockage is plotted versus the loading parameter.

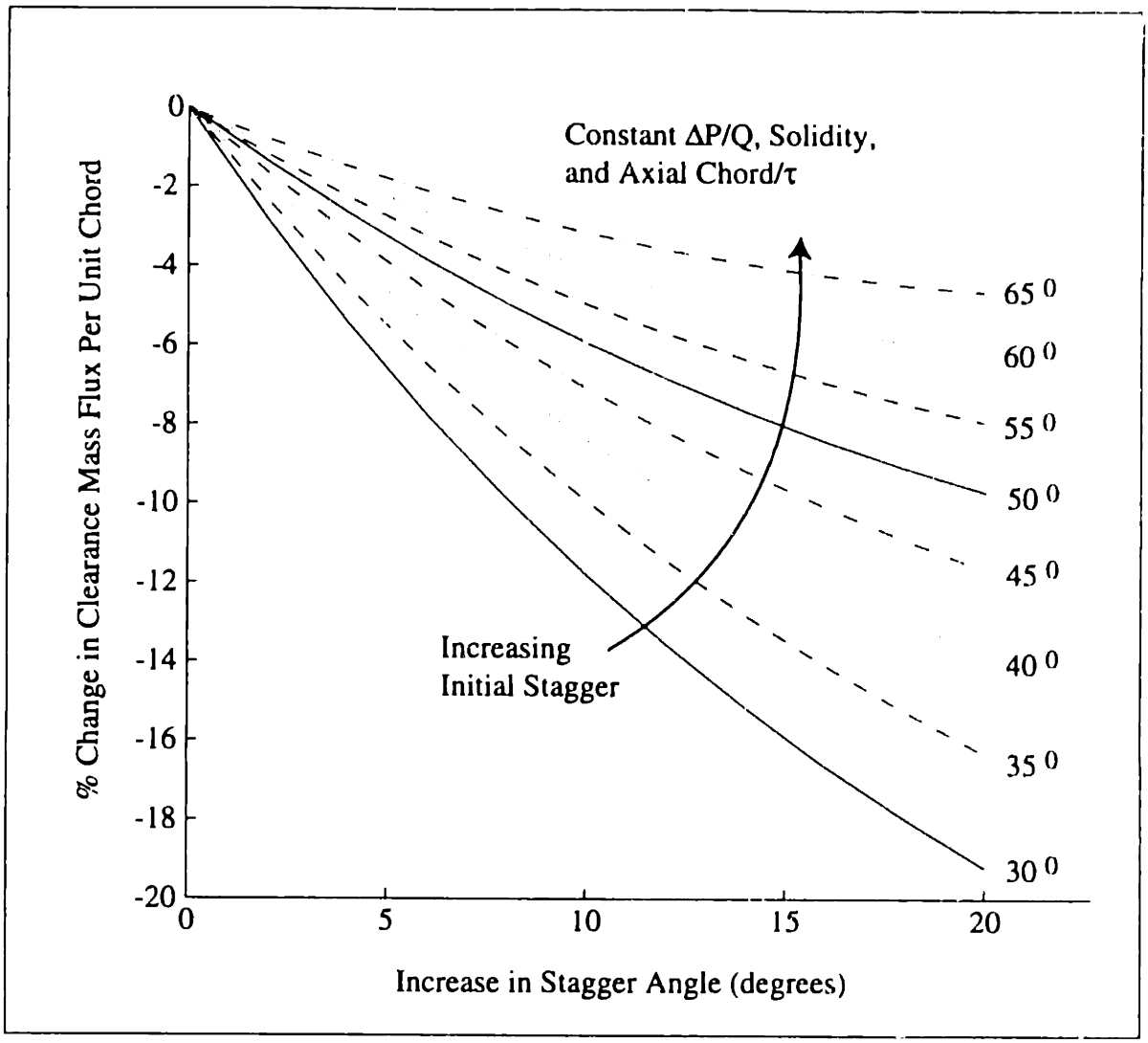

Figure 3-18: Effect of Changing Stagger Angle on Mean Leakage Angle for Initial Staggers Between 30^0 and 65^0 and $\Delta P/Q = 0.5$ and c/s=1.1

3.3.4 Inlet Boundary Layer Thickness

To examine the effect of inlet boundary layers on endwall blockage computations were carried out for three different inlet boundary layer thicknesses. Cumpsty (1995) indicated that typical values of inlet boundary layer displacement thicknesses in axial compressors may range from approximately one to three clearance heights, and the range studied, δ^* equal to zero (no inlet boundary layer), 1.3 clearance heights (considered the datum case), and 3.5 clearance heights, was chosen to bound this parameter range.

Computed speedlines for the three cases are presented in Figure 3-19. The stalling[1] mass

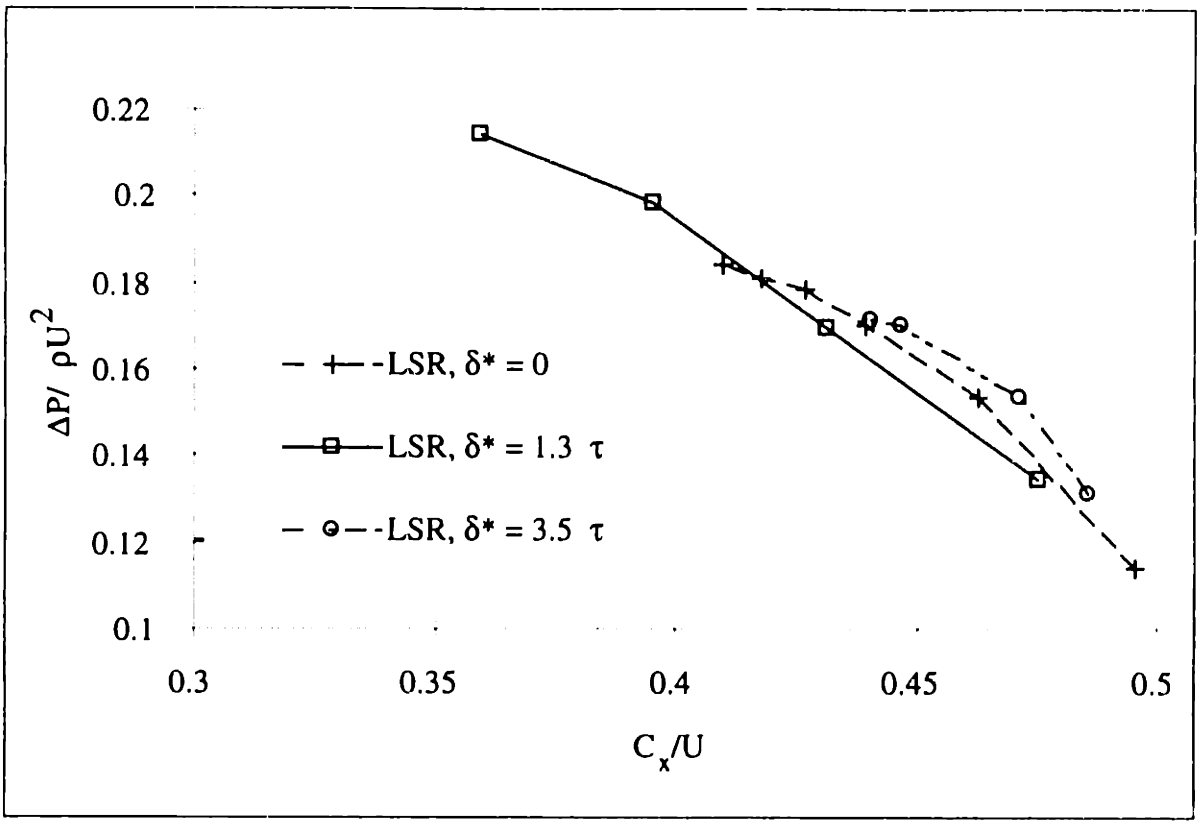

Figure 3-19: Computed Characteristics for Difference Inlet Boundary Layers for Low Speed Rotor, τ/c=3.0%

flow increases and the stalling pressure rise decreases as the boundary layer is thickened. Away from stall the thicker boundary layer characteristics show approximately 6% higher pressure rise for the same mass flow. This dependence of stalling pressure rise on inlet boundary layer thickness is similar to data presented by Hunter and Cumpsty (1982) who tested a low speed compressor with two different inlet boundary layer thicknesses. Their results are replotted in Figure 3-20.

The exit plane endwall blockage results for the three different inlet boundary layers are plotted in Figure 3-21. The three curves are similar in shape, but shifted vertically from one another, with the blockages for the thicker inlet boundary layer cases being larger. There is an increase in blockage of approximately 20% between each curve. The highest loading case for each boundary layer curve is the highest loading at which the code would converge.

---

1. The stall point here means the lowest mass flow at which a converged solution could be obtained.

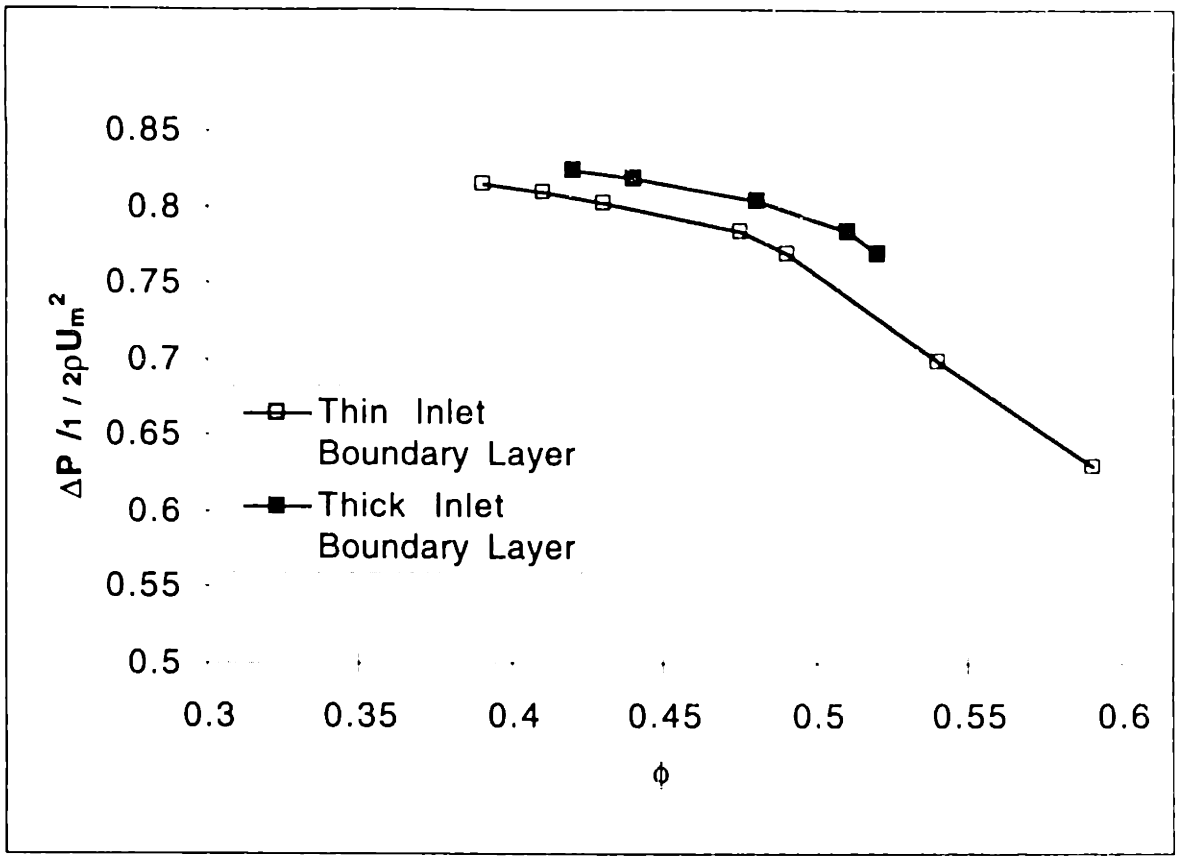

Figure 3-20: Data from Hunter and Cumpsty (1982)

Even though the limiting loading parameters for the three cases are within 2% of dynamic head of each other, the characteristics show that the maximum static pressure rises (captured in the CP_S term in the abscissa of Figure 3-21) vary by more than 10% of inlet dynamic head between the no inlet boundary layer and the thickest inlet boundary layer cases. To make this point more clearly, the blockage trends for the three different boundary layer thicknesses are replotted in Figure 3-22 with the local static pressure rise coefficient as the abscissa. Comparing Figures 3-21 and 3-22 illustrates the utility of using CP_S-CP_T as the abscissa instead of CP_S. There appears to be a general limiting loading parameter beyond which the blockage increases rapidly for many compressor geometries and configurations. In contrast, the limiting static pressure rise varies for different configurations and conditions. In this example, the thicker inlet boundary layer case has higher loss, balancing the lower static pressure rise to give similar limiting loading parameter values. The curves in Figure 3-22 also show that the highest loading cases, with the highest blockage, do not have the highest CP_S values. This is because CP_S is an average over the

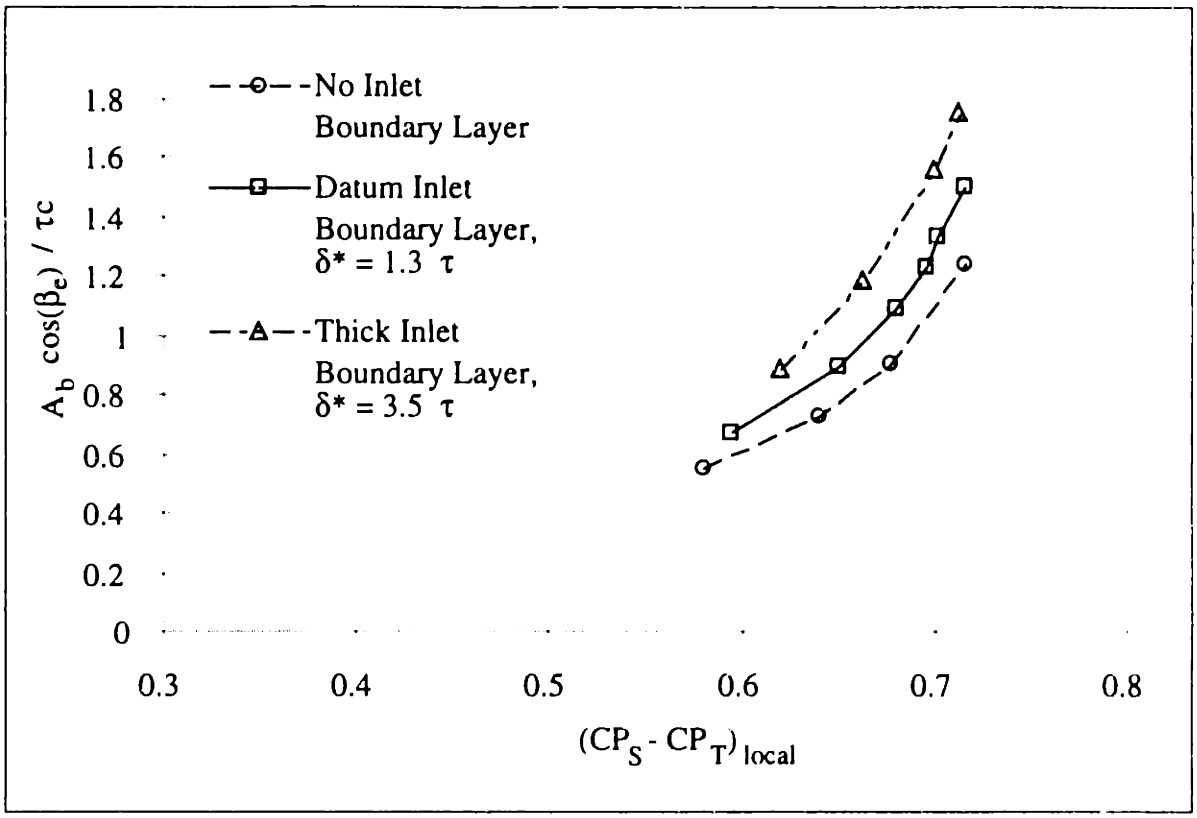

Figure 3-21: Blockage Trends with Varying Inlet Boundary Layer, Low Speed Rotor, τ/c=3.0%

blockage region, not just the static pressure on the casing, and the effect of local streamline curvature has a small but noticeable influence on the CP_S parameter.

Differences in exit plane loss with the three boundary layers are due primarily to differences in the total pressure of the clearance flow at the gap exit. For similar loading conditions Table 3-2 presents the mass-averaged total pressure coefficient of the fluid exiting the clearance gap for the three boundary layer cases. As described in subsection 3.3.2 the reduction in clearance jet total pressure increases the average leakage angle. How the changes shown in Table 3-2 impact blockage is addressed in Chapter 4.

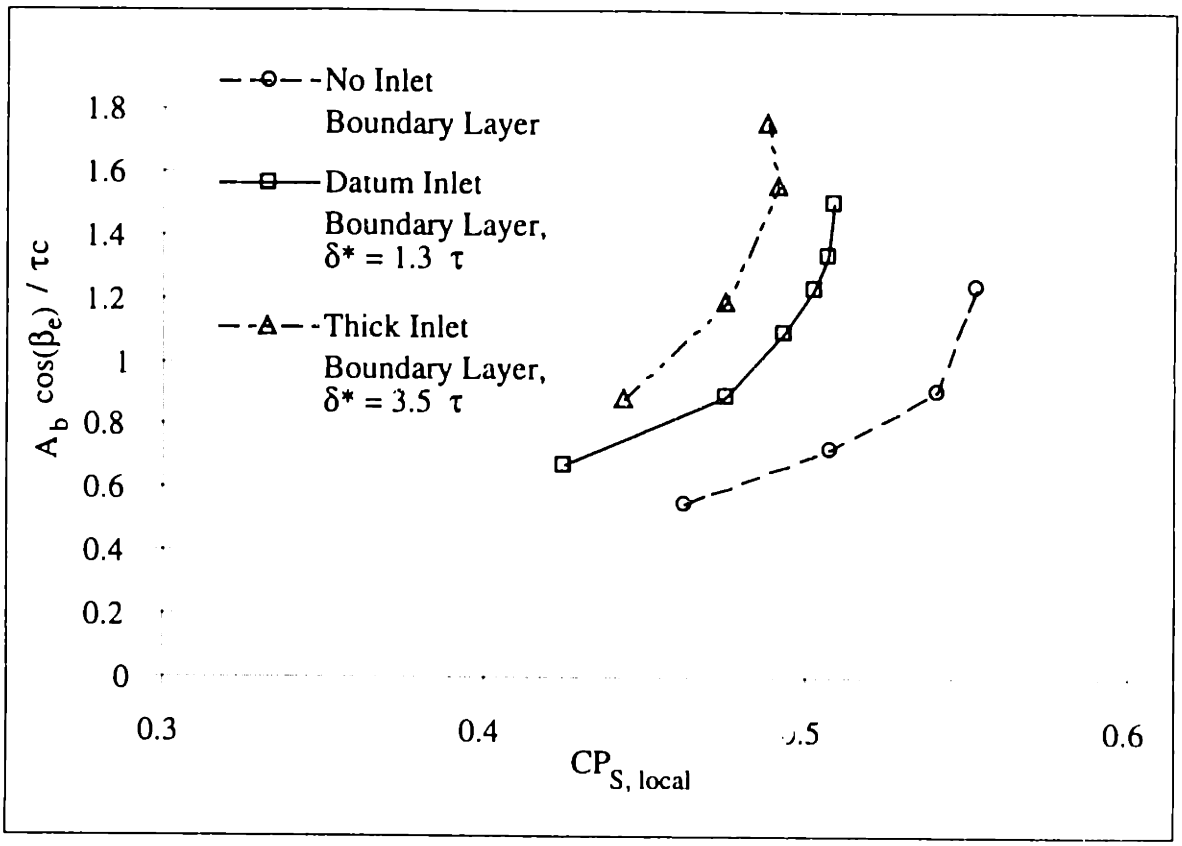

Figure 3-22: Blockage Trends for Various Inlet Boundary Layer Thicknesses versus Static Pressure Rise Coefficient, Low Speed Rotor, τ/c=3.0%

Table 3-2: Effects of Inlet Boundary Layer Thickness for Low Speed Rotor, τ/c=3.0%, 56° Stagger

Boundary Layer	$\overline{CP_T}^m$	$\bar{\alpha}^m$	$\frac{\dot{m}_{clrnc}}{\rho U_{tip} \tau c}$
none	-.031	38^0	.32
datum	-.170	42^0	.39
thick	-.347	51^0	.41

The effect of the inlet boundary layer on endwall blockage can be summarized as follows. There is a shift of the normalized blockage of approximately ± 20% from the datum case for the same value of the loading parameter as the inlet boundary layer displacement thickness is varied from 0 to 3.5 clearance heights. The inlet boundary layer affects the clearance jet total pressure, which changes the depth of the initial velocity defect. This causes a lower limiting static pressure rise for a thicker inlet boundary layer. For the cases exam-

ined here the stalling static pressure rise coefficient was 4% of inlet dynamic head higher for no inlet boundary layer than for a thick inlet boundary layer. Because the range of inlet displacement thicknesses tested was broader than generally expected in compressors, the magnitude of change in blockage is representative of the effect of inlet boundary layers on endwall blockage.

3.3.5 Solidity

To determine the effect of solidity on endwall blockage the low speed rotor, large clearance ($\tau/c=3\%$) geometry, which had a design solidity of 1.1, was regridded for a solidity of 1.6 by Khalid (1995a). Solutions were computed for two loading conditions, and the blockage results from these calculations are shown in Figure 3-23. For the same value of

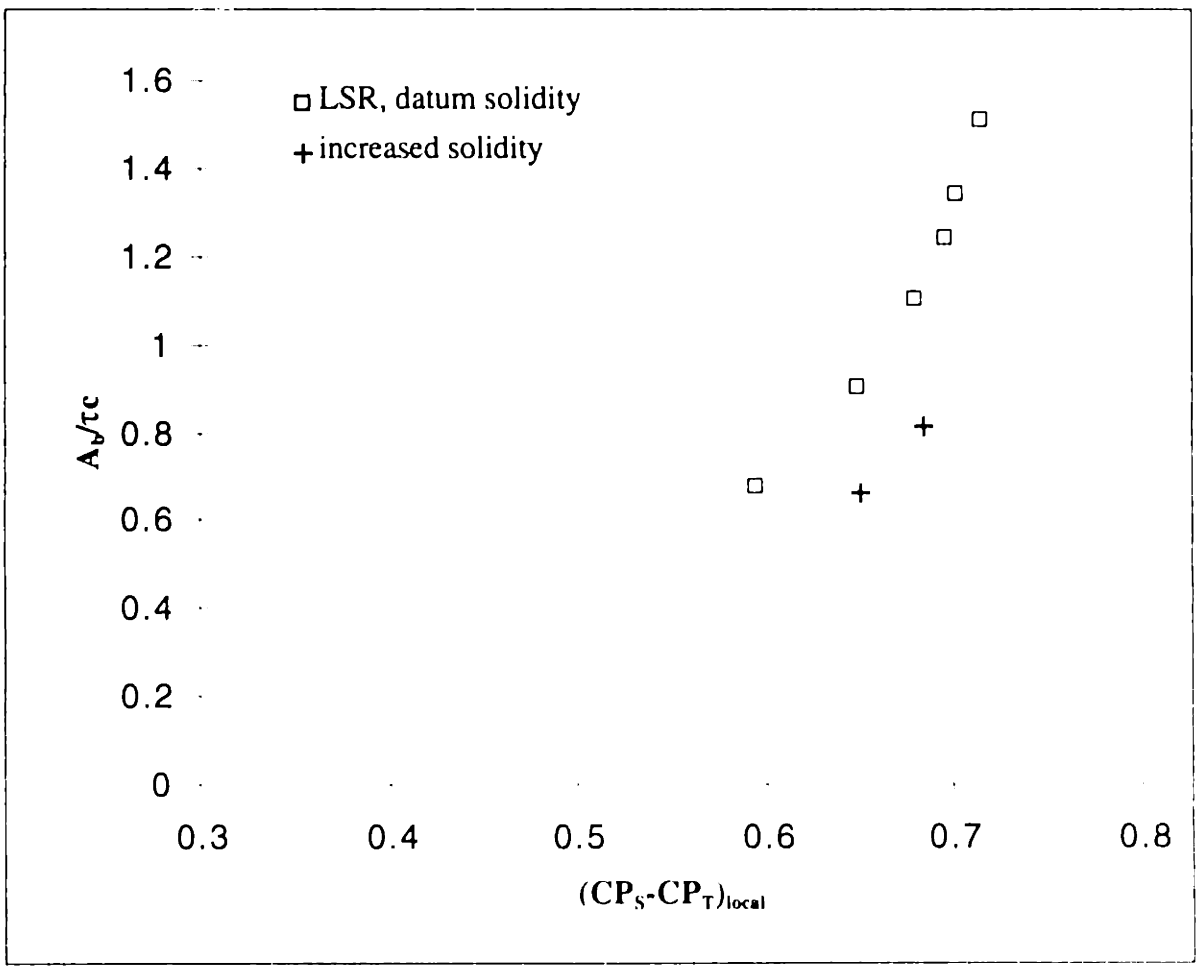

Figure 3-23: Effect of Solidity on Endwall Blockage

loading parameter the high solidity case shows approximately 30% lower blockage nor-

malized by clearance area.

If the compressor passage is viewed as a diffuser, the pressure rise can be related to the blockage and the inlet and exit areas as follows:

$$\frac{\Delta P}{\frac{1}{2}\rho U_1^2} = 1 - \left(\frac{A_{inlet}}{A_{exit} - A_b} \right)^2 = 1 - \left(\frac{A_{inlet}/A_{exit}}{1 - A_b/A_{exit}} \right)^2, \tag{3.9}$$

For a given inlet area, Equation 3.9 indicates that A_b/A_{exit} determines pressure rise changes. Even though $A_b/\tau c$ decreases as solidity is increased, for the cases examined here A_b/A_{exit} increased approximately 8%. Hence the pressure rise achieved for the same inlet mass flow is lower for the high solidity cases. This is reflected in the speedlines, which are displayed in Figure 3-24. The impact of changing solidity on the blockage nor-

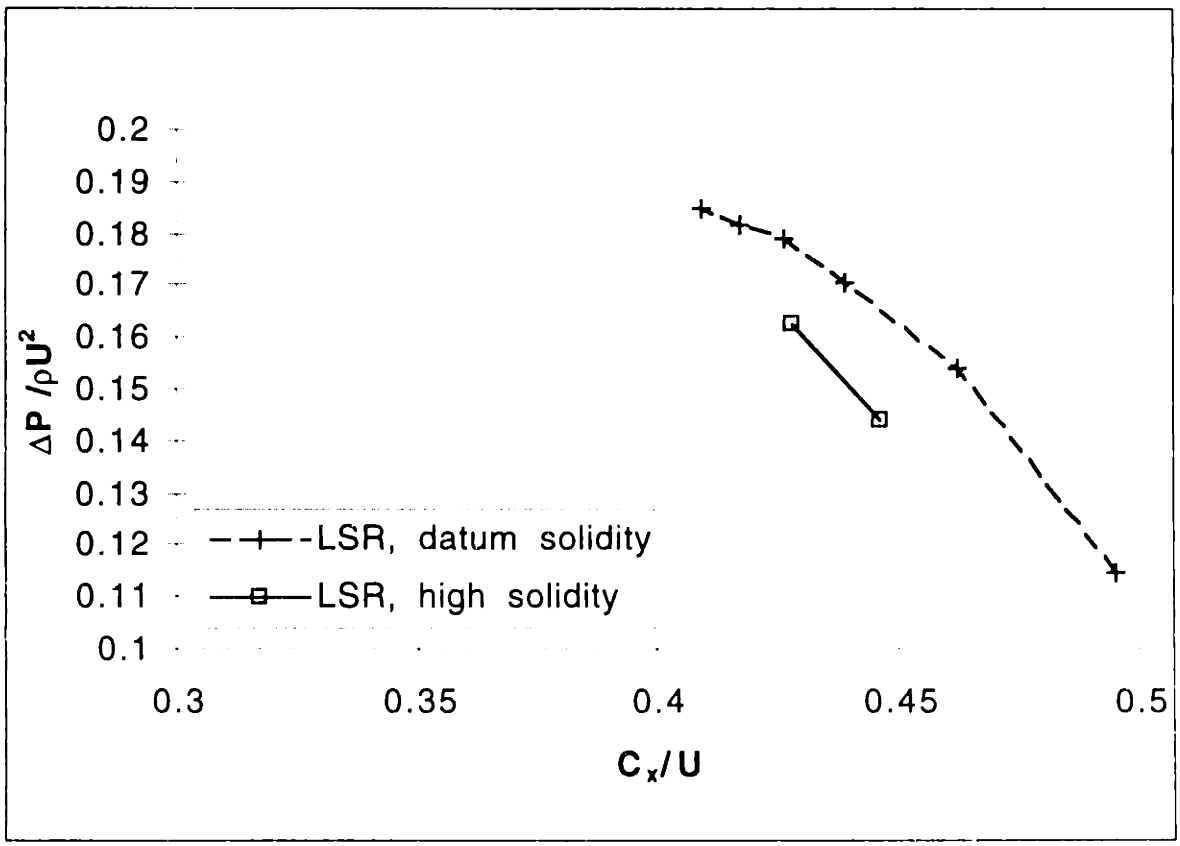

Figure 3-24: Compressor Characteristics for Datum (σ=1.1) and High Solidity (σ=1.6)

malized by the entire exit area will depend on the details of the passage geometry, such as

the blade span, which were not examined in this study, but the trends as outlined here (blockage normalized by clearance area) can be combined with such geometric information to provide the blockage versus exit area trends for a specific compressor.

Another effect of increased solidity in the cases examined here is an increase in double leakage. This results, as shown in Table 3-3, in increased clearance jet loss, increased leakage angle, and as shown in Chapter 4, increased blockage.

σ	CP_S	$\overline{CP_{T,clrnc}}^{m}$	$\bar{\alpha}^{m}$	$\Delta\dot{m}_{clrnc}$
1.1	.424	-.114	36^0	-
1.6	.431	-.244	42^0	-3%

Table 3-3: Effects of Solidity on Loss, Leakage Angle, and Clearance Mass Flux

The method for predicting the chordwise extent of the double leakage, described in subsection 3.2.3, suggests that for the nominal solidity case the vortex impinges onto the adjacent blade at approximately 95% chord, but for the increased solidity case the impingement location is approximately 70% chord. Hence for the increased solidity case the fluid that leaks over the rear 30% of the chord has a total pressure lower than the free stream.

The increase in double leakage in the σ=1.6 cases can be seen in the streamline traces shown in Figure 3-25, where the datum solidity is on the left and the increased solidity cases is on the right. Streamlines were seeded in the same places for both cases. In the datum solidity case, only a small amount of fluid, approximately 5%, exits one clearance gap and enters the next one, and this double leakage fluid is limited to approximately the 20% of the tip gap closest to the endwall[1]. In the increased solidity case, more streamlines can be seen leading from one clearance to the next, especially towards the trailing edge. This includes fluid across the entire radial extent of the clearance gap. Based on these streamline traces and others like them, it is estimated that approximately 5% of the clear-

1. The observation about the radial location of the double leakage fluid was made using a 3-D flow visualization package.

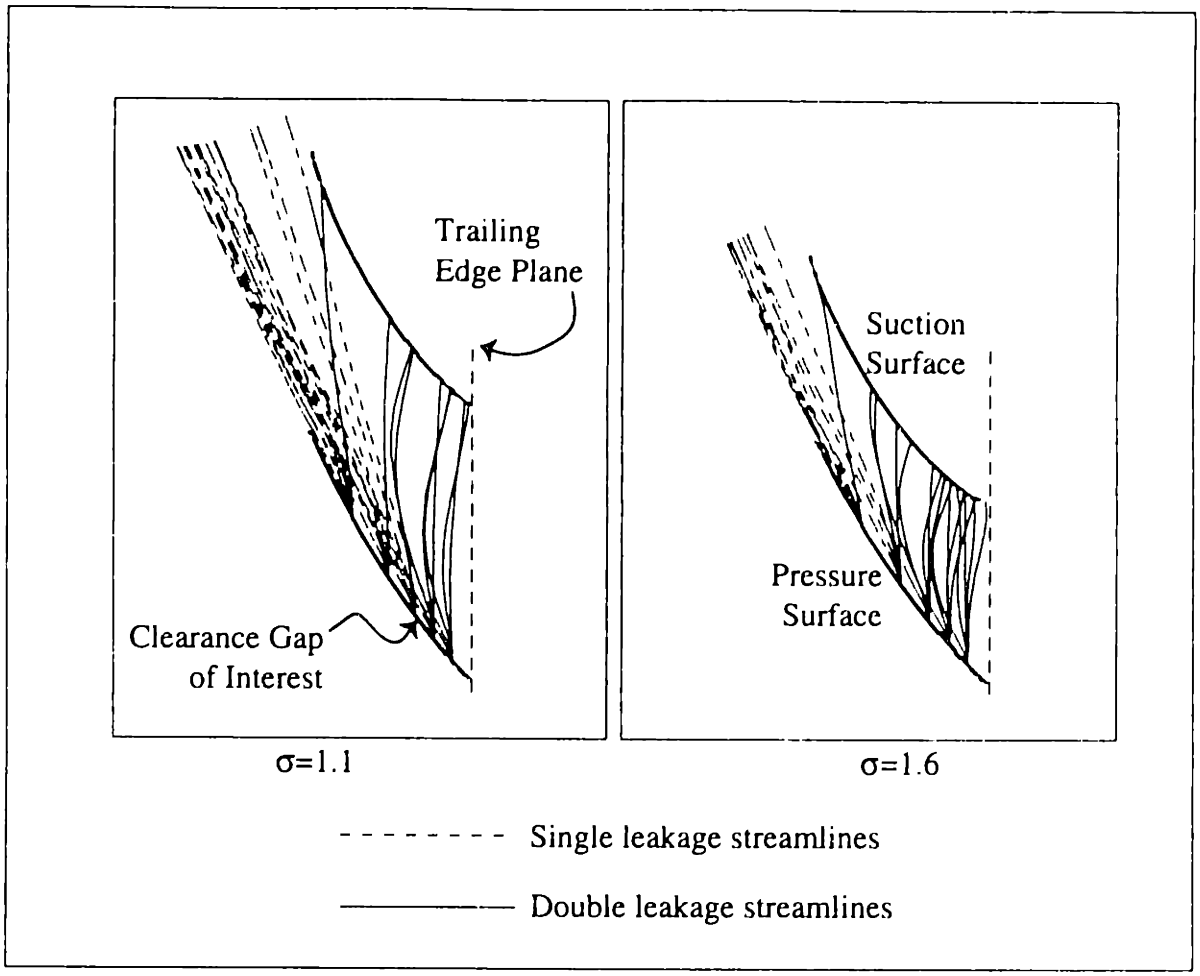

Figure 3-25: Streamline Traces Showing Double Leakage, Streamlines Traced Upstream from Clearance Gap

ance jet mass flow enters the next clearance gap for the datum solidity geometry. But in the increased solidity geometry, the fraction of the clearance mass flux that undergoes a double leakage is estimated to be 40%.

In summary, increasing solidity reduces the blockage normalized by clearance area but may increase blockage normalized by total passage exit area, depending on the passage geometry. For cases in which the tip leakage vortex trajectory intersects the next blade pressure surface, an increase in solidity will result in an increase in double leakage. This will increase the clearance jet loss, tending to increase blockage, acting to offset the blockage reduction caused by the decreased blade loading. A situation with an increase in solidity but no increase in double leakage was not examined in this study, but the blockage model developed in Chapter 4 was used to quantify the relative contributions of these two

competing effects (see subsection 4.4.3).

3.3.6 Blade Loading Profile

The effect of different blade loading profiles was studied by comparing the blockage trends of the low speed rotor, the low speed stator, and the Deverson rotor. The different pressure distributions for these three cases cased different distributions of leakage velocity along the chord (shown in Figure 3-26), but the blockage trends for all three are similar.

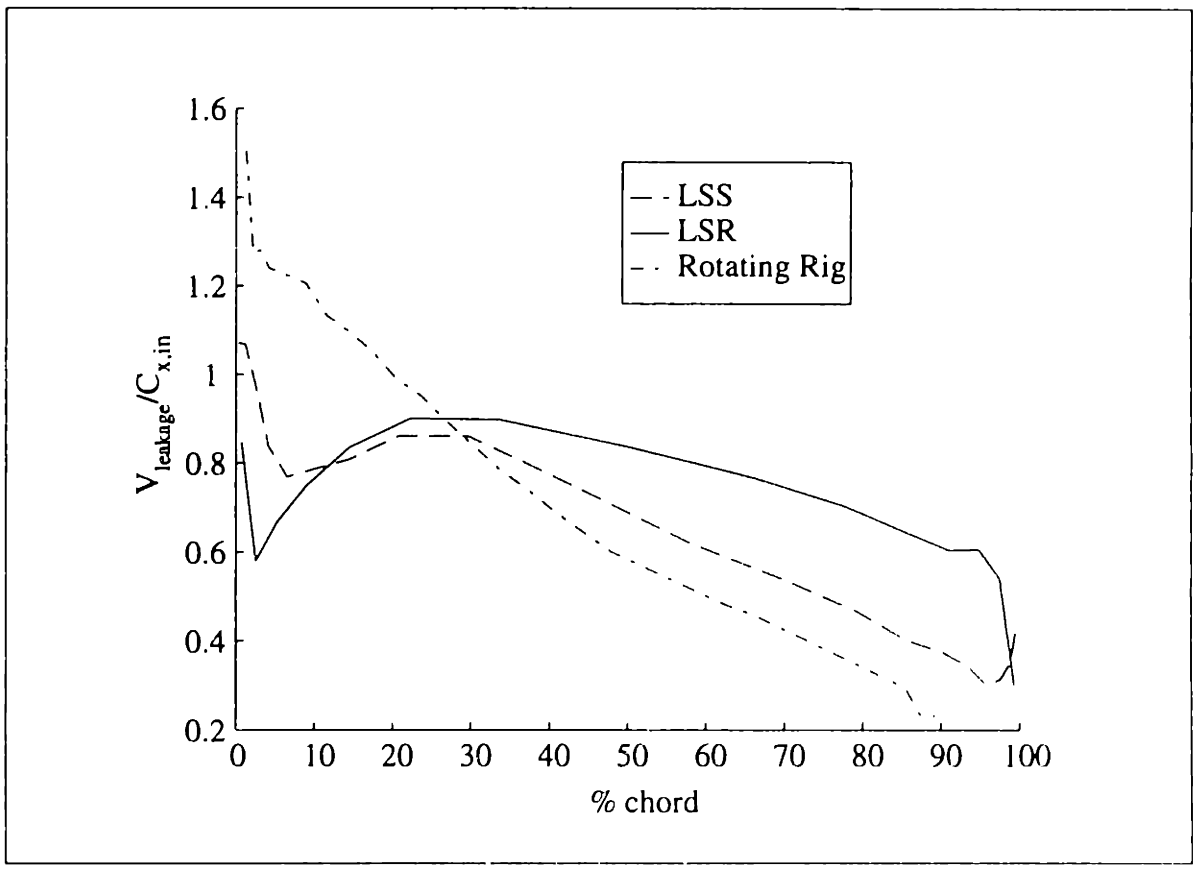

Figure 3-26: Leakage Velocity versus Chord for Low Speed Stator, Low Speed Rotor, and Deverson Rig Tests

The leakage velocity plotted was computed using Equation 3.2.

As can be seen in Figure 3-26, the Deverson rotor is more typical of modern controlled diffusion airfoils, with high loading near the leading edge, and a gradual reduction in adverse pressure gradient further along the chord. Despite the differences in blade loading profile, the blockage trends are similar, indicating that the details of the loading profile are

not a major factor in determining endwall blockage trends. This is the same conclusion that Storer (1991) reached by studying circular and parabolic arc camber line blades in a cascade with tip clearance. Unless one were considering a three-dimensional blade design that could reduce overall (chord-averaged) blade loading near the tip for the same passage pressure rise, it is expected that blade loading profile will not be a large factor in determining endwall blockage. The analysis of endwall blockage in Chapter 4 was used to quantify this further.

3.3.7 Clearance Vortex Swirl

There has been some speculation (Brookfield, 1993, for example) that endwall-critical compressor stall may be connected to a vortex bursting type phenomena. Work done by Brookfield (1993) and Khan (1994) has shown that a velocity defect growing in an adverse pressure gradient 1) grows more rapidly when the defect is swirling than when the flow is unidirectional, and 2) can, with enough swirl, reach a critical stage where the defect grows rapidly. When the swirl is expressed as a ratio of the core tangential velocity to axial velocity, the critical swirl ratio is approximately $\sqrt{2}$. For swirl ratios smaller than this, the vortex core will not display the rapid growth associated with vortex bursting.

Khalid (1995) observed swirl ratios of approximately 0.5 for the LSR, large clearance, high loading case; well below the critical $\sqrt{2}$ value. He therefore concluded that tip clearance vortices have too low a swirl angle to be close to vortex bursting. Using Khan's (1995) theory, the direct impact of swirl on the leakage vortex blockage is estimated as 5% for the cases examined here. In other words, if the flow were simply a slug of low total pressure fluid with zero swirl, the resulting blockage would be 5% smaller than the blockage as measured.

The effect of swirl on the mixing rate (which plays a role in determining the total pressure in the blockage region at the exit plane) is not clear. A zero-swirl slug of fluid may interact with the passage through-flow ina different way than does the leakage vortex. On a first level of approximation however, the blockage trends due to clearance flows are unaffected

by swirl.

3.4 Blockage Reduction

The empirical observations of blockage trends in this chapter indicate that the most important effect on endwall blockage (with the same passage pressure rise coefficient) comes through the clearance height. As subsection 3.3.1 has described, the exit plane blockage is directly proportional to the clearance height. The tip gap, however, is generally set by mechanical constraints, and designers have limited opportunity to reduce the clearance mass flux by reducing the tip gap. Therefore one must look to increasing the total pressure of the clearance jet or reducing the leakage angle. The discussion in this chapter gives insight into how design changes affect these two parameters, and Chapter 4 will quantify the effects on blockage.

A three-dimensional blade design that reduces the loading only very close (a few clearance heights) to the blade tip would reduce the leakage angle, and hence the endwall blockage, without impacting the overall pressure rise. Initial results of Bolger (1995), who has designed a three-dimensional blade with very low tip loading, support this conclusion. This method for reducing tip clearance related blockage is examined quantitatively using the blockage model in Section 5.1.

Increasing the jet total pressure to reduce blockage is one aspect of effective casing treatments (see for example Cho, 1995). This method is analyzed further in Section 5.3 where the results of wind tunnel tests with nominal and increased clearance total pressure are discussed and compared to predictions from the blockage model.

3.5 Summary of Parametric Trends

Using data from experiments and computations, the parametric trends of endwall blockage have been quantified. The effect of clearance size, passage loading, blade loading profile, inlet boundary layer thickness, stagger, swirl ratio, and solidity on blockage have been

examined. Because of their importance to the blockage model developed in Chapter 4, how these design parameters affect the conditions at the clearance exit was also described.

Clearance size is the factor that most influences blockage, with blockage scaling directly with the clearance height. Passage loading also has a large effect, with the blockage increasing rapidly just before stall. The data examined here asymptote at a local loading parameter between 0.65 and 0.72. This is true even for compressors with different stalling pressure rises (see for example the discussion on inlet boundary layers in subsection 3.3.4).

The effect of inlet boundary layers on blockage was observed to be modest, with a 20% increase in blockage observed for a 150% increase in inlet boundary layer displacement thickness. There is a 6% shift in limiting pressure rise with boundary layer thickness, as thicker inlet boundary layer profile increases the endwall loss for the same overall loading.

The blockage normalized by clearance area is reduced as solidity increases. For the compressors examined here the blockage as a fraction of total exit area increased slightly (8%) with increased solidity, as did the passage averaged loss coefficient, but these results depend on parameters like the blade span and the tip leakage vortex trajectory (because of the double leakage phenomenon), and hence may not be universally applicable.

Changes in stagger angle affect the pressure difference across the blades and hence the leakage velocity and leakage angle. If solidity, axial chord/tip clearance, and passage pressure rise coefficient are held constant, then increasing stagger angle will reduce the average leakage angle, by as much as 9^{o} for a 20^{o} increase in stagger. The blockage model developed in Chapter 4 will be used to quantify how this leakage angle change affects blockage.

The direct effects of swirl ratio on blockage are small, and the effect of blade loading profile, at least over the range of blade shapes examined here, is also small.

Chapter 4: Model for Clearance Related Blockage

4.1 Introduction

In this chapter a simplified calculation procedure for compressor endwall blockage is described and evaluated. The procedure also provides insight into the physics of endwall blockage growth and allows the effect of design changes on blockage to be quantified.

Khalid (1995b) developed a calculation procedure for endwall blockage based on an integral wake description of a velocity defect associated with the clearance jet. In Khalid's approach, Navier-Stokes solutions were used to calculate the wake initial conditions, limiting the procedure's usefulness as a predictive tool. This thesis uses a control volume analysis to estimate the wake initial conditions, allowing prediction of blockage trends without running Navier-Stokes solutions for each case.

In Section 4.2 a conceptual description of the analysis is presented, outlining the primary flow processes. In Section 4.3, endwall blockage is calculated for each of the computational solutions described in subsection 2.4.2. The utility of the model is judged by comparing this calculated blockage to the blockage computed from the Navier-Stokes solution. The blockage model is interrogated for information about the parametric trends of blockage, extending and further quantifying the empirical observations made in Chapter 3, and this application of the model is described in Section 4.4.

4.2 Conceptual Model

Khalid's (1995b) work showed that endwall blockage in axial compressors can be viewed

as the growth of a velocity defect in an adverse pressure gradient. As indicated by the one-dimensional analysis (subsection 2.2.2), computation of this growth must capture: 1) initial conditions (measures of the initial velocity defect depth and extent), 2) pressure gradient, and 3) the mixing between the defect and the free stream fluid. The complexity of the compressor endwall flow field offers many possible approximations for these three processes, and the approach developed here is one implementation. As will be shown, however, this blockage calculation procedure captures the experimentally observed parametric trends of endwall blockage.

A basic assumption in the conceptual framework is that each chordwise section of the leakage jet is taken to be independent of the other jet sections. Further, a number of fluid dynamic processes are assumed to occur in a serial rather than parallel fashion as the leakage jet traverses the passage. Figure 4-1, a modification of a figure from Khalid (1995a), shows a schematic of the flow field with the location of these various flow processes labeled. Each of these four processes is described below.

1. **Fluid leaks over the blade tip.** The leakage angle and total pressure of each section of the leakage jet are assumed to be uniform in both the radial and chordwise directions. Details about predicting the leakage angle and total pressure were given in Section 3.2.

2. **The jet travels in a straight line until impacting the jet/free stream interaction region or exiting the passage.** There is a distinct region of interaction between the jet and the free stream (demarcated by the closely spaced loss contours in Figures 3-7 and 3-8). Prior to the interaction region, shear layer mixing occurs at the interface between the jet and the free stream, increasing the loss and the radial extent of the defect that will be calculated in step #3.

3. **The jet and the free stream interact.** As in the analysis of Martinez-Sanchez and Gauthier (1990), each section of the jet interacts with the free stream resulting in flow in the vortex direction (see subsection 3.2.3). A control volume analysis (see Figure 3-11) allows solution (details are given in Appendix C) for the angle of the vortex direc-

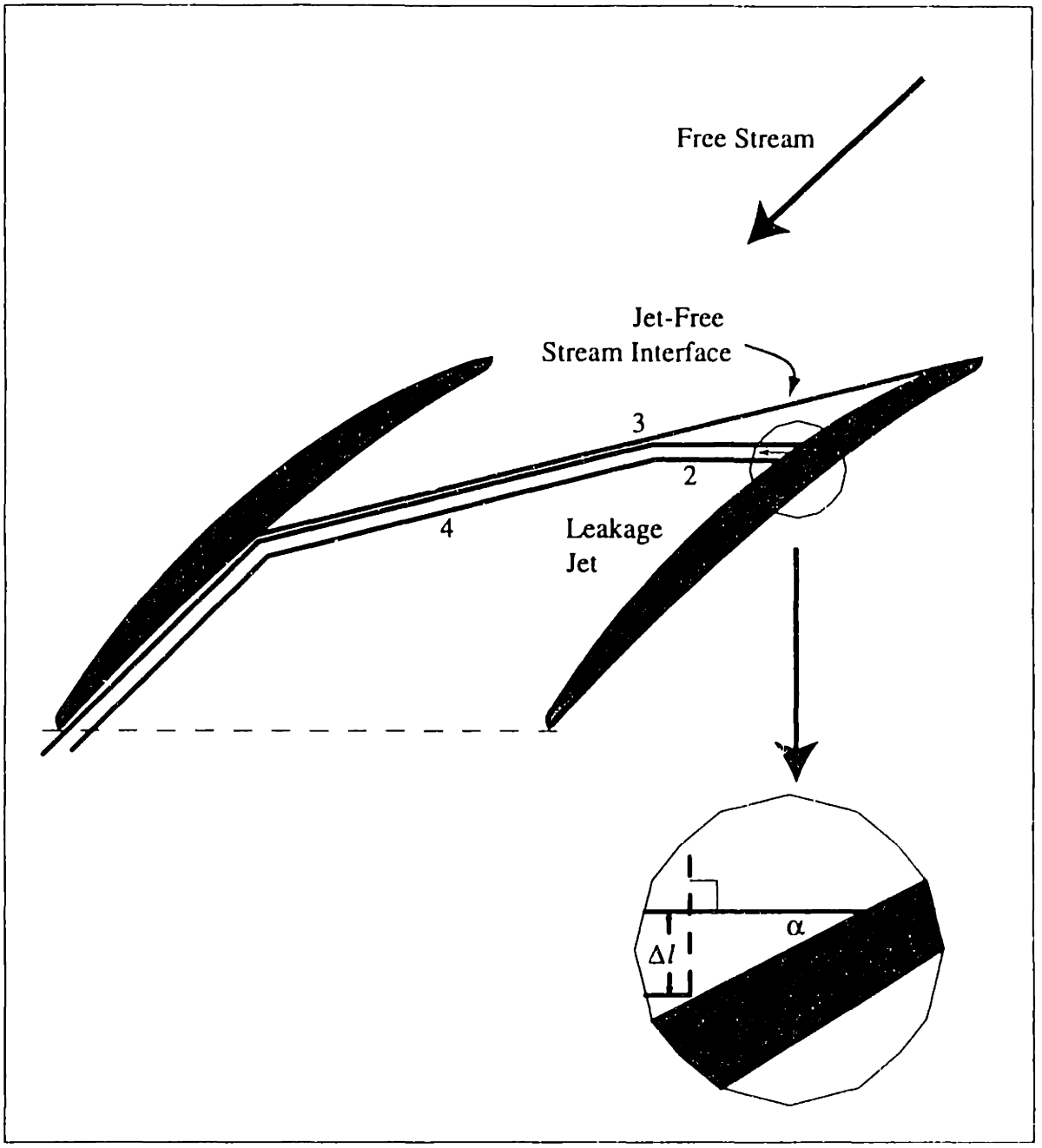

Figure 4-1: Radial View Illustrating Two-Dimensional Wake Segments Along the Chord

tion and the width and depth of the velocity defect. Loss is generated at the jet-free stream interface by the dissipation of the kinetic energy of the velocity components normal to the vortex direction.

4. **The defect growth is computed using an integral wake analysis.** The defect formed at the jet-free stream interaction region is assumed to behave in a manner similar to the

two-dimensional wakes described by the integral wake analysis of Hill et al. (1963). In the present application, the jet section grows in the radial direction, maintaining the same circumferential width from clearance exit to passage exit. The details of the integral mixing analysis are given in Appendix D.

4.3 Comparison of Blockage Model Calculations and Navier-Stokes Solutions

Computations of blockage using the procedure described above are presented in Figure 4-2 for the seven cases described in Table 2-2. The average difference between the blockages computed using the model and directly from the Navier-Stokes solutions is 33%, with a maximum difference of 46% for the high loading, low speed stator case. Although the absolute value of the blockage is underpredicted, the model accurately predicts the parametric trends of endwall blockage. This is shown in Figure 4-3 which plots the blockage normalized by the blockage where the loading parameter equals 0.65. The blockage calculation procedure captured the normalized blockage versus loading trend for the low speed rotor cases with an average error of 5.5%, and those for the low speed stator with an average error of 12%.

The computations show a 10% change in normalized blockage for the low speed rotor geometry when the clearance is doubled, for similar pressure rise conditions. The blockage analysis predicts a change of 12%. This is illustrated in Figure 4-4 which plots the ratio of the large to small clearance geometry blockages (at similar pressure rises) observed in the computational solutions (termed the "data" here) versus the same ratio of blockage values calculated using the blockage model. The largest difference between the predicted and observed effects is 21%, and the average difference is approximately 8%.

The trends captured by the blockage calculation procedure are further explored in Figure 4-5, which plots the ratio of blockages between the thick inlet boundary layer and the no inlet boundary layer cases for the computations and the model calculations. The predicted effect of increased boundary layer thickness is within 7% of the observed changes.

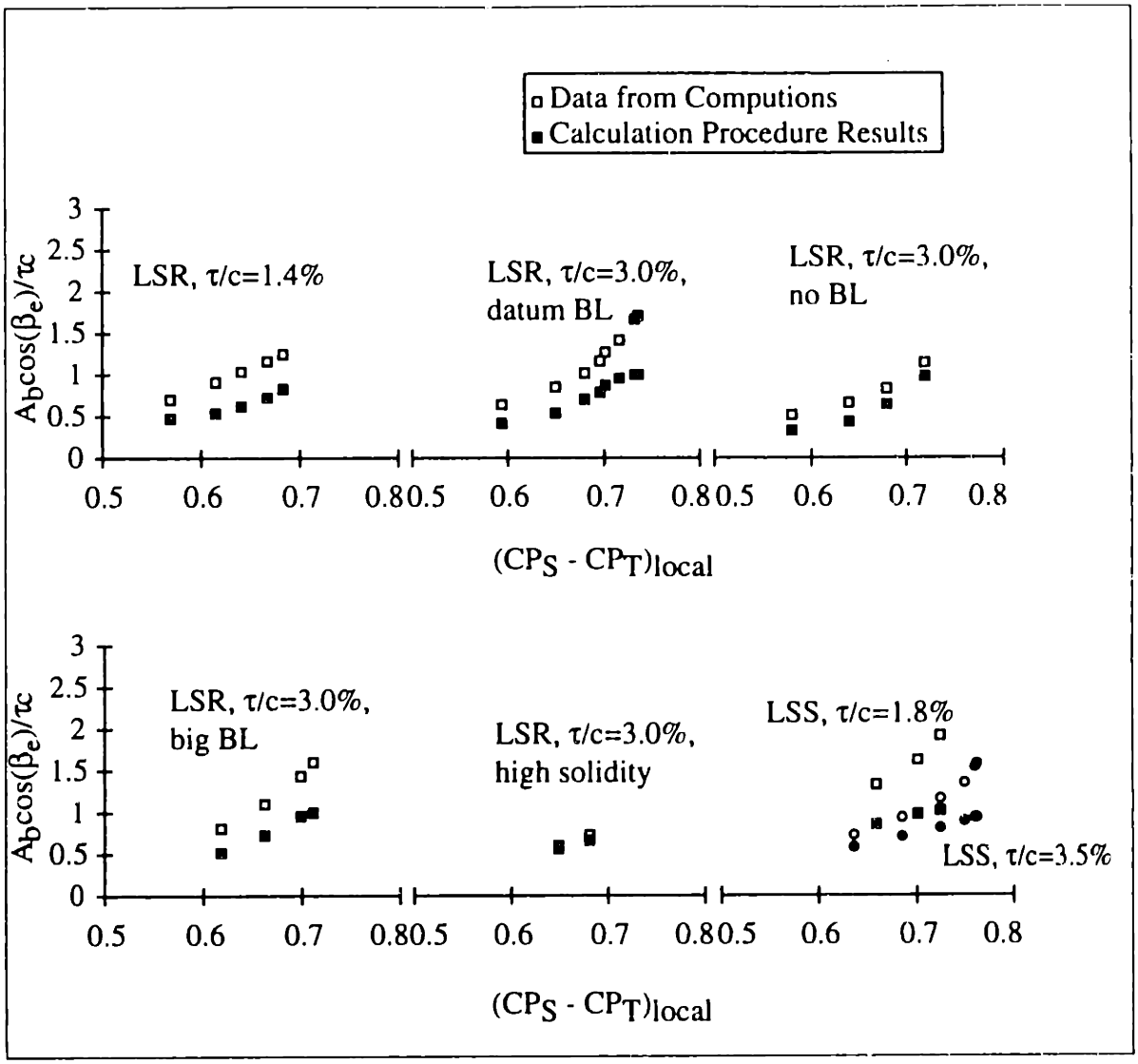

Figure 4-2: Normalized Blockage versus Loading Parameter from CFD solutions and Computed from Blockage Model for Same Conditions

Trends of blockage with loading changes in the data and the model calculations were also compared. For the low speed rotor, small clearance geometry, there is a 78% change in blockage between the low and high loading cases. The model also predicts a 78% change.

The agreement between the predicted and observed blockage trends suggests that the blockage model is a useful tool to extend the parametric trend analysis presented in Section 3.3. This was done, and the results are given below in Section 4.4. Estimations of the uncertainties due to the primary assumptions were also made, and these computations are detailed in Appendix C. One of these assumptions, that the pressure gradient in which the velocity defect grows is a linear function of distance, caused the largest error, resulting

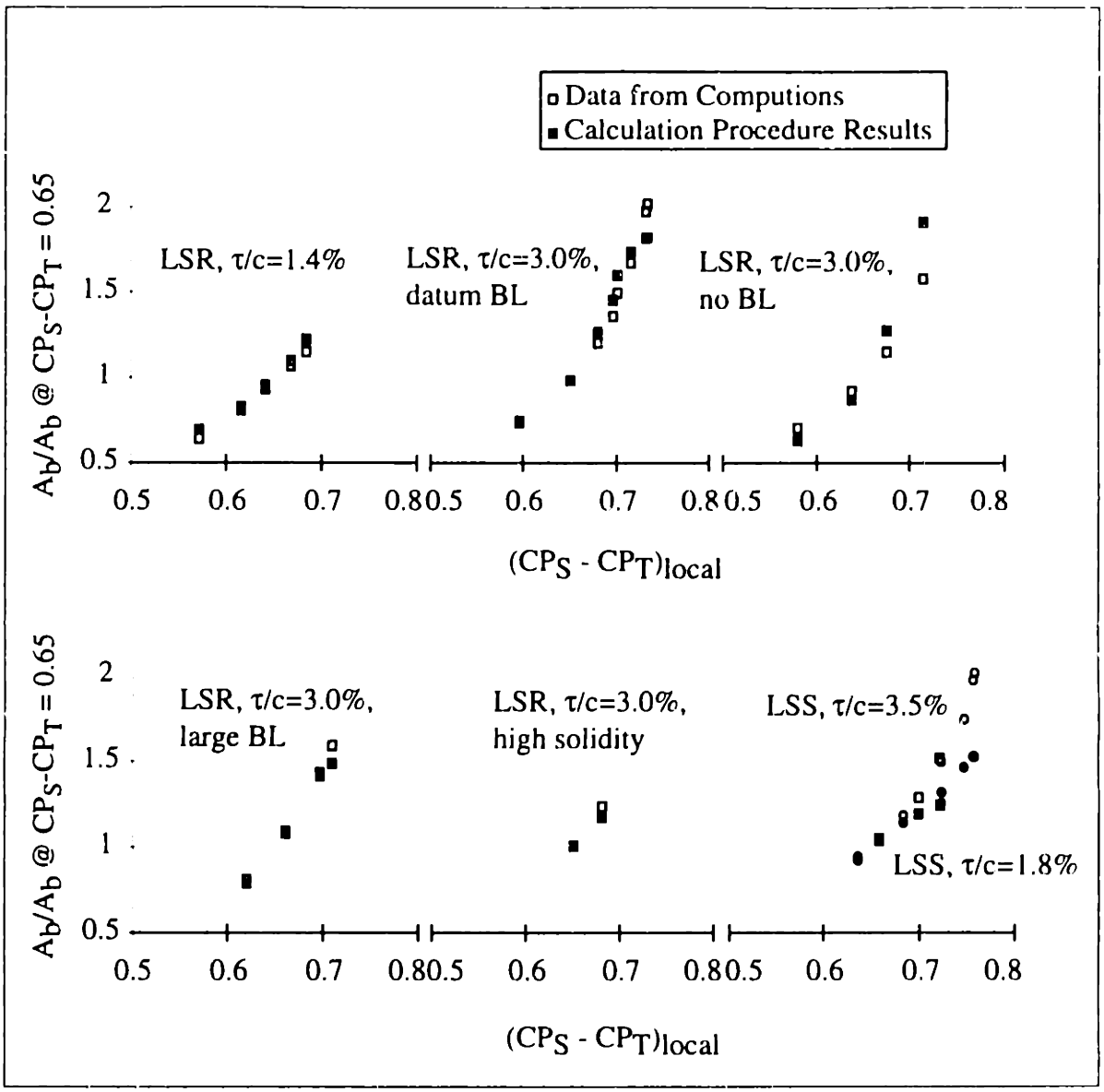

Figure 4-3: Blockage Normalized by Blockage at CP_S-CP_T = 0.65 versus Loading Parameter from CFD solutions and Computed from Blockage Model for Same Conditions

in a calculated blockage approximately 25-30% lower than that calculated with the actual pressure gradient.

The error introduced by neglecting double leakage causes the calculated blockage to be at most 20% larger than if double leakage was accounted for. A balance between the errors due to neglecting double leakage (causing the calculated blockage to be too high) and due to the pressure gradient assumptions (causing the calculated blockage to be too low) provides some explanation for the model's more accurate calculation of the increased solidity

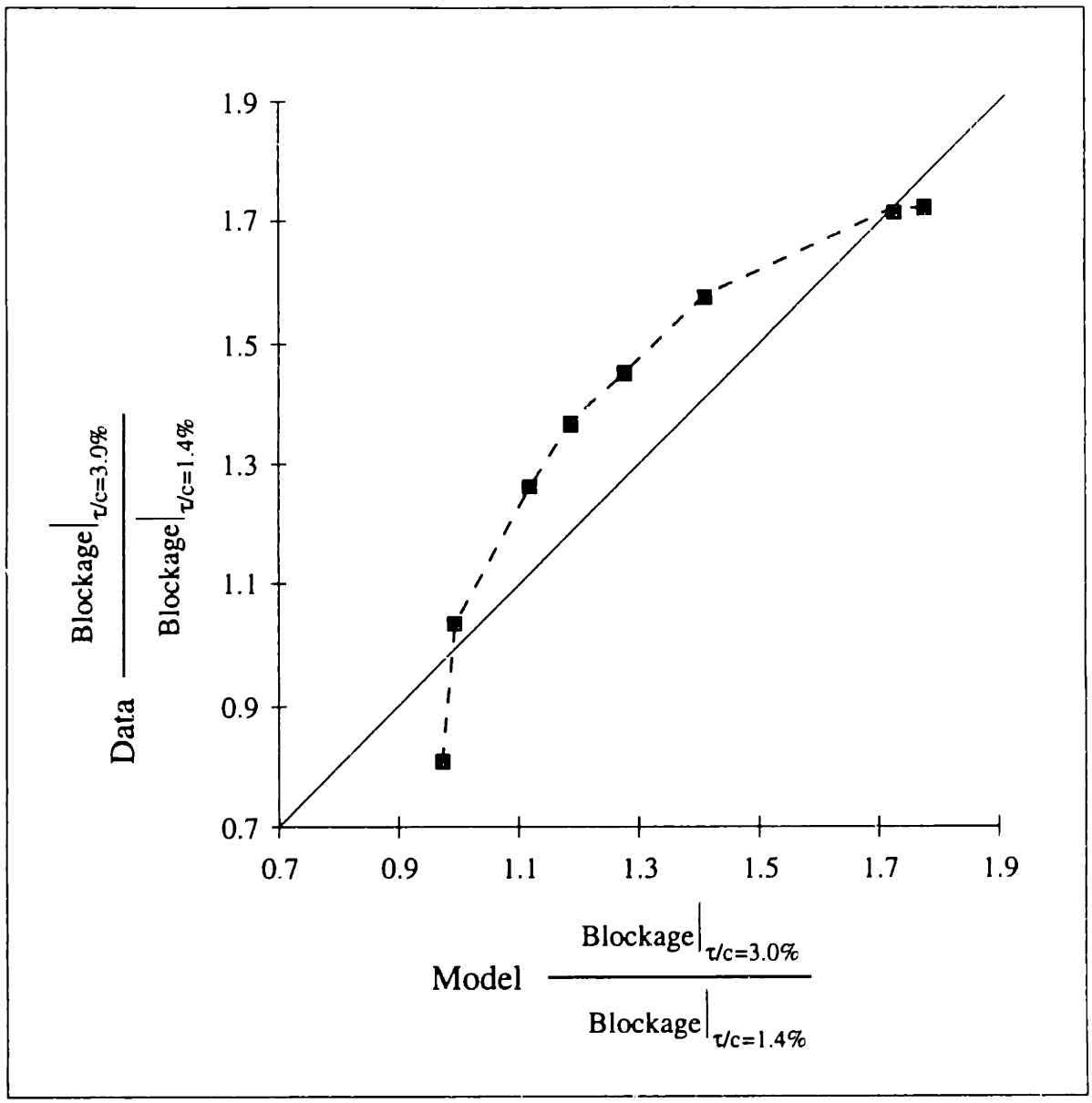

Figure 4-4: Calculated Effects of Clearance: Ratio of Blockages from Large and Small Clearance Geometries, Datum Inlet Boundary Layer, from Computational Solutions and Simplified Blockage Analysis

blockages than the nominal solidity cases. For similar passage loading conditions the increased solidity geometries have more double leakage than the nominal solidity cases (see Figure 3-25). Thus the overprediction error due to neglecting the double leakage was larger than in the nominal solidity cases, causing the model to more closely predict the blockage for the high solidity cases.

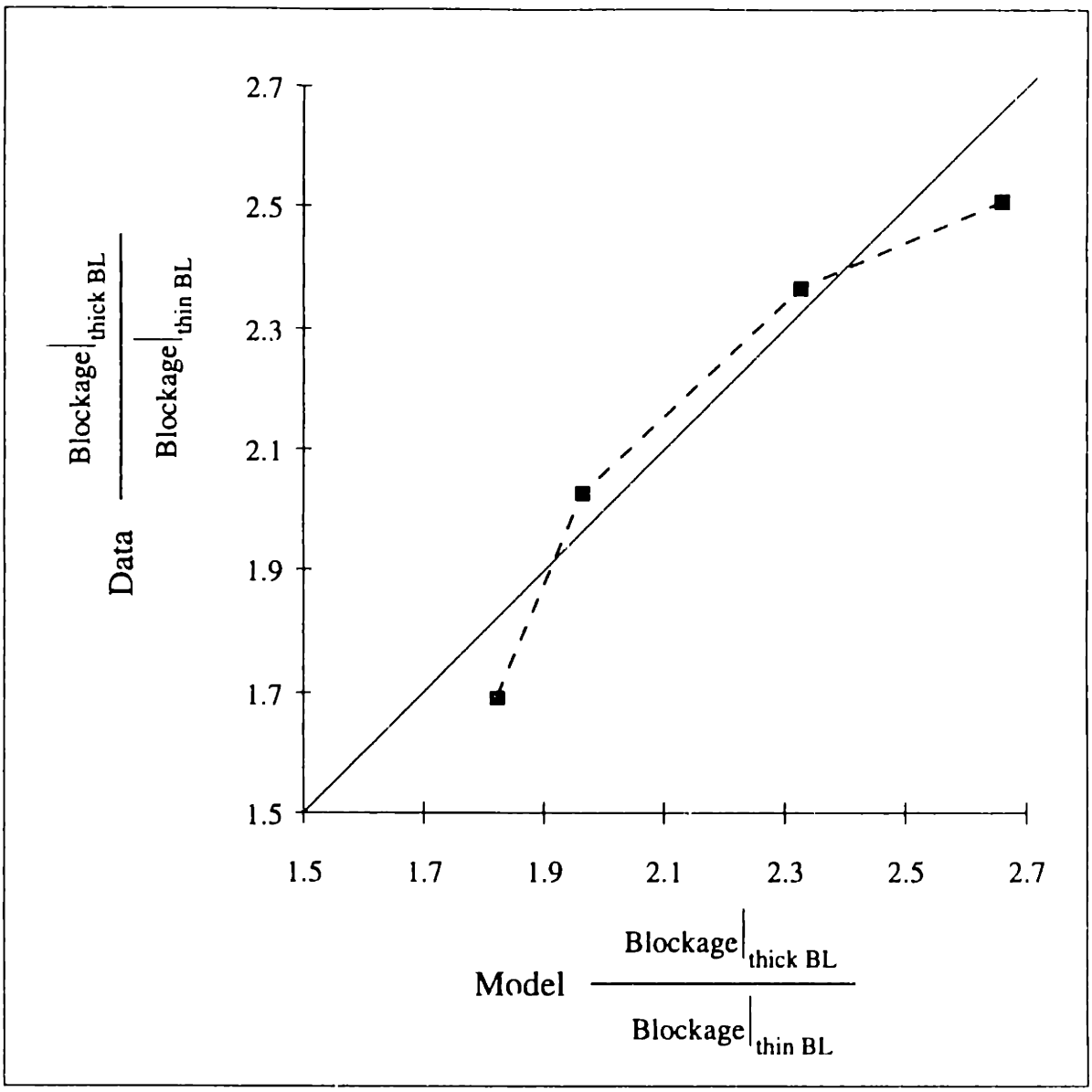

Figure 4-5: Predicted Effects of Inlet Boundary Layer: Ratio of Blockages from Thick (δ^*/τ=3.5) and Thin (δ^*/τ=0.0) Inlet Boundary Layer Cases, from Computational Solutions and Simplified Blockage Analysis

4.4 Parametric Trends

One of the main contributions of the simplified blockage analysis developed here is its ability to quantify the trends of endwall blockage. The description of the trends described in Chapter 3 (quantifying the effect of changes in design parameters such as clearance height, inlet boundary layer thickness) can now be extended. If clearance jet total pressure, leakage angle, and inlet boundary layer profile are known, the blockage model can be

used to predict the magnitude of the blockage change with changes in design parameters. Examples are given below for variations in stagger angle, clearance size, and solidity. For these examples double leakage is neglected, the inlet boundary layer is taken from the low speed rotor computations ($\delta^*/\tau = 1.3$), and the non-dimensional pressure rise is 0.5, representative of highly loaded blades.

4.4.1 Stagger Angle

Figure 3-18 showed the effect of stagger angle on average leakage angle. The effect of stagger angle changes on blockage are presented in Figure 4-6 which plots the percent change in blockage ($A_{b,nominal}$ is the blockage at the initial stagger angle) versus changes in stagger angle for initial stagger angles of 35°, 45°, 55°, and 65°. In Figure 4-6, as in

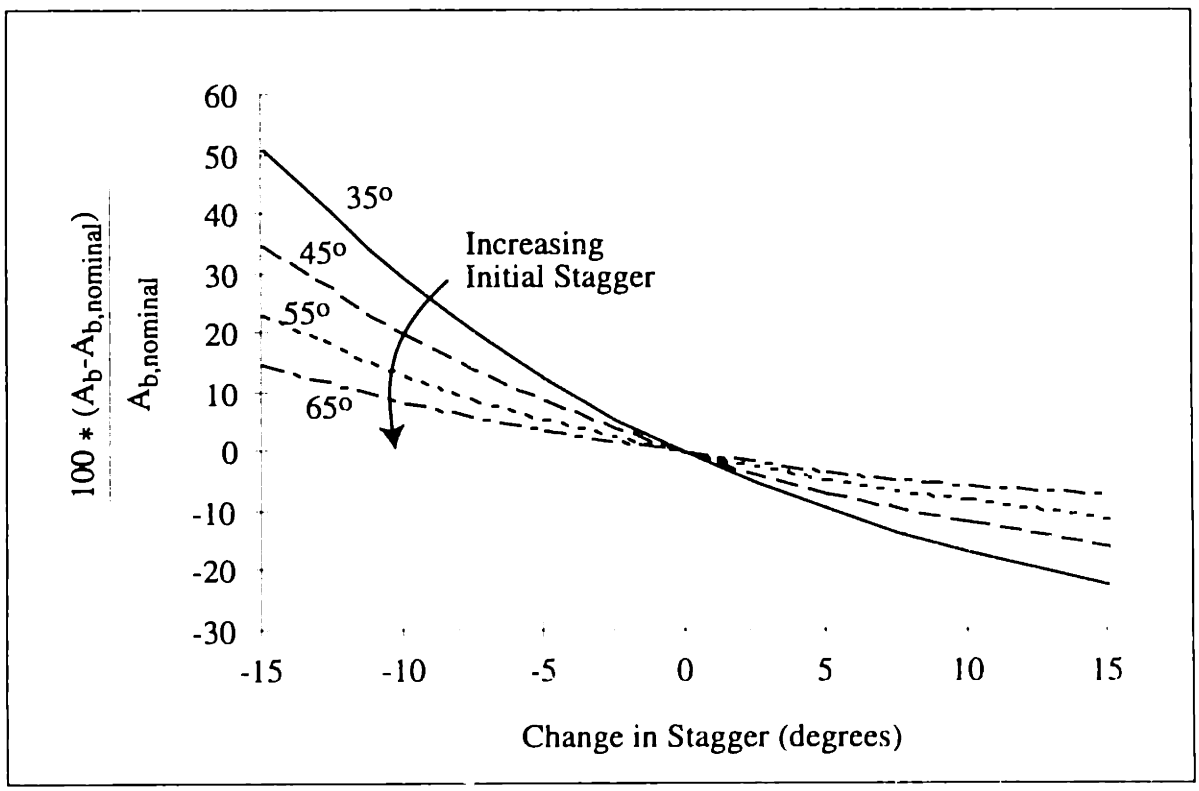

Figure 4-6: Predicted Changes in Blockage with Changes in Stagger Angle for Initial Staggers Between 35° and 65°, ΔP/Q=0.5, σ=1.1, τc = constant

Figure 3-18, the non-dimensional pressure rise is 0.5[1], the solidity is 1.1, and the clearance area, τc, is held constant as stagger changes. Blades with larger initial staggers have less sensitivity to stagger changes than cases with smaller staggers.

If the axial chord/clearance ratio is held constant with changes in stagger (as in Figure 3-15), the percent change in normalized blockage is as shown in Figure 4-7. There is little

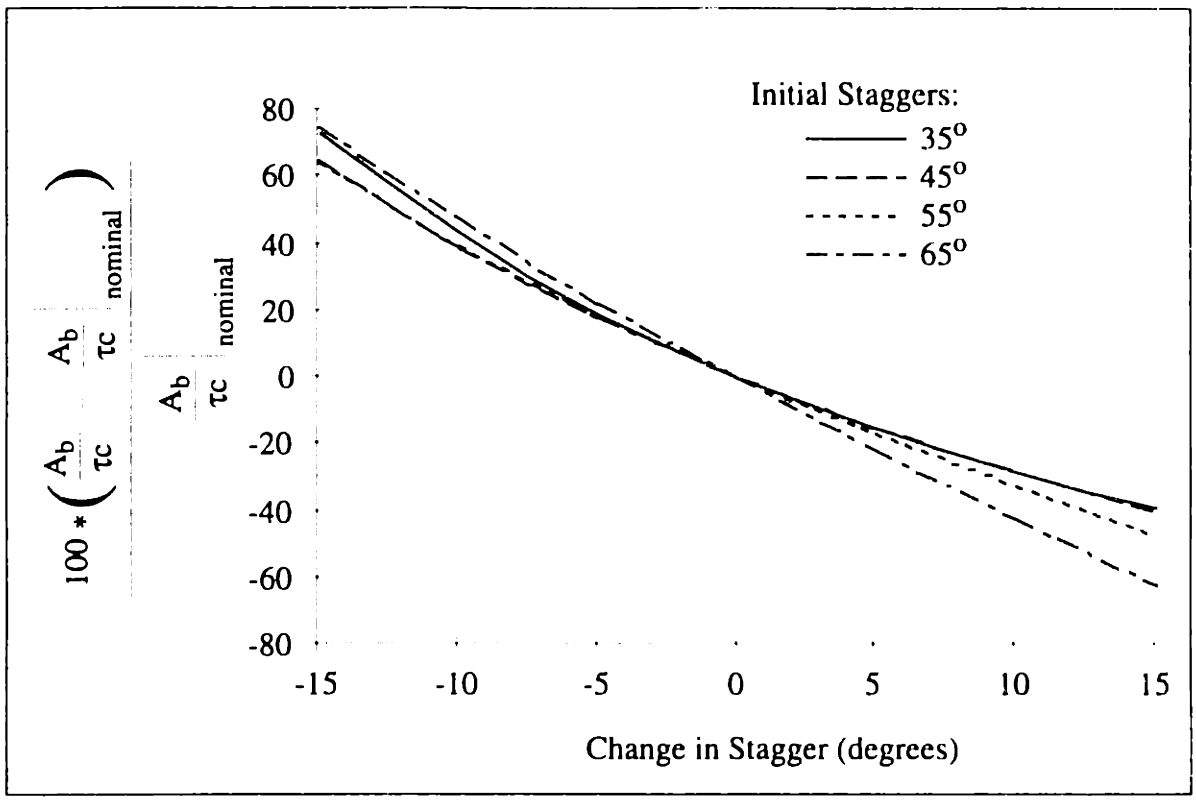

Figure 4-7: Predicted Changes in Blockage with Changes in Stagger Angle for Initial Staggers Between 35° and 65°, ΔP/Q=0.5, σ=1.1, axial chord/clearance = constant

change in blockage divided by clearance area in these cases because the increase (decrease) in blockage with decreasing (increasing) stagger is balanced by the decrease (increase) in clearance area.

4.4.2 Clearance Height

In the integral wake analysis the non-dimensional mixing length is the ratio of the distance over which the pressure change occurs to the initial defect height, x/b_0. The effect of

1. Previous researchers (Smith (1970) and Koch (1981) for example) have correlated parametric variations of peak pressure rise. The choice here of examining parametric variations at constant non-dimensional loading rather than at constant loading divided by maximum loading (the parameter used by Smith) allows variations to be examined without knowledge of the limiting pressure rise. The blockage calculation procedure could be used to produce curves of blockage versus Ψ/Ψ_{max} if Ψ_{max} were known.

increasing the clearance height is captured in the model by an increase in the initial defect height, b_0, and hence a reduction in the mixing length parameter, x/b_0. The values of b_0 from the low speed rotor, small clearance cases were doubled, and the normalized blockage was predicted to be 5% larger than the small clearance blockage (the empirically observed effect of doubling the clearance is shown in Figure 3-13). In the rotating rig data, the small clearance cases have a 20% smaller normalized blockage than the large clearance cases for low loading, and at high loading the blockage trends of the two clearances are identical. In the computational data the small clearance has between 7% and 20% higher blockage than the large clearance cases.

4.4.3 Solidity

For a given passage pressure rise, the blade loading and the jet leakage angle are functions of solidity (see Equation 3.8). For a non-dimensional pressure rise of 0.5 and a nominal solidity of 1.1, the predicted variation of blockage with solidity is given in Figure 4-8, which plots percent change in blockage versus percent change in solidity for initial staggers between 35° and 65°. For an initial stagger of 56° (the stagger of the low speed rotor examined computationally), the blockage model predicts that a 50% increase in solidity will decrease exit plane blockage by 28%. This result of the blockage prediction method compares well with the observed 30% decrease in blockage for a 50% increase in solidity (see subsection 3.3.5).

4.5 Chapter Summary

A model for tip leakage related blockage has been proposed and evaluated. The inputs to the model are the clearance jet total pressure, the pressure on blade suction surface, and leakage angle as functions of chord, the inlet boundary layer profile, and the exit plane static pressure. Comparing this blockage calculation procedure to Navier-Stokes solutions showed an average underprediction of endwall blockage of 33%, but the trends of blockage with parametric changes were captured to within 8%.

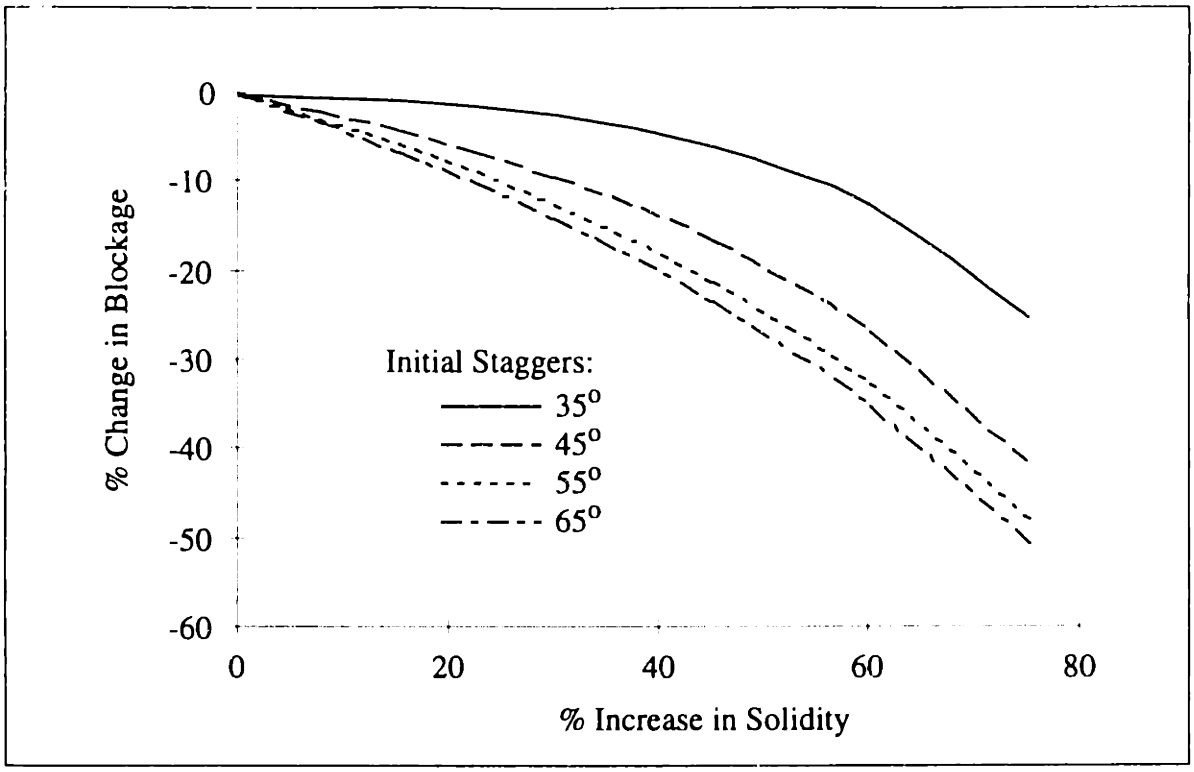

Figure 4-8: Predicted Changes in Blockage and Clearance Mass Flux with Changes in Solidity, High Loading Conditions

The parametric trends predicted by the blockage model are also similar to those observed in experiments, suggesting that the model not only captures the key processes that lead to blockage, but could be used to estimate the effect of design changes on blockage. Examples were given to quantify the effects of variations in stagger angle, clearance height, and solidity on blockage.

Chapter 5: Approaches to Blockage Reduction

In this chapter the procedure for estimating endwall blockage is applied to evaluate blockage reduction methods. The methods are not new, but the tools developed in this thesis allow their effects to be quantified. One of the methods evaluated here, increasing the clearance jet total pressure, was examined using the wind tunnel model described in Chapter 2. The experiments performed are described, and the data are compared to both computations of casing treatments and predictions from the blockage model.

5.1 Three-Dimensional Blade Design

One parameter on which endwall blockage depends is clearance jet leakage angle. The leakage angle is related to the blade loading near the tip, ΔP_B, as shown in Equation 3.5. A design with ΔP_B reduced, for the same passage pressure rise, would mitigate the adverse effects of tip clearance on the endwall flow field. In Figure 5-1 the predicted percent change in blockage is plotted against the percent decrease in blade loading for initial stagger angles of 35^o, 45^o, 55^o, and 65^o. This figure could be used by a designer to determine the amount of tip loading reduction required to achieve a desired blockage reduction. The large reductions in blade loading required indicates that this blockage reduction technique may be difficult to implement.

5.2 Enhanced Mixing

Increasing the mixing between the jet and the free stream would also reduce the exit plane blockage. By more rapidly mixing out the defect, the velocity non-uniformity, and hence

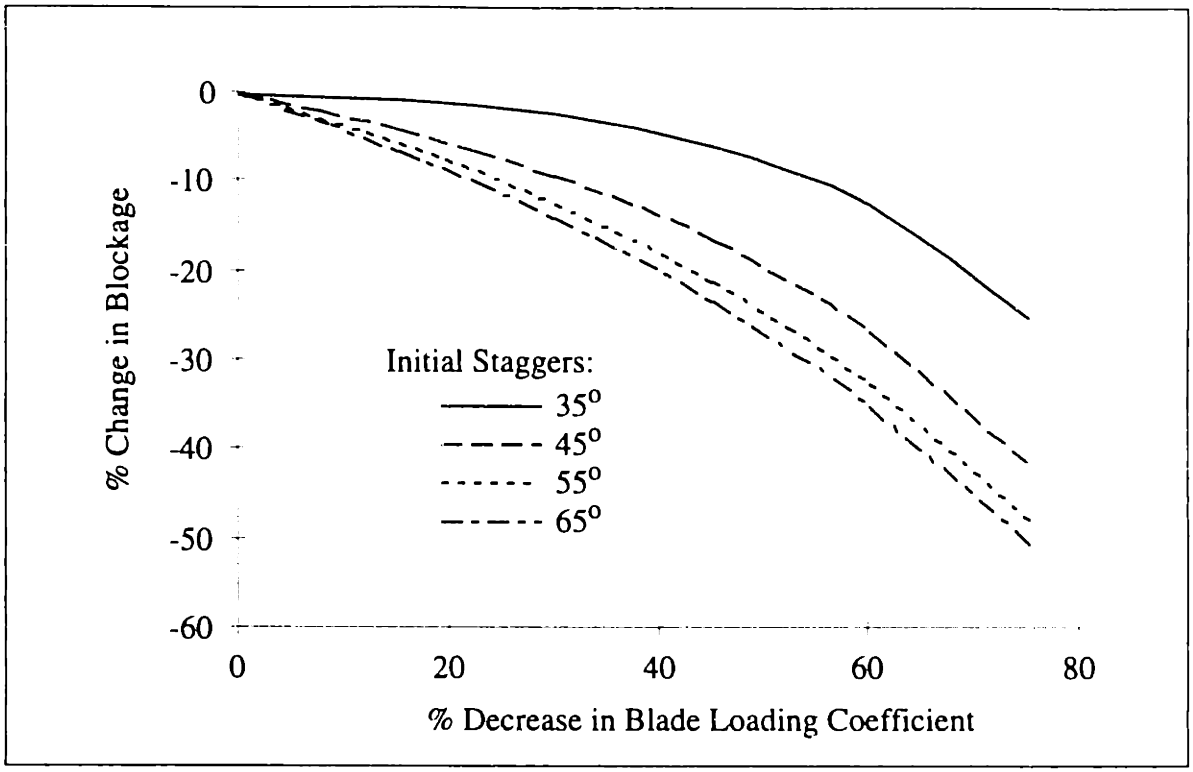

Figure 5-1: Predicted Effect of Changes in Blade Loading on Blockage, $\Delta P/Q = 0.5$, $\sigma=1.1$, Initial Stagger Angles of 35°, 45°, 55°, and 65°

the blockage, at the exit plane will be reduced. Figure 5-2 plots the predicted percent change in blockage versus the increase in eddy viscosity coefficient. The blockage model predicts that the mixing coefficient would need to be increased by more than a factor of 10 to affect a 50% reduction in blockage. The large increase in mixing required to significantly reduce endwall blockage suggests that this blockage reduction method not be pursued.

5.3 Effect of Leakage Jet Total Pressure

One of the most common techniques for controlling the endwall flow field is the use of casing treatments. The tools developed in this thesis were applied to the study of casing treatment flow fields, and the effect of one aspect of axial skewed slot casing treatments on endwall blockage was quantified. Both the wind tunnel (described in Section 2.5 and shown in Figure 2-15) and the blockage prediction method were used in this study.

Using Navier-Stokes solutions of a casing treatment model (see subsection 2.4.2), stream-

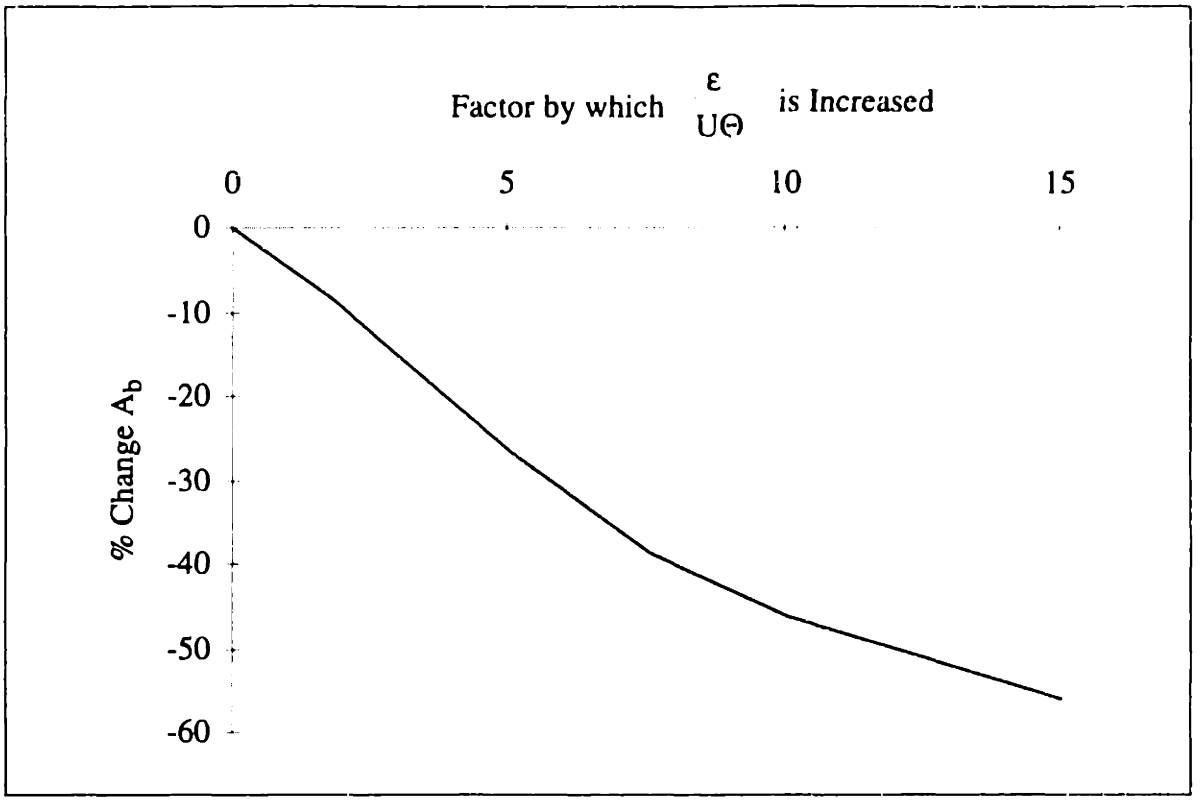

Figure 5-2: Predicted Decrease in Blockage with Increased Mixing for Low Speed Rotor, τ/c=3%, Near Stall Case

lines were traced upstream from the clearance gap. All of the clearance jet fluid that exits the tip gap between 5% chord (where the modelled treatment begins) and 50% chord (where the blowing region of the treatment ends) originated in the treatment and hence had high relative total pressure. This is shown in Figure 5-3 which plots the jet relative total pressure at the clearance exit as a function of chord for the five cases studied. In this figure the jet total pressure was mass averaged radially between the blade tip and the casing at each chordwise location, and the jet total pressure was referenced by the free stream total pressure and normalized by the inlet dynamic head. Four of the runs were performed with a specified blowing/suction mass flow rate equal to 3.5% of the inlet mass flux. One solution was run to determine the sensitivity of the observations to the blowing/suction rate by specifying a rate equal to 1.75% of the inlet mass flux.

In the wind tunnel two levels of increased jet total pressure were tested over two different chordwise extents. The clearance jet total pressure coefficients of the four jets tested are plotted in Figure 5-4 versus the chordwise distance. These profiles of total pressure coef-

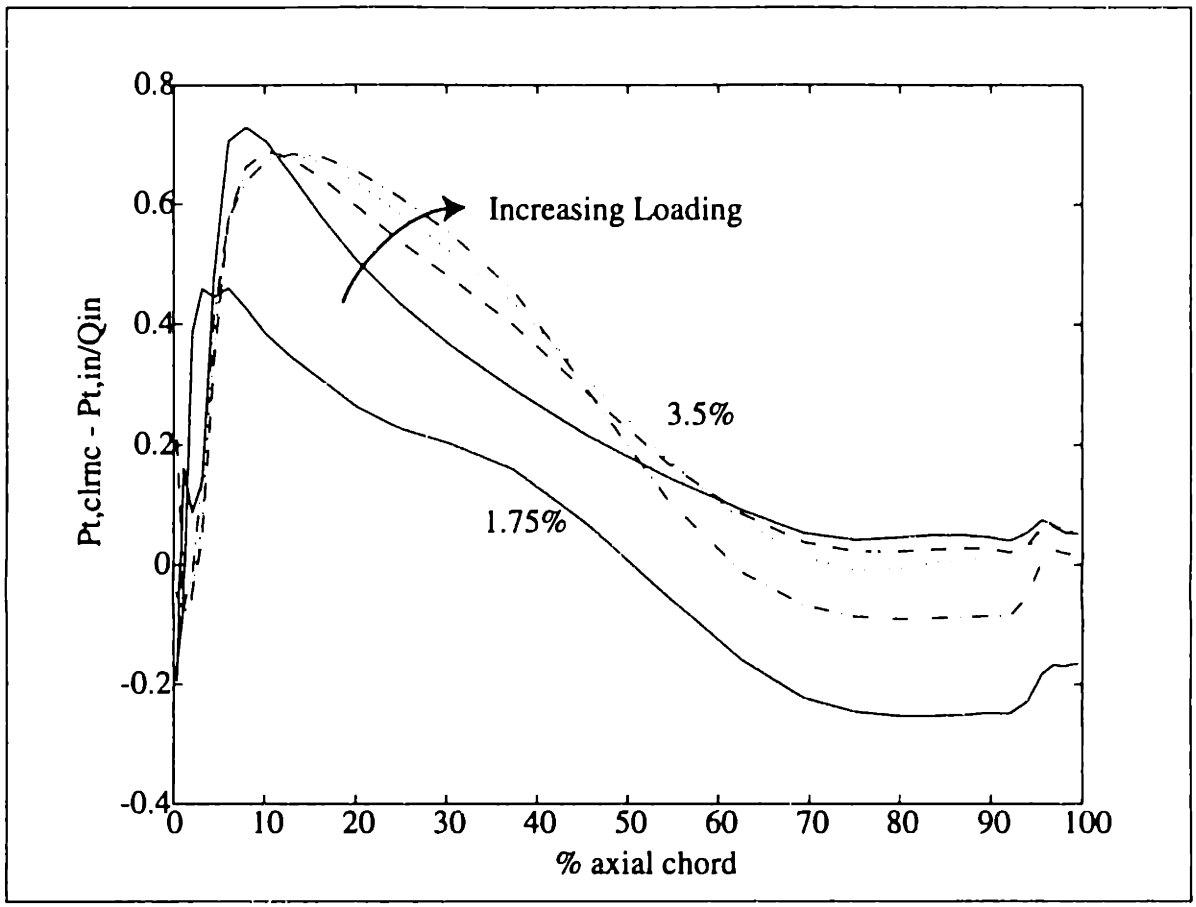

Figure 5-3: Navier-Stokes Computations of Clearance Jet Total Pressure versus Chord with 60° Skewed Axial Slot Casing Treatment for 1.75% and 3.5% of Inlet Mass Flux Removed and Injected Through the Casing

ficient were created in the wind tunnel using two different solidity screens placed behind the injector turning vanes as shown in Figure 5-5. The total pressure downstream of the screens was matched to the free stream total pressure, and the region of the jet not covered by the screen then had the desired elevated total pressure. These distributions of jet total pressure were tested under various loading conditions, and the blockage for each test was calculated.

The results from these tests are presented in Figure 5-6, where blockage from both the uniform jet total pressure runs and the casing treatment simulations are plotted. The blockage trend is unchanged with blowing. This suggests that the key process associated with blockage formation, the growth of a velocity defect in a pressure gradient, is unchanged by blowing. Blowing only reduces the depth of the initial defect.

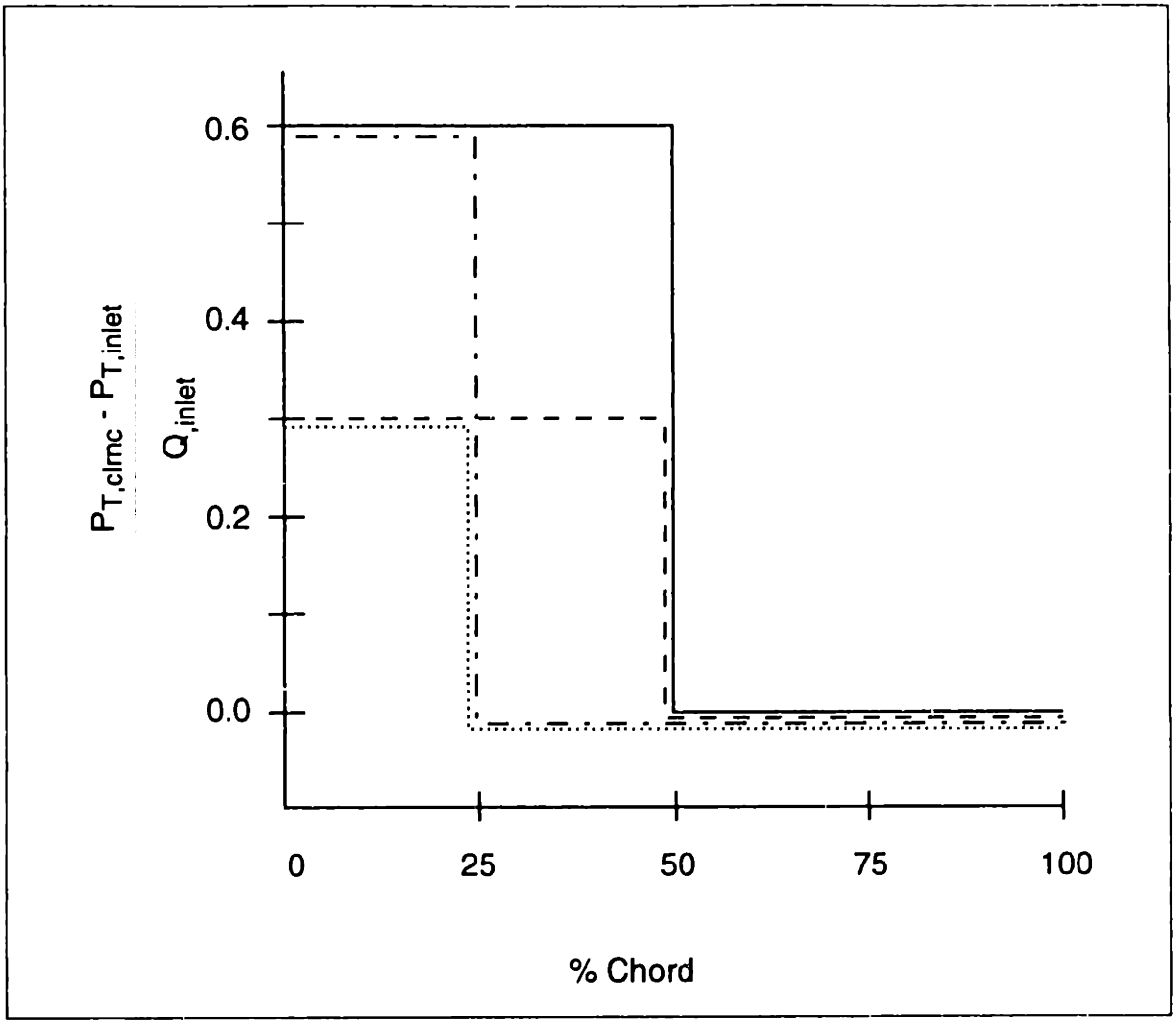

Figure 5-4: Jet Total Pressure Coefficient Distributions Tested in Wind Tunnel

In Figure 5-7 the measured changes in blockage for various loading conditions and blowing rates are shown. The stronger the blowing, the more reduction in blockage. Blowing over 50% of the chord reduces blockage 10 to 15% more than blowing over 25% of the chord at a given jet total pressure level. There was a reduced effectiveness in alleviating blockage at higher loading conditions. Near stall, blowing reduced blockage approximately 20% less than for the low loading cases.

In Cho's (1995) numerical experiments (with jet total pressure distributions between the strong 50% and 25% jets tested here and high loading conditions), a blockage reduction of 48% was observed. This compared well to the approximately 45% reduction observed in the wind tunnel data (the average of the reductions observed for the 50% and 25% jets), indicating that the primary mechanism for the blockage reduction due to blowing through

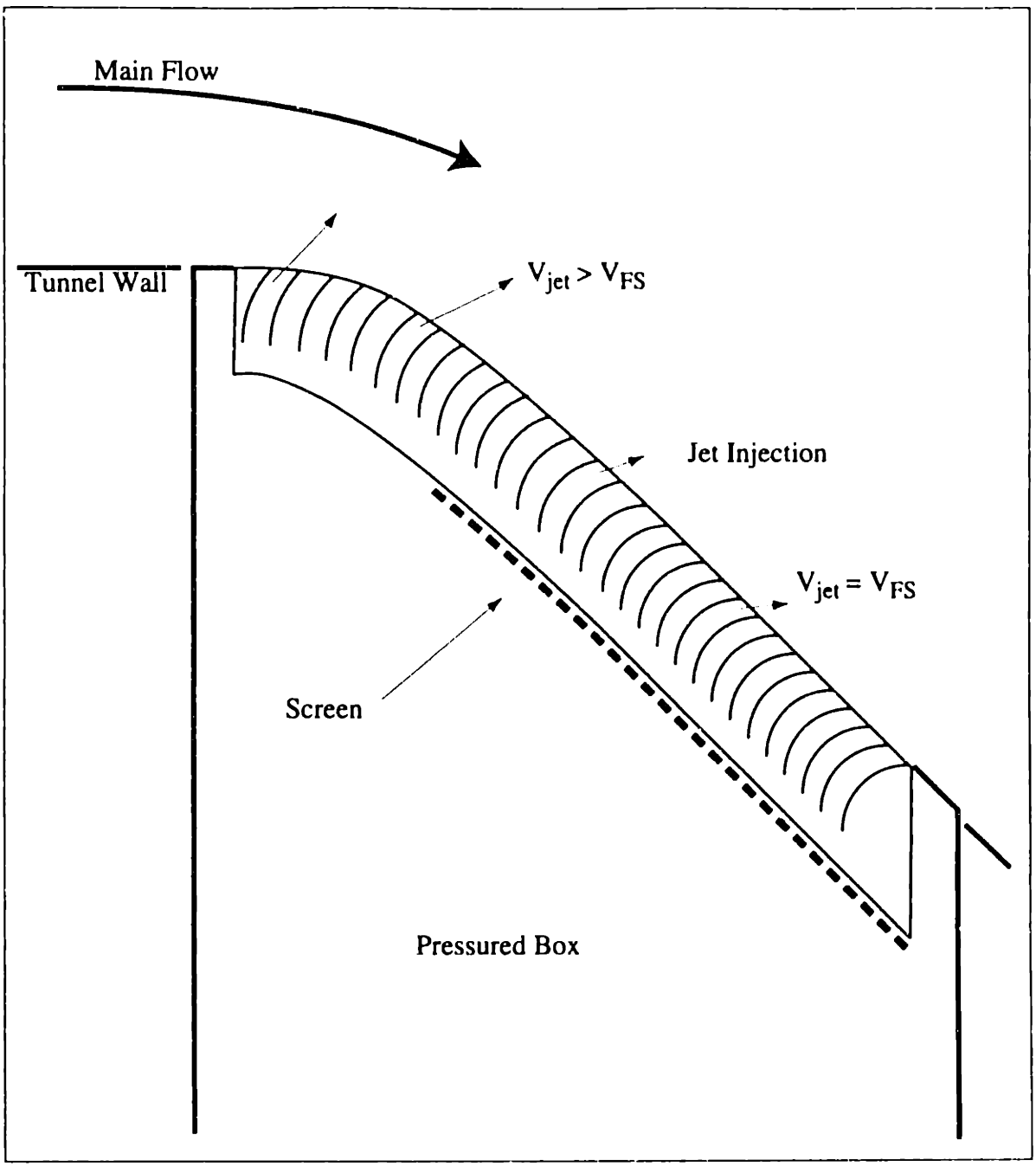

Figure 5-5: Jet Injection Modifications for Casing Treatment Simulation

a rotor casing (as would occur with an axial skewed slot casing treatment) is energizing of the clearance jet. Because the wind tunnel results, with blowing in just the clearance jet, and Cho's computations, with blowing across the entire pitch, show similar blockage reduction magnitudes, it appears that blowing into the mid-blade passage is not useful for blockage reduction.

The blockage model was used to estimate the blockage reduction due to increasing the jet

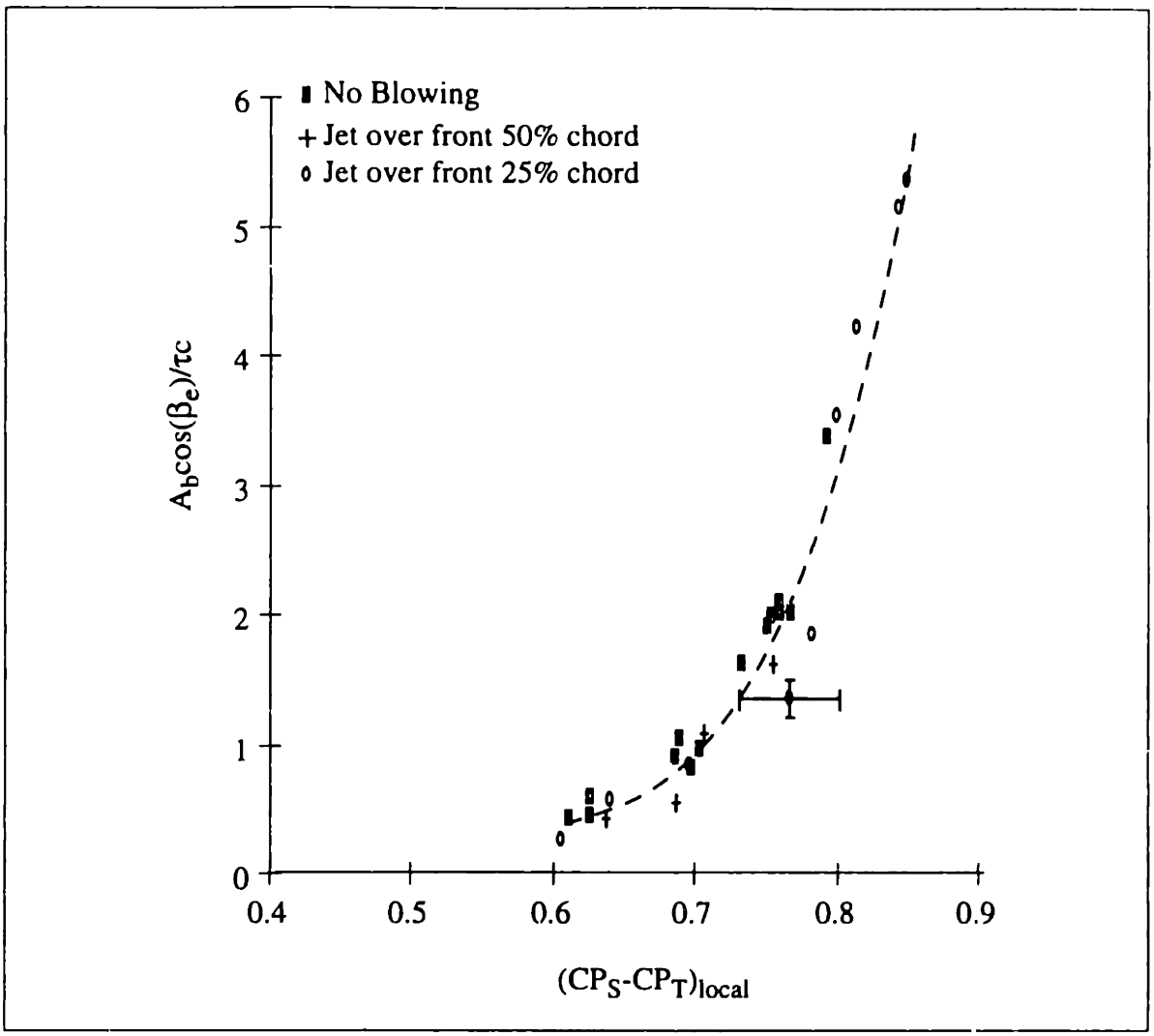

Figure 5-6: Effect of High Jet Total Pressure on Blockage, Normalized Blockage versus Loading Parameter for Uniform Jet Total Pressure and a Jet with 60% Q Increased Total Pressure Over the Front 25% and 50% of Chord

total pressure. Calculations were run with increased clearance jet total pressure coefficient over the front 50%. The amount of blockage reduction predicted by the blockage model is shown in Figure 5-8. The calculation indicates that a 60% increase in jet total pressure would result in a 45% reduction in blockage. This result is in good agreement to the experiments, supporting the validity of the blockage model, and providing a quantitative tool for designers seeking to control endwall blockage through modifications to the clearance jet total pressure.

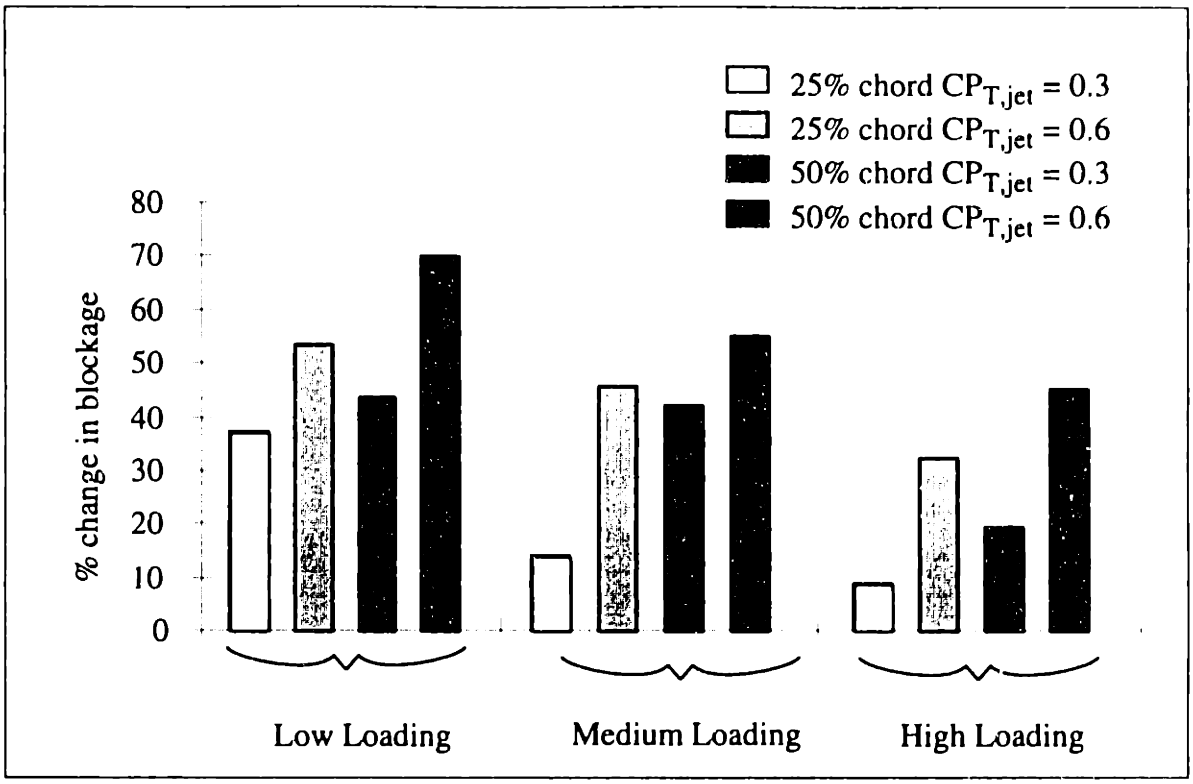

Figure 5-7: Reduction in Blockage Due to High Total Pressure Jet

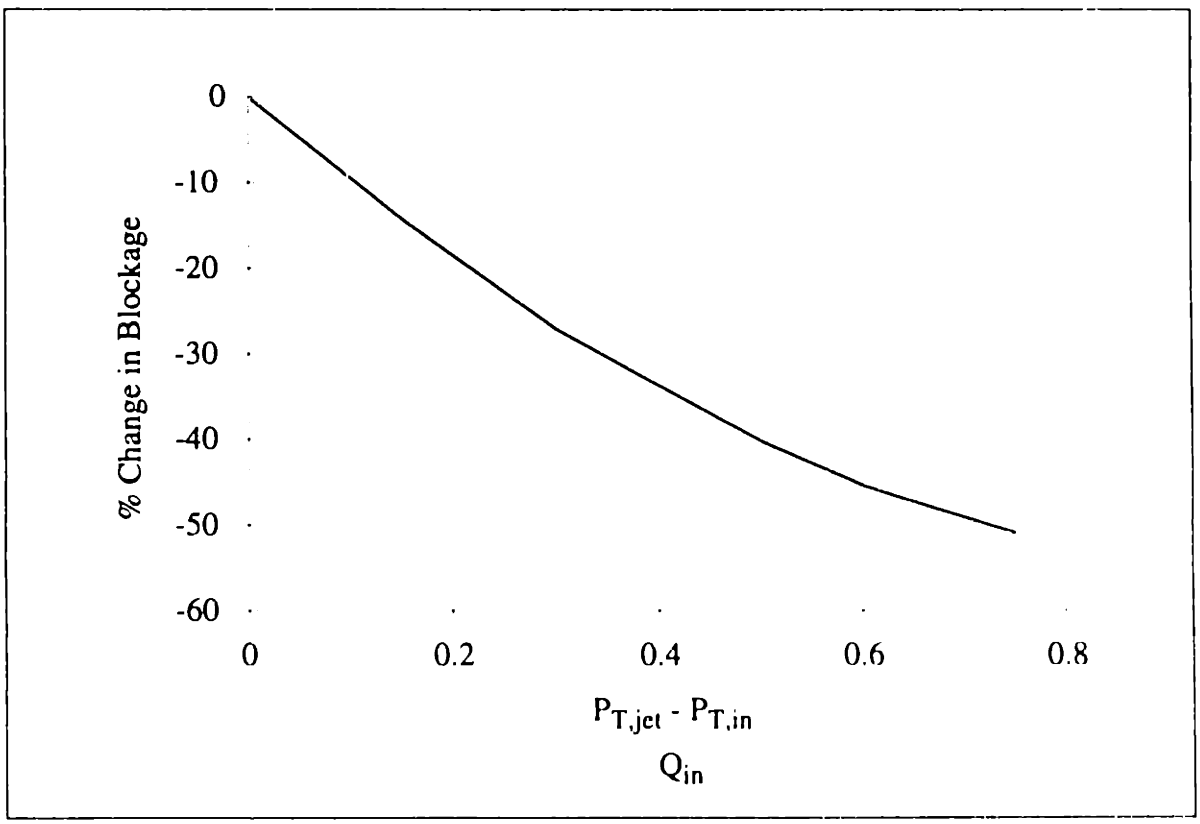

Figure 5-8: Reduction in Blockage when Jet Total Pressure is Increased Over Front 50% of the Chord

5.4 Chapter Summary

Tests in the wind tunnel and applications of the blockage model were used to evaluate blockage reduction methods. The effects on endwall blockage due to changes in mixing, tip loading, and leakage jet total pressure were quantified. It was found that for blades with an initial stagger of 56°, to reduce blockage by 50%, the leakage jet total pressure over the front 50% of the chord must be increased by approximately 60%, the blade loading near the tip must be reduced by 74%, or the mixing rate must be increased by a factor of 10.

Chapter 6: Conclusions and Recommendations

6.1 Summary

To gain a better understanding of the flow features that impact endwall blockage, to quantify the parametric trends of endwall blockage, and to develop a quantitative link between these trends and design parameter variations, experiments were performed numerically, in a low speed rotating rig, and in a wind tunnel model.

1. An analysis of endwall blockage has been developed that captures the observed trends within 8%.

2. A parameter set for presenting endwall blockage results was proposed that collapsed the experimental data into a single trend, offering a consistent figure of merit for this and future blockage studies.

3. A wind tunnel simulation of the tip leakage flow was developed, and found to capture the parametric trends of blockage, for various leakage angles and pressure gradients, observed in rotating rig tests to within 7%. However, the blockage model (developed in Chapter 4) appears to capture the parametric trends the wind tunnel does in a simpler manner. Hence pursuing the wind tunnel as a tool to study parametric trends of blockage is not useful. It should be used, however, to further the understanding of the loss generated at the jet-free stream interaction.

4. The endwall blockage calculation procedure and the experimental data were used to quantify effects of clearance height, stagger angle, inlet boundary layer thickness, loading level and loading profile, solidity, and clearance jet total pressure on endwall

blockage.

5. Three blockage reduction methods, three-dimensional blade design, enhanced mixing, and increased leakage jet total pressure, were quantitatively evaluated using the wind tunnel model and the blockage prediction method.

6. The double leakage of fluid from one clearance gap into the adjacent blade's tip gap, a previously unreported flow field feature, has been described. A method for predicting when this phenomenon will exist has been developed.

7. The blockage reduction due to the mass injection region of skewed axial slot casing treatments has been shown to be almost entirely attributable to the increase in clearance jet total pressure these treatments cause.

6.2 Suggestions for Future Work

To become a practical design tool, the blockage model presented here needs to be extended and further validated. The blockage model requires the clearance jet total pressure and leakage angle as inputs. If double leakage does not occur, the inviscid analysis of Storer (1990) can be used to predict these inputs from the blade loading. At present there is no tool for predicting the clearance exit conditions when double leakage occurs. If such a relationship could be quantified, a predictive scheme for endwall blockage requiring only the blade loading profile and the exit plane pressure as inputs would be possible.

Martinez-Sanchez (1996) has suggested a control volume model for the jet-free stream interaction that does not assume the independence of each chordwise section of the clearance jet. Integrating this interaction model into the blockage calculation procedure developed here would make the analysis simpler and more physically appropriate. This approach may lead to a more accurate blockage prediction method, and hence should be investigated.

The sensitivity analysis, described in Section D.3, indicates that uncertainties in the initial

defect depth are reflected in an equal uncertainty in the blockage prediction. To improve the accuracy of the blockage model the calculation of the initial defect should be made more accurate (error in the initial conditions cause an approximately equal error in calculated blockage). The blockage model is not sensitive, however, to the details of the mixing downstream of the jet-free stream interaction region (see Figure D-2 for example). Detailed measurements at the jet-free stream interaction region would enable the initial conditions to the integral wake model to be refined. The wind tunnel test section described in Chapter 2 would be a useful tool for such a study. The specific experiments suggested are that the axial and tangential velocities at both the jet-free stream interaction location and the passage exit plane be mapped for various jet injection angles.

This thesis examined incompressible flow fields. Khalid's (1995a) work included transonic fan cases and it was found that the blockage trends were substantively the same for both compressible and incompressible flow fields. It would be useful to attempt to extend the blockage model to high speed fans where shocks and compressible effects play a role in blockage development.

Three-dimensional compressor design codes now exist that may make possible the design of a blade with significantly reduced blade loading close to the tip. This has been suggested as a method for reducing the leakage jet mass flux and leakage angle and hence the negative effects of tip clearance.

This work has shown (compare Figures 3-21 and 3-22 for example) that compressors with different stalling pressure rise coefficients (CP_S) have similar limiting loading parameters (CP_S-CP_T). If a predictive method were developed for CP_T, the loss in the blockage region, the stalling pressure rise could be predicted. Extending the blockage model presented here to a blockage region loss prediction method would be a useful future research avenue.[1]

---

1. Storer and Cumpsty (1994) proposed a theory for the mixed out loss averaged over the entire exit plane, but this is not directly applicable to the calculation of CP_T.

References

Adamczyk, J. J., Celestina, M. L., Beach T. A., and Barnett, M., 1989, "Simulation of Three-Dimensional Viscous Flow within a Multistage Turbine," ASME Journal of Turbomachinery, Vol. 112, pp. 370-376.

Baldwin, B. and Lomax, H., 1978, "Thin Layer Approximation and Algebraic Model for Separated Turbulent Flows," AIAA Paper No. 78-257.

Beers, Y., 1953, *Introduction to the Theory of Error*, Addison-Wesley Publishing.

Bolger, J., 1995, personal communication.

Brookfield, J.M., 1993, "Vortical Flows in an Adverse Pressure Gradient," Masters thesis, Department of Aeronautics and Astronautics, Massachusetts Institute of Technology.

Chen, Gwo-Tung, 1991, "Vortical Structures in Turbomachinery Tip Clearance Flows," Doctoral thesis, Department of Aeronautics and Astronautics, Massachusetts Institute of Technology.

Chen, G. T., Greitzer, E. M., Tan, C. S., and Marble, F. E., 1991, "Similarity Analysis of Compressor Tip Clearance Flow Structure," ASME Journal of Turbomachinery, Vol. 113, pp. 260-271.

Cho, D. L., 1995, "Effect of Vortex Core Stagnation Pressure on Tip Clearance Flow Blockage in Turbomachines," Masters thesis, Department of Aeronautics and Astronautics, Massachusetts Institute of Technology.

Clauser, F. H., 1956, "The Turbulent Boundary Layer," *Advances in Applied Mechanics*, vol. 4, Academic Press, New York, NY.

Crook, A. J., Greitzer, E. M., Tan, C. S., and Adamczyk, J.J., 1993, "Numerical Simulation of Compressor Endwall and Casing Treatment Flow Phenomena," ASME Journal of Turbomachinery, Vol 115, pp. 501-512.

Cumpsty, N. A., 1989, *Compressor Aerodynamics*, Longman Scientific and Technical Publications.

Cumpsty, N. A., 1995, personal communication.

Fujita, H. and Takata, H., 1984, "A Study on Configurations of Casing Treatment for Axial Flow Compressors," Bulletinm of JSME, Vol 27, #230, pp. 1675-1681.

Greitzer, E.M., Nikkanen, J. P., Haddad, D. E., Mazzawy, R. S., and Joslyn, H. D., 1979, "A Fundamental Criterion for the Application of Rotor Casing Treatment," ASME Journal of FLuids Engineering, Vol 101, pp. 237-243.

Hill, P. G., Schaub, U. W., and Senoo, Y., 1963, "Turbulent Wakes in Pressure Gradients," Trans. ASME, pp. 518-524.

Horlock, J. H. and Greitzer, E. M., 1983, "Non-Uniform Flows in Axial Compressors due to Tip Clearance Variation," Proc. Instn. Mech. Engrs., Vol 197C, pp. 173-178.

Hunter, I. H. and Cumpsty, N. A., 1982, "Casing Wall Boundary-Layer Development Through and Isolated Compressor Rotor," Journal of Engineering for Power, Vol. 104, pp.805-818.

Johnson, M. C., 1985, "The Effects of Hub Treatment on Compressor Endwall Flowfields," Masters thesis, Department of Aeronautics and Astronautics, Massachusetts Institute of Technology.

Kerrebrock, J. L., 1992, *Aircraft Engines and Aircraft Engines,* MIT Press, Cambridge, Massachusetts.

Khalid, S. A., 1995a, "The Effects of Tip Clearance on Axial Compressor Pressure Rise," Ph.D. thesis, Department of Aeronautics and Astronautics, Massachusetts Institute of Technology.

Khalid, S. A., 1995b, "The Effects of Tip Clearance on Axial Compressor Pressure Rise," internal Gas Turbine Laboratory Report, revised verion of Ph.D. thesis.

Khan, Rajesh, 1995, "A Quasi One-Dimensional Analysis for Confined Vortex Cores," Masters thesis, Department of Aeronautics and Astronautics, Massachusetts Institute of Technology.

Kirtley, K. R., Beach, T. A., and Adamczyk, J. J., 1990, "Numerical Analysis of Secondary Flow in a Two-Stage Turbine," AIAA Paper No. 90-2356.

Koch, C. C., 1981, "Stalling Pressure Rise Capability of Axial Flow Compressor Stages," ASME Journal of Engineering for Power, Vol. 103, pp.645-656.

Lee, N. K. W., and Greitzer, E. M., 1990, "Effects of Endwall Suction and Blowing on Compressor Stability Enhancement," ASME Journal of Turbomachinery, Vol. 112, pp. 133-144.

Marble, F. E., 1991, Personal Communication.

Martinez-Sanchez, M. and Gauthier, R. P., 1990, "Blade Scale Effects of Tip Leakage," Gas Turbine Laboratory Report #202.

Martinez-Sanchez, M., 1996, Personal Communication.

Place, James J.M., 1994, Personal Communication.

Rains, D. A., 1954, "Tip Clearance Flow in Axial Compressors and Pumps," California Institute of Technology, Hydrodynamics and Mechanical Engineering Laboratories Report No. 5.

Rediniotis, O. K., Hoang, N. T., and Telionis, D. P., 1993, "The Seven-Hole Probe: Its Calibration and Use," FED-Vol 152, Instructional Fluid Dynamic Experiments, pp.21-26.

Schlichting, H., 1960, *Boundary Layer Theory*, McGraw-Hill Book Company, Inc., New York, NY.

Smith, L. H. Jr., 1970, "Casing Boundary Layers in Multistage Axial-Flow Compressors," Flow Research in Blading, ed., L. S. Dzung, Elsevier, Amsterdam.

Smith, G. D. J. and Cumpsty, N. A., 1984, "Flow Phenomena in Compressor Casing Treatment," ASME Journal of Engineering for Gas Turbines and Power, Vol. 106, No. 3, pp 532-541.

Storer, J. A., 1991, "Tip Clearance Flow in Axial Compressors", Ph.D. thesis, Department of Engineering, Cambridge University.

Storer, J. A. and Cumpsty, N. A., 1994, "An Approximate Analysis and Predicition Method for Tip Clearance Loss in Axial Compressors," Journal of Turbomachinery, Vol 116, pp. 648-656.

Wisler, D. C., 1977, "Core Compressor Exit Stage Study, Volume I - Blading Design," NASA CR-135391.

Wisler, D. C., 1981, "Core Compressor Exit Stage Study, Volume IV - Data and Performance Report for the Best Stage Configuration," NASA CR-165357.

Wisler, D. C., 1985a, "Aerodynamic Effects of Tip Clearance, Shrouds, Leakage Flow, Casing Treatment and Trenching in Compressor Design," Von Karman Institute Lecture Series 1985-05 on Tip Clearance Effects in Axial Turbomachinery.

Wisler, D. C., 1985b, "Loss Reduction in Axial-Flow Compressors through Low Speed Model Testing," ASME Journal of Engineering for Gas Turbines and Power, Vol 107, pp. 354-63.

Appendix A: Data Analysis and Error Analysis

A.1 General

This Appendix describes the methods used to reduce and analyze the experimental data and to determine the propagation of experimental errors. All error analysis was done using standard error methods as described in Beers (1953) for combining independent and correlated errors. All errors are 95% confidence bands.

For both the wind tunnel and the rotating rig experiments, the data reduction yielded two parameters, the normalized blockage, and the local loading parameter. These are expressed as follows:

$$\text{Normalized Blocakge} \equiv \frac{A_b \cos(\beta_e)}{\tau c}, \text{ and}$$

$$\text{Local Loading Parameter} \equiv \frac{\overline{CP_S}^{local} - \overline{CP_T}^{local}}{\overline{Q_{local}}}.$$

The blockage is an area integral of one minus the streamwise velocity within the endwall defect region divided by the velocity at the edge of the defect region integrated over the area defined as per Khalid's (1995a) blockage definition:

$$A_b \equiv \iint \left(1 - \frac{v_{sw}}{V_{edge}} \right) dA, \quad . \tag{A.1}$$

To calculate A_b the streamwise velocity must be known across the plane of interest. The

magnitude of the gradient of streamwise velocity defines the edge of the defect region. In this thesis, as in Khalid (1995a), the edge of the defect region was chosen where this magnitude was equal to the inlet axial velocity divided by the chord. V_{edge} varies along the edge of the defect, and so the integrand in Equation A.1 was evaluated using the value of V_{edge} nearest to the each differential area, dA.

The local loading parameter, as explained in Chapter 2, is a measure of the exit plane static and total pressures, with the reference quantities defined "locally," varying along the chord and averaged. Figure A-1 is given to provide an example of this computation.

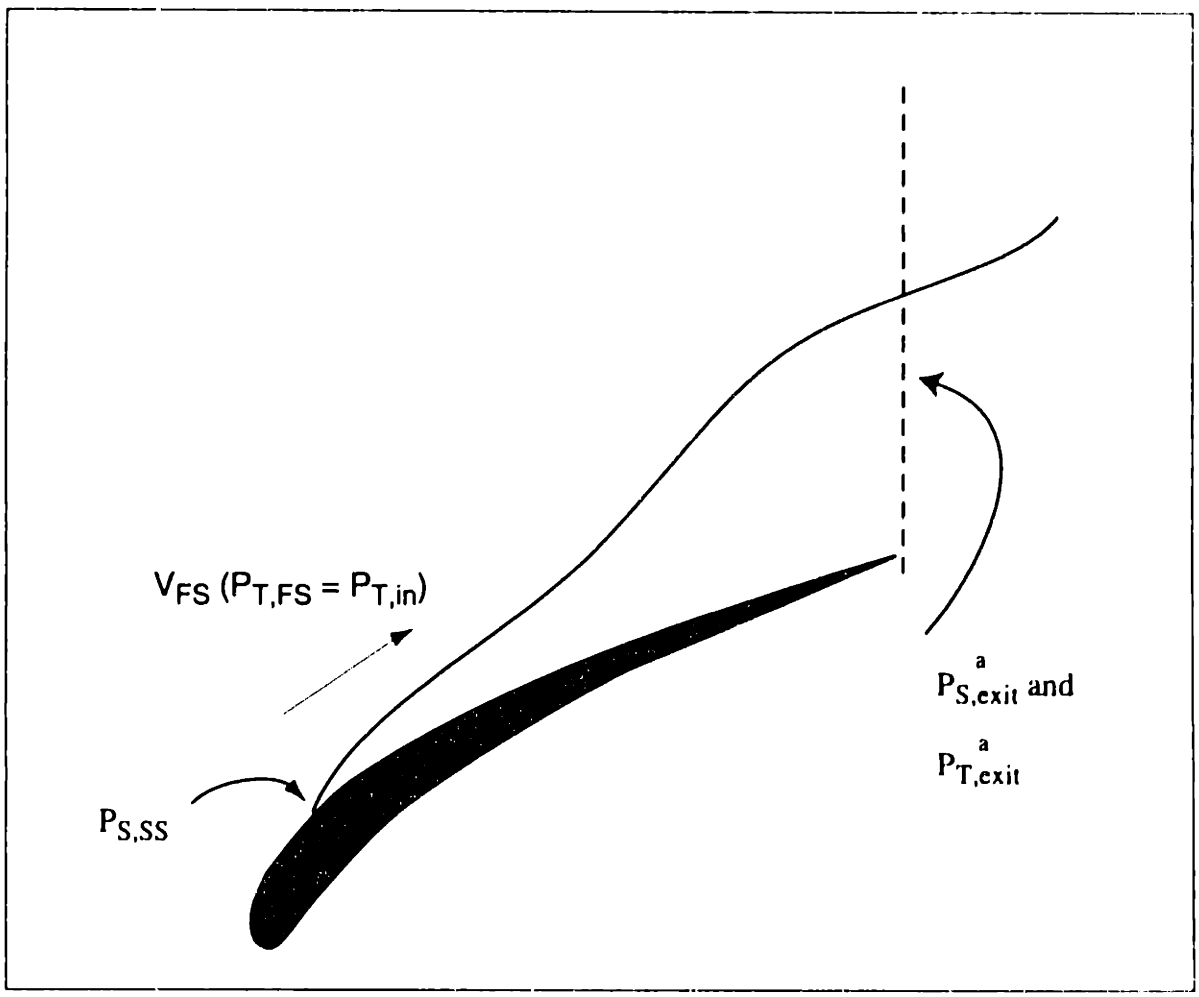

Figure A-1: Schematic for the Computation of the Local Loading Parameter

For each chordwise location a loading parameter is calculated by assuming that the exit conditions are the area average pressures (both static and total) averaged over the blockage region, that the initial static pressure is the suction surface pressure two clearance heights

inboard of the blade tip, the initial total pressure is equal to the inlet free stream total pressure, and the local free stream dynamic head is approximately the inlet total pressure minus the suction surface static pressure. For each chordwise location the following can be written:

$$\text{local loading parameter} = \left[\frac{\overline{P_{S,\text{exit}}}^{a} - P_{S,\text{local}}}{P_{T,\text{inlet,FS}} - P_{S,SS}}\right] - \left[\frac{\overline{P_{T,\text{exit}}}^{a} - P_{T,\text{inlet,FS}}}{P_{T,\text{inlet,FS}} - P_{S,SS}}\right]. \qquad (A.2)$$

Once this parameter is calculated for each chordwise location a mass average is performed, weighting each chordwise loading parameter by the clearance mass flux at that location, calculated using the pressure difference across the blades two clearance heights inboard of the blade tips to estimate the leakage velocity. This gives the final expression for the local loading parameter as:

$$\begin{aligned}\text{average local loading parameter} &= \overline{\left[\frac{\overline{P_{S,\text{exit}}}^{a} - P_{S,\text{local}}}{P_{T,\text{inlet,FS}} - P_{S,SS}}\right]}^{m} - \overline{\left[\frac{\overline{P_{T,\text{exit}}}^{a} - P_{T,\text{inlet,FS}}}{P_{T,\text{inlet,FS}} - P_{S,SS}}\right]}^{m} \\ &= \overline{\left[\frac{\overline{P_{S,\text{exit}}}^{a} - P_{S,\text{local}}}{Q_{\text{local}}}\right]}^{m} - \overline{\left[\frac{\overline{P_{T,\text{exit}}}^{a} - P_{T,\text{inlet,FS}}}{Q_{\text{local}}}\right]}^{m} \\ &= (CP_S - CP_T)_{\text{local}}\end{aligned}$$

A.2 Wind Tunnel

The seven hole probe used to measure velocities and pressures at the trailing edge of the injection slot was calibrated by the Aeroprobe Corporation, with a large lookup table taking the seven probe measurements and the inlet dynamic head as inputs and outputting the three velocity components, static, and total pressure. A multi-tube slant manometer was used to measure the static pressure along the curved wall of the tunnel, corresponding to the rotor blade suction surface pressure.

The pressure transducers used to measure the seven pressures from the probe and the inlet

dynamic head were calibrated using the wind tunnel and a pitot tube with the pressure being measured simultaneously by the transducer and the slant manometer. The transducers were accurate to ±1 % of full scale.

To propagate the ±1 % error in the transducer measurements into the velocity and pressure calculations a statistical study of the probe's calibration matrix was done. An actual measurement point (consisting of 7 pressures from the probe and the upstream reference pressure) was chosen as a datum. Each of the eight pressures were then randomly perturbed assuming a Gaussian distribution with 1% of full scale, the maximum transducer error, used to set the three σ value. These new, perturbed pressures were processed through the probe's calibration matrix and the resulting static and total pressures and velocities compared to the datum. This process was repeated 10,000 times to ensure a valid sampling, and the mean variance in the static and total pressures and velocities due to the 1% uncertainty in probe pressure measurements was calculated. The result of this statistical test was that the streamwise velocity was known with 95% certainty to ±5 %, the total pressure was known to ±4 %, and the static pressure was known to ±8 %.

The statistical test just described gave the uncertainty in the pressures and velocities at each measurement point. The local loading parameter was computed by averaging the appropriate pressure coefficient over the blockage region, and the blockage was calculated by summing the streamwise velocity ratio over the blockage region. Positioning errors in the location and movement of the pneumatic probe caused a ±0.9 % error in calculating the blockage region area. The errors in the individual measurements were propagated using the standard root-sum-squared method for independent errors. The results of this analysis were that the loading parameter was known to ±9 % and the normalized blockage was known to ±14 %.

A.3 Rotating Rig

The data from the rotating rig experiments did not include reliable static and total pressure

measurements at the rotor trailing edge plane. To calculate a loading parameter, the flow was assumed to be incompressible (the Mach number was ~0.08), and to have negligible radial velocity. With these assumptions the loading parameter could be related to the velocity magnitude (the axial and tangential components were measured by the hotwire measurements described in Section 2.3) via Bernoulli's equation giving the following expression for the inlet normalized loading parameter:

$$\frac{CP_S - CP_T}{Q_{in}} \equiv 1 - \frac{\iint v_e^2 dA}{V_i \cdot A}.$$

to convert this inlet normalized loading parameter to the desired local loading parameter. Because the exit plane static and total pressure were not individually known, Equation A.1 could not be computed directly. A two step process was used to approximate the local loading parameter. The on-rotor static pressure tap measurements from 96% span were used to compute the ratio of the average local dynamic head to the inlet dynamic head. Then an empirical correction factor was added. This factor was determined by computing this approximate local loading parameter from the Navier-Stokes computational solutions and comparing this to the actual local loading parameter. The comparison between the actual and approximated local loading parameter gave an estimate of a ±7 % error in the local loading parameter.

The slant-wire hot wire was calibrated once for variations in flow angle by putting it at known angles to a one dimensional flow. Before each run the wire was calibrated to produce a voltage versus velocity curve. The accuracy of the entire two-stage calibration was checked experimentally by putting the probe at a known angle to a reference flow and comparing the calculated flow angle and velocity to the known values. The results were that the velocity magnitude was known with 95% confidence within ±5 %, and the flow angle was measured to ±0.9 %.

The tunnel used a calibrated bellmouth inlet to measure the mass flow through the facility. Pressures for the calibration were measured with a manometer and a pitot-static probe downstream of the bellmouth was used to measure the velocity. The errors involved in

reading the manometer, in measuring the velocity, the tunnel area, and the density of the air were estimated and propagated by Place (1994), with the result that the inlet axial velocity was known to ±0.7 %.

The rotational speed of the rotor was measured using an optical sensor, and during data collection the data acquisition computer would not accept any data until the rotor speed was adjusted to within 0.3% of the desired speed, which was 400 RPM for these tests.

To compute blockage using Khalid's (1995) method, the free stream velocity profile must be extrapolated to the endwall. This extrapolation was performed "by eye." Comparing different possible extrapolations gave an estimated error in blockage introduced by this choice of 5.3%.

The blockage that was computed attempts to isolate the endwall flow from the blade wakes. Distinguishing what fluid to include as "endwall" blockage and what to exclude as "wake" fluid is an arbitrary choice. As only one person preformed all the analysis, these distinctions should at least be consistent throughout the data set. By comparing different delineations between "wake" and "endwall" fluid, it was estimated that the error this choice introduces into the blockage measurement is 2.4%.

Hot wire measurements were made across more than two blade passages, allowing the blockage and the loading parameter to be calculated separately for each passage and then averaged. It is these averages that are presented in subsection 2.3.2, and they are written with an overbar in the follow error propagation trees. Figure A-2 shows how errors in the individual measurements combine to give the final normalized blockage error estimation of ±6.6 %. The largest source of error is the hot wire measurements that are accurate to within 5%.

The uncertainty in the velocity is also the largest error source in the calculation of the loading parameter. An error propagation tree for the inlet normalized loading parameter is presented in Figure A-3, showing how the measurement errors combine to give a 95% confidence band of ±0.9 %. Combining this with the 7% error to calculate the local load-

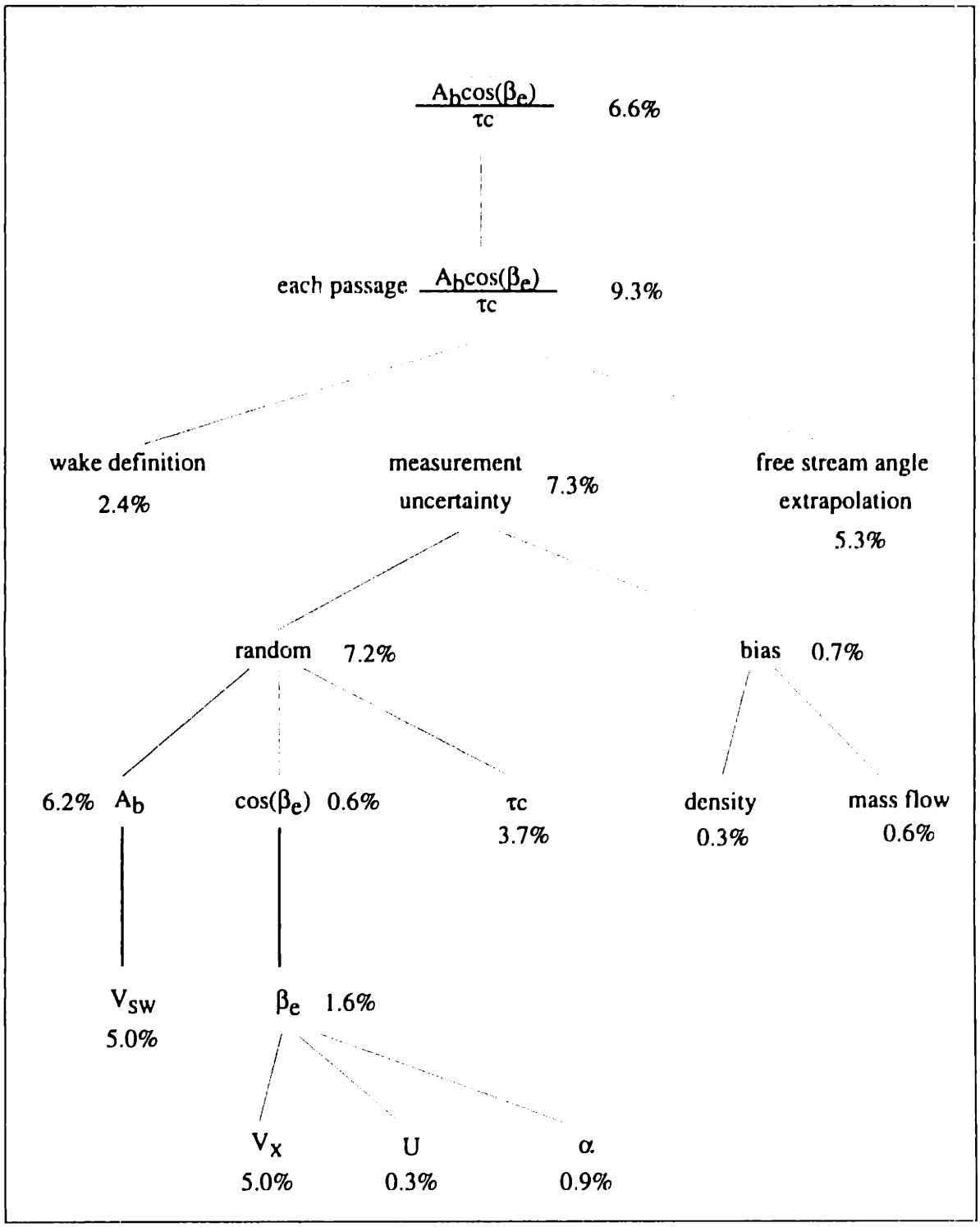

Figure A-2: Blockage Error propagation Tree, Rotating Rig Experiments

ing parameter gave the ±7 % error in the local loading parameter.

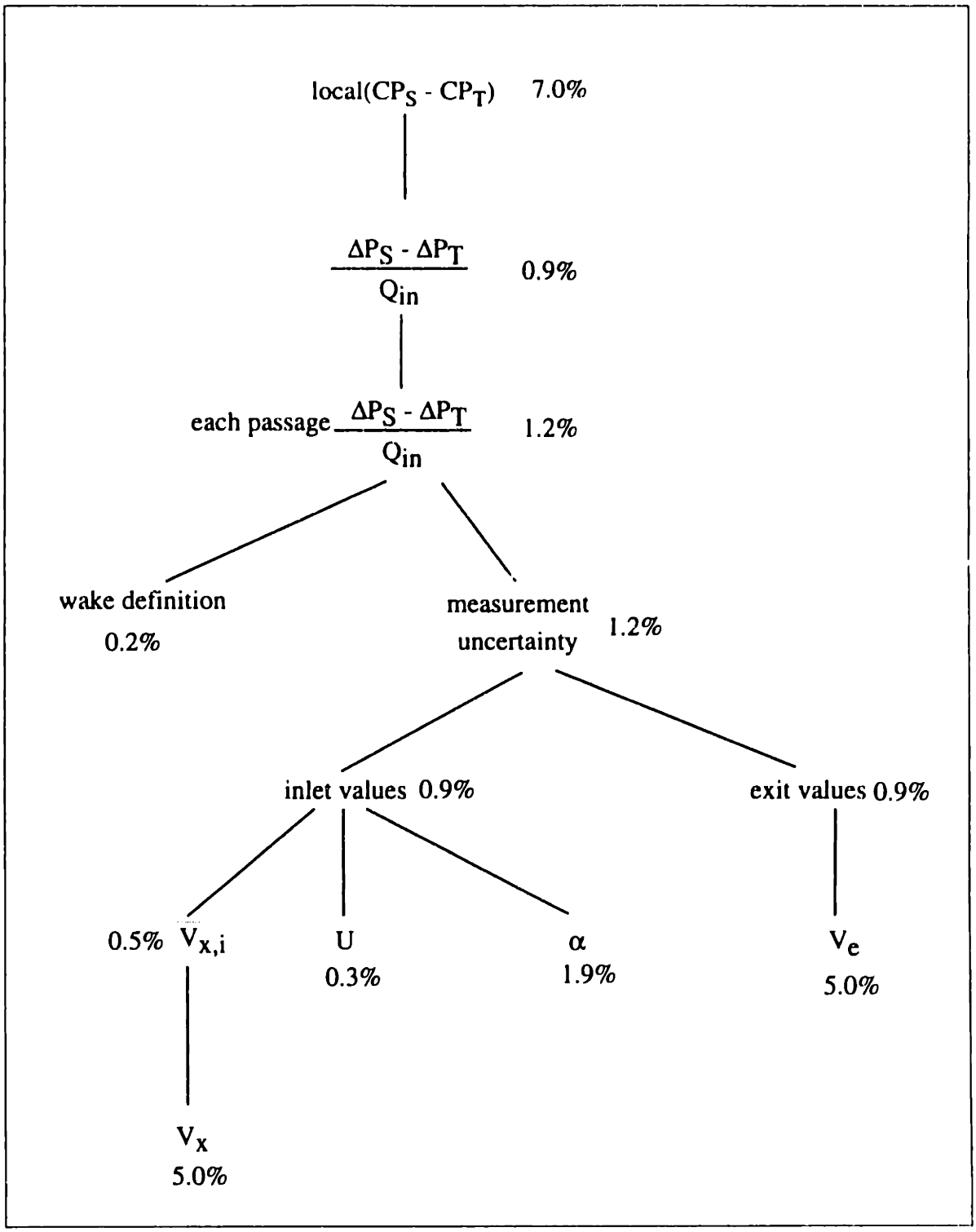

Figure A-3: Loading Parameter Error propagation Tree, Rotating Rig Experiments

Appendix B: Assessment of the Wind Tunnel Model

To more rigorously support the validity of the simplified wind tunnel model, analysis was performed to quantify differences between the model and the real compressor flow field. Each difference between the model and a real flow was examined and an estimate was made of the size of the effect, in terms of how the blockage would be affected. The estimates of how much these effects would affect the blockage were based on data in the literature, analysis, and Navier-Stokes computations. The following sections describe the modeling assumptions one at a time, presenting the evidence that indicates that these effects are small in the parametric range of interest.

B.1 Constant Leakage Angle

In the wind tunnel tests the jet leakage angle was constant along the chord, whereas in a compressor the leakage angle varies along the chord. To examine the effect of this simplification on blockage the Navier-Stokes solver used by Brookfield (1993) was employed. Brookfield calculated a flow field similar to the wind tunnel model, and the good agreement between his calculated and a predicted vortex trajectory, shown in Figure B-1, supports the validity of his method.

These computations allowed for the wind tunnel flow field to be modelled with an arbitrary specification of jet injection angle. Two tests were run, one with a constant leakage angle of 41 degrees and one with a parabolically varying leakage angle to simulate an actual blade condition. The mass average leakage angle for the non-uniform leakage angle case was 41 degrees. The two tested leakage angle profiles are shown in Figure B-2.

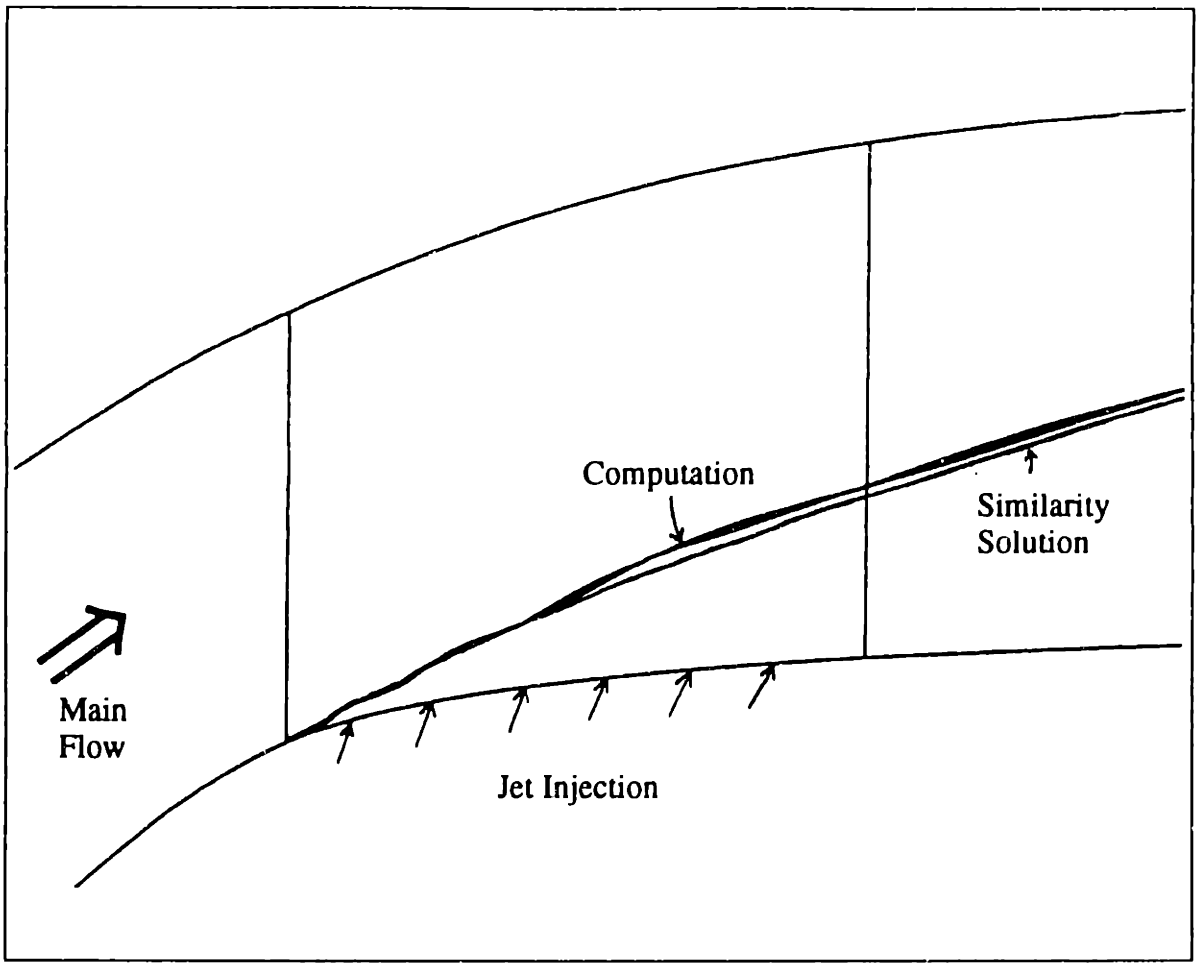

Figure B-1: Computational Vortex Trajectory versus Similarity Solution Prediction (from Brookfield, 1993)

Also shown in this figure for comparison is a leakage angle profile from the rotating rig tests. This experimental curve was calculated from the blade loading measured by static pressure taps at 96% span. These two leakage angle profiles were tested under moderate loading conditions and the loss and blockage were calculated for both.

The exit plane blockage that results from a non-uniform leakage angle was 20% greater than the blockage with a constant leakage angle. Associated with this blockage increase was an increase in average loss of 18%. Although data at different loading conditions with both constant and varying leakage angles was not available, this single data point suggests that the wind tunnel model may be in error by as much as 20% on the absolute level of blockage. The effect on the blockage trends, the limiting loading for example, of this assumption of constant leakage angle along the chord was not examined *pre-facto*, but was tested by directly comparing the wind tunnel data to rotating rig experiments. The agree-

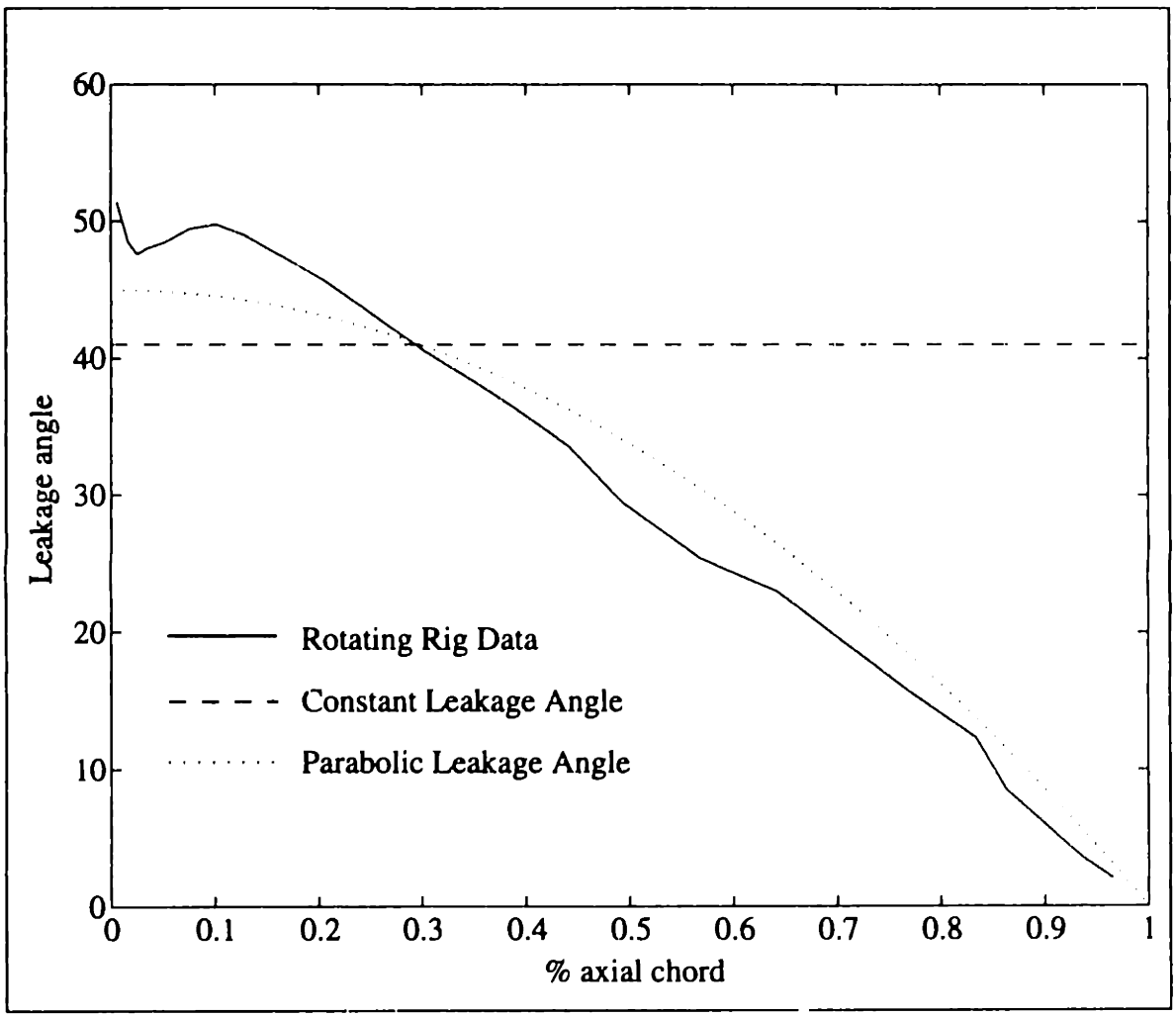

Figure B-2: Wind Tunnel CFD Leakage Angle Profiles

ment between these two data sets to within 7% of limiting loading value, shown in Figure 2-24, suggests that the variation of leakage angle along the chord is of only secondary importance in setting the blockage trends.

The results of the theory of Martinez-Sanchez and Gauthier (1990)[1] also indicate that the variation of leakage angle along the chord is of secondary importance. They model the tip clearance jet-free stream interaction region as a straight line as shown in Figure B-3. The angle the trajectory makes to the suction surface, Θ, is theorized to be equal to half of the angle between the leakage jet and the free stream, α. In their theory they use the average leakage angle to predict the trajectory, and they found good agreement between their pre-

1. Their theory was extended in Section 3.2, but the results described here apply equally to their results and the results of the extended theory.

dictions and various experimental results, suggesting that the variations of leakage along the chord are less important than the average value of leakage angle.

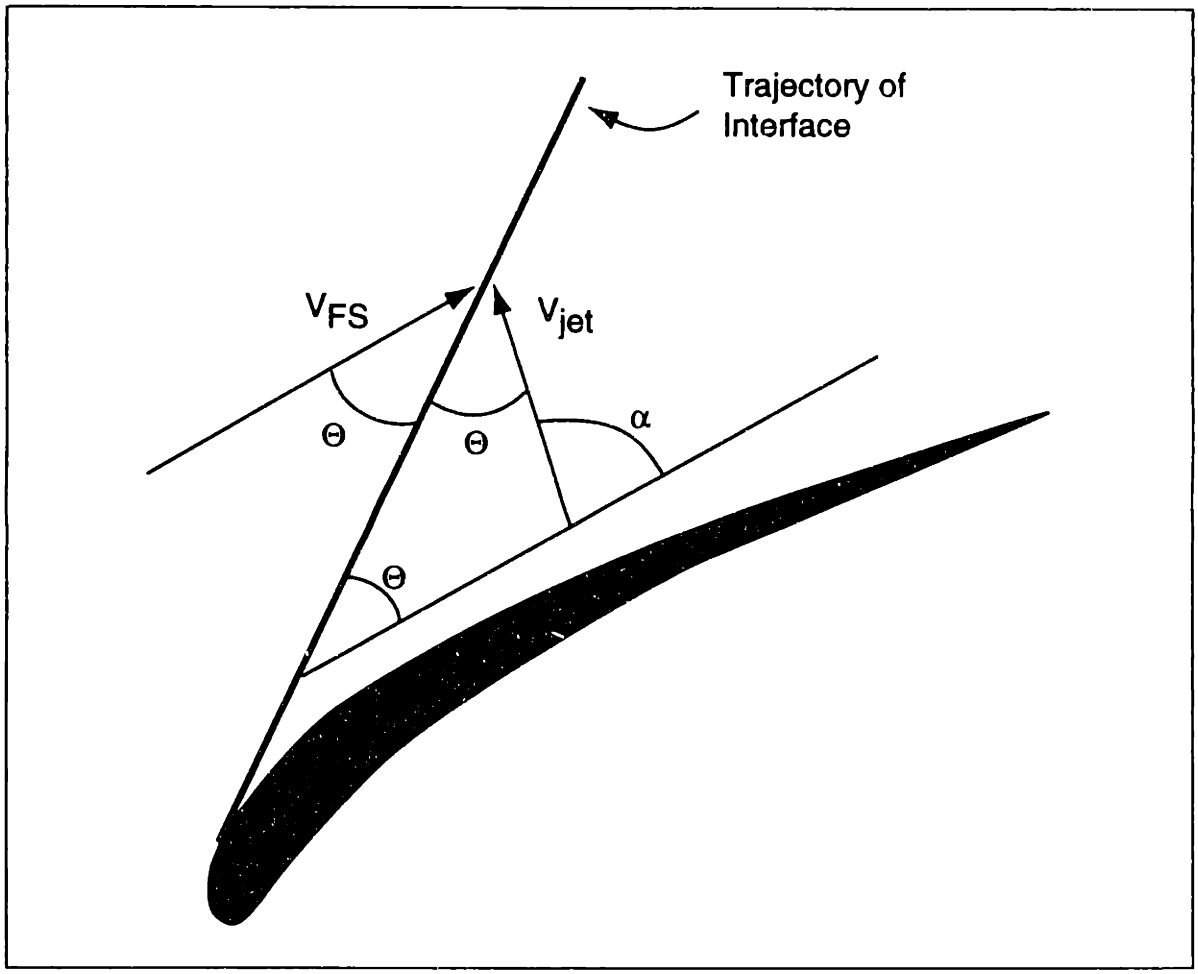

Figure B-3: Martinez-Sanchez and Gauthier Model for Leakage Vortex Trajectory

Further evidence of the small impact on blockage of chordwise variations in leakage angle was found by using the blockage model developed in Chapter 4. The blockages for the low speed rotor cases were calculated both for the actual leakage angles and with the mass average leakage angle assumed along the entire chord. The results of this calculation showed that the difference between these two cases was less than 4% for all loading levels.

B.2 Absence of an Adjacent Blade Pressure Surface

In a compressor blade row there exists a pressure gradient roughly normal to the through flow direction due to the pressure difference between the pressure and suction surfaces

across the blade passage. This normal pressure gradient is important in setting the vortex trajectory as it helps to oppose the leakage jet's cross passage momentum. Brookfield (1993) has shown that the wind tunnel geometry produces a realistic pressure gradient normal to the flow direction, and a comparison of a vortex trajectory observed in the computations to the Chen et al. (1991) theory, which predicts compressor tip leakage vortex trajectories using a similarity argument, agree to within 4% of chord, as was shown in Figure B-1.

Another effect of adjacent bladed in a compressor is a direct influence on the vortex when the leakage vortex travels across the entire passage and impacts the next blade pressure surface upstream of the blade trailing edge. This results in some of the leakage fluid from one tip gap crossing the passage and leaking over into the next blade passage. This double leakage phenomenon is explained in detail in Section 3.2. The primary effect of double leakage is to reduce the total pressure of the clearance jet. The fluid undergoes loss as it travels across the passage into the next tip gap. Because the wind tunnel allows for the total pressure of the jet to be varied independently of any other parameter, the tunnel not only can capture this effect, it can be an effective tool for studying it. This was done in the context of studying the effect of jet total pressure on blockage as it applies to casing treatments. This is described in detail in Section 5.3.

B.3 Pressure Driven Jet

There is some disagreement in the literature as to the relative magnitudes of the forces driving the leakage jet. In the relative frame of the compressor rotor, the casing is moving in the same direction as the leakage jet, suggesting that viscous forces may act to "drag" fluid through the clearance gap. There are a number of pieces of evidence that strongly suggest that for most compressor blades the pressure force across the blade is much larger than the viscous force, and these are reviewed below.

Experimental evidence for the primarily inviscid nature of the leakage phenomenon was given by Storer (1991). His measurements of the radial distribution of the flow velocity

exiting the clearance gap of a linear cascade show that the region of viscous influence is contained within the 20% of the clearance gap closest to the endwall.

Another piece of experimental evidence is from Moyle (1991), who presents data purported to be contradictory to this assumption. He measured wall shear on the casing beneath a compressor rotor and found a region just under the blade tips of zero wall shear. He inferred from this that the fluid must be moving at wall speed, and hence was being strongly influenced by viscous forces. However when a pressure driven velocity prediction based on the blade pressures presented in Moyle (1991) is computed one finds that a pressure driven leakage jet would have approximately 96% of wall speed. Rather than undermining the idea that compressor leakage jets are primarily pressure driven, Moyle's data actually supports it.

Further support for the pressure driven nature of the clearance jet can be found in the results of the leakage vortex trajectory analysis of Chen, et al. (1991). They assume that the leakage flow is entirely pressure driven, and their predictions of the leakage vortex trajectory are within 20% of the actual trajectories for a broad range of compressor configurations. This agreement supports their original assumption that the jet is pressure driven.

The pressure driven/viscous driven question was also briefly examined by Khalid (1995). He computed a predicted clearance mass flux as a function of chordwise distance based on the assumption that the jet was entirely pressure driven. He then compared this mass flux to what was actually computed by the Navier-Stokes solver. This comparison is replotted in Figure B-4, which shows agreement between actual and pressure-driven mass flux to within 6%.

One further piece of evidence for the applicability of the assumption that the leakage jet is pressure driven comes from an analysis done by Chen (1991). By examining the ratio of the pressure driven velocity magnitude to the velocity that would be produced due to viscous forces alone, Chen derives a relation between the clearance to chord ratio and the Reynolds number based on chord and inlet relative velocity. The relation can be used to indicate when viscous forces will be important in the leakage flow and when they can be

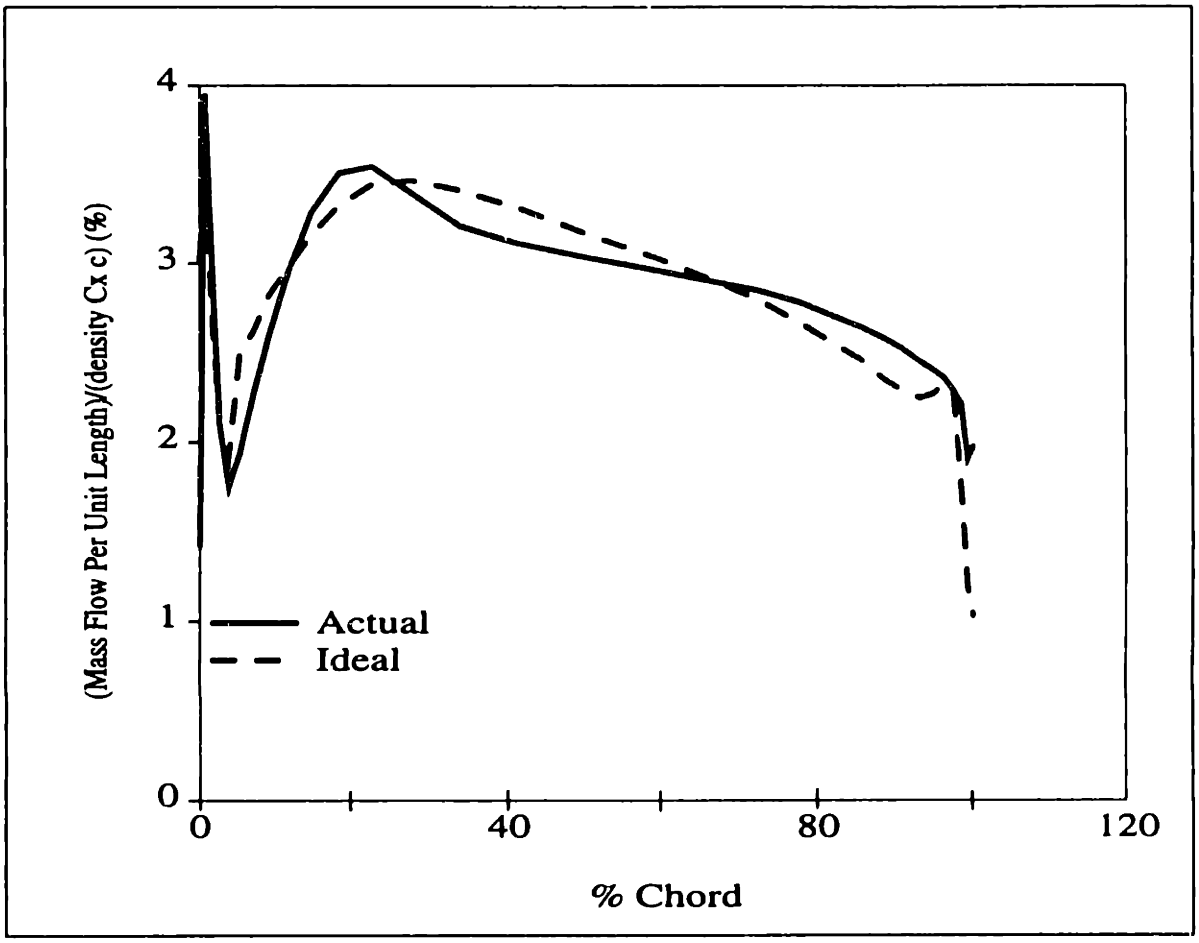

Figure B-4: Pressure Driven versus Actual Clearance Mass Flux, from Khalid (1995)

ignored. For

$$\frac{\tau}{c}\sqrt{Re} \geq 2.3 \tag{6.1}$$

the wall effects will be small (the velocity due to viscous effects will be less than one tenth the pressure driven velocity). For the low speed rotor calculations, $\frac{\tau}{c}\sqrt{Re} = 8.3$, and for the rotating rig experiments described in Section 2.3 $\frac{\tau}{c}\sqrt{Re} = 5.5$[1]. Based on this analysis, in the parameter range of interest, the leakage jet can be considered to be predominately pressure driven.

1. In the experiments of Moyle (1991), this factor is greater than 4.0, also indicating that the leakage jet was primarily pressure driven in these experiments.

Evidence from a variety of sources, both experimental and theoretical, suggest that for the compressors examined in this thesis the leakage jet is primarily pressure driven. Viscous forces are expected to have a negligible influence on the leakage velocity. Therefore the lack of a moving endwall in the wind tunnel model is not an impediment to its usefulness.

B.4 Vortex Pair Asymmetry

The jet in the wind tunnel rolls up into a pair of counter-rotating vortices. Observations with smoke flow visualization and measurements of blockage and loss indicated slight asymmetries between the two vortices. Typically the differences in blockage were on the order of 10%. The fact that the experimentally observed trajectory of the vortex pair, which is a strong function of vortex strength, compares to within 4% of CFD simulations (as in Figure B-1), where the second vortex is an image vortex and hence the pair is perfectly symmetrical, which indicates that the asymmetry does not significantly influence the vortex dynamics. The effect of the tunnel asymmetry on the presented results is also mitigated by averaging. For each test run, the blockage and loading parameters of both vortices were averaged together. Because of the averaging and the agreement in trajectory, the observed vortex asymmetry was not considered a significant difference between the wind tunnel flow field and a compressor endwall flow field.

B.5 Pressure Gradient

The streamwise pressure gradient produced by the tunnel was similar but not precisely the same as that produced in the compressor blade row. To estimate the effect this difference would have on blockage growth, the two-dimensional wake theory of Hill, et al. (1963) was used. This integral wake model is described in detail in Appendix D, and it provides an integral expression for the development of a wake passing through a pressure gradient. The growth of a wake representative of a tip clearance flow, with a minimum velocity 30% of the free stream, was calculated for the two pressure profiles shown in Figure B-5, one based on static pressure taps in the wind tunnel and the other from a CFD solution of the

E^3 rotor.

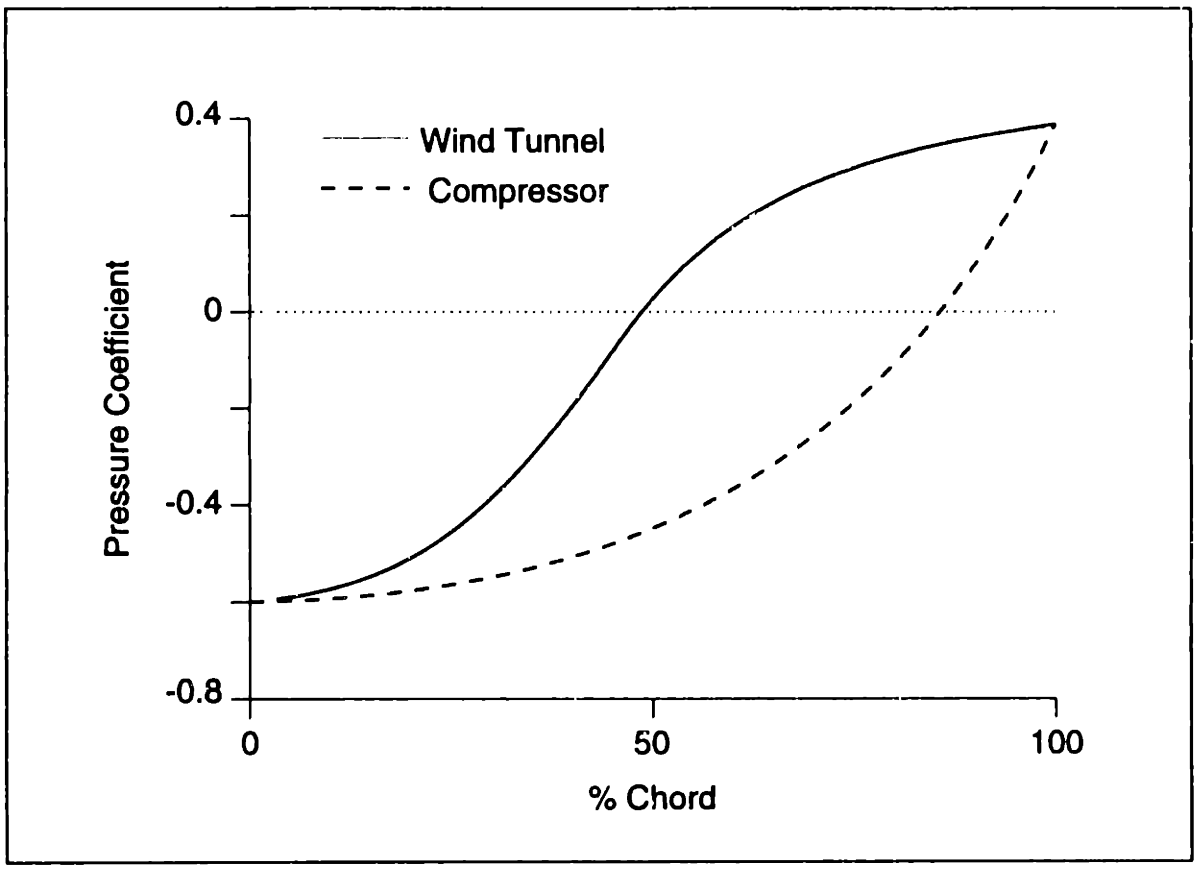

Figure B-5: Streamwise Pressure Gradients

Based on this analysis the difference in blockage between a defect growing in the wind tunnel pressure gradient and one growing in the compressor pressure gradient is expected to be approximately 3%. Thus the difference in streamwise pressure gradient between the wind tunnel and a typical compressor does not compromise the validity of the wind tunnel results. Further, modern controlled-diffusion airfoil blade designs generally have pressure distributions that are more similar to that of the wind tunnel than the distribution used for this comparison, making the impact of this modeling assumption even less significant for these geometries.

B.6 Absence of an Inlet Boundary Layer

The symmetry plane of the wind tunnel acts as a high total pressure boundary, as exists in a compressor, but the wind tunnel lacks an inlet casing boundary layer. These two situa-

tions are shown schematically in Figures B-6and B-7.

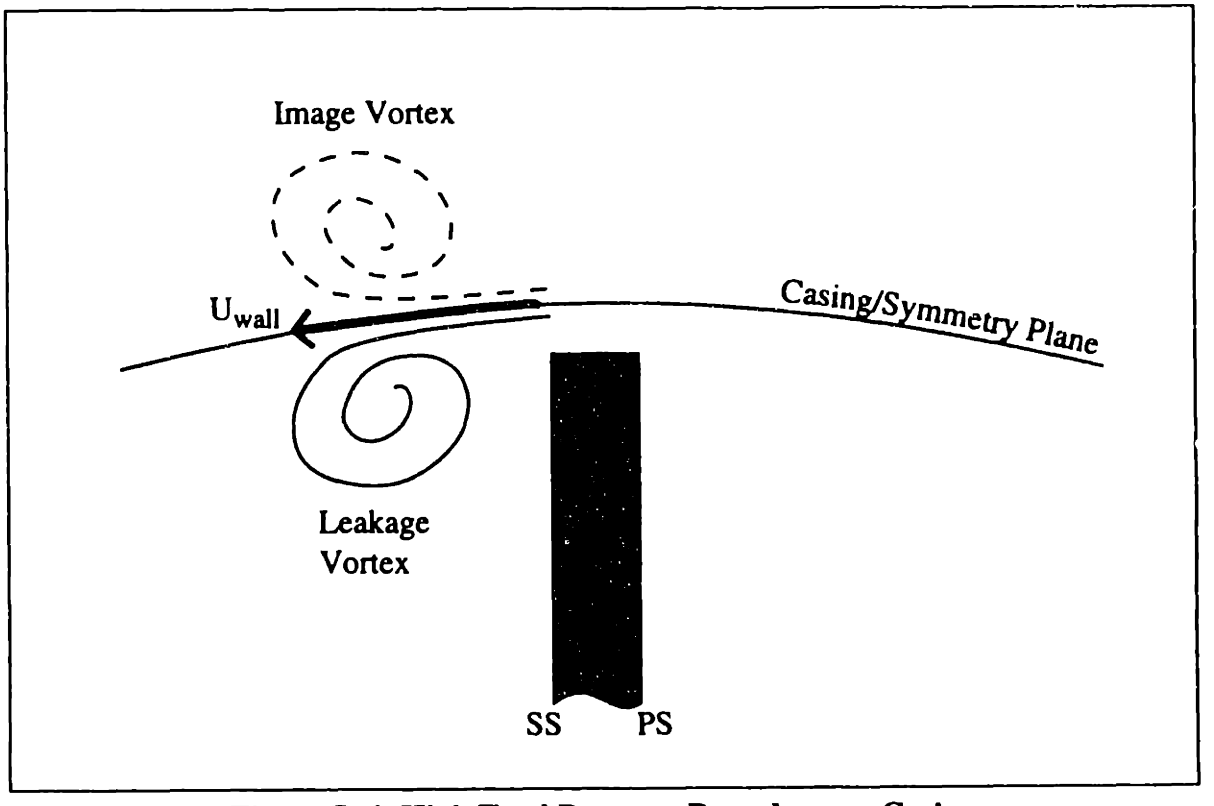

Figure B-6: High Total Pressure Boundary on Casing

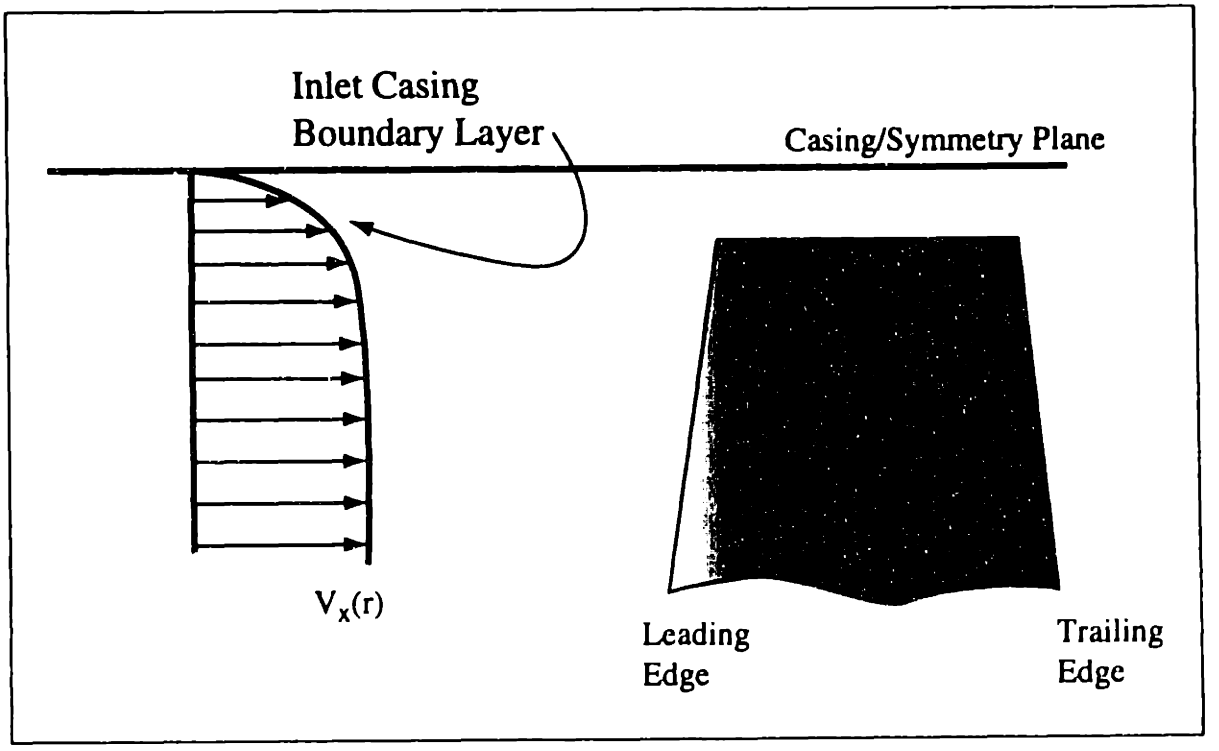

Figure B-7: Inlet Casing Boundary Layer

One of the properties of a compressor casing boundary layer is skew, where the relative flow angle increases rapidly within the endwall boundary layer to 90^0 right at the wall. The wind tunnel model has no mechanism to simulate this inlet skew. However, work done by Storer (1991) suggests that this is not a large factor for determining endwall blockage. Storer used computations to examine flow fields with inlet boundary layer skew and without. He found that the differences are confined to the front 12% of the chord, where inlet skew increased the blade loading at the blade tip (due to increased incidence) and hence increased the local leakage angle. The leakage flow over the majority of the blade was essentially unchanged by the addition of inlet skew.

An inlet casing boundary layer will also effect the endwall flow in a compressor in other ways, as explained in Section 3.3.4. The wind tunnel does not capture these effects, rather they were studied using the computational tools as previously discussed.

B.7 Appendix Summary

The primary assumptions implicit in the wind tunnel model discussed in Section 2.5 have been identified and quantified. The effects of these assumptions on the blockage trends are expected to be small, and the agreement between the wind tunnel and rotating rig data shown in Figure 2-24 supports this conclusion. This evidence suggests that the wind tunnel model does capture the primary flow features that control blockage development, namely the skewed axial slot injection of fluid in an adverse pressure gradient.

Appendix C: Calculation Procedure for Blockage Model and Consistency Checks

This Appendix details the procedures used to quantify the various flow processes in the blockage prediction method described in Chapter 4. The primary assumptions of the model are also discussed and quantified.

C.1 Calculation Procedure

1. **Fluid leaks over the blade tip.** As discussed in Section 3.2, inviscid predictions of the jet leakage angle are not valid for some of the cases studied here because of double leakage. If inviscid methods are used to compute the clearance leakage angle (as in Equation 3.4), the blockage model described in this chapter underpredicts the blockage by as much as 30%. A predictive method is not known for those situations where double leakage occurs, and hence the conditions at the exit of the clearance, the mass averaged leakage angle and total pressure for each chordwise section of the leakage jet were calculated from the Navier-Stokes solutions.

2. **The jet travels in a straight line until it impacts the jet/free stream interaction region or exits the passage.** A three-dimensional schematic of one chordwise section of the leakage jet is shown in Figure C-1, showing the location of a shear layer between the jet and the free stream prior to what is called the interaction region. To calculate the growth of the shear layer between the jet and the free stream, the following equation (from Schlichting, 1960) was used.

$$b = 3\beta^2 \frac{(U_1 - U_2)}{(U_1 + U_2)} x_{mix}, \tag{6.2}$$

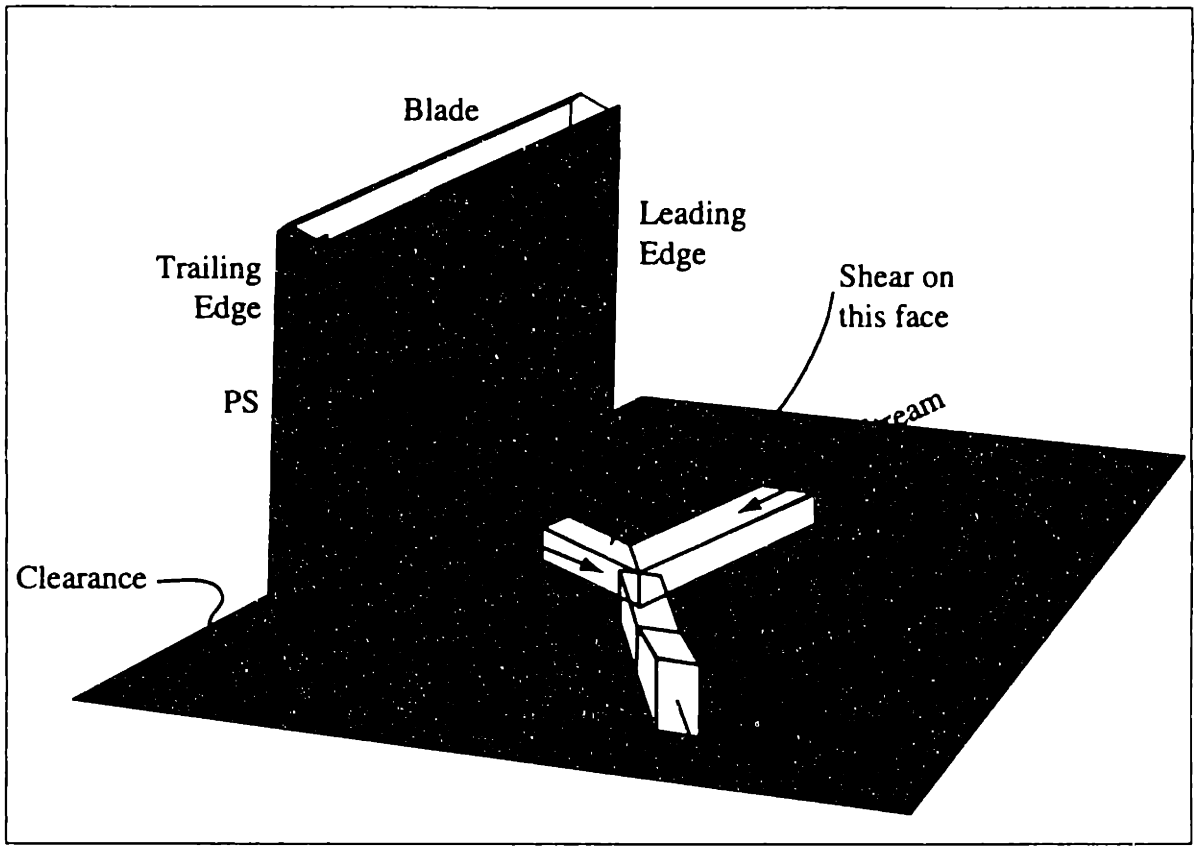

Figure C-1: Three-Dimensional Schematic of Jet-Free Stream Interaction

where b is the shear layer width, β is an empirical constant equal to 0.18, U_1 and U_2 are the velocities of the two streams, and x is the mixing length.

To calculate the mixing length the location of the jet-free stream interaction is approximated as a straight line extending from the blade leading edge at an angle Θ to the blade stagger. Θ was calculated by applying the conservation of cross-vortex momentum to the jet-free stream interaction, as described in subsection 3.2.2. Figure C-2 shows the distance between the blade surface and the interface region, x_{mix}, to be:

$$x_{mix} = x_0 \frac{\cos(\Theta+\gamma) \cdot (\tan(\Theta+\gamma) - \tan(\gamma))}{\sin(\alpha-\Theta)}.$$

The assumption of zero pressure gradient between the clearance exit and the jet-free stream interaction region was examined by computing the static pressure coefficient along streamlines released from the clearance exit and traced downstream. Two representative plots of the pressure along a streamline versus the distance along the stream-

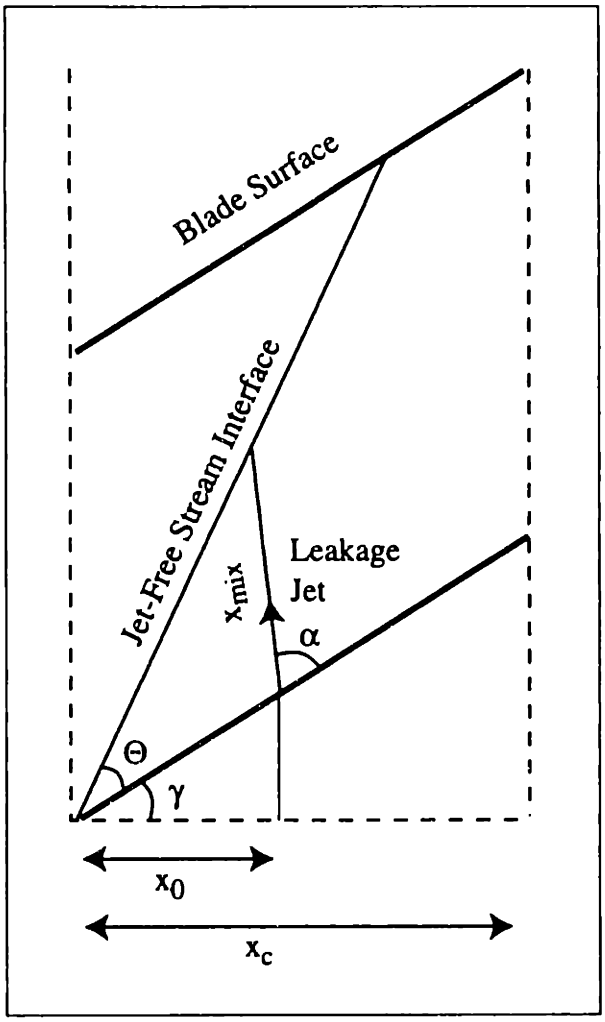

Figure C-2: Schematic for Calculating the Distance to the Interaction Region

line are shown in Figures C-3 and C-4. Both of these plots are from the solution of low speed rotor, moderate loading, large clearance geometry, with the streamlines released from approximately 25% and 50% chord respectively. The location where the streamline intersects the jet-free stream interaction region is marked in both figures.

The integral wake analysis (described in more detail in Appendix D) was used to estimate the growth of a representative velocity defect through the pressure fields shown in Figures C-3 and C-4 (between the clearance exit and the jet-free stream interaction location). A comparison between these predictions and the shear layer growth predicted by Equation 6.2 showed that neglecting the pressure gradient underpredicts the shear layer size by approximately 4% for the 25% chord streamline and 9% for the

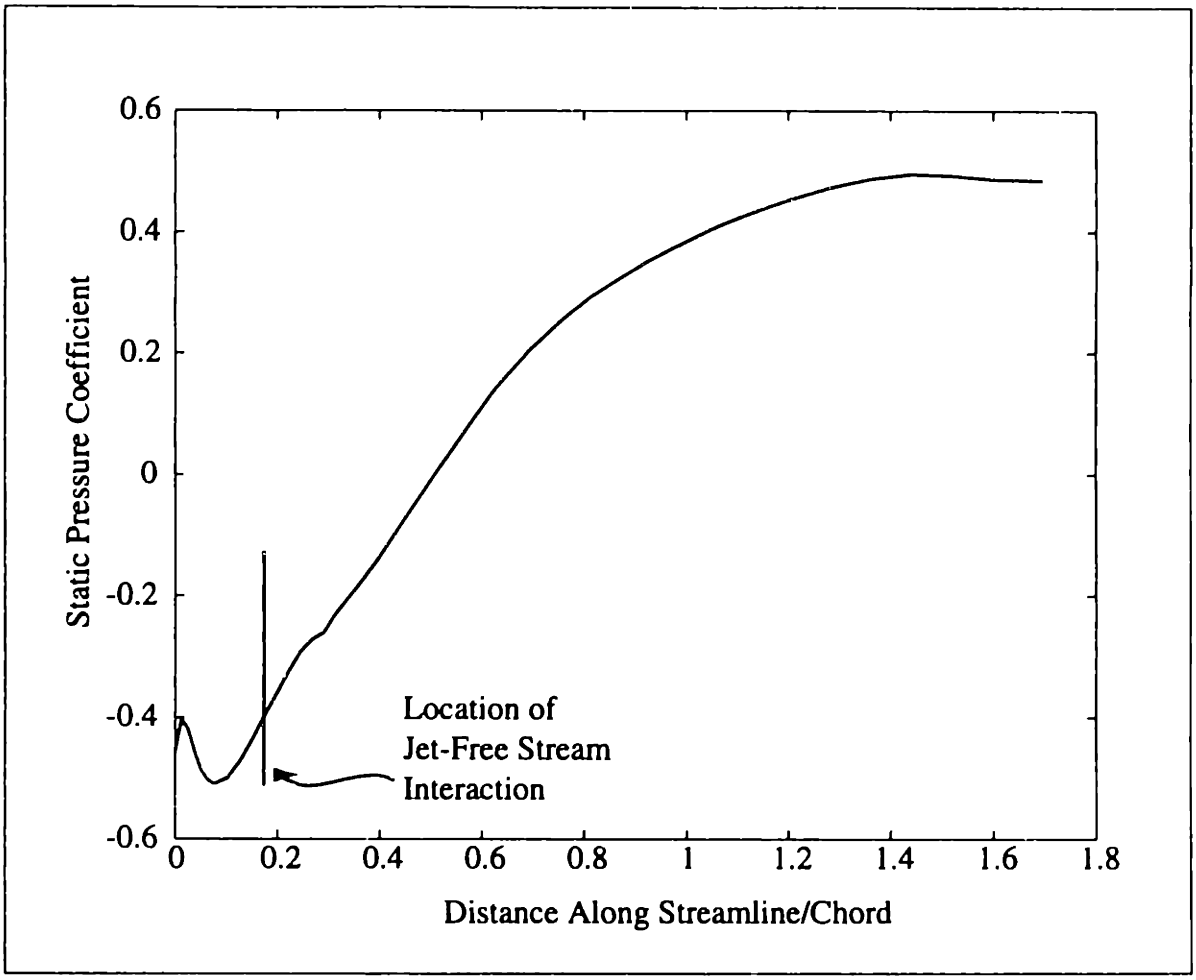

Figure C-3: Static Pressure Along a Streamline Released from the Clearance Exit, 25% Chord

50% chord streamline. These differences would to cause the blockage prediction to be between 5% and 8% too low. Relative to the other assumptions described below, the effect of this assumption on blockage is small.

3. **The jet and the free stream interact.** To quantify the results of the jet-free stream interaction a control volume analysis is used, as described in subsection 3.2.3. The schematic of the control volume was given in Figure 3-11. The direction of the vortex trajectory, determined by balancing the cross-vortex momentum, was given by Equation 3.7.

   The cross-vortex momentum balance results in a uni-directional flow in the direction of the vortex trajectory. The kinetic energy of the velocity components normal to the resulting direction are dissipated. In applying the mixing model, the velocity defect

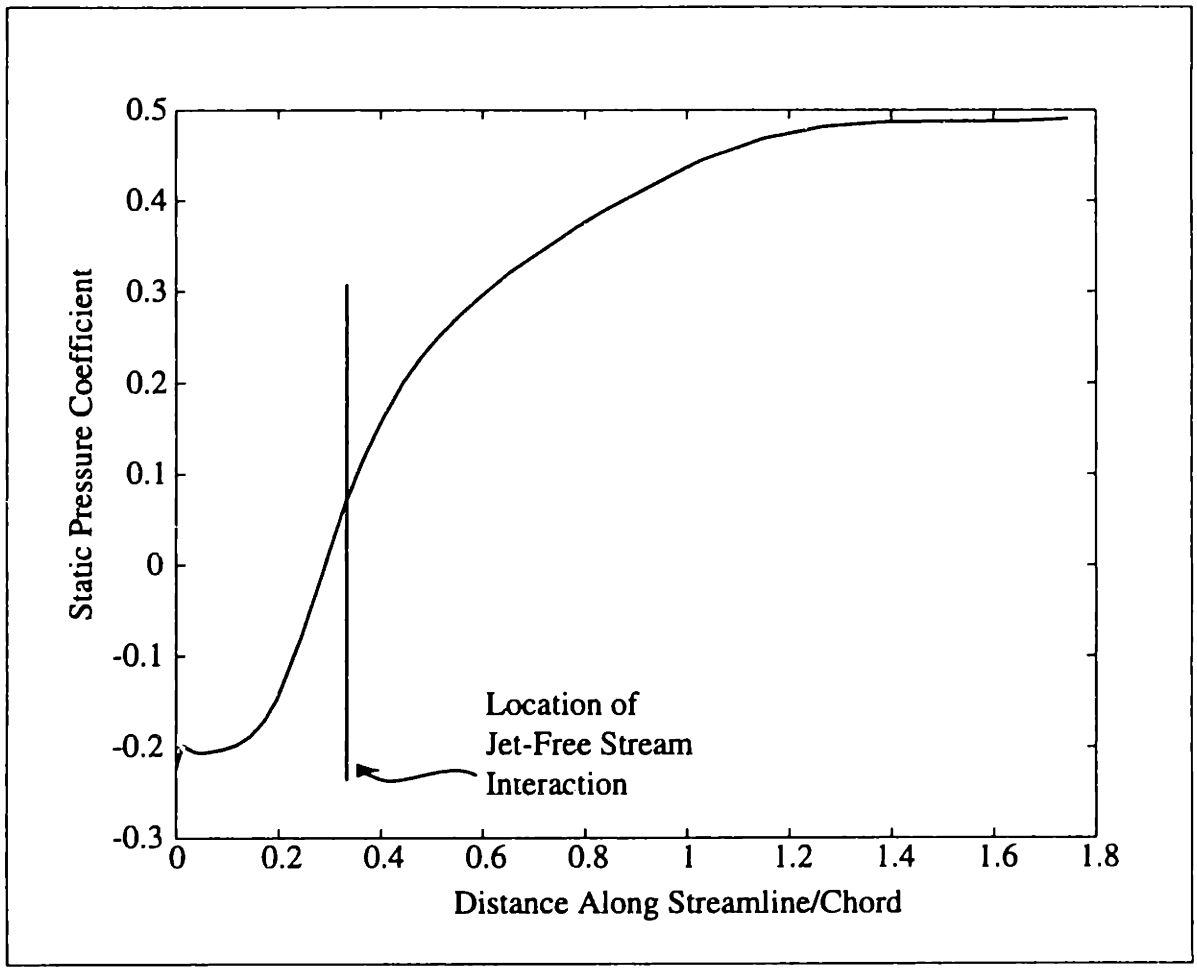

Figure C-4: Static Pressure Along a Streamline Released from the Clearance Exit, 50% Chord

caused by this dissipation is presumed to have a cosine shaped radial profile of the form

$$\frac{v(r)}{V_{FS}} = 1 - \frac{\beta}{2}\left[1 + \cos\left(\frac{\pi r}{b}\right)\right].$$

The wake depth and height parameters of this equation, β and b, are found by simultaneously solving the conservation of mass and conservation of vortex-trajectory direction momentum equations.

4. **The defect growth is calculated using an integral wake analysis.** The integral wake analysis allows the calculation of the mixing of a velocity defect in a pressure gradient. The assumptions and further details of this approach are explained in Appendix D.

Three inputs are required; an initial wake depth and height, and the ratio of the initial and final free stream velocities.

The initial wake depth and height are calculated as described in Section 4.2. Bernoulli's equation was used to calculate the free stream velocity ratio from the initial and exit static pressures. To eliminate the effect of streamline curvature very close to the clearance exit, the initial free stream static pressure was chosen to be the pressure on the blade suction surface two clearance heights inboard of the location from which the jet section originated. The final pressure was set equal to the exit plane blockage region area average static pressure. The mixing distance is calculated along the interface line as shown in Figure C-2. If this line intersects the adjacent blade pressure surface, the distance along the blade pressure surface to the passage exit was used.

C.2 Consistency Evaluation

An assumption of this model is that the static pressure change from the jet-free stream interface, where the velocity defect is presumed to be formed, to the passage exit can be approximated by the static pressure change from the blade surface to the passage exit. This assumption was assessed by comparing the blockage growth of a representative velocity defect experiencing the actual and the assumed static pressure rises. Figures C-5 and C-6 replot the streamline static pressure traces from Figures C-3 and C-4 with the static pressure distributions used in the model. The integral wake analysis used with the assumed pressure distribution produced an exit blockage 11% smaller than that using the actual pressure distribution for the 25% chord streamline, and a 38% smaller blockage for the streamline released from 50% chord. Because the depth of the velocity defect examined here was representative of most of the computed clearance jets, the magnitude of the effect of the pressure gradient assumption is also representative. Hence the assumptions about the static pressure distribution in the model are expected to cause an underprediction of blockage.

Another implicit assumption in the model is that all of the clearance jet fluid contributes to

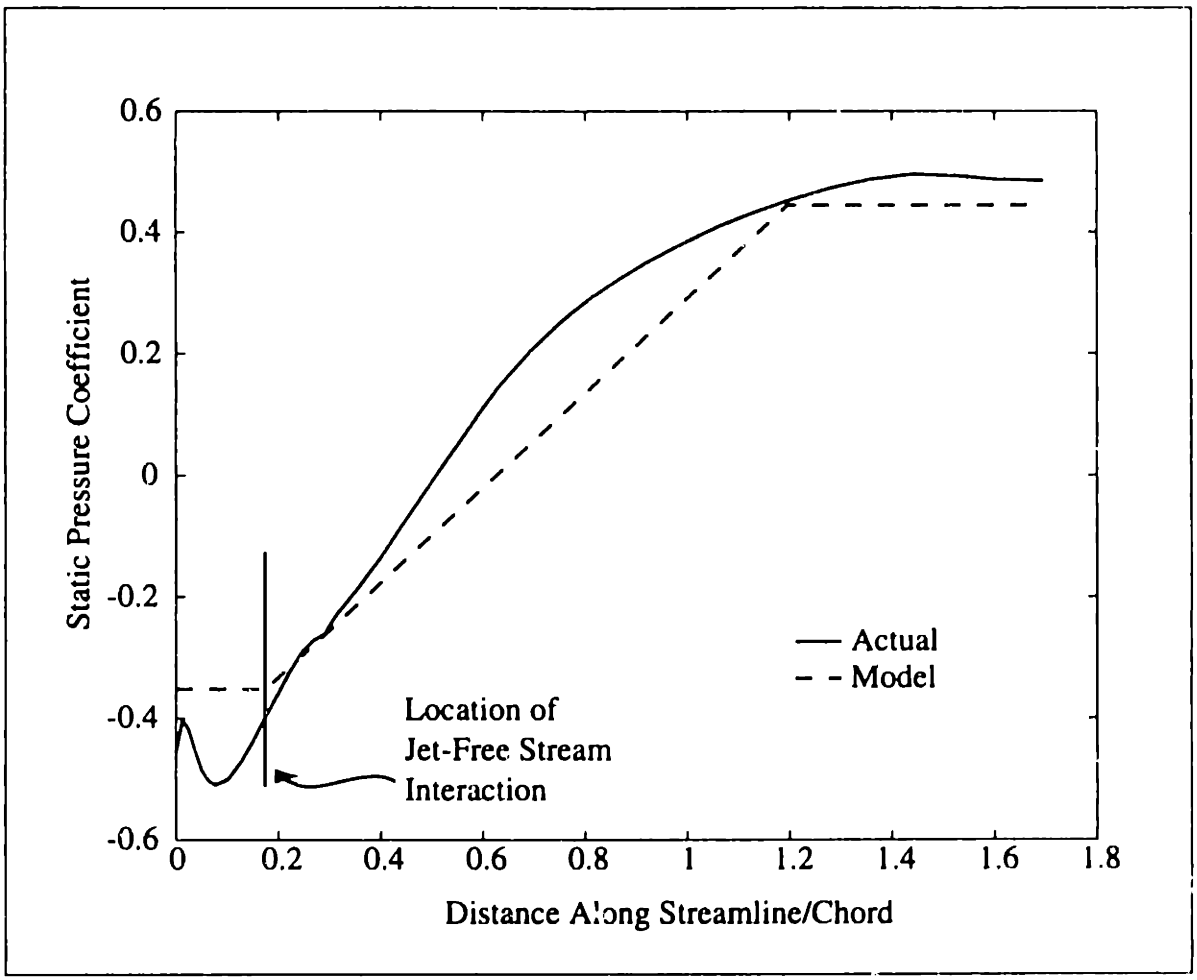

Figure C-5: Actual and Modelled Static Pressure Distribution Along Streamline Released from 25% Chord

the exit plane blockage. As discussed in subsection 3.3.5, fluid from one clearance gap crosses the passage and enters in the clearance gap of the adjacent blade in some cases. The blockage model does not account for double leakage. The model double counts the blockage contribution of any double leakage fluid, tending to cause the model to overpredict the actual blockage for cases where double leakage occurs. The results of the model, presented in the following section, suggest that this overprediction is at most 20% for the cases examined here.

As discussed in subsection 3.3.7, the effect of swirl is to increase tip clearance related blockage by approximately 5%. The blockage model described in this chapter does not account for swirl in the flow, and hence a 5% underprediction is expected to contribute to the overall inaccuracy of the model.

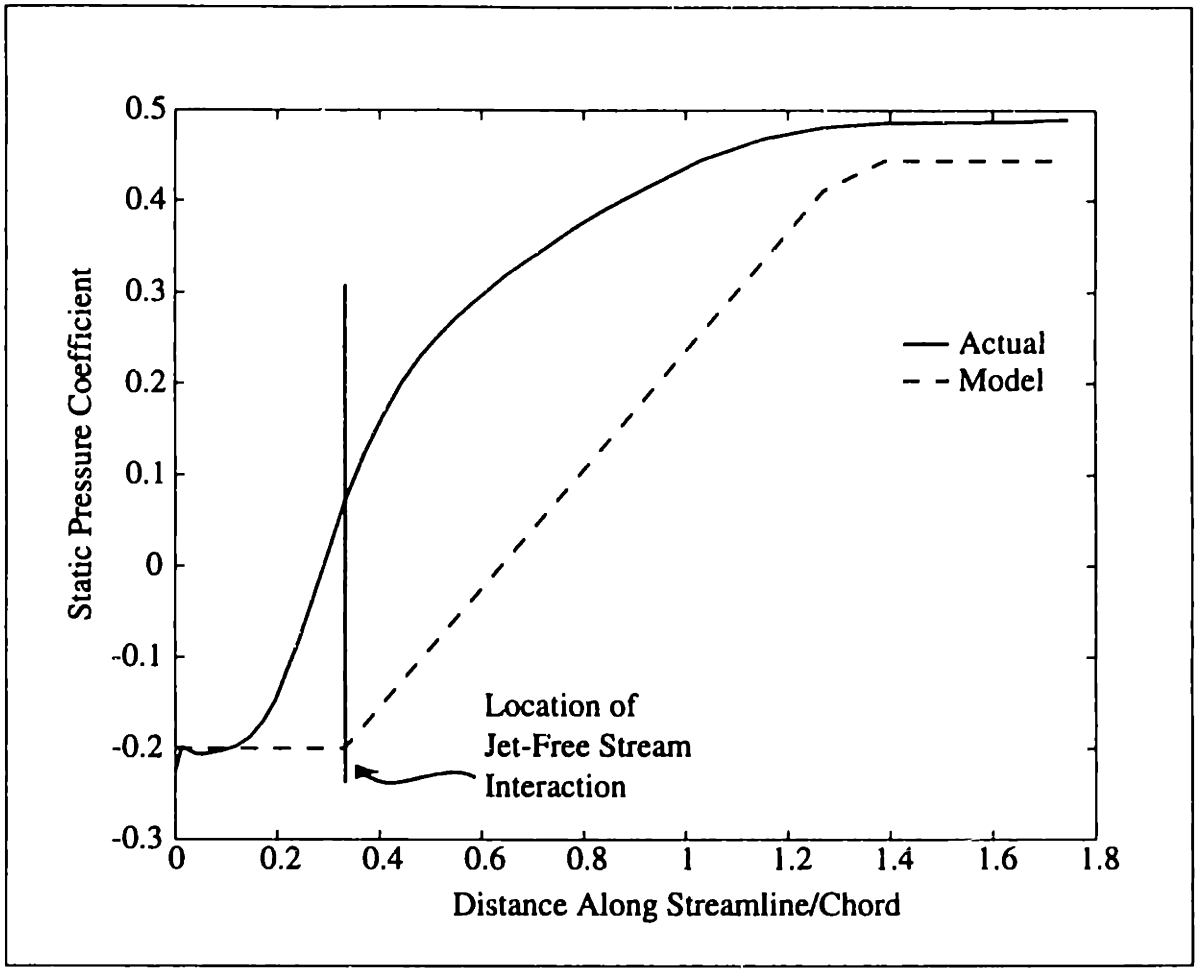

Figure C-6: Actual and Modelled Static Pressure Distribution Along Streamline Released from 50% Chord

The error introduced by neglecting double leakage was approximated by plotting the contribution to the total blockage from each chordwise section. Sections of the clearance jet that leak into the adjacent tip gap do not contribute to the exit plane blockage. Streamline traces identified the double leakage locations. The estimated contribution to blockage from these locations is an approximation for the error introduced by neglecting double leakage.

In Figure C-7 the fraction of the total blockage versus fraction of chord for the low speed rotor, high loading, large clearance case (the case with the most double leakage) is shown. The blockage is presented as a running total. Streamline traces from this case were shown in Figure 3-4, with streamlines that exit the passage shown dashed, and those that leak into the adjacent passage shown as solid lines. At all chordwise locations the streamlines

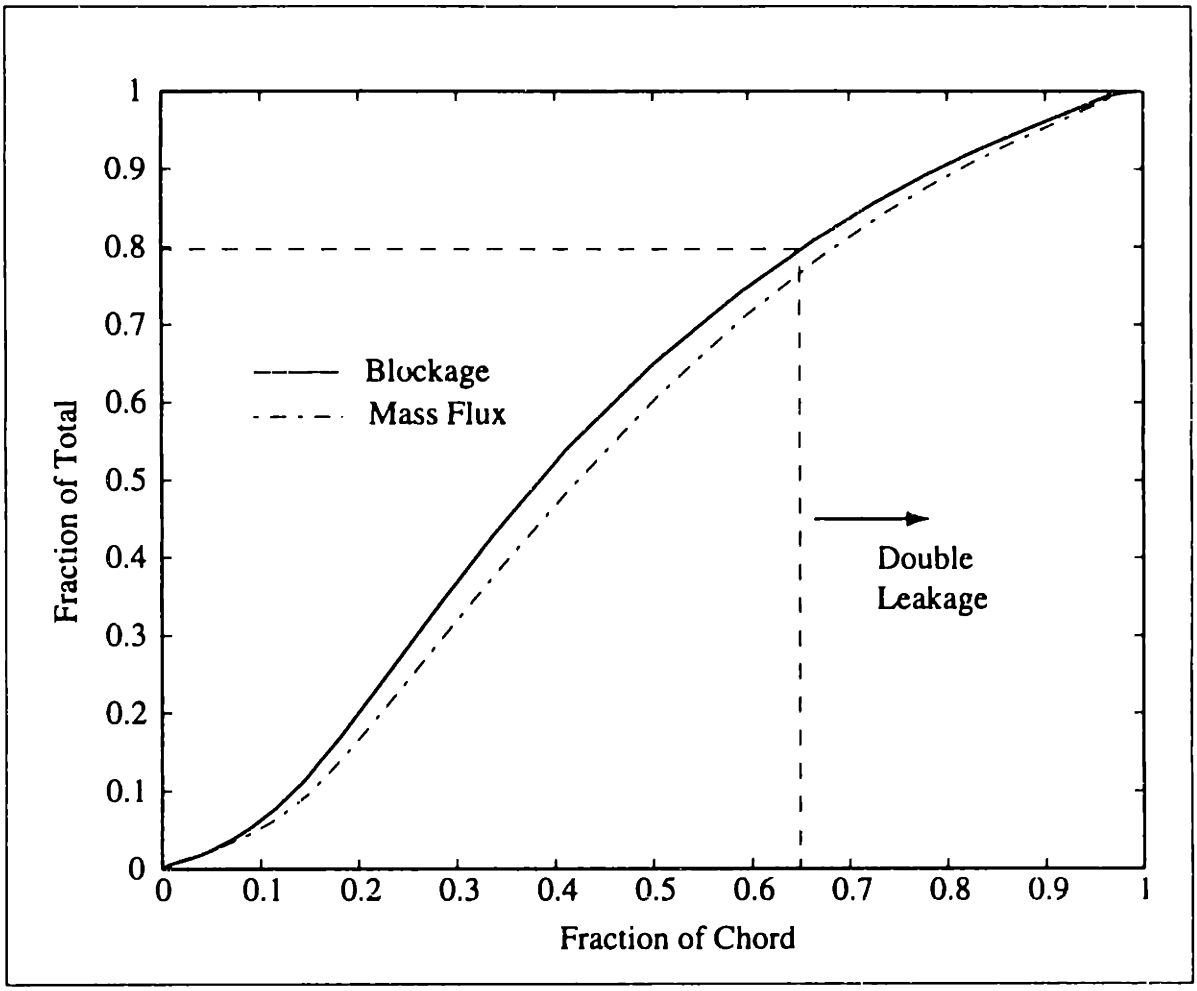

Figure C-7: Chordwise Contributions to Blockage and Total Mass Flux from Low Speed Rotor, τ/c=3.0%, Near Stall

released closest to the casing double leak. From approximately 65% chord downstream all clearance jet fluid passes into the adjacent clearance gap. Figure C-7 shows that approximately 20% of the total exit plane blockage is attributed to fluid that actually never exits that passage. This is the for the case with the most double leakage, setting an upper bound on this error.

A balance between the errors due to neglecting double leakage and due to the pressure gradient assumptions provides an explanation for the model's more accurate calculation of the increased solidity blockages than the nominal solidity cases. For similar passage loading conditions the increased solidity geometries have more double leakage than the nominal solidity cases (see Figure 3-25). Thus the overprediction error due to neglecting the double leakage was larger than in the nominal solidity cases, causing the model to

more closely predict the blockage for the high solidity cases.

Appendix D: Integral Wake Model

D.1 Description

To model the growth of a velocity defect in an adverse pressure gradient the integral wake model of Hill et al. (1963) was used. This appendix briefly describes the model and the primary results as they apply to the interaction of the clearance jet and the free stream.

Hill et al. performed experiments in which the wakes from a two-dimensional bluff body in a uniform stream were subjected to various pressure gradients. It was found that the wake profiles at all downstream locations could be collapsed in terms of the wake depth, β, and width, b as shown in Figure D-1, which is from Hill et al. (1963).

The wake depth parameter, β, is defined as:

$$\beta \equiv \frac{U - u_c}{U},$$

where U is the free stream velocity and u_c is the wake centerline velocity. A suitable curve fit to the similar wake profile was found to be

$$\frac{U - u}{\beta U} = \frac{1}{2}\left[1 + \cos\left(\frac{\pi y}{b}\right)\right]. \qquad \text{(D.1)}$$

Using Equation D.1 and the assumptions of two-dimensional, incompressible flow, $\beta << 1$, shape factor near unity, and a constant value of the eddy viscosity, ε, normalized by the product of the wake momentum thickness and the local free stream velocity Hill et al. evaluate the integral streamwise momentum and the moment of momentum equations.

The assumption about the eddy viscosity, namely that

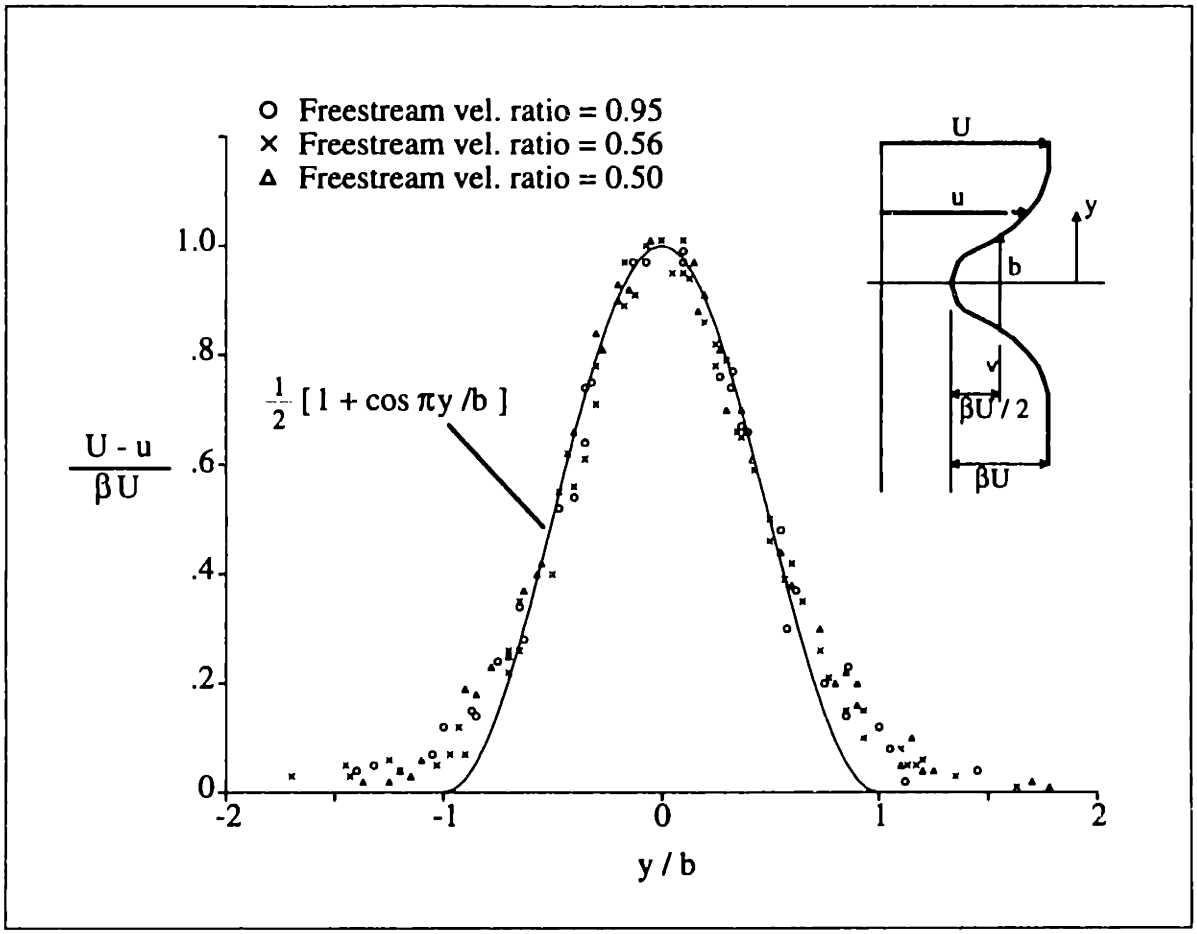

Figure D-1: Normalized Wake Profiles, from Hill et al. (1963)

$$\frac{\varepsilon}{U\Theta} = \text{constant}$$

has been verified experimentally by Schlichting (1960) and Clauser (1956), among others.

Using these assumptions the ratios of the final to initial wake parameters are:

$$\frac{\beta}{\beta_0} = \left(\frac{U_0}{U}\right)^2 \left[1 + \frac{8\pi^2}{\pi^2 - 4}\left(\frac{\varepsilon}{U\Theta}\right)\int_{x_0} \frac{U_0}{U} d\left(\frac{\beta_0^2 x}{\Theta_0}\right)\right]^{-\frac{1}{2}} \tag{D.2}$$

$$\frac{b}{b_0} = \left(\frac{U_0}{U}\right)^3 \frac{\left(\frac{1}{\beta_0} - \frac{3}{4}\right)}{\left(\frac{1}{\beta_0} - \frac{3}{4}\frac{\beta}{\beta_0}\right)\frac{\beta}{\beta_0}}. \tag{D.3}$$

Assuming that $b_0 \approx \delta$, Equation D.1 can be substituted into the definition of momentum

thickness to give:

$$\frac{\Theta_0}{b_0} = \beta_0 - \frac{3\beta_0^2}{4}. \tag{D.4}$$

Hill et al. (1963) found that their results matched experimental data to within 10% for β_0 as large as 0.5 over a wider range of pressure gradients than exist in the compressor endwall flow field.

D.2 Application to Compressor Flow Fields

Because a goal of the model described in Chapter 4 is to predict endwall blockage without requiring a three-dimensional Navier-Stokes solution, some approximations are used to solve Equation D.2, rather than using the Navier-Stokes solutions to provide "exact" values. It is assumed that the static pressure along the blade and the passage exit pressure, would be known *a priori*, and the implementation scheme uses these values to approximate U(x) in Equation D.2.

Following Khalid (1995a), the assumption is made for the application of this model to compressor tip clearance flows that the velocity change from its initial value, assumed to be approximately at the clearance exit, to its final value at the passage exit is linear in x. The initial to final velocity ratio is calculated by assuming that the free stream is inviscid and incompressible, so that

$$\frac{U(x)}{U_0} = \left(\frac{U_{final}}{U_0} - 1\right)\frac{x}{x_{total}} + 1\text{, where} \tag{D.5}$$

$$\frac{U_0}{U_{final}} = \sqrt{\frac{P_T - P_{SS}}{P_T - P_{exit}}} = \sqrt{\frac{1}{1 - \dfrac{P_{exit} - P_{SS}}{P_T - P_{SS}}}} = \sqrt{\frac{1}{1 - CP_S}}. \tag{D.6}$$

Substituting Equation D.5 into Equation D.2 and carrying out the integration yields

$$\frac{\beta}{\beta_0} = \left(\frac{U_0}{U_{final}}\right)^2 \left[1 + \frac{8\pi^2}{\pi^2 - 4}\left(\frac{\varepsilon}{U\Theta}\right)\left(\frac{\beta_0^2 x_{total}}{\Theta_0}\right)\frac{\frac{U_0}{U_{final}}\ln\left(\frac{U_0}{U_{final}}\right)}{\frac{U_0}{U_{final}} - 1}\right]^{-\frac{1}{2}} . \qquad \text{(D.7)}$$

Equations D.3, D.4, D.6, and D.7 were used as the model for a velocity defect growing in an adverse pressure gradient. The inputs needed for this model are the initial and exit pressures, P_{SS} and P_{exit}, the length over which the mixing and the pressure gradient takes place, x_{total}, and the initial wake depth and height, β_0 and b_0. The model outputs are the exit wake depth and width, β and b, from which the blockage can be calculated.

D.3 Sensitivity Analysis

The blockage calculated from Equations D.6 and D.7 is a function of three variables, the static pressure rise coefficient, CP_S, the initial wake depth, β_0, and a mixing parameter equal to the product of the eddy viscosity parameter and the mixing length normalized by the initial wake height, $\left(\frac{\varepsilon}{\Theta U}\right)\cdot\frac{x}{b_0}$. A sensitivity analysis was done by holding one of these parameters constant and plotting contours of blockage as the other two parameters change. The ranges examined were determined by evaluating the three parameters at various chordwise locations, for large and small clearance geometries, and at low and high loading conditions. CP_S was found to vary between 0.0 and 0.88, β_0 between 0.0 and.56, and the mixing parameter between 0.1 and 5.1. For all cases studied the value of the $\left(\frac{\varepsilon}{\Theta U}\right)$ was taken, as in Schlichting (1960), to be 0.044.

In each of Figures D-2, D-3, and D-4 the labeled contours indicate the exit blockage of the wake after it has passed through the pressure gradient, normalized by the initial blockage of the wake. Figure D-2 shows blockage contours for various mixing parameter and CP_S values with an initial wake depth fixed at 0.15, a depth representative of the clearance jet at low loading. It was observed that the maximum value of the mixing parameter was

approximately 5.0 (near the leading edge of the blade for the small clearance geometry). Near the trailing edge of the blade this parameter was its minimum value of approximately 0.1. Where $\beta_0 \approx 0.15$, the static pressure coefficient varied between 0.2 and 0.65. Figure D-2 shows that, for β_0=0.15, the blockage is relatively insensitive to changes in the mixing parameter, and somewhat sensitive to changes in pressure rise, with a 10% increase in CP_S resulting in approximately a 20% increase in blockage at the higher loadings.

An estimation with a deeper initial defect, represented by β_0=0.5, is shown in Figure D-3. The most notable difference between this figure and Figure D-2 is that the blockage is more sensitive to changes in pressure rise with this deeper initial defect than with the more shallow wakes, especially at the higher loading values. For the cases examined here, this deep initial defect was present in the clearance jet towards the blade trailing edge, where the total pressure of the jet is much lower than the free stream total pressure (see Figures 3-2 and 3-6). At these chordwise locations CP_S was between 0.1 and 0.2, away from the region where blockage is most sensitive to CP_S.

Another blockage contour map, shown in Figure D-4, was generated by fixing the static pressure rise coefficient at 0.8, approximately the largest value obsereved in the computations, and plotting the variation of blockage with changes in the mixing parameter and β_0. This loading level was chosen as representative of the maximum pressure rise experienced by the leakage fluid. In those regions where this high pressure rise existed β_0 varied between 0.1 and 0.3, and the mixing parameter between 1.0 and 2.0.

These blockage contour maps indicate that over the parameter range observed in the compressor flow field the blockage is almost equally sensitive to the initial defect, β_0 and the pressure rise CP_S. It appears that the sensitivity of blockage to these two parameters is approximately one to one, with a 10% change in one of the parameters causing about a 10% change in blockage. The blockage does not appear to be a strong function of the mixing parameter, $\left(\frac{\varepsilon}{\Theta U}\right) \cdot \frac{x}{b_0}$.

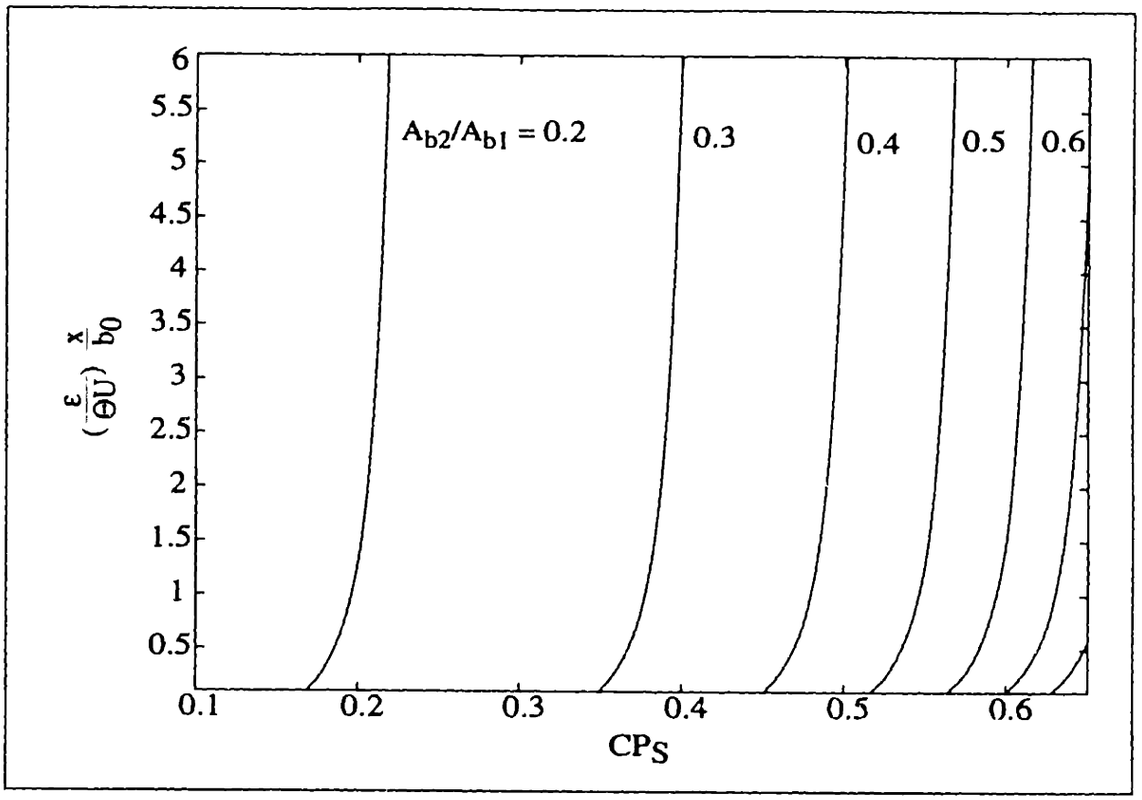

Figure D-2:Blockage Contours from Integral Wake Analysis for β_0=0.15

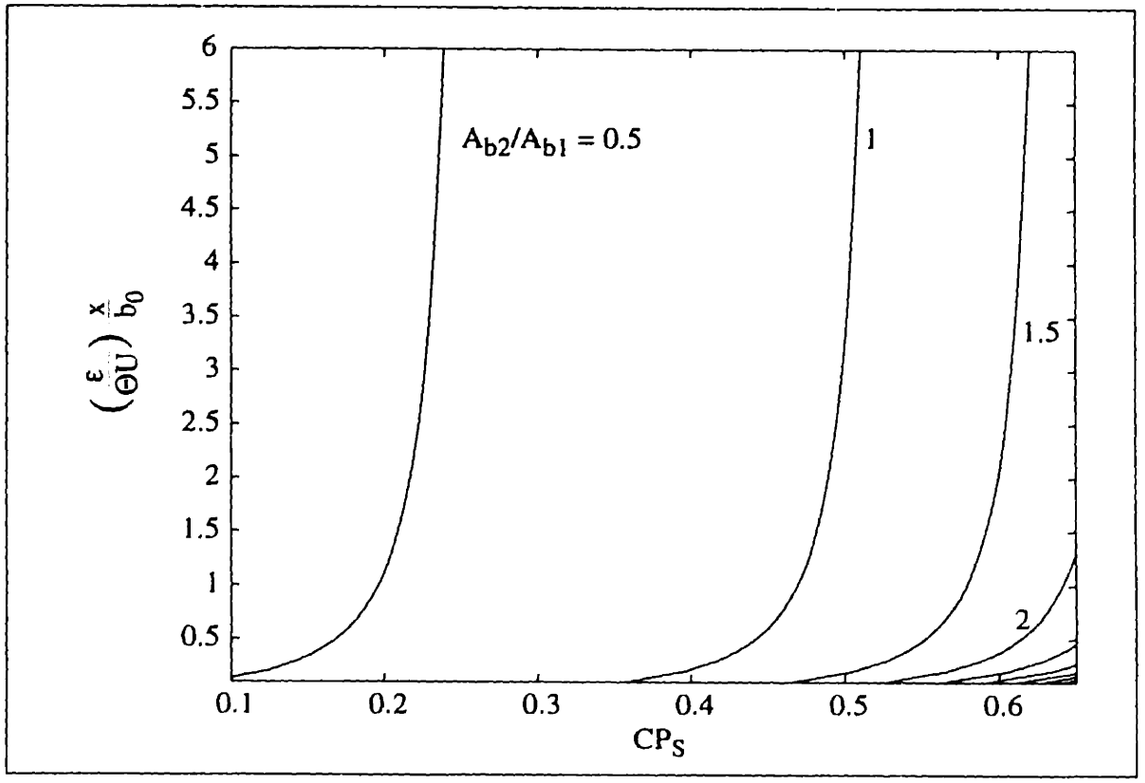

Figure D-3:Blockage Contours from Integral Wake Analysis for β_0=0.50

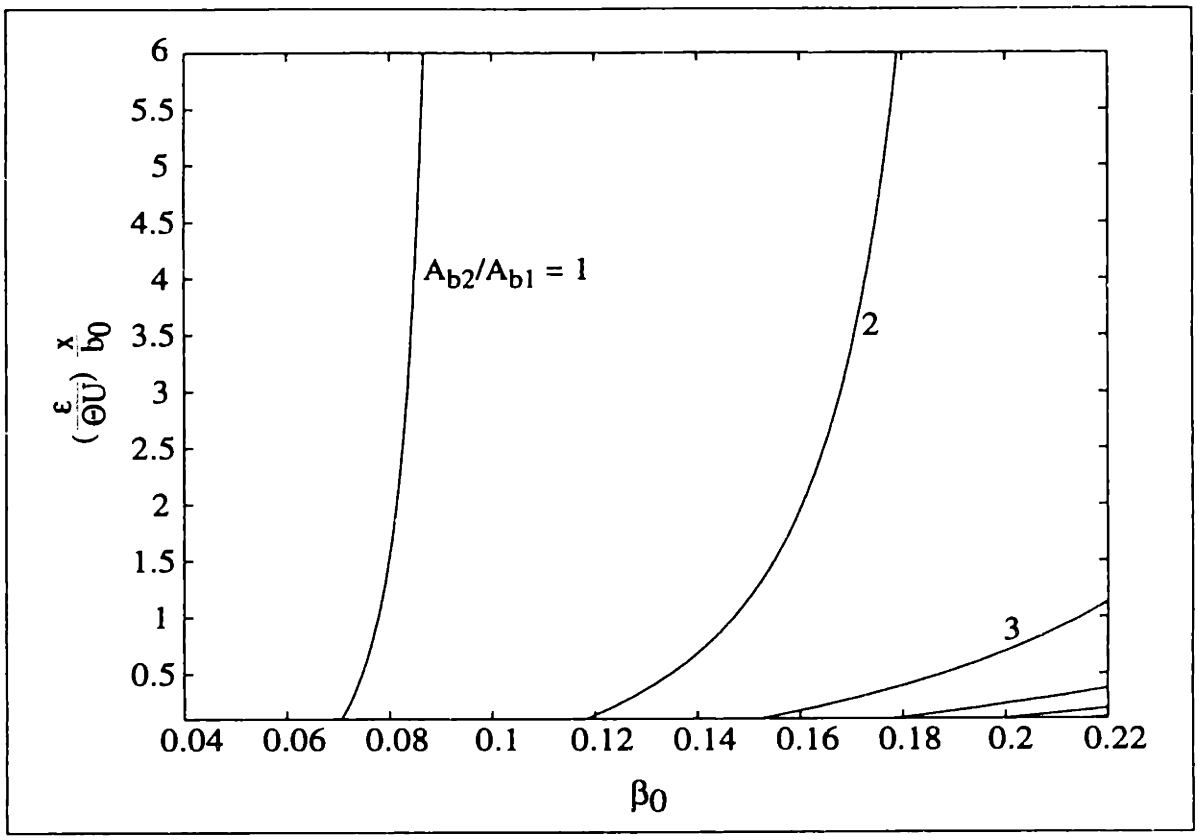

Figure D-4:Blockage Contours from Integral Wake Analysis for CP_S=0.8